Studies in Vibrofluidized Beds and Synthesis of Silica Catalysts

by

Renato Sprung

Dissertation submitted to the Faculty of the

Virginia Polytechnic Institute and State University

in partial fulfillment of the requirements for the degree of

Doctor of Philosophy

in

Chemical Engineering

APPROVED:

Arthur M. Squires, Co-Chairman

A. Liu, Co-Chairman

Mark E. Davis

Thomas E. Diller

James P. Wightman

George B. Wills

August, 1987

Blacksburg, Virginia

Studies in Vibrofluidized Beds and Synthesis of Silica Catalysts

by

Renato Sprung

Arthur M. Squires, Co-Chairman

Y. A. Liu, Co-Chairman

Mark E. Davis

Chemical Engineering

(ABSTRACT)

The effect of the solid-circulation rate and pattern as well as the air-gap size on heat-transfer coefficients between a horizontal, cylindrical heater and vibrated beds of Master Beads (spherical alumina) and glass spheres was studied. Solid piles were observed to form at specific bed locations. Solid-circulation paths were directed from the shallowest toward the deepest region of the vibrated bed. For beds in which the solid pile formed above the heating surface, local solid-circulation loops were observed above and below the heater. Air gaps developed at the top and bottom of the cylindrical heater. Heat-transfer coefficients of 140-350 W/m^2K in beds of glass spheres and 180-480 W/m^2K in beds of Master Beads were determined for a temperature difference of 30 ^oC between the heater and vibrated bed. The trends in the behavior of the heat-transfer coefficient could be explained in terms of a model that accounted for the air-gap size and particle renewal in the layer closest to the heater. Increased solid-circulation rates improved the heat-transfer performance until larger air-gap sizes eventually compromised any increase in solid circulation.

The expansion of the interlayer spacing of H-Magadiite (a layered silicic acid) by the introduction of pillars containing silicon atoms was investigated. A trisiloxane and two trichloroorganosilane compounds were used as the pillaring agents. The interlayer space of H-Magadiite was successfully expanded by pillaring with trichloroorganosilanes. The minimum dimensions of the pores that access the interlayer space of the pillared compounds were determined as being 6.2 Å and 9.5 Å (dimensions at perpendicular directions). Pillaring of H-Magadiite at low pH and temperatures

close to 0 °C yielded the highest surface areas, e.g., increasing the surface area from 35 to 130-200 m^2/g. The pillared compounds were found to be thermally stable up to temperatures of 650 °C.

Dedication

I dedicate this dissertation to my late parents , my wife and my son .

Acknowledgements

I would like to thank Dr. Arthur M. Squires and Dr. Y. A. Liu for their assistance and the useful discussions during the development of the first part of this dissertation. I am indebted to Dr. Squires for my placement at Virginia Tech and to Dr. Liu for proofreading the first part of the dissertation.

I am profoundly grateful to Dr. Mark E. Davis for his patience in introducing me into the exciting field of catalysis. I am thankful for his advice and guidance during the second part of this dissertation. Our discussions deeply affected my assessment of the importance of catalyst synthesis and testing as well as of catalytic processes.

I would like to acknowledge and thank the following persons for providing assistance during the development of this dissertation. Dr. Carlos Saldarriaga taught me the basics of catalyst synthesis and XRD analysis. He and Consuelo Montes obtained the XRD patterns of the catalytic compounds. Paul Hathaway obtained the Infrared spectra. Leo Lopez performed the SEM microscopy. Riley Chan designed the power supply and built the pressure measuring system utilized in the first part of the dissertation. Benku Thomas, my research partner in vibro-bed studies, built the vibrating system. Billy Williams and Wendell Brown provided the support of the ChE mechanical shop. My wife Celi made the drawings of the figures presented in the body of the dissertation.

I am deeply indebted to Dr. W. Conger, head of the Department of Chemical Engineering, and faculty members of the Department for their support during my stay at Virginia Tech. I appreciated very much the assistance of Diane Patty, Diane Cannaday, Sandy Simpkins, Mary Robinson, and Sheila Blankenship, members of the staff of the Department. My thanks are extended to all of you.

I will not forget the confidence and encouragement of family members and friends. Neither will I forget the volleyball seasons and the Friday-evening meetings in Blacksburg. They are part of this dissertation.

Finally, I would like to thank the Department of Chemical Engineering of Virginia Tech, Conselho Nacional de Desenvolvimento Cientifico e Tecnologico (CNPq - Brazil), and Maringa State University (Brazil) for financially supporting my graduate studies. LASPAU (Latin American Scholarship Program of American Universities) made the arrangements for my placement at Virginia Tech as a graduate student.

Table of Contents

List of Illustrations

List of Tables

Part I. Studies in Vibrofluidized Beds

1.0 Background and Scope

1.1 Background

The utilization of vibrations for improving heat- and mass-transfer rates in gas-solid systems has been frequently reported in the literature over the past few decades. Pakowski et al.[1] reviewed most of the literature; they cited 135 references with many from Poland and U.S.S.R..

The first result concerning heat transfer was apparently published by Reed and Fenske[2], who studied the effect of agitation on gas fluidization of solids. Their experimental arrangement consisted of a vertical rectangular vessel supported on a gas distributor. Vibrations were imparted on the bed of solids through a vertical vibrating shaft, to which were attached several horizontal screens or perforated plates, and which could also hold flat, vertical heat-transfer elements. Reed and Fenske[2] called their arrangement as an aerated agitated bed. Heat-transfer coefficients between the vessel walls and the agitated bed, and between the bed and the oscillating vertical surface were improved when the "amplitude of the vibrational velocity" exceeded the velocity of the gas percolating through the bed. The "amplitude of the vibrating velocity" is defined as the maximum magnitude of the instantaneous velocity of the vibrating shaft.

Bretsznajder et al.[3] studied both heat and mass transfer in aerated beds contained in cylindrical vessels, and supported by a membrane made of fabric. The membrane was subjected to vibrations, which were then transmitted to the bed of particles. Bretsznajder et al. called this bed an aerated vibrated bed. Heat-transfer coefficients between an immersed heating surface and the bed of particles were found to be greater, sometimes by a factor of about 20, than the coefficients for an equivalent bed in the absence of vibrations. Mass transfer between a bed of particles containing naphthalene and an air stream percolating through the bed, expressed in terms of naphthalene concentration in the exit air stream, was increased up to five times by vibrating the bed compared with the naphthalene concentration resulting from similar tests without vibrations.

Mechanical vibrations had long been used in connection with conveying of solid materials. Bachman[4] and Kroll[5-6] pioneered studies of the dynamical behavior of particles within a vertical, cylindrical, vibrated vessel, which was used to simulate the behavior of layers of particles in conveying troughs. The bed of particles was observed to separate from the floor of the vessel during a fraction of the vibrating cycle, while a percolating gas rushed through the layer of particles, and moved periodically into and out of the bed. Under certain conditions, the bed of particles was apparently fluidized by the percolating gas.

Interest in applications using vibration seems to have grown only after Chlenov and Mikhailov[7-8] reported their "new principle in the production of fluidized beds". According to this principle, a fluidized bed can be generated when a vessel containing solid particles is subjected to vertical vibrations. The floor of the vessel may be either an impermeable solid plate leading to a non-aerated bed, or a permeable plate leading to an aerated bed. In the latter case, the gas-flow rate is not sufficiently high to fluidize the bed by itself. The authors suggested two states of a vibrated bed: (i) if the intensity of the vibrations is sufficiently high to make particles move relative to each other, the bed is called a vibrofluidized bed; (ii) when the vibrating intensity is not sufficiently high, the bed is said to be in a vibro-pseudo-liquid state. Chlenov and Mikhailov claimed that vibrofluidized beds could eliminate gas channelling and particle aggregation, and reduce particle carryover. These potential advantages over gas fluidized-beds would be supplemented by a greater flexibility in selecting aeration flow rates.

Several vibrofluidized-bed applications have been reported in the chemical engineering literature. Lyul'ko et al.[9] studied the annealing of iron powder in a vibrofluidized bed. Kossenko et al.[10] reported their heat-transfer studies between a bundle of tubes and a vibrofluidized bed intended for coal combustion. Mal'chenko and Bograd[11] discussed the design and operation of a recuperative air preheater, consisting of a closed-loop vibrated solid conveyor that extracts heat from hot gases at one section of the loop and preheats air at another section. Bukareva et al.[12] investigated the drying of solids in a vibrated conveying trough equipped with an impermeable solid floor; heating was added through either the floor or the side-walls of the trough. Pakowski et al.[1] estimated that drying covers 90% of all applications of vibrated beds.

There has been some confusion in the available literature over the terminology of regimes of vibrated-bed behavior. Strumillo and Pakowski[13] addressed this issue. Based on whether a bed is aerated or not and on the minimum fluidizing velocity without vibrations, they proposed the following classification:

Vibro-fluidized bed: when the bed is *aerated*, and the gas velocity is *below* the minimum fluidizing velocity of the bed without vibrations.

Vibrated or vibrating fluidized bed: when the bed is *aerated*, and the gas velocity is *above* the minimum fluidizing velocity without vibrations.

Vibrated bed: when the bed is *non-aerated.*

The work reported here follows the above terminology, but it will also speak of *"vibro-beds"* (Sprung et al.[50]) as a synonym of vibrated beds. Vibro-beds, or vibrated beds, were the subject of the present research effort.

The characteristics of a vibro-bed are strongly dependent on the intensity of the vibrations. The vertical displacement x of a plate vibrated vertically and sinusoidally is $x_0 \sin \omega t$, where x_0 is the maximum displacement, ω is the angular frequency ($= 2\pi f$, where f is frequency), and t is time. The acceleration of the plate is $-x_0\omega^2 \sin \omega t$. A sufficient quantity of a granular solid forms a

vibro-bed when a *"vibrational intensity parameter"* $K = x_0\omega^2/g$ is greater than unity. Here, K is essentially a dimensionless acceleration, indicating the ratio of the peak acceleration of the applied vibration to the gravitational acceleration, g.

In Figure 1 on page 6, part (a) illustrates the relative position of the vibrating vessel and the bed after the formation of an air gap, and part (b) shows both the vessel displacement and the bed trajectory over a vibrating cycle. If one places just a few coarse particles on a floor vibrating at 25 Hertz and K = 5, the particles bounce irregularly some 8 mm above the floor. The behavior can be understood simply by calculating trajectories of particles that, acting independently from one another, hit the floor at random times. If one slowly adds more particles to the plate, a point is reached at which some of the particles begin to move in concert. Bachman[4] reported that a layer of six particles deep moves in a mass. A gap forms between the layer and the floor; above the layer is an "expanded zone" - particles looking a bit like the initial situation, before one had added sufficient solid to form a coherent bed, but expanding less than the earlier, freely bouncing particles. A percolating gas moves vertically across the bed, reversing its direction of flow approximately 50 times per second. A "supernatant" gas moves downward while the gap forms, and it moves upward when the gap closes, maintaining an expanded condition in the surface zone.

1.2 Scope

The present research in vibro-beds was motivated by the heat-exchanger concept for recovering heat from hot gases shown in Figure 2 on page 7. The heat exchanger consists of a vibrating trough containing a "shallow" layer of solid particles, up to 100 mm deep. A horizontal flow of a supernatant gas exchanges heat with the bed at a number of stages of contact created by vertical baffles descending a short distance into the bed. Particles then deliver the heat absorbed to a fluid circulating inside tubes placed within the vibrated bed.

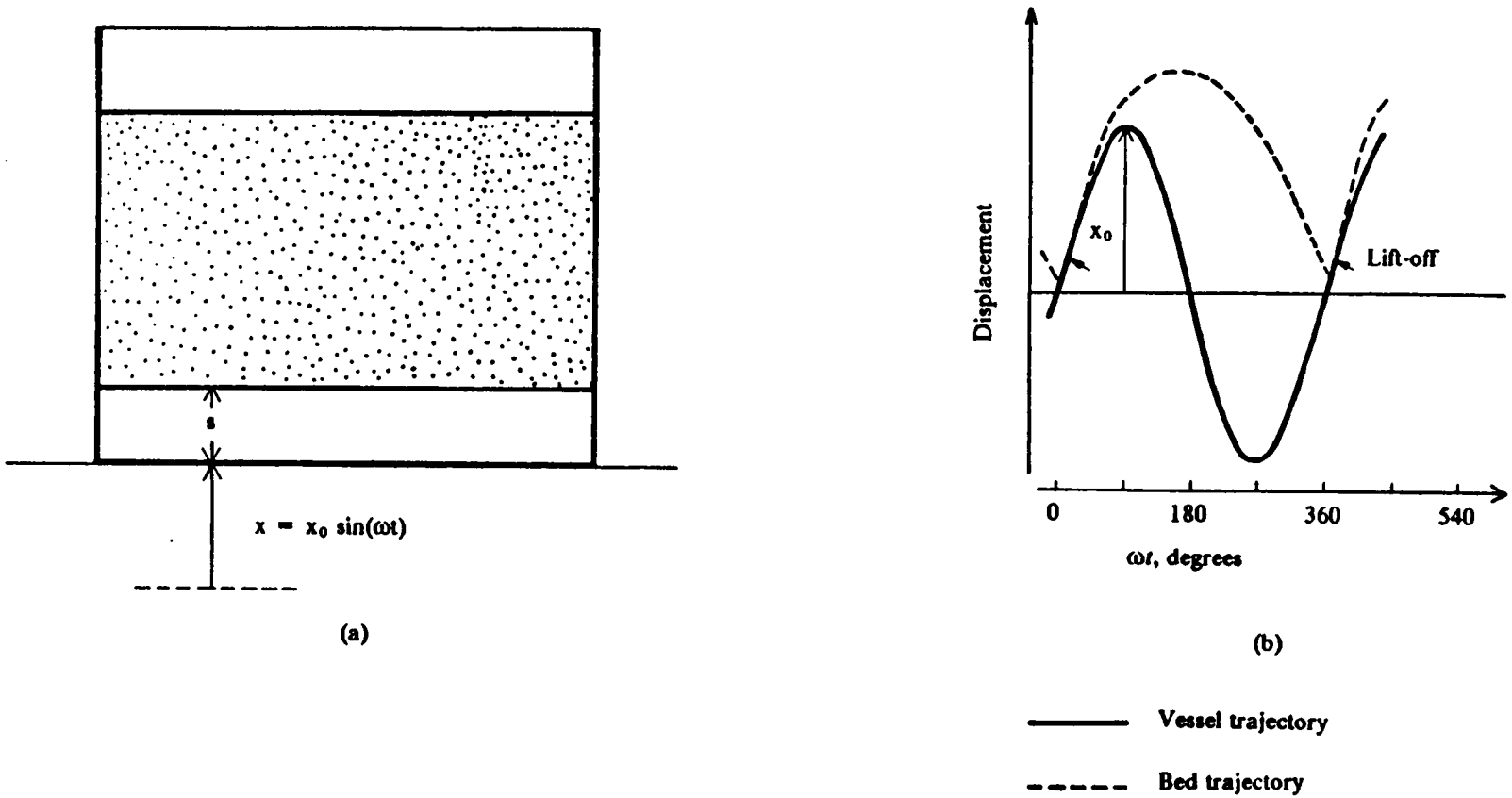

Figure 1. Schematic diagram of a vibrated bed: (a) Formation of the air gap s, (b) Instantaneous displacements of the bed of solids and of the vibrating vessel, $x + s$ and x, respectively.

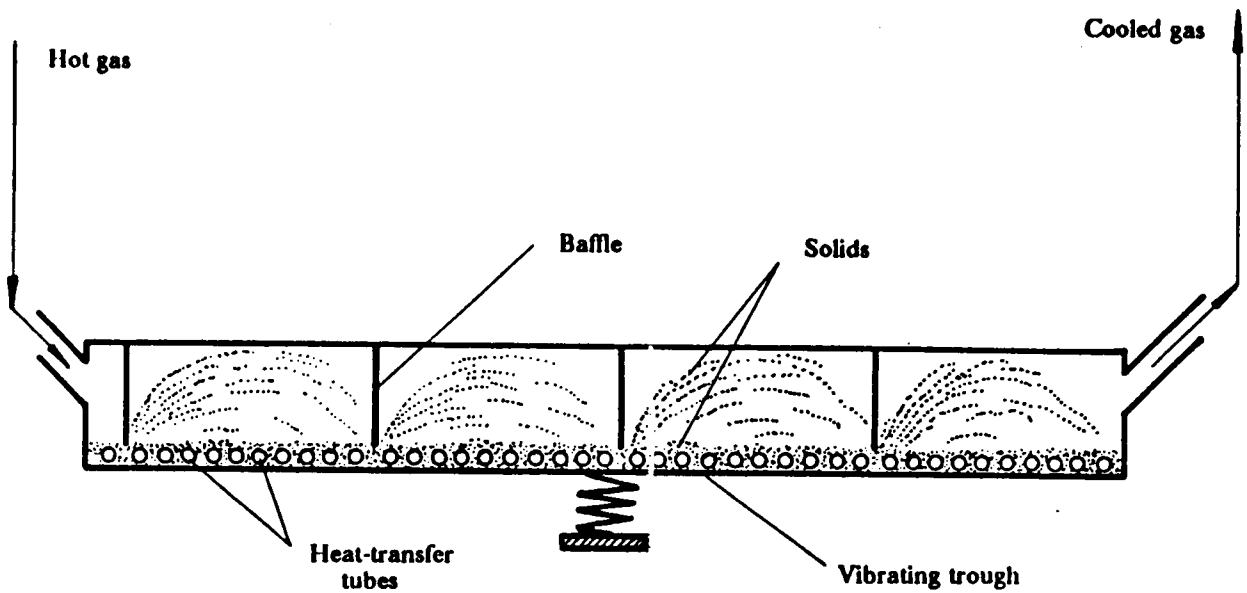

Figure 2. Heat-exhanger concept for recovering heat from a hot gas: Vibrations induce solid convection from the right to the left side of the trough. Gas is forced into the bed of particles by baffles and entrains solids from the left to the right side of the trough. Heat is transferred from the hot gas to the particles, which are then cooled by a fluid circulating in the heat-transfer tubes (Sprung et al.[50]).

A preliminary study of the device, performed by Hirt[31], has indicated that the distance which the baffles descend into the bed can be "small" - i.e., creating but a low pressure drop at each contact stage - while providing a satisfactory approach between the supernatant-gas temperature and the vibrated-solid temperature at each stage. It is expected that such a device requires a much lower power input than an equivalent gas-fluidized bed. Gutman[14] described two commercial applications of vibro-beds that seem to support this expectation. In one case, the vibratory power to handle 800 tons per day of cement clinker in a horizontal vibratory-trough cooler was very low, being only 15 kW. In the other case, the power required by a gas-fluidized dryer with a cross-sectional area of 7 m^2 was cut down by 75% by using vibrations. To handle 1000 kg/hr of material, air-pumping power was reduced from 22 to 5 kW by an extra vibratory power of only 2.2 kW.

Such favorable economic aspects created further motivation for the exploration of the heat-recovering system illustrated in Figure 2 on page 7. The work reported here was undertaken to elucidate the heat transfer between vibrated solids and a heat-transfer tube placed within a vibro-bed. Some emphasis was devoted to solid-circulation patterns and to the formation of air gaps around the heating tube placed within the vibrated bed.

The contents of the rest of Part I of this dissertation are as follows. A detailed review of the relevant literature on the experimental findings of the vibrated-bed dynamics as well as the heat transfer between a vibrated bed and its immersed heat-transfer surface is presented in Chapter 2. In Chapter 3, a critical assessment of theoretical models for the dynamics of and heat transfer in vibrated beds is described. Chapter 4 presents experimental results obtained from studies on the dynamics of vibro-beds. It also summarizes the general conclusions and recommends some directions for further research in vibrated-bed dynamics. Finally, Chapter 5 presents results, summarizes conclusions, and recommends directions for further research in vibrated-bed heat transfer.

2.0 Literature Review

Heat-transfer literature of gas-fluidized beds usually begins with a discussion of the heat-transfer mechanisms between an internal heat-transfer surface and the bed, considering also the dynamics of solid particles and of the gas percolating through the fluidized bed. Xavier and Davidson[15] and Botterill[16] suggest the mechanism to be composed of two additive components: (i) the particle-convective component, which allows for the transfer due to the particle motion within the bed; and (ii) the gas-convective component, which allows for the transfer due to the gas percolating through the bed. Grace[17] and Zabrodsky[18] adopt the same classification, but call the former component the conductive-transfer component. They suggest that heat transfer between an immersed surface and the particles occurs by conduction. Radiation seems to become important only at tempearatures of approximately 500 ^{0}C and above.

The basic components of heat transfer in vibro-beds should be the same as those in gas-fluidized beds. The particle movement induced by mechanical vibration of the vessel and the associated inflow and outflow of a supernatant gas might present distinct flow patterns, but they are the actual components of the dynamics of a vibrated bed. A better understanding of those physical features is therefore essential to any attempt to describe the mechanism of heat transfer between an immersed heat-transfer surface and the vibrated bed of solids.

The first section of this Chapter presents a review of the literature on experimental findings of vibrated-bed dynamics. Experimental findings of heat transfer in vibro-beds are reviewed in the second section. Based on these reviews, the final section addresses some of the key problems that remain to be solved, and summarizes the objectives of the studies on vibro-bed dynamics described in Chapter 4 and on heat transfer reported in Chapter 5.

2.1 Dynamics of Vibro-beds

Industrial vibrated beds are normally contained in rigid rectangular troughs that allow continuous flow of solids through the equipment. In the laboratory, however, the great majority of studies on vibro-bed dynamics has been done in small vessels, usually cylindrical in shape, which contained a batch of solids and were vibrated vertically. Mikolajczuk[19] showed that if the trough is sufficiently rigid, the bed behaves like a stiff body. The latter implies that the whole bed vibrates as a single mass, permitting no relative deformations between different sections of the bed of particles. This suggests that one can simulate the behavior of a vibro-bed in small batch systems.

Experimental research in vibro-bed dynamics is summarized in Table 1 on page 11. All of the observations reported in the table were performed in vessels subjected to vertical, sinusoidal vibrations.

The following literature review was classified according to a number of topics:

(1) Air gaps and bed porosity;

(2) Solid circulation;

(3) Pressure oscillations;

(4) Effect of unsteady pressure fields;

(5) Wall and interparticle effects;

(6) Effect of bed internals; and

(7) Classification of vibrated beds.

Table 1 : Experimental research in vibro-bed dynamics

Investigators	Particles	Particle size, μm	Vibro-bed parameters[1]	Remarks
Bachman[4]				Vibro-bed single-mass behavior for bed depths above six particle diameters. Formation of air gaps at $K \geq 1$.
Kroll[5,6]	Glass beads Sea sand Lycopodium powder	≤ 1000 ≤ 1000 30	L = 20-110 mm $x_0 \leq 4$ mm f = 10-120 Hz	Floor-pressure oscillations reduce air-gap size. Solid circulation and porosity variations induced by gas currents. Non-linear pressure gradients in beds of small particles. Maximum floor pressures increased with bed depth up to a depth of 60 mm and then decreased. Vibro-beds first compacted and then expanded as K was increased.
Chlenov and Mikhailov[7,20]	Quartz sand Steel spheres	165-2500 8000-8500	$x_0 \leq 1$ mm f = 20-200 Hz	"Fluidization" by vibration when K exceeds one. Solid circulation reduced to vertical oscillations at low gas pressures.
Gutman[14,24]	Glass beads	84-935	L ≤ 140 mm K ≤ 6 f = 20,50 Hz	Maximum floor pressures dependent on vessel size. Decrease of maximum pressures for bed depths above 60 mm because of gas compressibility. Average floor pressures always positive. Air volumes between pressure transducer and measuring point decreased amplitude of measured pressure oscillations. Bed-porosity variations about ± 5 percent of average bed porosity.
Belyi and Yurkevich[21]	Polymers	< 150	K < 8 L < 900 mm	Bed compaction at K-values up to 5.
Pakowski et al.[1]				Bed configurations with non-horizontal surfaces.

Table 1 (Continued)

Investigators	Particles	Particle size, μm	Vibro-bed parameters[1]	Remarks
Ryzhkov et al.[22]	Aluminum oxide	< 2000	x_0 = 2.73 mm f = 16-30 Hz L < 500 mm	Non-horizontal bed surfaces for small particles.
Chlenov and Mikhailov[20]	Sand			Average floor pressure always negative.
Ivashchenko and Golubev[23]				Difference in levels of particles smaller than 400 μm in a vibrated U-tube.
Buevich et al.[28]	Corundum	80-120	L < 500 mm x_0 = 2.7 mm f = 15,20 Hz	Vibro-bed allows deformation during flight period only Average floor-pressure differentials induce solid circulation and solid piling at specific vessel locations.
Gray and Rhodes[33]	Phosphor-bronze Alumina Glass beads	50,3000 50 50	K < 40 f < 400	Air-gap size decreased by wall-frictional forces. Single-mass behavior broke down at f > 200 Hz.
Ryzhkov and Baskakov[34]	Corundum	1320	K < 7	Wall-frictional forces retarded air-gap formation.
Sapozhnikov et al.[36]	Aluminum oxide	120-800	L = 120-160 mm x_0 = .1-2.5 mm f = 20-60 Hz	Particle velocities greater at the laterals of horizontal tubes immersed into the vibro-bed.
Malhorta and MujumdarUsup3.[7]	Glass beads	454-667	x_0 = .425 mm f < 100 Hz L = 90-130 mm	Air-gap formation at the top and bottom of cylindrical surfaces placed in an aerated vibrated bed (2-dimensional vessel).
Markowski et al.[32]	Corundum			Classification of vibated-bed behavior.

[1] L = bed depth
x_0 = vibrational amplitude
f = vibrational frequency
K = vibrational intensity parameter

2.1.1 Air gaps and bed porosity

When discussing their new principle in the production of a fluidized bed, Chlenov and Mikhailov[7] suggested that the intensity of "fluidization" of a vibrated bed could be controlled by changing the vibrational conditions, specifically the frequency and amplitude of vibrations. By using equations describing the movement of a single particle, they established that "fluidization" is achieved when the vibrational intensity parameter K exceeds one. At this moment, particles are removed from the floor of the vibrating vessel, and a relative movement of particles to each other sets in. The instant of collison between the floor and particles later in the vibrational cycle was detected by a spike in the observed vessel-acceleration wave. Figure 3 on page 14 shows a plot of the vibrational frequency f versus the amplitude of the vibration x_0 at K = 1. This theoretical curve seems to represent well the vibro-bed behavior of steel spheres and quartz sand particles, both of diameter greater than 0.35 mm. In the region below the curve, the vibrated bed exhibited only some compaction.

The pioneering work done by Bachman[4] had resulted in similar observations by utilizing stroboscopes and photographic techniques. Bachman[4] determined that vibrated beds behaved as a single mass when bed depths were greater than six particle diameters. Layers of large particles would leave the floor of the vessel at the instant the deceleration of the vibrating vessel surpassed the gravitational deceleration of the particles, that is, when the vibrational intensity parameter corresponding to the vessel deceleration exceeded unity. They move under the acceleration of gravity until colliding with the vessel later in the vibrational cycle, and then immediately follow the vessel trajectory until a new lift-off occurs. During the flight period of the bed, an air gap would form between the bottom of the particle layer and the floor of the vessel. The typical bed trajectory and vibrating-vessel displacement are illustrated in Figure 1 on page 6. Bachman treated the movement of the rigid bed as a single particle moving under the action of gravity after leaving the floor of the vessel with an initial velocity corresponding to the vessel velocity at the time of lift-off.

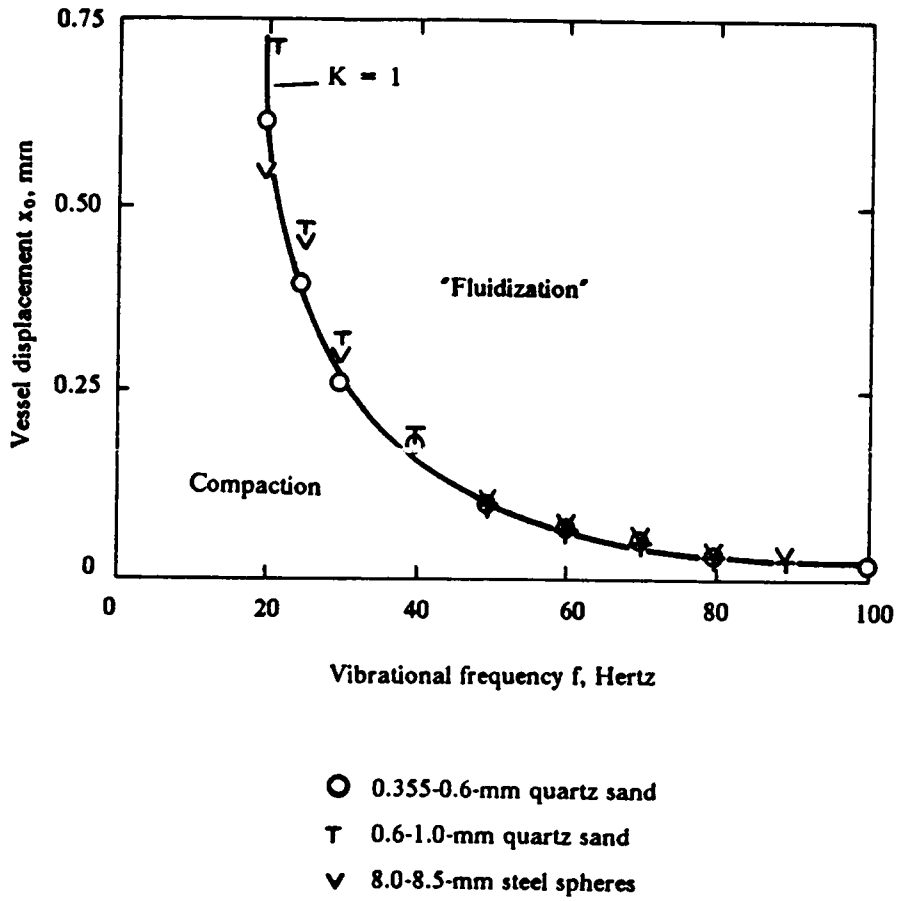

Figure 3. Classification of vibro-bed behavior: Theoretical (K = 1) and experimental vibrational conditions for "fluidizing" a layer of particles by vibrations. (Chlenov and Mikhailov[7])

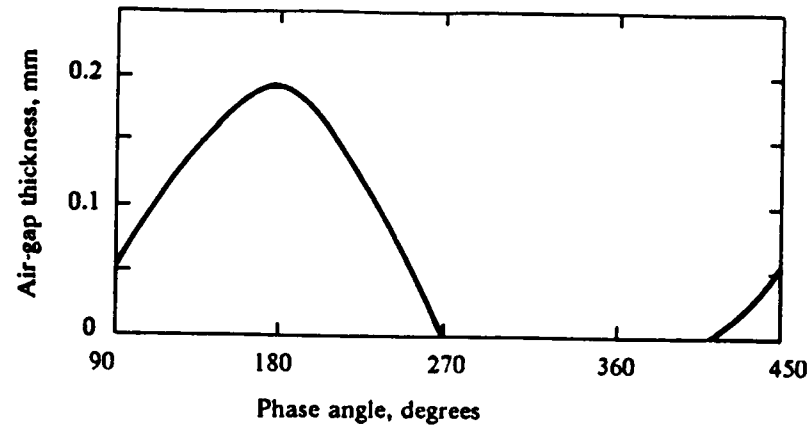

(a) Particle diameter: 89-124 μm

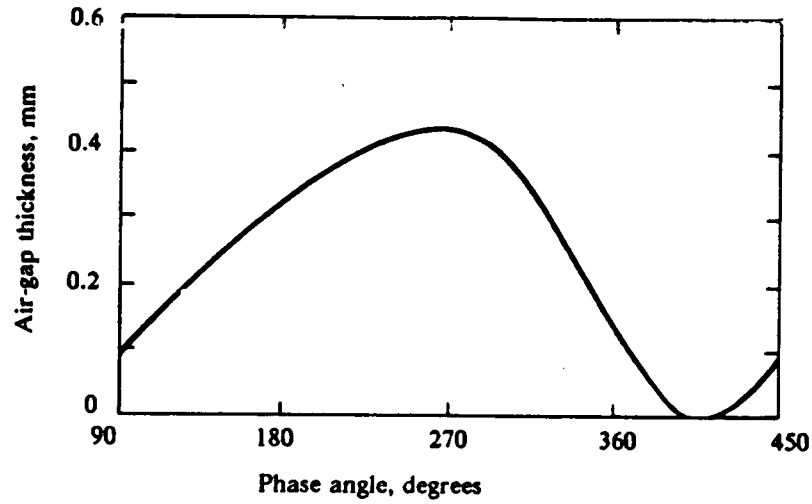

(b) Particle diameter: 700-850 μm

Figure 4. **Air-gap size in vibro-beds:** Beds of glass beads vibrated at a frequency of 20 Hertz and an amplitude of of 1.28 mm. Bed depth: 40 mm. (Gutman[14])

Kroll[5] made pressure measurements at the floor of the vibrating vessel and recognized the importance of the effect of floor pressure on bed dynamics. His measurements indicated pressure fluctuations around the atmospheric pressure existing at the bed surface, and these fluctuations tended to induce a vertical, oscillatory gas motion downward and upward through the bed. This gas motion exerted an additional force on the bed of particles, reducing the size of the air gap formed between the floor of the vessel and the bottom of the vibrated bed, and also reducing the period of time that particles spend in free flight. The effect was more noticeable as the particle size was decreased. Kroll incorporated the drag force exerted on the particles into Bachman's description of bed dynamics by assuming that the gas behaved as an incompressible fluid.

Figure 4 on page 15 shows air-gap sizes measured by Gutman[14] in beds of glass spheres vibrated at a frequency of 20 Hertz and an amplitude of 1.28 mm. Gutman's method involved measuring the electrical capacitance between a pair of metal plates placed across the bottom of a rectangular bed. The maximum size of the gap and the period of time that the gap remains open were larger in beds of glass spheres of 710-850 μm in diameter than in those of 89-124 μm in diameter. If Bachman's single-particle behavior[4] were followed, the size and development of the gaps would be identical.

As shown in Figure 5 on page 17, Kroll[6] also found that the average specific volume of a vibrated bed of particles was dependent on the vibrational conditions and on the particle properties. The average specific volume of a vibro-bed is defined as the mass of particles in the bed divided by the vessel volume, and is directly proportional to the average porosity of the vibrated bed. As seen in the Figure, for constant vibrational frequencies of 30 and 50 Hertz, a bed of 130-μm sea sand particles first showed compaction as the vibrational amplitude was increased, and then it continually expanded. At identical amplitudes, bed expansion was greater for higher vibrational frequencies, corresponding to larger K-values. However, as the amplitude was increased, the specific volume of the bed became only slightly greater than that of the bed without vibrations. Bed compaction of a light 30-μm Lycopodium powder, for the same vibrational frequency of 30 Hertz, extended over a greater span of amplitudes than compaction for the larger and heavier sand particles. In

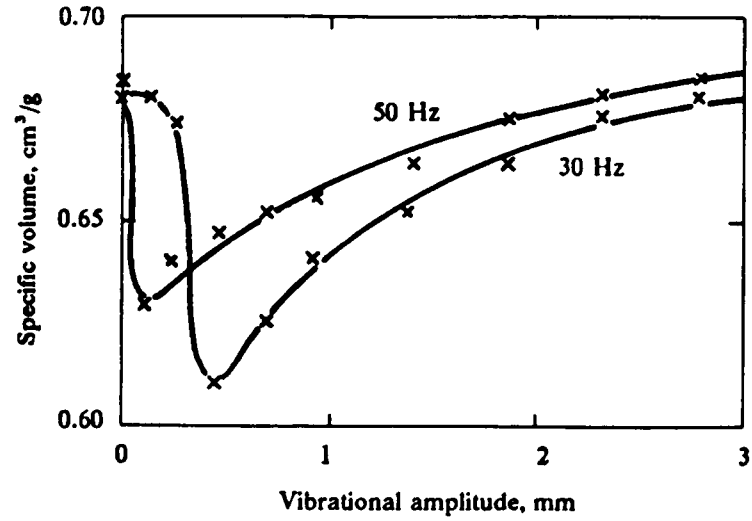

(a) 130-μm sea sand

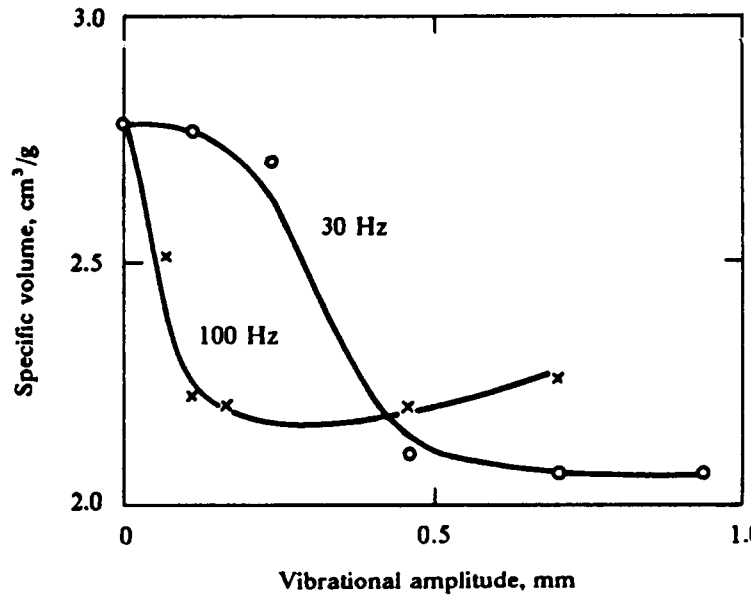

(b) 30-μm Lycopodium powder

Figure 5. Variation of the specific volume of vibrated beds: Effect of the vibrational frequency and amplitude (Kroll[6]).

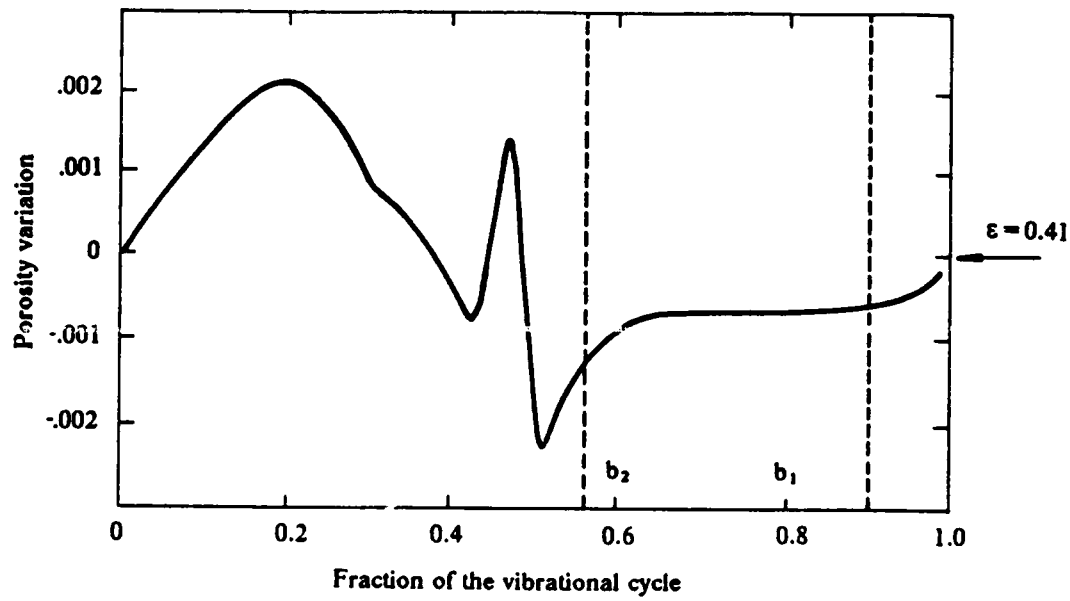

Figure 6. Variation in porosity of a vibro-bed: 80-mm bed of 90-135 μm glass spheres vibrated at a frequency of 20 Hertz and an amplitude of 1.56 mm (b_1, b_2 are the measured bed lift-off and collision points, respectively). (Gutman[14])

studying the behavior of finely dispersed materials, Belyi and Yurkevich[21] observed that significant expansion of the vibro-bed began only at K-values between three and five.

Gutman[14] measured instantaneous porosities averaged over the bed depth of vibrated beds by using a capacitance method. Figure 6 on page 18 presents his data for a 80-mm bed layer of glass spheres of 90-135 μm in diameter. The bed was vibrated at a frequency of 20 Hertz and an amplitude of 1.56 mm, corresponding to a K-value of 2.51. Bed expansion occurred during the flight period, and bed compaction existed when the bed and vessel were in contact. Voidage variations less than 0.01 from an average value of 0.41 were found in the range of K-values between one and four.

2.1.2 Solid circulation

According to Chlenov and Mikhailov[20], the pressure differential between the bed surface and the floor of the vibrating vessel is dependent on a number of factors such as the vibrational conditions, the dimension and permeability of the bed, the particle size distribution, the moisture content of solids, and the interparticle frictional forces. Gas flows generated by the pressure differential induce spouting at the bed surface as well as solid circulation and mixing within the bed, with their intensity increasing with increasing values of the pressure differential. When the system is under a very low absolute pressure, spouting disappears and the characteristic particle motion is restricted to vertical oscillations.

Kroll[6] observed the solid-circulation pattern shown in Figure 7 on page 20 in vibro-beds of particles of diameters between 100 μm and 1000 μm. In cylindrical vessels up to 100 mm in diameter, particles would flow downward the walls, and then upward at the central portion of the vessel. At a constant vibrational amplitude, solid circulation seemed to become faster as the vibrating frequency was increased. When the size of the particles was decreased below 100 μm, the surface of the bed was no longer flat; instead, piles of solids accumulated at the side walls, and gas channelling was frequently noticed. For these smaller particles, an expanded zone of particles was

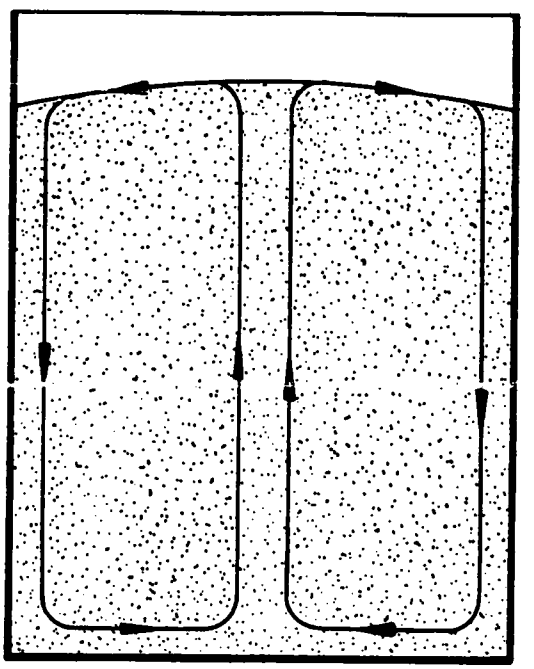

Figure 7. Solid-circulation pattern in a vibro-bed: Layers of particles of diameters of 100 to 1000 μm (Kroll[6]).

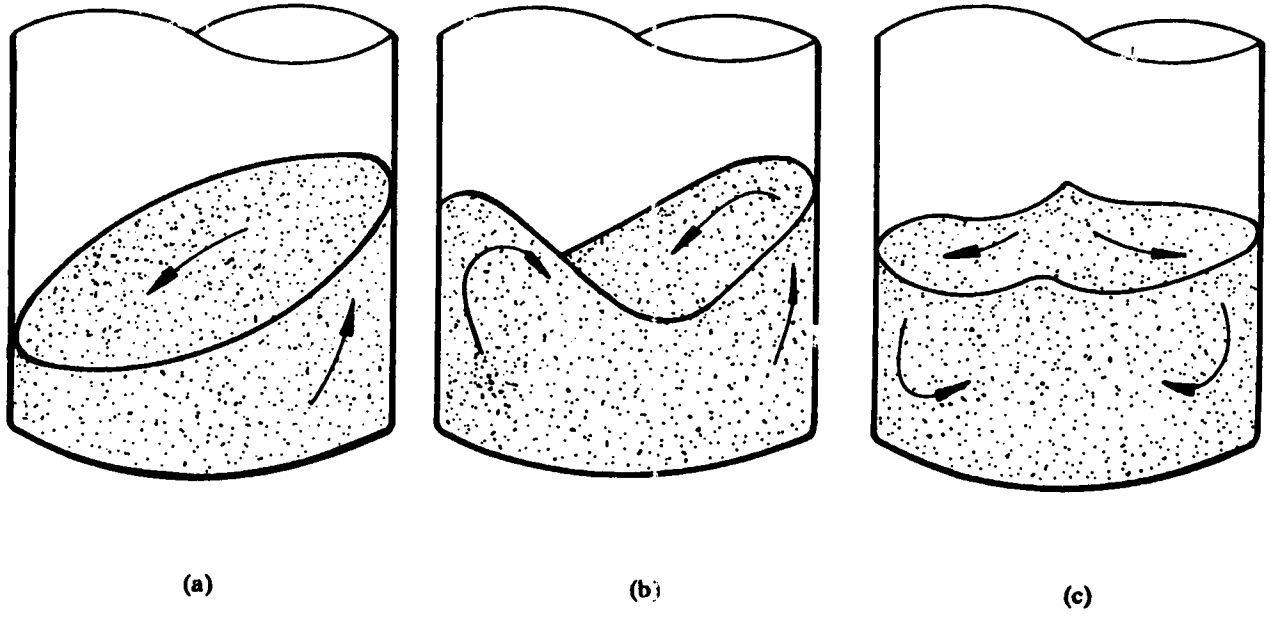

Figure 8. Unstable surface configurations of vibro-beds: Layers of coarse and dry particles (Pakowski[1]).

observed at the bed surface. This expanded zone became deeper as the vibrational intensity was increased.

The distinct behavior of vibro-beds of coarse and fine solids was also reported by other researchers. Reported studies on the dependence of the shape of top surfaces of vibrated beds on the particle diameter also show some disagreements. Pakowski et al.[1] claim that the bed configurations shown in Figure 8 on page 21, called unstable surface configurations, refer to to coarse, dry particles. They have not cited specific particle-size ranges. Ryzhkov et al.[22] observed configuration (a) in Figure 8 on page 21 for fine particles, and horizontal surfaces in vibrated beds of large particles. According to Ryzhkov et al., solid accumulation at one side of the vessel is caused by a horizontal gas velocity generated in addition to a vertical-velocity component, thus producing a closed-loop circulation of particles. Particles flow downward at the shallowest part of the bed and upward at the deepest part of the bed. On the bed surface, solid flow is directed toward the shallowest part of the bed; while in the bulk of the bed, the flow is directed in the opposite direction. Solid circulation starts in the upper part of the vibrated bed as a consequence of bed lift-off. As K is increased, the bed becomes less consolidated. Solid motion eventually extends over the entire bed volume.

2.1.3 Pressure oscillations

Pressure oscillations induced by vibrations seem to be a key factor in determining the dynamic characteristics of a vibrated bed. Figure 9 on page 23 shows instantaneous pressure differentials between the floor of the vessel and the top of the bed as measured by Kroll[5-6]. These measurements refer to different bed heights of 130-μm glass beads vibrated at a frequency of 50 Hertz and an amplitude of 1.42 mm. They illustrate the cyclic nature of pressure oscillations with reference to the pressure above the bed. With the exception of the deepest bed (110 mm), the maximum positive pressure differential is always larger than the absolute value of the maximum negative pressure differential. In shallow beds, the maximum negative pressure differential occurs earlier in a vibrational cycle than the positive one does. Both maximum pressure differentials are displaced

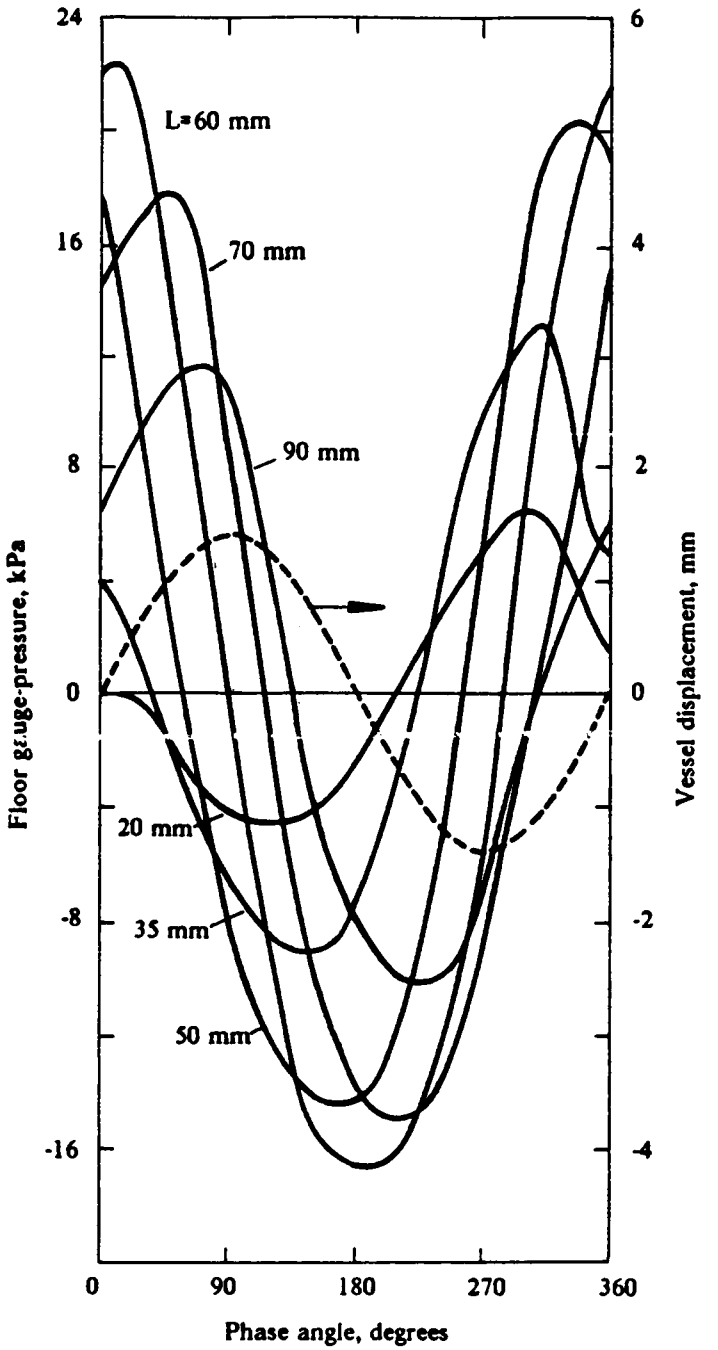

Figure 9. Effect of bed depth on floor pressures in vibro-beds: Gauge pressures at the base plate of beds of 130-μm glass beads vibrated at a frequency of 50 Hertz and an amplitude of 1.42 mm. Bed depth = L (Kroll[6]).

toward the end of a vibrational cycle as the bed height is increased. At bed depths above 50 mm, the maximum positive differential occurs at the beginning of the next cycle. Thus, for a single vibrational cycle, the maximum positive pressure differential now appears before the negative one. However, neither does the maximum negative pressure differential move beyond the lowest instantaneous position of the vibrating vessel, nor does the maximum positive differential move beyond the highest instantaneous position of the vessel. The maximum pressure differential increases with increasing bed heights up to a depth of 60 mm, and then continually decreases.

Chlenov and Mikhailov[25] measured the time-averaged pressure difference between the floor of the vessel and the upper surface of a bed of sand particles by a remote differential manometer connected to the bed through a narrow tube. As shown in Figure 10 on page 25, they consistently found negative floor pressures, indicating a net suction effect over the vibrational cycle. This suction effect increased with increasing values of the vibrational parameters. Investigations of Bukareva et al.[26] showed that, for identical vibrational conditions, the absolute negative mean pressure increases when the bed depth and particle density are increased, and when the particle size or bed permeability is decreased. According to Bukareva et al.[27], the preceding dependence of the mean pressure on the bed permeability is responsible for smaller air gaps in beds of lower permeability.

More accurate measurements of instantaneous and average pressures at the base of vibrated beds were obtained by Gutman[14,24]. In discussing the measurement techniques, he showed that the frequency response of the pressure transducer and the air volume between the transducer and the measuring point can both affect the results. Gutman argued that Kroll's pressure data were not reliable because of the low-frequency response of the transducer utilised in the measurements. He further suggested that Chlenov and Mikhailov's data were affected by the large air volume present in the tube connecting the manometer to the base of the vibrating vessel.

Figure 11 on page 26 illustrates the pressure measuring system utilized by Gutman for determining the effect of the air volume between the transducer and the measuring point on the experimental floor pressure. By using a low-frequency transducer and increasing the air volume, he obtained pressure oscillations of different shape. The amplitude of the fluctuations decreased, and

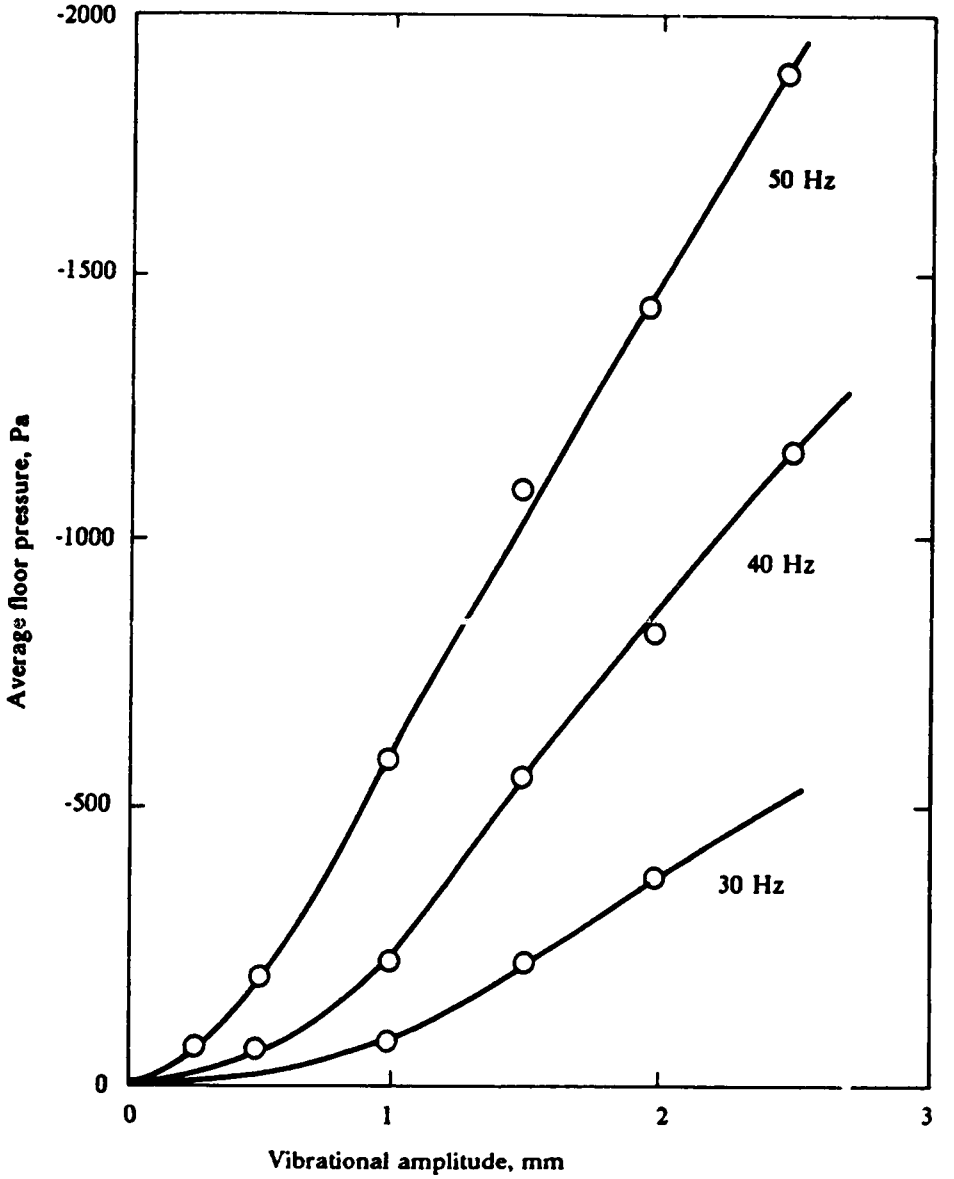

Figure 10. **Average floor pressures in vibro-beds of sand particles:** Dependence on the vibrational parameters (Chlenov and Mikhailov[25]).

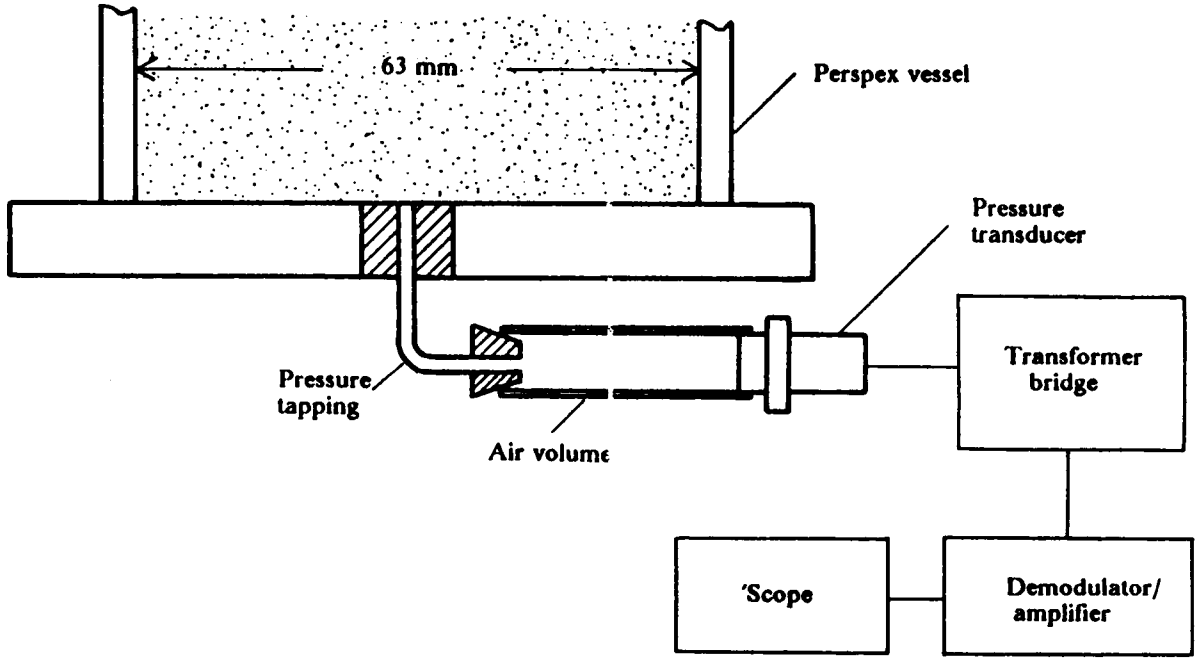

Figure 11. Floor-pressure measuring system: System utilized by Gutman[14] for determining the effect of air volumes between the pressure transducer and measuring point on experimental pressures.

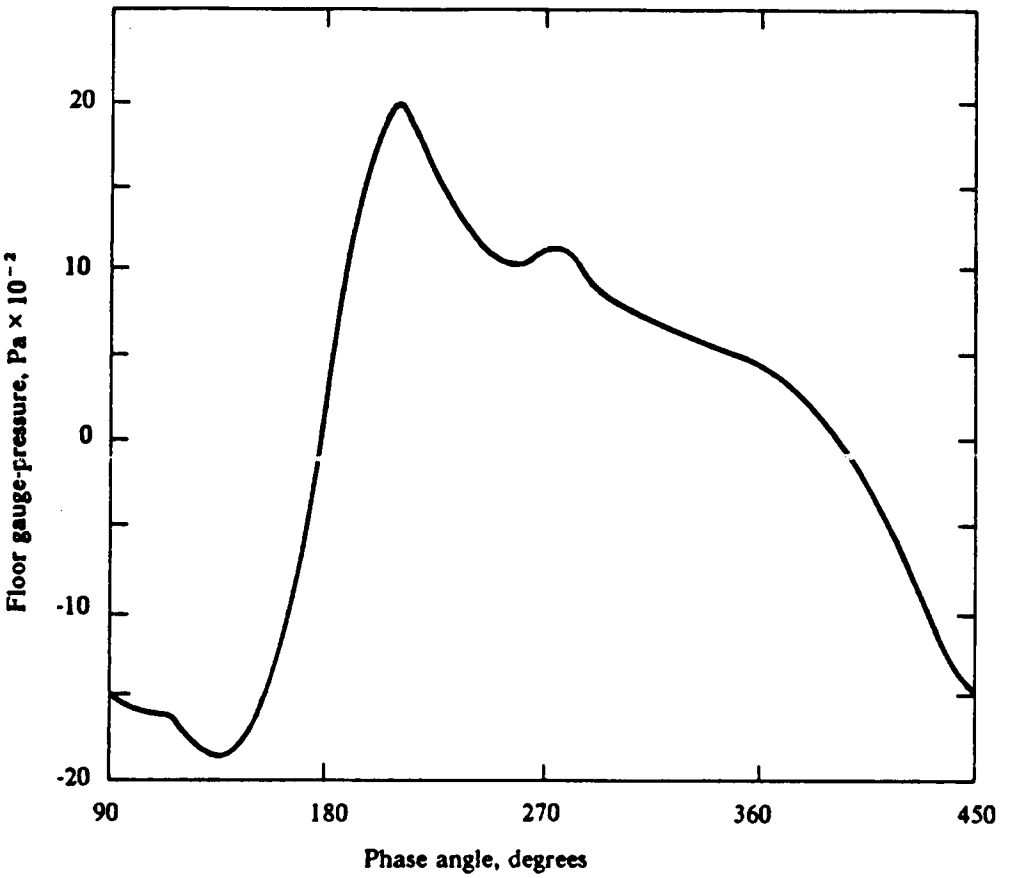

Figure 12. Instantaneous pressures in a vibro-bed of 89-124 μm glass beads: 40-mm layer of particles vibrated at a frequency of 50 Hertz and an amplitude of 0.28 mm (Gutman[14]).

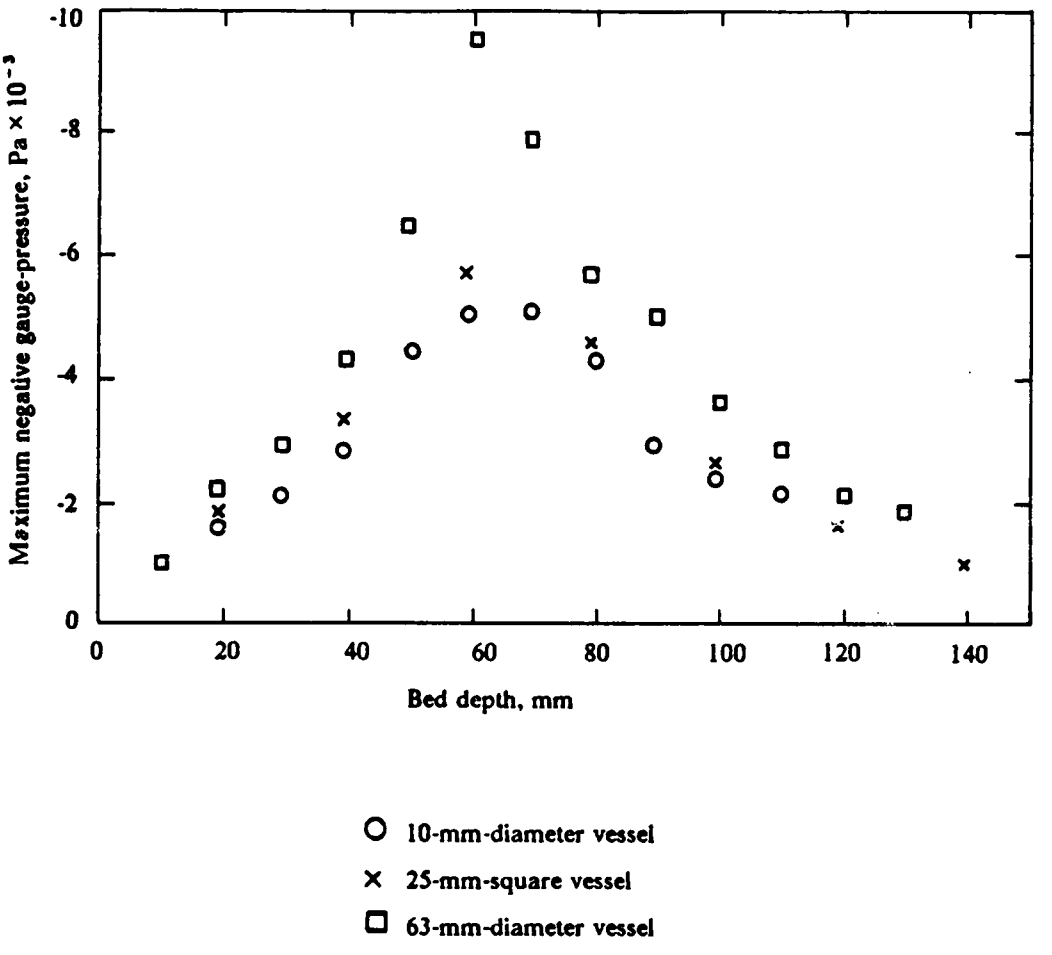

Figure 13. Effect of vibro-bed depth on maximum floor pressures: Layer of 90-135 μm glass beads vibrated at a frequency of 50 Hertz and an amplitude of 0.43 mm (Gutman[14]).

its form approached more closely to a pure sine wave. The mean pressure differential became an increasingly larger fraction of the dynamic pressure fluctuations and switched from positive to negative values. This behavior was more noticeable for smaller particle sizes.

By keeping a very small air volume between the pressure transducer and the measuring point, and by using a measuring system with a frequency response of 15 kHz, Gutman showed that the average pressure differential is always positive, and just a small fraction, about 3 to 4%, of the dynamic pressure fluctuations. The shape of instantaneous pressure variations over a vibrational cycle is illustrated in Figure 12 on page 27. It shows that the shape is not as smooth as that of the variations obtained by Kroll, previously presented in Figure 9 on page 23. With execption to beds of fine particles vibrating at 20 Hertz, Gutman's measured maximum positive pressure differentials were greater than the absolute maximum negative differentials in beds of 40-mm depth. Maximum pressure differentials were observed to increase with increasing K-values, and with decreasing particle sizes. The dependence of the maximum pressure differential on bed depth for particles of 90-135 μm in diameter is shown in Figure 13 on page 28. The bed was vibrated at a frequency of 50 Hertz and an amplitude of 0.43 mm. The dependence is similar to that observed by Kroll. The amplitude of the fluctuations first increases with bed depth, goes through a maximum at a bed depth of 60 mm, and then decreases. This figure also reveals some dependence of the maximum pressure differential on the cross-sectional area of the vessel; such dependence becomes more significant for larger particles.

2.1.4 Effect of pressure oscillations on vibro-bed behavior

Pressure oscillations in vibrated beds of particles have been related to: (i) the difference in the levels of particles in the two limbs of an U-tube filled with solids and subjected to vibration; (ii) the development of a non-horizontal bed surface in a vibro-bed of fine particles; and (iii) porosity variations in vibrated beds.

When the two limbs of a U-tube are filled unequally with solid material and subjected to vibrations, the final levels of the particles in the limbs are dependent on the particle size of the solids. Ivashchenko and Golubev[23] observed that the levels quickly equilibrated for particles of diameter greater than 400 μm; while for fine particles, the difference in levels could even increase. Gutman[14,24] reported the same kind of behavior. He explained the phenomenon by a balance between mean pressures and interparticle stresses at the bottom of the limbs. For coarse particles, the pressure difference is small, so the stresses define the equilibrium position. For fine particles, however, the mean pressure below the shorter limb can be greater than that below the taller limb. The resulting gas flow induces a particle flow that eventually will be equilibrated by unequal vertical interparticle stresses.

Buevich et al.[28] explained the non-horizontal nature of the free surface of a vibrated bed of fine particles, and the associated solid-circulation patterns, in terms of instabilities created by small perturbations in the floor pressures of the bed. They observed that beds of particles of approximately 100 μm in diameter did not respond to small inclinations of the vibrational axis. Therefore, the inclination of the axis could not be the cause of such a non-horizontal nature of the surface. They also observed that the bed-surface non-uniformity would disappear when larger particles were used, for which the force of interaction with the gas was smaller than for fine solids.

Buevich et al.[28] assumed that a granular material in a vibrated bed allowed a relative deformation only during the flight period, when particles could be entrained by gas currents. In an unperturbed state, the bed would have a horizontal free surface, and the pressure distribution would be a function only of time and of the vertical ordinate z. Any perturbation in this pressure field would cause the appearance of secondary gas currents, which, in the case of fine solids, could entrain solids and develop bed-surface non-uniformities. Their analysis accounted for perturbations on the mean floor pressure, which was obtained by averaging the instantaneous values over the period of time the bed stayed in flight.

Figure 14 on page 31 presents the average floor pressure over a period of bed flight as a function of bed height. These data refer to a bed of 0.08-μm corundum particles vibrated at a frequency of 20 Hertz and an amplitude of 2.7 mm. For bed depths below 0.11 m and above 0.32

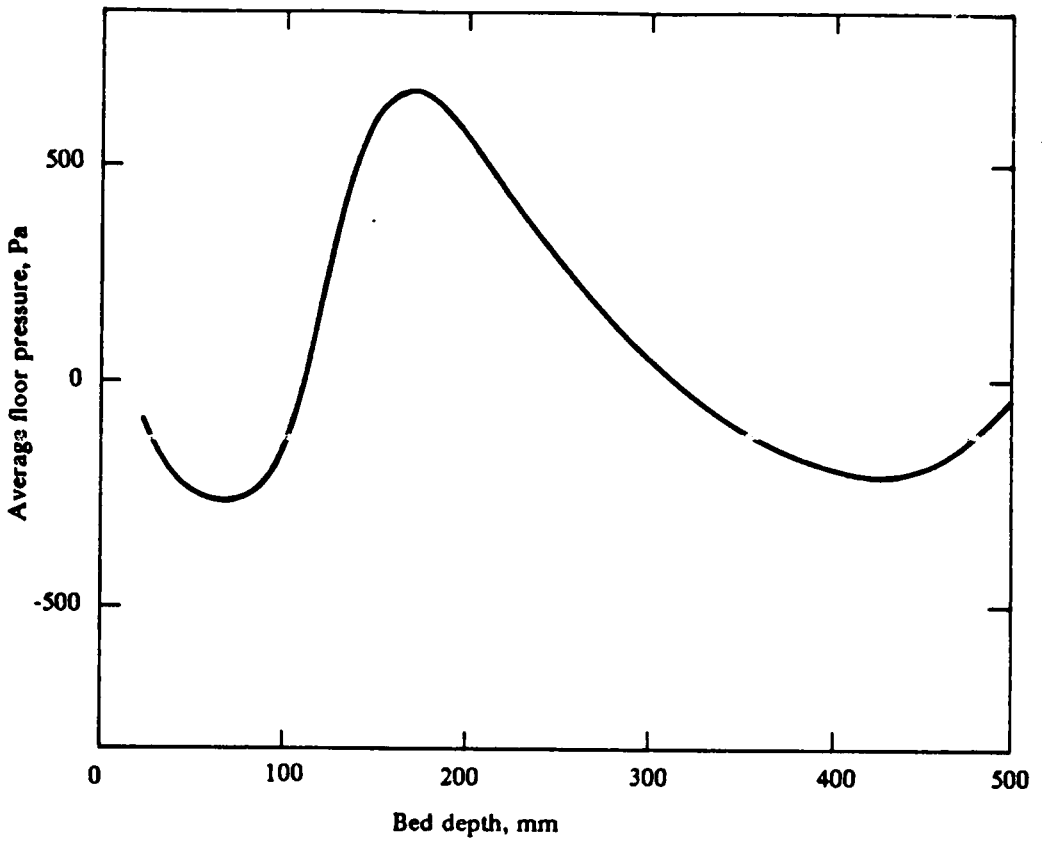

Figure 14. **Dependence of average floor pressures on bed depth:** Bed of 80-μm corundum particles vibrated at a frequency of 20 Hertz and an amplitude of 2.7 mm. Floor pressures averaged over the bed-flight period (Buevich et al.[28]).

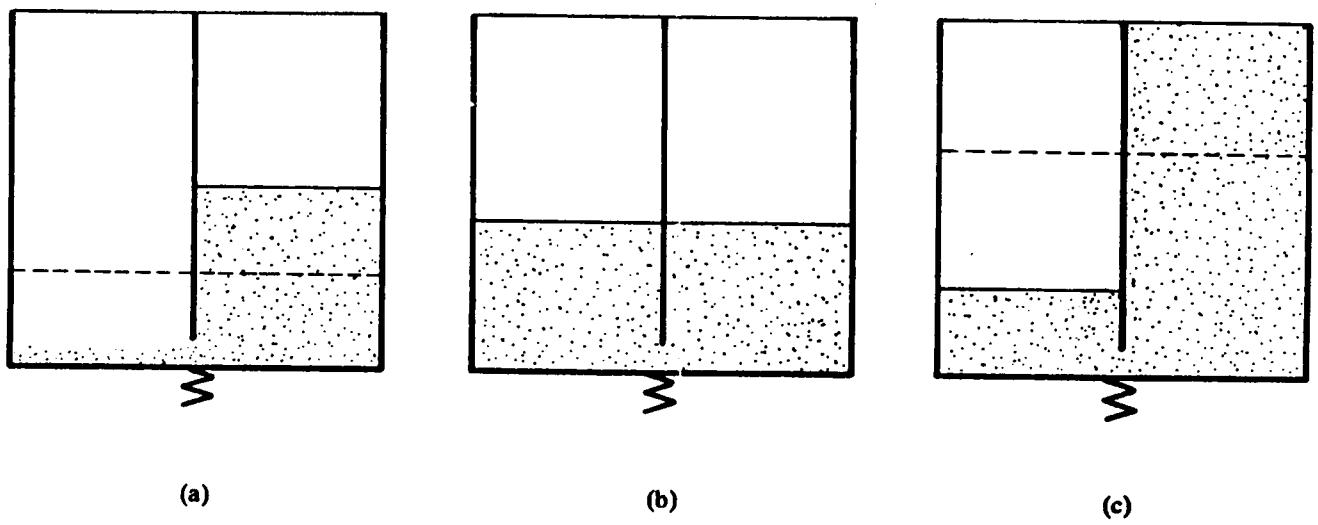

Figure 15. **Vibro-bed configurations for small particles: Final states for different initial loads of solids (dashed lines). An initial perturbation caused a slight decrease in the depth of the left-half of the bed (Buevich et al[28]).**

m, the average floor pressure is negative; for bed depths between 0.11 and 0.32 m, the average pressure is positive. Perturbations in the average floor pressure may lead to the deformation of an initially horizontal bed surface with solids building up at some specific location in the vibrated bed.

Figure 15 on page 32 illustrates the initial and final configurations of a vibrated bed divided in two halves by a vertical solid barrier. According to Buevich and al.[28], this barrier was separated from the floor of the vessel by a gap far smaller than the static bed depth. Perturbations in the floor pressure would develop in the left half of vessel, causing a little decrease in the bed depth at this half of the vessel. Diagrams a and c of the Figure illustrate situations for which a decrease in the bed depth increased the average floor pressure at the left bed-half. This generated gas currents from the left to the right bed-half. As a consequence, solids were also transported from the left half to the right half of the vessel. The bed depth of the left half continuously decreased. The depth of the right half continuously increased until either almost all solids were transferred to the right bed-half or the pressures below both halves became equalized. As shown in diagram b, if the initial perturbation decreased the average floor pressure at the left bed-half, solids were transported from the right to the left bed-half, and the initial uniform bed-depth regenerated again. Referring to Figure 15 on page 32, diagram b corresponds to initial bed depths for which the average floor pressure increases with an increase in bed depth. Diagrams a and c correspond to initial bed depths for which the average pressure decreases with an increase in bed depth. In this figure, dashed lines indicate the uniform static bed-depth before vibrations had been started.

Pressure oscillations at the floor of the vibrating vessel and the drag force excerted on the solids by the corresponding induced air currents have also been related to the porosity variations observed in vibrated beds since the work of Kroll[6]. Kroll compared vibro-beds to gas-fluidized beds and suggested that fluidization and bed expansion occur when the instantaneous pressure difference between the floor and the top surface of the vibro-bed overcomes the bed-weight per unit cross-sectional area. Growth of air gaps with stronger vibrational conditions in shallow beds of small particles was related to higher gas-flow rates, which would cause greater bed expansion. Compaction would still occur over part of a vibrational cycle, after the air gap had disappeared. Increasing the bed depth resulted in smaller air gaps - an indication of less air inflow. Beds of coarse

particles were observed to be less susceptible to expansion by vibrations; this behavior was associated with the much larger permeabilities of beds of coarser solids.

Gutman[14], and Gutman and Davidson[29], in testing experimentally the validity of Darcy's law in vibrated beds, found increasing compressibility effects as the bed depth and vibrational frequency were increased, and as the particle size was decreased. As shown in Figure 13 on page 28, beds of glass beads of approximately 100 μm in diameter vibrated at 50 Hertz experienced a decay in the maximum negative floor-pressure fluctuation at bed depths above 60 mm. Gutman[14 24] attributed this effect to steeper pressure gradients at the lower portion of the bed, where porosity would be subjected to variations. The upper portion of the bed would just bounce up and down on the lower part without any change in its porosity.

2.1.5 Wall and interparticle effects

Gray and Rhodes[33], utilizing vibrating frequencies up to 400 Hertz, identified the presence of wall-frictional forces in vibro-beds by performing experiments at very low pressures. In the absence of drag forces, wall friction decreased both the maximum bed-throw height and the period of time the bed remained in flight.

Gutman[14] pointed out the importance of wall-frictional forces by analyzing floor-pressure data obtained for different bed depths and vessel cross-sections. Figure 13 on page 28 and Figure 16 on page 35 show maximum negative gauge pressures at the floor of the vessel for beds of small and large glass beads, respectively. For small particles, the maximum negative gauge-pressure was not appreciably dependent on the vessel size over the range of bed depths investigated. For large particles, however, a significant increase in the pressure magnitude occurred when the vessel diameter was increased. When compared to drag forces, wall-frictional forces should therefore be considered in beds of large particles when the ratio of bed depth to vessel diameter becomes greater than one.

Direct evidence of the effect of wall friction was presented by Ryzhkov and Baskakov[34]. They measured the normal stress exerted by a bed of corundum particles of 1.32 mm in diameter on the

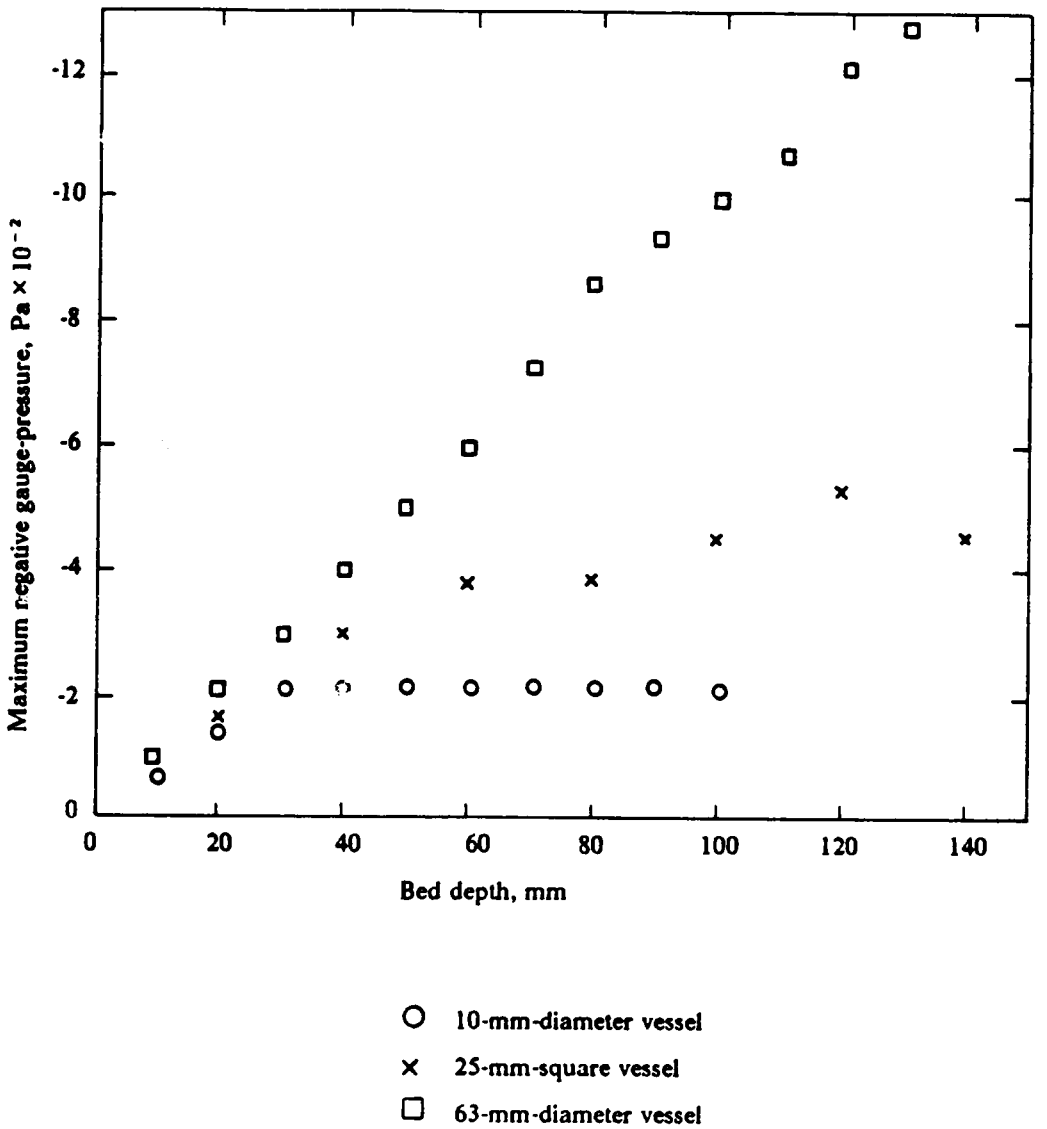

Figure 16. Effect of bed depth on the maximum negative floor pressures: Layer of 675-935 μm glass beads vibrated at a frequency of 50 Hertz and an amplitude of 0.43 mm (Gutman[14]).

wall of the vessel over the vibrational cycle. The stress was larger near the bottom of the vessel during the fraction of the cycle when the bed was in contact with the floor of the vessel. During the period of flight, the normal stress was retained in the middle of the bed only. Therefore, the lift-off would be initially retarded by the bottom wall-stress. After this stress had vanished, additional wall-frictional forces could further retard the lift-off as well as the relative motion between bed and wall. Friction forces retarded the formation of the air gap in beds deeper than 50-100 mm vibrated at K-values below 3. In shallower beds, and in deep beds vibrated at K-values above 3, bed lift-off was retarded by wall stresses that developed at the bottom of the vessel.

2.1.6 Effect of bed internals

Not much work on the effect of bed internals has been reported. Some work has been done in determining the flow behavior around cylindrical surfaces immersed in the bed. By using high-speed motion pictures and X-ray diffraction analysis, Sapozhnikov et al.[36] observed the largest solid and gas velocities around multiple tubes placed within vibro-beds at the lateral surfaces of the tubes, and the lowest ones near the bottom surfaces. The velocities near the top surfaces of the tubes were dependent on the vibrational conditions and on the tube location.

Malhotra and Mujumdar[37] observed the existence of air gaps above and below a cylindrical surface immersed in a vibro-fluidized bed; the size of the gaps was found to increase with the vibrational intensity, but was not strongly affected by the tube diameter. Similar air gaps should also exist in vibro-beds.

2.1.7 Classification of vibrated beds

The distortion in the acceleration wave existing when the bed and vessel collide has been used to indicate the formation of air gaps, and also to support the assumption that the bed behaves like

a rigid mass. Gray and Rhodes[33], in using this technique, observed that the number of collisions per vibrational cycle was a function of particle size and of vibrating conditions. Beds of phosphor-bronze particles of 3 mm in diameter displayed four different behaviors: (i) at 50 Hertz and low vibrating amplitudes, regular collisions and constant flight periods were detected in every vibrational cycle; (ii) on increasing the vibrational amplitude, bed separation was observed immediately on collision at each cycle, but the period of bed-flight and throw-height were repeated only at every other vibrational cycle; (iii) by further increasing the amplitude, a full vibrational cycle was eventually left out by the flight period; and (iv) at 200 Hertz, several distortions in the acceleration wave were observed in the same vibrational cycle. This latter phenomenon was interpreted as the bed no longer behaving as a single mass.

When classifying vibrated bed behavior, Buevich and Galontsev[30] suggest that beds must be first classified into shallow and deep beds. In shallow beds, it is reasonable to neglect wall-frictional forces and the effect due to the propagation of stress waves during compaction and of porosity waves during bed expansion. In deep beds, these factors cannot be neglected. Next, it is important to identify the intensity of the vibrational conditions. Mild conditions allow the bed to compact before the next detachment from the floor of the vessel. Severe conditions do not allow complete compaction, and generate collisions between different layers of material during the period of flight.

Markovskii et al.[32] classified beds vibrated at K-values greater than one into: (1) *"moving beds"*, when bed expansion takes place; (2) *"vibro-spouted beds"*, when a multitude of microspouts develops in the bed; (3) *"suspended beds"*, when the upper surface of the bed is at rest, while the lower part of the bed vibrates; and (4) *"plug-type beds"*, when the bed vibrates as a rigid piston of porous material, and the air gap is periodically formed. The importance of bed porosity and porosity propagation is apparent in the first three groups of the proposed classification. In addition, the described behavior was shown to be dependent on the vibrational parameters, the particle diameter, the bed depth, and the pressure above the bed. Plug-type bed behavior in beds of 120-mm depth of 160-μm corundum particles vibrated at 40 Hertz was observed only at very low pressures, below 4-mm Hg, at K-values above 3.9. The absence of an air- gap at K-values below 3.9 seems to be related to particle-wall frictional forces. Such an observation suggests that the concept of

shallow and deep beds is related to the effect of drag forces on vibro-bed behavior. If the effect is negligible, even "deep" beds can be treated as a single, rigid mass.

2.1.8 Summary on vibro-bed dynamics

The reported experimental results on vibro-bed dynamics can be summarized as follows:

(1) Air gaps tend to form at the floor of a vibrating vessel containing a bed of particles when the vibrational intensity parameter K exceeds one. The air-gap size increases as K is increased.

(2) Pressure oscillations develop at the floor of the vessel and induce a vertical, oscillatory gas motion. This gas motion exerts a drag force on the bed of particles, reducing the air-gap size.

(3) Bed compaction occurs during the period of time that the bed and the floor of the vibrating vessel are in contact. For small particles, bed expansion can occur during the bed-flight period.

(4) The gas motion induced by the pressure oscillations generates solid-circulation patterns in beds of small particles. This particle motion yields non-horizontal bed-surface configurations.

(5) Wall-frictional forces tend to delay the bed lift-off and to reduce the bed-flight period.

2.2 Heat Transfer in Vibro-beds.

Although Kroll[6] was first in reporting some of the characteristics of solid-flow patterns in vibro-beds, Chlenov and Mikhailov[7,8,20] seemed to be first in recognizing the potential applications of vibrations in processes involving heat and mass transfer. Their reasoning was mainly based on the following observations: (i) the intensity of solid circulation and mixing could be controlled by the vibrational parameters alone and is essentially independent of additional gas passage through the bed[7]; (ii) nearly isothermal temperature profiles could be maintained in the bed when heat was

added through the base plate of the vessel[8]; and (iii) air currents generated by pressure differentials within the bed tended to improve solid motion and mass transfer in drying operations.

Table 2 on page 40 summarizes the experimental research on heat transfer in vibrated beds. Literature data on heat-transfer coefficients in vibro-beds present a wide range of values. This wide range of values resulted from the variety of experimental conditions employed in their determination, such as different bed temperatures, vibrational conditions, and sizes as well as geometries of the vibrating vessel and heat-transfer surface.

Most of the experimental determinations of heat-transfer coefficients has been performed in batch systems containing a single heat-transfer surface. These systems were subjected to vertical, sinusoidal vibrations. Vibrations applied to continuous systems were also sinusoidal in shape, but their direction were slightly inclined with respect to the vertical direction. The resulting horizontal component of the vibrational field would induce the continuous movement of solids along the vibrating vessel.

Steady-state heat-transfer coefficients have been determined from

$$Q = h A_h (T_h - T_b) \qquad [2.1]$$

where Q is the total heat input to the bed per unit time, A_h is the active surface area of the heating surface, T_h is its surface temperature, T_b is the average bed temperature, and h is the heat-transfer coefficient. In unsteady-state determinations, this equation was usually integrated over the period of time of interest.

The discussion that follows is divided into a number of topics:

(1) Vibrated beds and gas-fluidized beds;

(2) Effect of vibrational conditions;

(3) Effect of probe geometry and location;

(4) Importance of the gas medium;

(5) Effect of particle circulation and air gaps;

(6) Multi-tube systems;

(7) Continuous systems.

Table 2 : Experimental research in vibro-bed heat transfer

Investigators	Particles	Particle size, μm	Vibro-bed parameters[1]	Heating surface	Remarks on heat-transfer rates
Zabrodskii et al.[43]	Sand Corundum	280-630 24-95	L = 70 mm x_0 < 4 mm f < 25 Hz	Vertical cylindrical	Larger in vibro-beds than in gas-fluidized beds. Increased rates when increasing either the vibrational frequency or amplitude.
Kalt'man and Tamarin[44]	Corundum	7-290	L = 70-80 mm f = 16-36 Hz x_0 = 3-12 mm	Spherical	Maximum rates independent on vibrational conditions
Ryzhkov et al.[22]	Aluminum oxide	60-2000	L < 500 mm x_0 = 2.73 mm f = 16-32 Hz	Spherical and flat plate	Rates independent of probe geometry when flat plate was placed vertically in the bed. Horizontal heating surfaces yielded lower rates. Rates higher in the upper than in the lower part of the bed.
Bukareva et al.[12,27]	Quartz sand Sodium chloride	280-355 < 1000	L < 70 mm K < 10 f = 20-100 Hz	Vertical and horizontal flat plates	Higher rates for vertical heaters.
Sapozhnikov and Zyromyatnikov[46,47]	Corundum	160-320	L = 45-65 mm x_0 < 1 mm f = 30-80 Hz	Cylindrical and spherical	Rates decreased as the air pressure was reduced
Muchowski[42]	Glass beads Tin-bronze Polystyrene	100-1000 100-1000 100-1000	x_0 = .25-2.5 mm K ≤ 4	Horizontal flat plate	Rates increased as solid-circulation rates increased and particle size decreased. Highest rates for tin-bronze particles; lowest ones for polystyrene.

Table 2 (Continued)

Investigators	Particles	Particle size, μm	Vibro-bed parameters[1]	Heating surface	Remarks on heat-transfer rates
Gutman[14,48]	Glass beads	84-965	$L \leq 150$ mm $K \leq 6$ $f < 50$ Hz	Horizontal and vertical flat	Rates higher for vertical heaters For the same K-value, rates lower at higher frequencies.
Ringer[41]	Glass Beads Granal Polystyrene	200-2050 800 1050	$f = 50$ Hz $L = 1$[illegible] mm Flowing layer of solids	Floor of the conveying trough	Rates controlled by particle-residence time in the trough. Rates higher for small particles at low residence times. Lowest rates for polystyrene.
Sapozhnikov et al.[36]	Aluminum oxide	120-800	$L = 120$-160 mm $x_0 = .1$-3.5 mm $f = 20$-60 Hz	Rows of horizontal tubes	Local rates higher at the laterals of the tubes
Kossenko et al.[10]	same	same	same	same	Rates not significantly affected by tube diameter.

[1] L = bed depth; f = vibrational frequency
x_0 = vibrational amplitude; K = vibrational intensity parameter

2.2.1 Vibrated beds and gas-fluidized beds

Zabrodskii et al.[43] observed that heat-transfer coefficients in a vibro-bed were greater than those measured in a gas-fluidized bed. Coefficients in the gas-fluidized bed were determined in a quartz column of 1000 mm in height and 64 mm in diameter filled with solids to an initial bed depth of 175 mm. The heating surface consisted of a stainless steel strip wound in a spiral of 40 mm in diameter and 120 mm in height. Surface temperatures during the tests were as high as 1000 ^{0}C. Experiments with the vibro-bed were performed under widely different conditions. The bed, 70-mm deep, was contained in a cylindrical vessel of 110 mm in diameter. A cylindrical heating surface of 8.6 mm in diameter and 30 mm in height was used, and its surface temperature was kept constant at only 60^{0}C. The heating surface was positioned vertically along the axis of the vibrating vessel. Sand and corundum were used as bed materials of the gas-fluidized and of the vibro-beds.

As shown in Figure 17 on page 43, experimental results were plotted in the form of the group $h_m/\lambda^{0.6}\rho_s^{0.2}$ as a function of the particle diameter d_p. Here, h_m is the maximum heat-transfer coefficient obtained for a particular particle diameter, λ is the thermal conductivity of the gas, and ρ_s is the density of the solid. Coefficients in the vibro-bed were determined at a vibrational frequency of 23.4 Hertz, and at an amplitude of 4 mm, which corresponds to a vibrational intensity parameter K = 8.8. According to Zabrodskii et al.[43], the results suggested that solid mixing was more intense in a vibro-bed than in an air-fluidized bed. It would be more efficient to transmit energy to *"fluidize"* a bed of particles by vibrations than by gas flow alone. As the particle size was decreased, heat-transfer coefficients in both types of beds increased until a maximum was attained. Further decreasing the particle size resulted in lower heat-transfer coefficients. In an air-fluidized bed, the maximum occurred at a particle diameter of approximately 80 μm; while in the vibro-bed, it occurred at about 25 μm. The occurrence of a maximum was explained by the onset of particle agglomeration, which could be destroyed efficiently by vibrations.

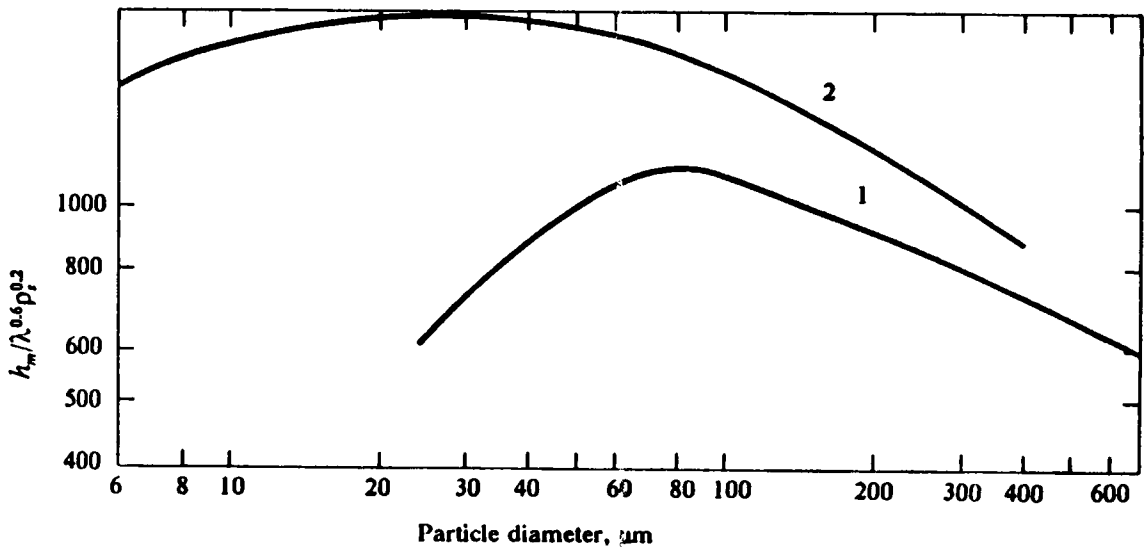

Figure 17. Heat transfer in vibrated and gas-fluidized beds: Dependence of the maximum heat-transfer coefficient on the particle diameter in gas-fluidized (1) and vibrated (2) beds of sand and corundum particles. Notation: h_m = maximum heat-transfer coefficient; λ = thermal conductivity of the gas; ρ_s = particle density (Zabrodskii et al.[43]).

The dependence of the heat-transfer coefficient on bed temperature was investigated by Zabrodskii et al.[43] in gas-fluidized beds, and by Kal'tman and Tamarin[44] in vibrated beds. In both types of beds, the heat-transfer coefficient was found to increase with increasing bed temperatures.

2.2.2 Effect of vibrational conditions

Zabrodskii et al.[43] observed that heat-transfer coefficients in vibro-beds were very dependent on the vibrating conditions in addition to the particle diameter. Figure 18 on page 45 presents some of their data for corundum particles of 68 μm in diameter. One order of magnitude separated the lowest value of about 100 W/m^2-C from the highest value of 1000 W/m^2-C. At a constant vibrational amplitude, heat-transfer coefficients increased with increasing vibrational frequencies before passing through a maximum, and then decreased. This behavior was characteristic for all particle sizes, except for the finest 6-μm particles. Those fine particles showed a continuous growth of the heat-transfer coefficient up to 25 Hertz, the maximum frequency utilized in the experiments.

For the smaller vibrational amplitudes, a very abrupt increase in the value of the coefficient occurred at a vibrational frequency of approximately 18 Hertz. In neither case, was the heat-transfer coefficient improved by further increasing the vibrational frequency, although the larger amplitude of 2 mm led to higher coefficients. Therefore, higher heat-transfer coefficients can apparently be obtained by increasing the vibrational amplitude at a constant frequency than by increasing the vibrational frequency at a constant amplitude.

Some of the results by Zabrodskii et al.[43] were confirmed by Kal'tman and Tamarin[44] in 75-mm deep beds of 45.9-μm corundum particles vibrated at 16.8 Hertz in a cylindrical vessel of 140 mm in diameter. At low heating-surface temperatures, the measured value for the heat-transfer coefficient was about 100 W/m^{2}C at a vibrational amplitude of 1.5 mm, and approximately 1000 W/m^{2}C at a 6-mm amplitude. The experiments were performed with spherical heating probes of 20 mm in diameter made of copper or nickel. The probes were first heated in a furnace to approximately 900^{0}C, and then fixed at the center of the bed. It was not clear whether the probes

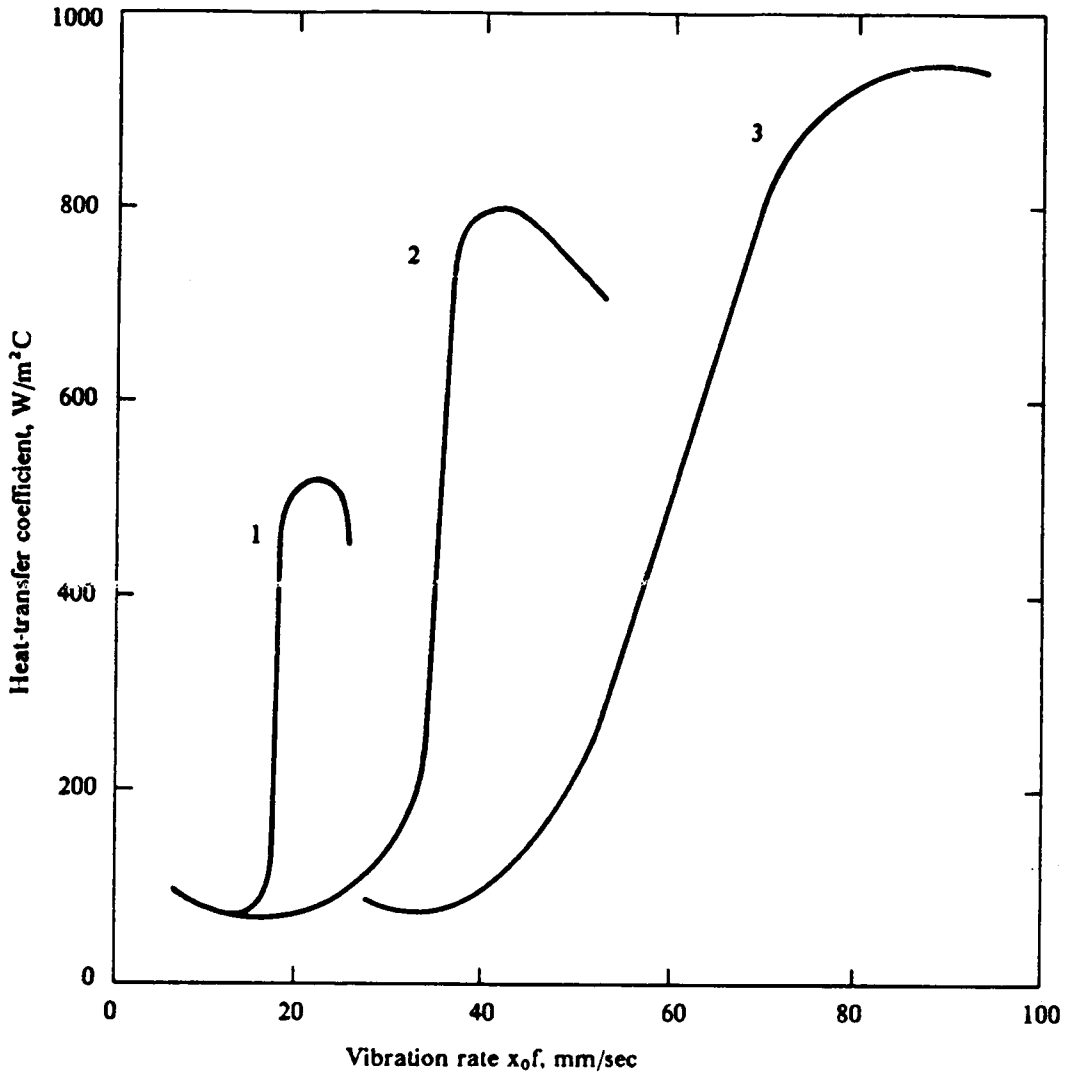

Figure 18. Effect of the vibration rate on heat-transfer coefficients: Beds of 68-μm corundum particles vibrated at a frequency f and an amplitude x_0. Vibrational amplitudes: (1) 1 mm; (2) 2 mm; (3) 4 mm (Zabrodskii et al.[43]).

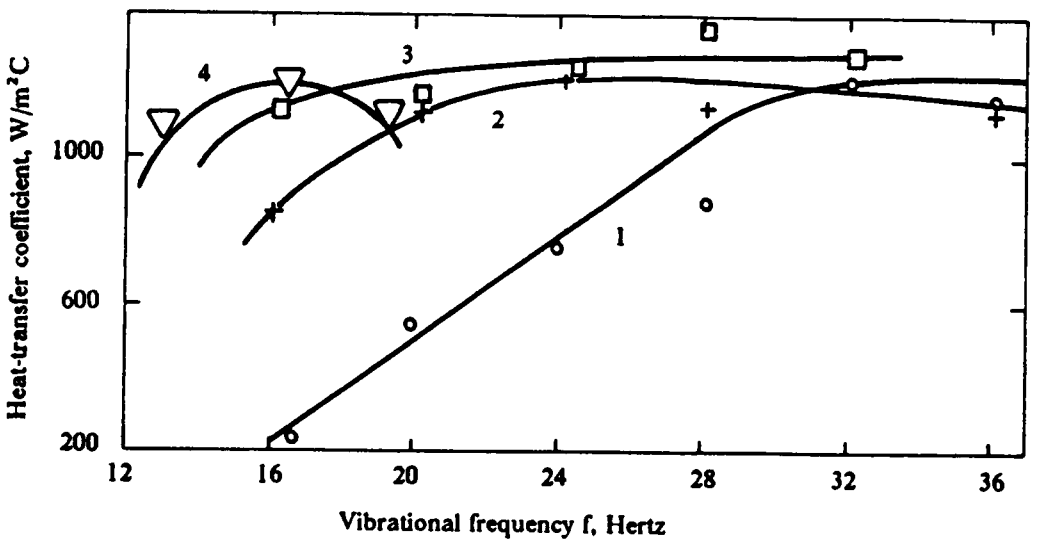

(a) Heat-transfer coefficients

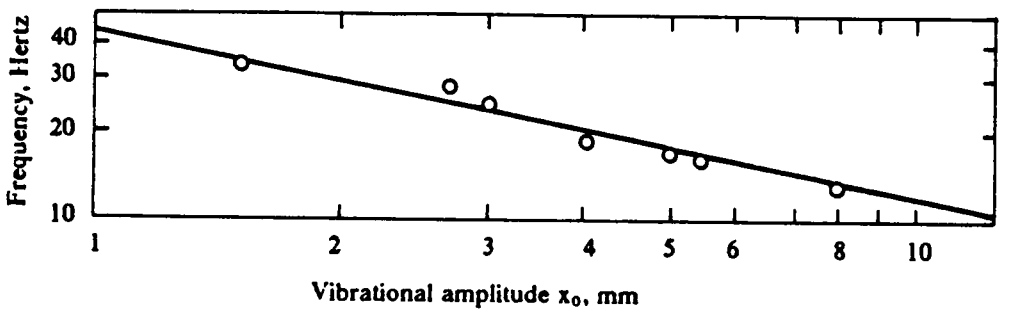

(b) Optima vibrational parameters for maximum heat-transfer rates: $x_0\omega^{1.6} = 7.6$ m/sec

Figure 19. Effect of vibrational parameters on vibro-bed heat transfer: Layers of 45.9-μm corundum particles vibrated at a frequency f and an amplitude x_0. Vibrational amplitudes: (1) 1.5 mm; (2) 3.0 mm; (3) 4.0 mm; (4) 6.0 mm (Kal'tman and Tamarin[44]).

were held stationary, or if they were mounted to the vibrating table. The heat-transfer coefficients for this unsteady-state process were calculated from

$$h = \frac{\rho_h V_h C_{ph}}{A_h t} \ln \left[\frac{\Delta T_1}{\Delta T_2} \right] \qquad [2.2]$$

where ρ_h is the density of the probe, V_h is its volume, C_{ph} is its heat capacity, A_h is its surface area, t is the time period over which the measurement is made, and ΔT_1 and ΔT_2 are the temperature differences between the probe and the bed at the beginning and at the end, respectively, of the time period t.

As seen in graph (a) of Figure 19 on page 46, the dependence of the heat-transfer coefficient on the vibrational frequency, at constant amplitude, seemed to follow the same pattern as the one shown in Figure 18 on page 45. The maximum value of the coefficient was, however, fairly independent of the vibrational amplitude, and occurred at lower frequencies as the amplitude was increased. Also, at small amplitudes, the heat-transfer coefficient continued to grow when increasing the frequency above 20 Hertz. There are insufficient data indicating whether these differences in behavior were related to the probe size and geometry, or to the particle size.

The constancy of the maximum heat-transfer coefficient with vibrational conditions was attributed by Kal'tman and Tamarin[44] to an identical contact time between the surface of the probe and the particles. The occurrence of the maximum in the coefficient was correlated to the vibrational conditions by $x_0 \omega^{1.6} = 7.6$ m/s. Here, x_0 is the amplitude and ω the angular frequency of the vibrations. Graph (b) in Figure 19 on page 46 shows this dependence expressed in a logarithmic form.

2.2.3 Effect of probe geometry and probe location

Ryzhkov et al.[22] investigated heat transfer between vibrated beds of aluminum oxide particles contained in cylindrical vessels of 100-300 mm in diameter and heating probes of spherical and

flat-plate geometries. The heating probes were held stationary with respect to the vibrating vessel. The diameter of the sphere was 20 mm, and the dimensions of the flat plate, 40 mm x 40 mm. The bed depth was varied between 50 mm and 500 mm. Heat-transfer coefficients were found to be virtually independent of the vessel diameter over the range of diameters investigated, and of the probe geometry when the flat plate was placed vertically either inside the bed or at the wall of the vessel. At a vibrational amplitude of 2.73 mm and frequencies of 16 to 30 Hertz, values of 125-155 W/m^2C were obtained for beds of 2-mm particles, 250-520 W/m^2C for 0.2-mm particles, 320-650 W/m^2C for 0.12-mm particles, and 420-680 W/m^2C for beds of 0.06-mm particles. Lower coefficients were, however, obtained when the flat plate was placed horizontally on the floor of the vessel.

Figure 20 on page 49 illustrates the observed dependence of the heat-transfer coefficient on the vibrational frequency for different probe geometries and locations. A 150-mm deep bed of 0.12-mm aluminum oxide particles was vibrated in a 100-mm vessel at an amplitude of 2.73 mm. Heat-transfer coefficients between the bed of particles and a spherical heating-surface placed 130 mm above the floor of the vessel increased very fast with increasing frequency below 12 Hertz, and remained practically constant as the frequency was further increased beyond 12 Hertz. The sharp increase was related to the onset of solid circulation at the upper bed boundary of the bed. Such circulation was not observed at a distance of 30 mm from the base plate of the vessel, which would explain the small coefficients measured at this location up to 15 Hertz. At the latter frequency, solid circulation had been extended down to the lower bed boundary. An immediate sharp increase in the heat-transfer coefficient was noticed close to the bottom of the bed. Higher coefficients in the upper part of the bed were attributed to intense solid activity and circulation in this region. As shown in the same figure, heat-transfer coefficients between a vibrated bed and a horizontal heating-plate placed on the floor of the vessel always lower than the corresponding coefficients determined for the spherical probe.

Investigations done by Bukareva et al.[12,27] on the influence of the position of a flat heating surface on the magnitude of heat-transfer coefficients yielded results similar to those of Ryzhkov et al.[22], which are shown in Figure 20 on page 49. Heat-transfer coefficients for a vertical heater were in general greater than those for a horizontal heater placed on the base plate of the vibrating

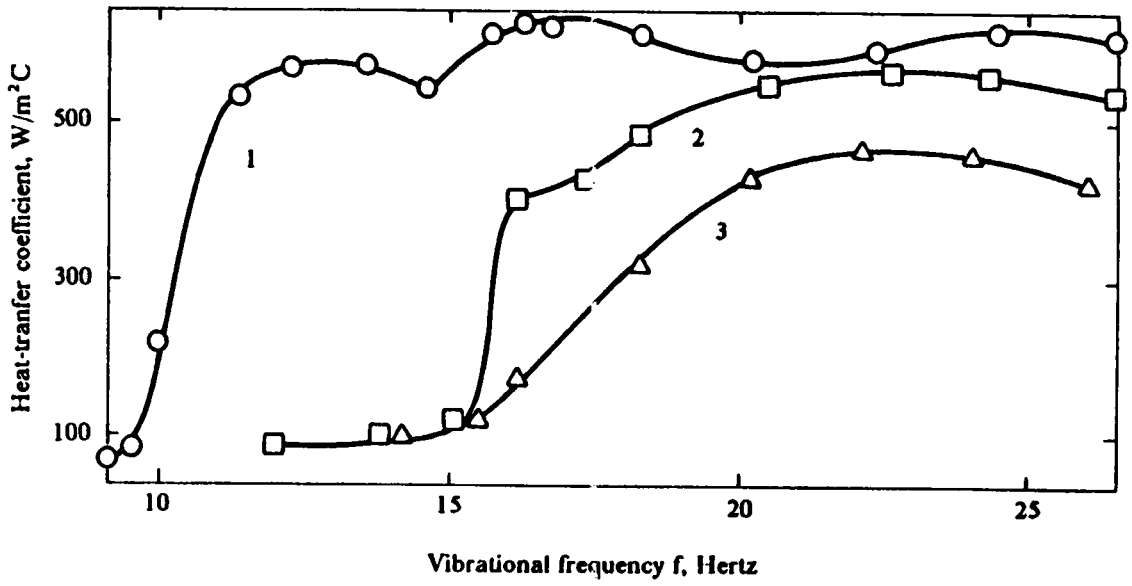

Figure 20. **Effect of probe location on heat transfer in vibro-beds:** Heat-transfer coefficients in a 150-mm deep bed of 120-μm corundum particles vibrated in a cylindrical vessel of 100 mm in diameter at an amplitude of 2.75 mm. Notation: (1) Spherical heat probe located 130 mm above the vessel floor; (2) Spherical heat probe located 30 mm above the vessel floor; (3) Horizontal flat probe located on the vessel floor (Ryzhkov et al.[22]).

vessel. Bukareva et al.[27] utilized a vibrating vessel of 110 mm in diameter and two types of solids: sand and sodium chloride. The average size of both solids was approximately the same, but the size distribution was different. The size distribution of sand was confined to 280-355 μm; sodium-choride size distribution included about 11% of particles below 60 μm, and about 3% of particles between 500 and 1000 μm in diameter. The dimensions of the vertical heater were 43 mm by 12 mm, and those of the horizontal heater, 40 mm by 40 mm. Vibrating frequencies ranged from 20 to 100 Hertz at K-values up to 10.

Heat-transfer data for a bed of sand particles of 70-mm bed depth are presented in Figure 21 on page 51. As a function of the the product $x_0 f$ (x_0 is the vibrational amplitude and f is the vibrational frequency), the heat-transfer coefficients could be correlated by a single curve for the vertical heater. No maximum was observed in this curve, which was attributed to the continuous intensification of solid mixing as $x_0 f$ was increased. Bed-porosity increase was assumed to be prevented by the suction action underneath the bed. For the horizontal heater, a different curve was obtained for each vibrational frequency. At constant $x_0 f$, which is directly proportional to the vibrational velocity, the combination of high vessel amplitudes and low frequencies yielded larger heat-transfer coefficients than the combination of low amplitudes and high frequencies. The lower performance of the horizontal heater was explained by the presence of air gaps between the bed and the floor of the vessel.

Almost the same behavior was observed in beds of sodium-chloride particles. As shown in Figure 22 on page 52, no maximum heat-transfer coefficient was detected on the curves for the horizontal heater over the investigated range of experimental conditions. According to Baskakov et al.[27], the presence of fine particles reduced the bed permeability to air flow, and, consequently, the size of the air gap at the same vibrational conditions. The net effect would be the displacement of the extremum in the heat-transfer coefficient toward higher values of $x_0 f$.

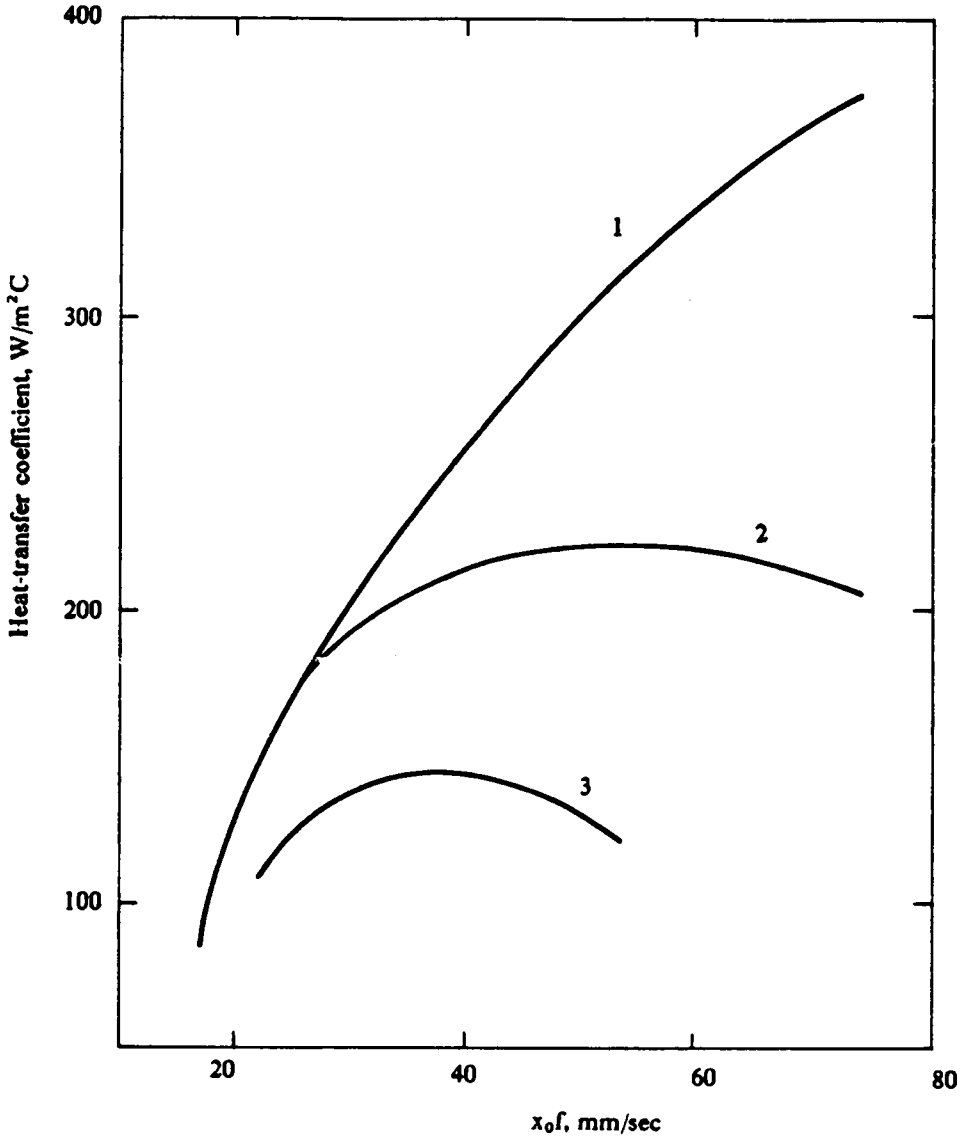

Figure 21. **Heat transfer in vibro-beds of quartz-sand particles:** 70-mm deep layers of particles vibrated at a frequency f and an amplitude x_0. Notation: (1) Vertical flat heater at the center of a bed vibrated at frequencies of 25 to 60 Hertz; (2) Horizontal flat heater on the floor of a vessel vibrated at 40 Hertz; and (3) Horizontal flat heater on the floor of a vessel vibrated at 60 Hertz (Bukareva et al.[27]).

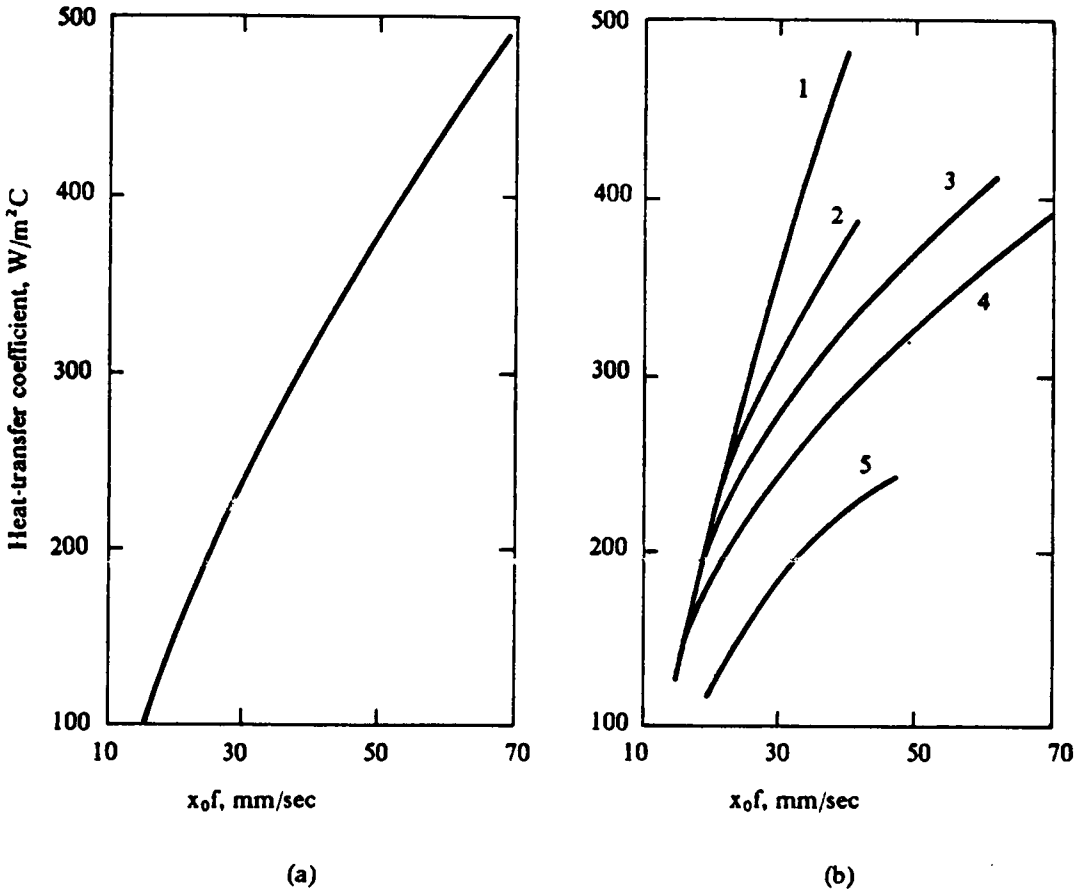

Figure 22. **Heat transfer in vibro-beds of sodium chloride:** Layers of particles vibrated at a frequency f and an amplitude x_0. (a) Vertical flat heater in a bed of 50 mm in depth vibrated at frequencies of 25 to 60 Hertz; (b) Horizontal flat heater on the vessel floor of a bed of 30 mm in depth vibrated at 25 (1), 30 (2), 40 (3), 50 (4), and 60 (5) Hertz (Bukareva et al.[27]).

2.2.4 Importance of the gas medium

Experimental heat-transfer results discussed so far were determined in open systems at atmospheric pressure. Zamnius et al.[45] investigated the effect of changing the gas medium on the heat-transfer coefficients in vibro-beds of corundum powder. They utilized air, helium, and carbon dioxide, covering a range of thermal conductivities whose extremes were separated by a factor of ten. Under fixed vibrational conditions, coefficients were found to increase with increasing values of the thermal conductivity of the gas.

The dependence of heat-transfer coefficients on low air pressures was studied by Sapozhnikov and Syromyatnikov[46] in beds of corundum particles. Bed depth was 45 to 50 mm, and the heating surface was a spherical probe of 15 mm in diameter. Figure 23 on page 54 illustrates the variation of the maximum heat-transfer coefficient as the absolute pressure is reduced below atmospheric pressure in a bed of 160-μm particles vibrated at 41 Hertz and different amplitudes. For small vibrational amplitudes, the coefficients first increased with a pressure reduction, which could not be explained. Below 10 kPa, heat-transfer coefficients decreased with decreasing gas-medium pressures at all amplitudes. At about 40 Pa, heat-transfer coefficients were below 40 W/m^2C. The decrease in the maximum heat-transfer coefficient was attributed to a reduction in the thermal conductivity of the gas. Therefore, one may conclude that the presence of the gas medium is essential for obtaining high heat-transfer coefficients.

Sapozhnikov and Syromyatnikov[47] also determined the effective thermal conductivity in the horizontal direction in a vibro-bed of 65 mm in depth contained in a cylindrical vessel of 154 mm in diameter. Corundum particles of 0.32 and 0.16 mm in diameter were used as the bed material. A cylindrical heater of 60 mm in height and 15 mm in diameter was placed along the axis of the vibrating vessel. At very low absolute pressures, the effective vibro-bed thermal conductivity in the horizontal direction, λ_{eff}, was determined by the equation,

$$\lambda_{eff} = \frac{Q}{2\pi H (T_{b1} - T_{b2})} \ln \left[\frac{R_2}{R_1} \right] \qquad [2.3]$$

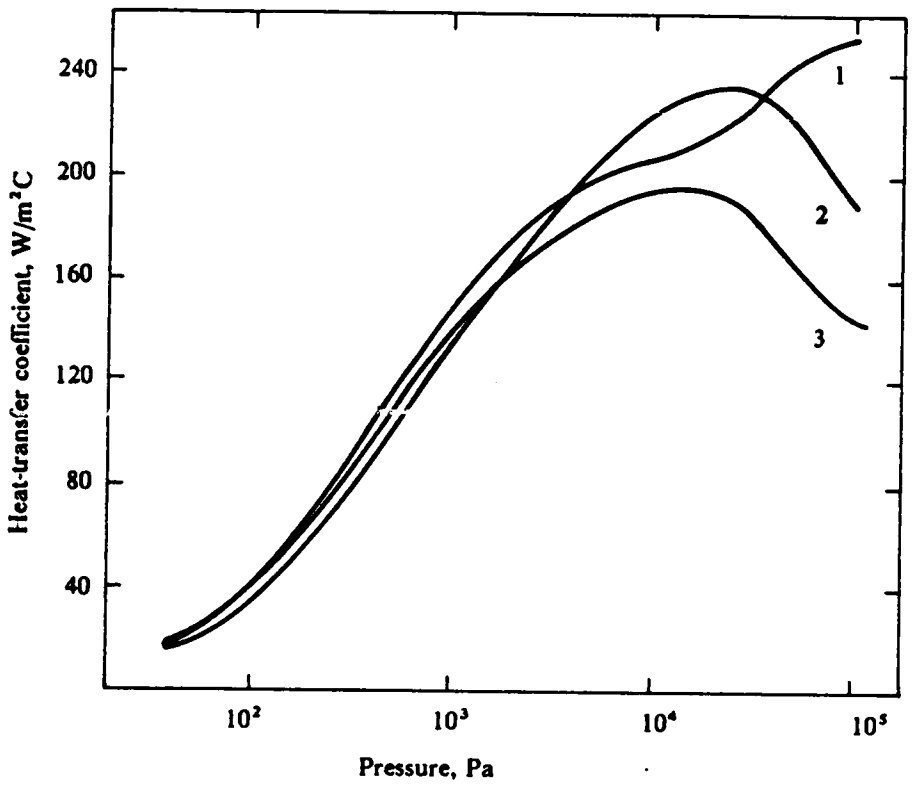

Figure 23. Effect of air pressure on heat transfer in vibro-beds: 45-50 mm deep layers of 160-μm corundum particles vibrated at a frequency of 41 Hertz. Amplitudes: (1) 0.60 mm; (2) 0.44 mm; (3) 0.30 mm (Zapozhnikov and Syromyatnikov[46]).

In this equation, Q is the total heat input to the bed per unit time, H is the height of the cylindrical heating probe, T_{b1} is the bed temperature near the heating surface, T_{b2} is the bed temperature near the wall of the vessel, R_1 is the radius of the heating probe, and R_2 is the radius of the cylindrical vibrating vessel. At atmospheric pressure, Q was corrected for heat losses through the percolating gas flow in and out of the bed of particles.

Sapozhnikov and Syromyatnikov[47] assumed that the effective thermal conductivity in the vibro-bed would represent primarily heat transfer by convection of the particles. They also assumed that the parameter $x_0^2\omega^3$ (x_0 is the vibrational amplitude and ω is the angular vibrational frequency) would give a better representation of the intensity of particle motion because it provided a measure for the vibrational power input to the system. Maximum effective thermal conductivities of about 30 W/m-C were determined at pressures of about 100 Pascals. These values are comparable to the thermal conductivity of corundum, which is about 36 W/m-C. Conductivities first increased with increasing values of the parameter $x_0^2\omega^3$, then passed through a maximum, and finally decreased slightly. This decrease was interpreted as an increase in bed-porosity. No dependence on particle size was noticed.

At atmospheric pressure, effective conductivities were found to be about 60% higher than those determined at reduced pressures. The increase was caused by the improvement in gas circulation and in solid circulation and mixing which are generated by drag forces exerted by the gas on solid particles.

2.2.5 Effect of particle circulation and air gaps

Muchowski[42] investigated the relative importance of particle circulation, solid properties, and air layer between particles and the heating surface by determining heat-transfer coefficients between the base plate of a vibrating vessel and the contents of the vessel. For particles of 0.5 mm in diameter and larger, solid circulation was assumed to be caused by solid-wall friction forces. Well-ordered circulation loops were observed within the bed with particles moving downward at the wall

of the vessel, and upward at the center. The particle velocity at the base plate was estimated to be about four to five times smaller than that at the vessel wall. For smaller particles, this well-ordered flow degenerated into a kind of random, turbulent motion.

Heat-transfer coefficients for 0.5-mm glass particles and for 0.9-mm tin-bronze particles at atmospheric pressure, are shown in Figure 24 on page 57 and in Figure 25 on page 58, respectively. At a constant vibrational amplitude, increasing the vibrational acceleration induced stronger particle circulation, but also larger air gaps. The maximum heat-transfer coefficient or the tendency to reach a maximum in the figures reflects the competing influences of particle circulation and air gap. At the maximum, the resistance to heat transfer in the air layer started to control the process. Any improvement in solid circulation was offset by a deterioration of heat transfer caused by the air gap. The effect was more pronounced for large particles.

In general, the heat-transfer coefficient became smaller as (i) the particle size was increased, and (ii) the pressure of the gas medium decreased. The resistance to heat transfer between the heating surface and the layer of particles was increased by increasing the thickness of the gas layer in case (i), and by decreasing the thermal conductivity of the gas in case (ii). The highest heat-transfer coefficients obtained for 1.0-mm glass beads were in the range of 75-90 W/m^2C. As the particle size was reduced, the coefficient increased to about 125 W/m^2C for 0.5-mm beads, and to about 300 W/m^2C for 0.1-mm particles. At 13 kPa, the maximum heat-transfer coefficient was measured to be below 20 W/m^2C.

Figure 24 on page 57 and Figure 25 on page 58 illustrate the relative importance of particle properties in determining the magnitude of heat-transfer coefficients. Slightly higher coefficients were obtained for the larger 0.9-mm tin-bronze particles than for the smaller 0.5-mm glass particles. Tin-bronze particles are much denser and have a larger volumetric heat capacity than glass beads. The lowest heat-transfer coefficient was measured in beds of polystyrene particles, being about 60 W/m^2C at atmospheric pressure.

Gutman[14,48] determined heat-transfer coefficients between beds of glass beads and a flat heating-surface placed either vertically within the bed, or horizontally on the floor of the vessel. Bed depths ranged from 80 to 150 mm. Figure 26 on page 59 illustrates the dependence of the

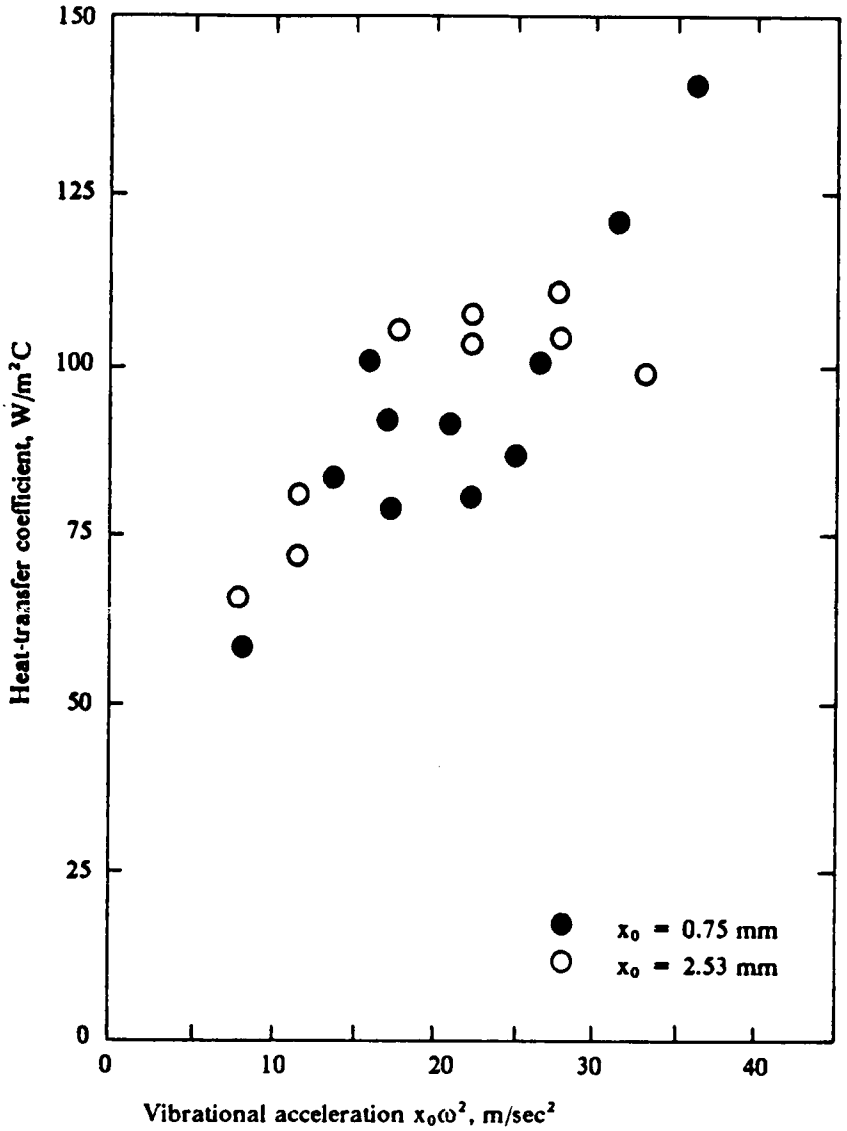

Figure 24. **Heat transfer in a vibro-bed of 500-μm glass spheres:** Horizontal heating surface on the floor of a vessel vibrated at an angular frequency ω ($= 2\pi f$) and an amplitude x_0 (Muchowski[42]).

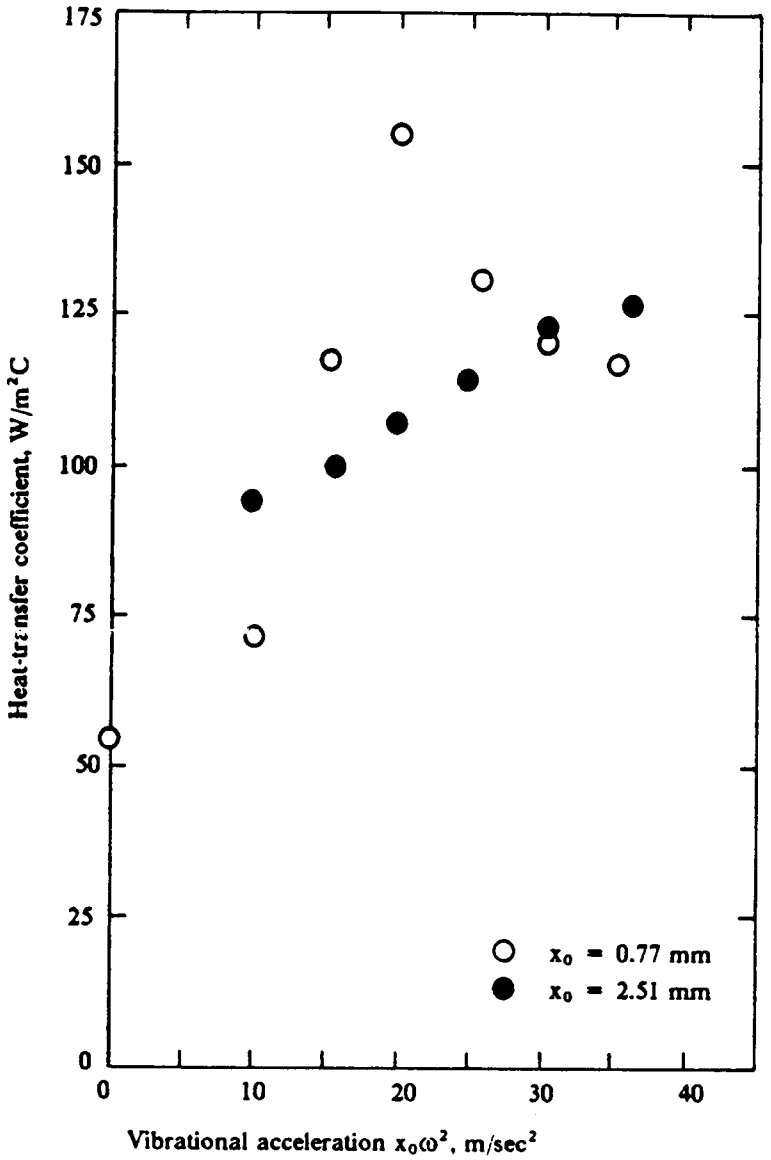

Figure 25. Heat transfer in a vibro-bed of 900-μm tin-bronze particles: Horizontal heating surface on the floor of a vessel vibrated at an angular frequency ω ($= 2\pi f$) and an amplitude x_0 (Muchowski[42]).

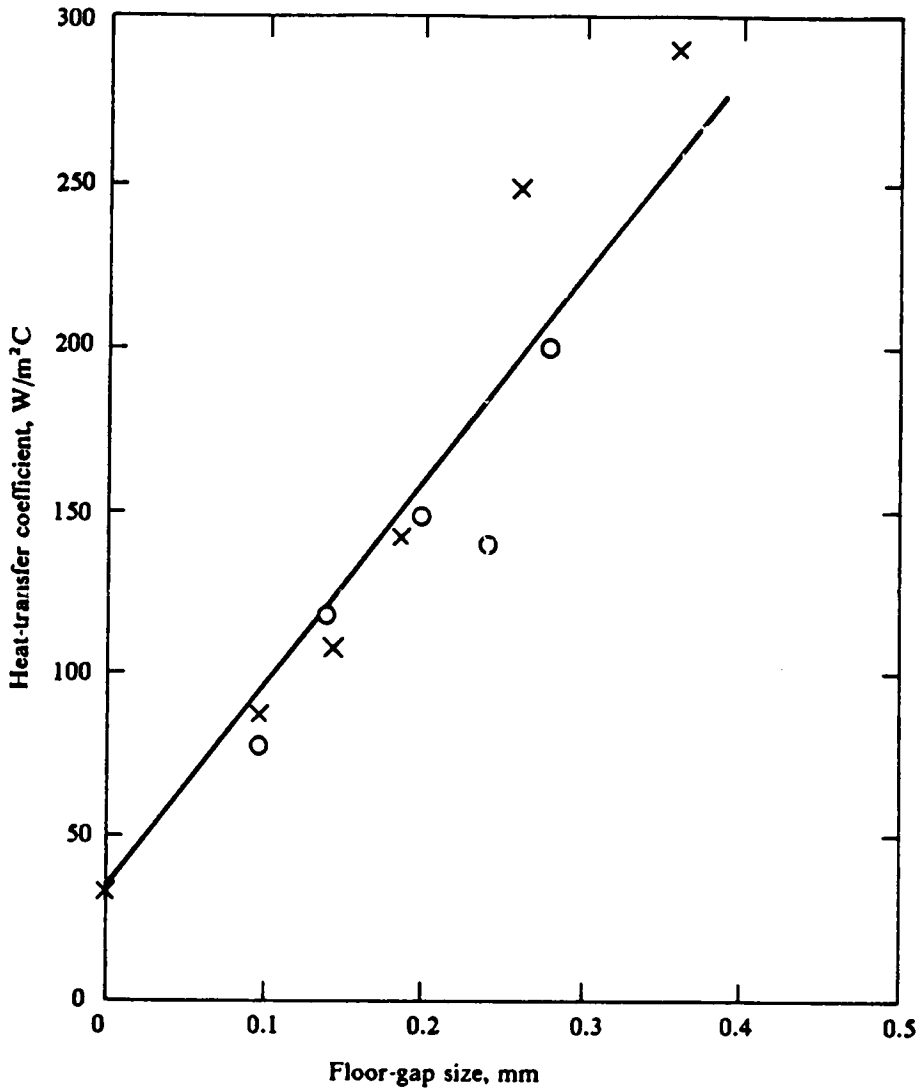

Figure 26. **Heat transfer in a vibro-bed of 90-135 μm glass beads:** Correlation between the maximum floor gap and the heat-transfer coefficient for a vertical flat heater placed at the center of a 80-mm deep bed of particles. Vessel diameter: 150 mm (Gutman[14]).

heat-transfer coefficient on the maximum air-gap size s_0 for a 80-mm layer of glass beads of 90-135 mm in diameter vibrated at frequencies of 20 and 50 Hertz. The flat heat-transfer surface was placed vertically at the center of the bed. Gutman assumed that the resistance to heat transfer was confined in the gas-sublayer between particles and the heating surface. Vibrations would decrease the effective size of this gas-sublayer and, therefore, improve the heat-transfer performance. He found that the reduction in the gas-sublayer was directly proportional to the size of the floor air gap. As a consequence, heat-transfer coefficients increase with increasing air-gap sizes as shown in the figure.

2.2.6 Continuous vibro-beds

Ringer[41] investigated heat transfer in a continuous conveying trough between the flat floor of the trough and the moving-bed of particles. The trough, which was about 1.0 m in length and 0.15-m wide, was used for conveying a continuous layer of particles that was 10-mm thick. The applied vibratory action was composed of two components: a vertical component to lift the particles off the floor of the trough, and a horizontal component to convey the solids along the trough. The rate of heat input per unit floor-area was kept constant in time and over the total floor area. The behavior of the particle layer resembled a fixed bed with no mixing action, and the flow could be assumed as piston flow. Under the conditions used in the experiments, the temperature of the top layer of the bed of particles was observed to remain constant over the conveying path. Experimental data were analyzed in terms of a two-step heat-transfer mechanism: heat transfer through the gas layer between the heating surface and the layer of particles, followed by heat transfer inside the layer of particles.

Figure 27 on page 61 presents heat-transfer data as a function of the residence time of particles in the trough for two different conveying velocities and several sizes of glass spheres. For small residence times, heat-transfer coefficients were very dependent on the particle size. As the residence time was increased, this size dependence became weaker. At very large residence times, the coefficients were almost the same for the 200-μm, 630-μm, and 2050-μm glass particles. At the same

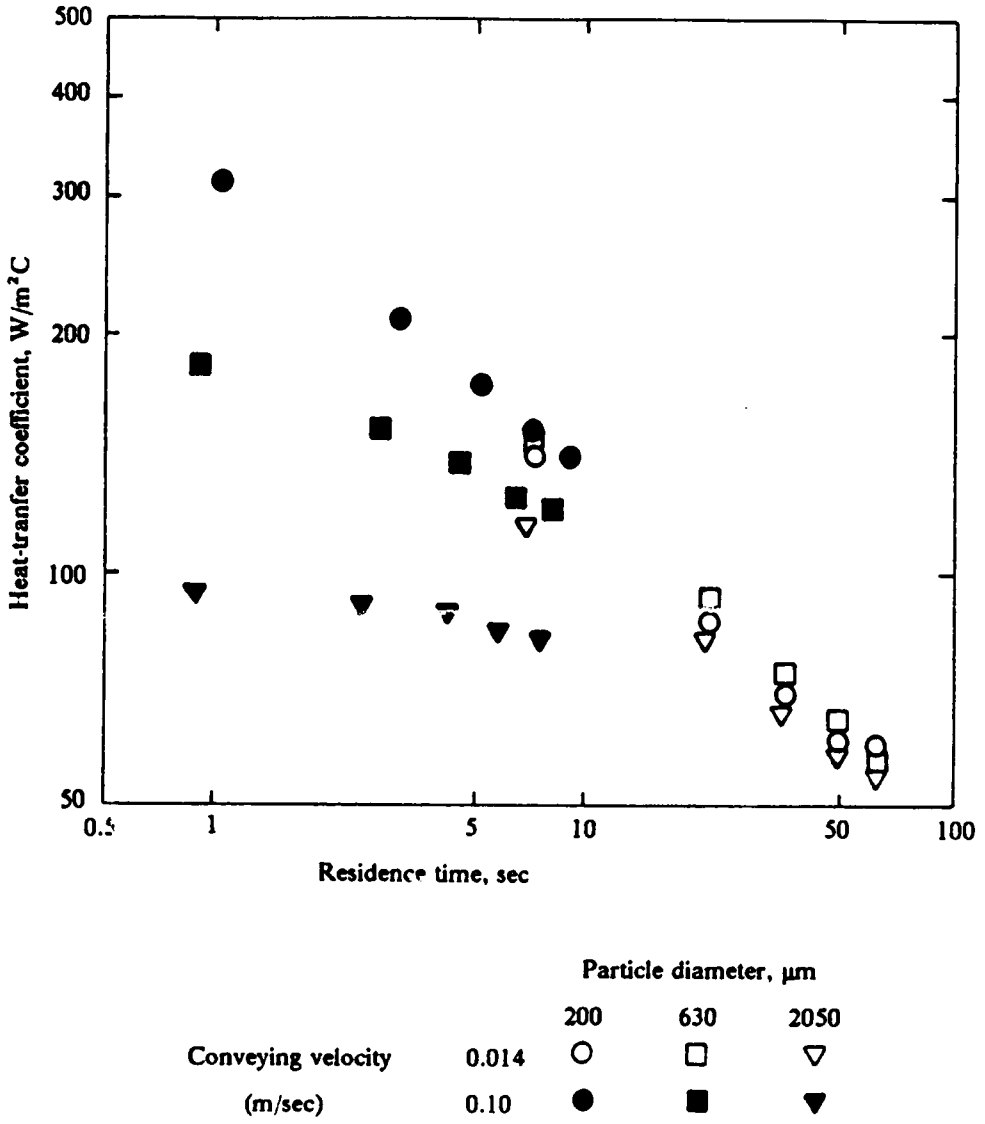

Figure 27. **Effect of particle renewal at the heat-transfer surface:** Heat-transfer coefficients between a 10-mm deep flowing layer of glass spheres and the bottom of a conveying trough vibrated at a frequency of 50 Hertz (Ringer[41]).

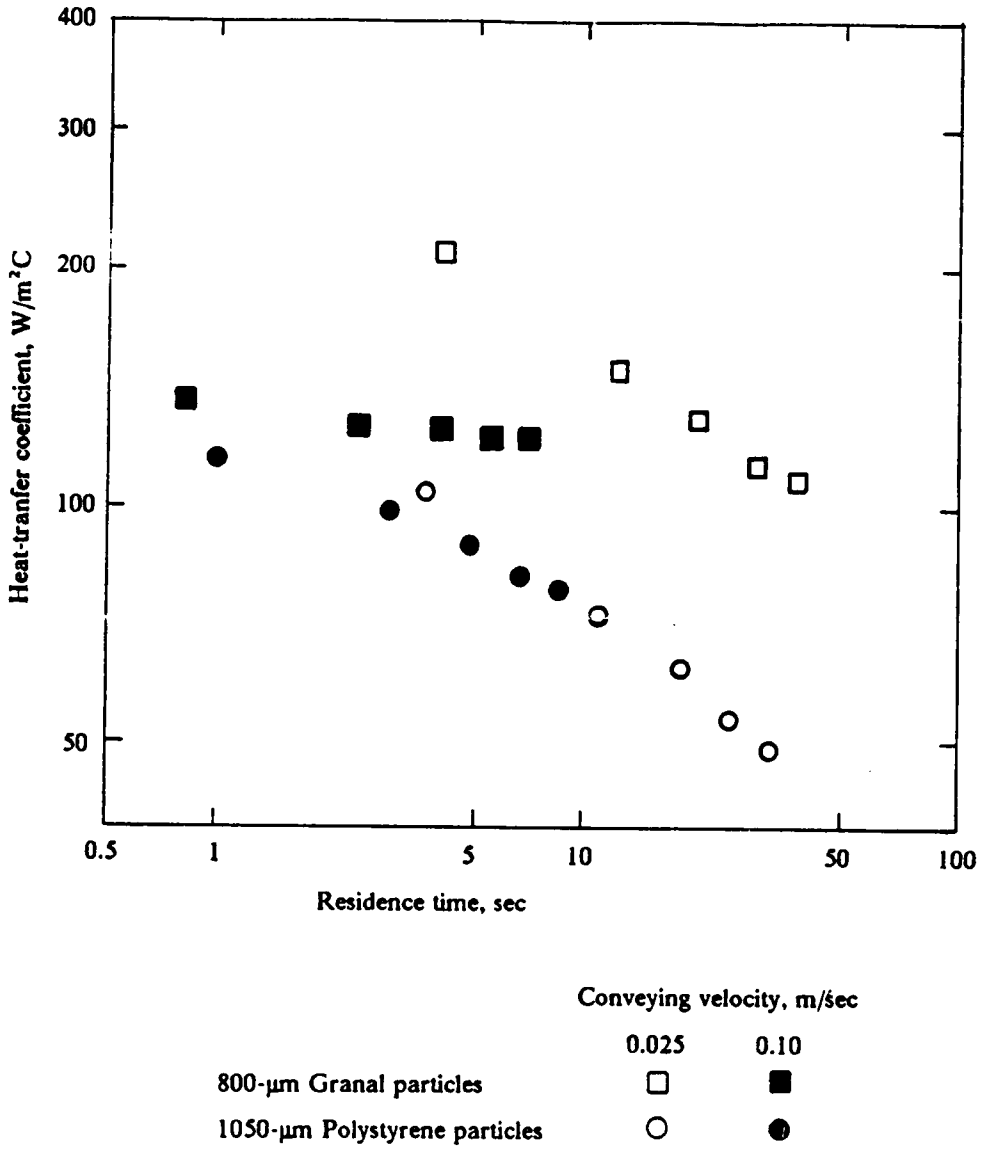

Figure 28. Effect of particle type on heat tranfer in vibro-beds: Heat-transfer coefficients between a 10-mm deep flowing layer of glass spheres and the oottom of a conveying trough vibrated at a frequency of 50 Hertz (Ringer[41]).

conveying velocity, the heat-transfer coefficient decreased continuously as the residence time was increased. According to Ringer[41], at small residence times, the heat-transfer process was controlled by the the resistance in the air layer. Since this layer increased with increasing particle diameters, heat-transfer coefficients for smaller particles were observed to be higher than those for larger particles. As the residence time was raised, the resistance to heat transfer within the layer of particles became increasingly more significant. Since this resistance was not very dependent on the particle size, but rather on particle thermal properties, heat-transfer coefficients for different particle sizes tended to become indistinguishable from one another. The heat-transfer coefficient at a residence time of 10 seconds was greater for largest particles, and this result was related to a reduction in the vibrational amplitude used to obtain a smaller conveying velocity. The latter led to thinner air gaps.

Figure 28 on page 62 shows the dependence of the heat-transfer coefficient on particle properties for equivalent particle sizes. At small residence times, when the resistance in the air gap was expected to control the heat transfer, nearly the values for the coefficients were obtained. As the residence time was increased and the resistance in the particle layer became appreciable, the effect of particle properties became noticeable. Larger coefficients were obtained for Granal (99%-aluminum spheres), because its density and thermal properties are higher than those of polystyrene.

2.2.7 Multi-tube systems

Some of the characteristics of heat transfer between cylindrical surfaces and vibro-beds were investigated by Sapozhnikov et al.[36], and by Kossenko et al.[10]. Both groups of researchers utilized bundles of tubes instead of a single tube.

Efforts by Sapozhnikov et al.[36] were directed towards the determination of local heat transfer coefficients around the tube periphery. Beds of aluminum-oxide particles of several diameters were vibrated in vessels containing either a single row of tubes, or a double row. Only one tube in each row was actually an active heat-transfer surface; the remaining tubes induced the preferred solid-

circulation pattern. Each heating tube contained at least 12 stainless-steel heating strips on its surface, which allowed an independent determination of at least 12 local heat-transfer coefficients. Two tube diameters were used: 25 mm and 38 mm. Bed depths were varied from 120 to 160 mm, frequencies from 20 to 60 Hertz, and vibrating amplitude from 0.1 to 3.5 mm.

Under all experimental conditions considered, the maximum local coefficients were usually observed at the lateral surfaces of the tube, at about +/- 30 degrees from the outermost location. The lowest coefficients were always found at the surface below the tube at its lowest position. The relative magnitude of the local coefficients changed with vibrational conditions. As the vibrational amplitude was increased, lateral coefficients decreased a little, while increases in the coefficients were detected at other locations. The distribution of local coefficients on the tube periphery approached some uniformity. With increasingly large tube diameters, heat-transfer coefficients at the lateral surfaces increased, but decreased at other locations. Decreasing the particle size improved the coefficients over all the perimeter of the tube. Enhancement in heat transfer was also achieved by using deeper beds of particles.

Those observations were explained in terms of bed dynamics. Sapozhnikov et al.[36] utilized high-speed motion pictures and X-ray diffraction analysis to measure solid- and gas-circulation rates. Both rates were observed to be largest at the lateral surfaces of the tubes. The lowest rates were determined to exist below the tubes at the lowest position of the surface. On the top of the tubes, the rates were dependent on the vibrational parameters.

Kossenko et al.[10] reported overall heat-transfer coefficients between tubes and vibro-beds for the same experimental conditions used by Sapozhnikov et al.[36]. Figure 29 on page 65 presents heat-transfer coefficients for a single row of tubes placed in a rectangular chamber (160 mm by 250 mm) as a function of the vibrational intensity parameter K. At 20 Hertz, the maximum value of overall heat-transfer coefficients was observed at K-values situated between 2 and 3. Increasing the particle size moved the location of the maximum to slighter higher values of K, and decreased the magnitude of the coefficient. The displacement of the maximum coefficient toward higher K-values was stronger when the vibrational frequency was increased. At 60 Hertz, a continuous growth of the heat-transfer coefficient was observed with increasing values of K. The magnitude of the coef-

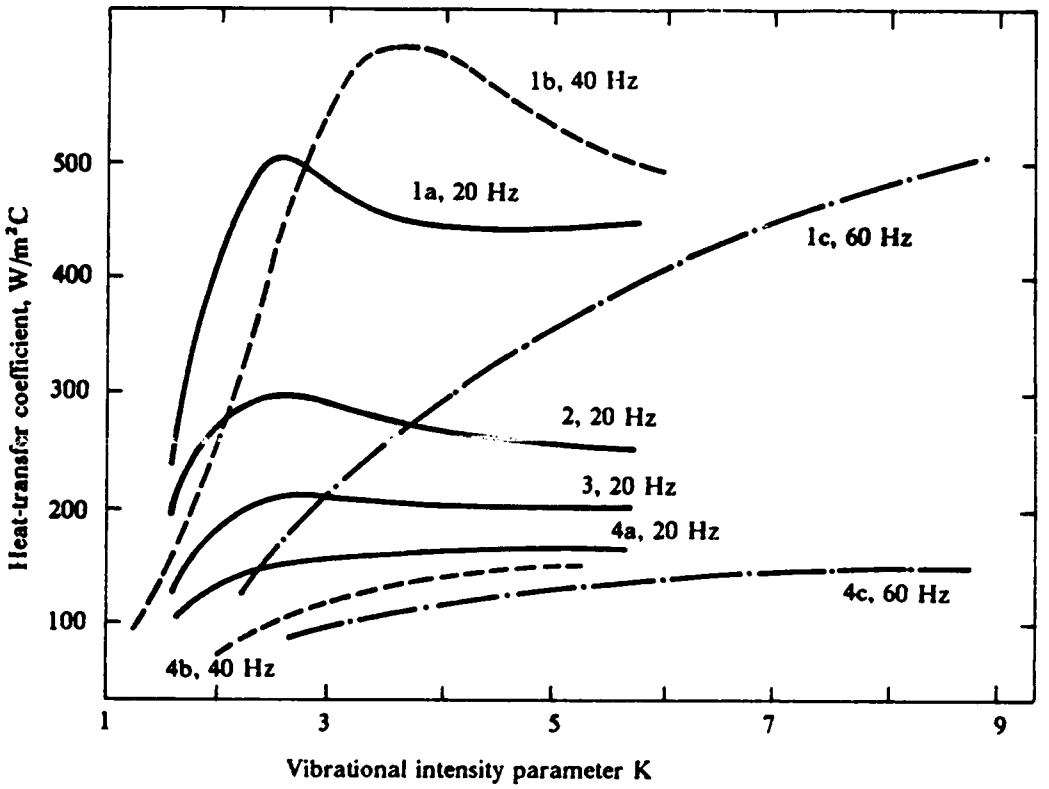

Figure 29. **Heat-transfer in a vibro-bed containing a single-row of tubes:** Tubes of 38 mm in diameter immersed in a 160-mm deep bed of aluminum-oxide particles. Particle diameter: (1a), (1b) and (1c) 120 μm; (2) 320 μm; (3) 500 μm; (4a), (4b) and (4c) 800 μm (Kossenko et al.[10]).

ficients for the same bed of particles vibrated at different frequencies tended to equalize at high K-values. Changing the tube diameter did not have significant effect on the heat-transfer coefficient.

2.2.8 Summary on vibro-bed heat transfer

The avaliable literature in vibrated beds reveals heat-transfer coefficients ranging from 100 to about 1500 $W/m^2.C$. Such a wide range of results appears to be related to the variety of experimental conditions utilized in the reported investigations. The important results can be broadly summarized as follows:

(1) Heat-transfer coefficients are larger in vibro-beds than in gas-fluidized beds.

(2) Heat-transfer coefficients increase as the vibrational intensity parameter K is increased. A maximum is eventually attained at sufficiently high K-values.

(3) Heat-transfer coefficients between a vibrated bed and the floor of the vibrating vessel are lower than those for heating surfaces immersed into the bed.

(4) The heat-transfer coefficient decreases as the absolute pressure of the gas medium is decreased.

(5) Local heat-transfer coefficients are higher at the lateral surfaces than at other surface locations of a cylindrical heater immersed into the vibrated bed.

(6) The magnitude of the heat-transfer coefficient is governed by the dynamics of the vibrated bed. The solid circulation and the gas gaps between the bed and heat-transfer surface are the primary factors that control the rate of heat exchange.

(7) Higher solid-circulation rates improve the heat-transfer coefficient. Larger gas gaps decrease the magnitude of the coefficient.

2.3 *Conclusions and Proposed Investigation*

From the previous discussion of the reported experimental results on vibro-bed dynamics and heat transfer, one may conclude that the following factors require further investigation:

(1) The nature of solid circulation and the development of air gaps at cylindrical heat-transfer surfaces immersed into a vibro-bed;

(2) The effect of the vibrational conditions and particle properties on solid circulation and air-gap formation at cylindrical heat-transfer surfaces.

The heat-exchanger concept illustrated in Figure 2 on page 7 is intended to take advantage of the high heat-transfer rates reported for vibrated beds. As described in Chapter 1, this type of heat-exchange device corresponds to a shallow bed and its design and optimization require clear understanding of the dynamic factors that affect heat-transfer rates between the bed of solids and the immersed horizontal, cylindrical heating surfaces. The work reported in the following Chapters of Part I of this dissertation is intended to contribute to this understanding through a study of the solid circulation and air-gap formation around cylindrical surfaces.

In order to accomplish this objective, the work undertaken was divided in three steps:

(1) Utilization of existing theoretical models to establish possible trends in vibro-bed behavior and in heat-transfer rates.

(2) Experimental investigation of the dynamics of beds of solids vibrated in vessels containing a "dummy", horizontal, cylindrical surface simulating an actual heat probe and interpretation of the results.

(3) Experimental investigation of heat-transfer rates between a horizontal, cylindrical heater and a vibrated bed, and analysis of the results in terms of bed dynamics.

3.0 Theoretical Models

Theoretical models of vibro-bed dynamics and vibro-bed heat transfer were reviewed by Gutman[14], Strumillo and Pakowski[13], and by Pakowski et al[1]. Gutman explores in some depth his own models for vibro-bed dynamics and heat transfer, as well as Kroll's model[5] for vibro-bed dynamics.. The other reviews include most of the existing models, and cover vibro-fluidized beds as well. This Chapter is not intended to be a repetition of these reviews. Instead, the objective is to use some of the proposed models to predict trends in vibro-bed dynamics and heat-transfer behavior.

The first section of this Chapter, concerned with vibro-bed dynamics, initially presents the single-particle model as proposed by Bachman[4]. This model treats the vibro-bed during the flight period as a single particle, whose motion is affected by the gravitational acceleration only. Kroll's model[5] is then utilized to consider the effect of drag forces on bed behavior. Compressibility effects are discussed in connection with Kroll's model and with respect to their consideration in Gutman's model. The section ends with a summary of the theoretical predictions for vibro-bed dynamics.

The second section introduces a model utilized by Zabrodsky[18] to explain the trends of heat-transfer rates in normal gas-fluidized beds. This model was originally developed for constant heating-surface temperature and for renewal of particles in a direction normal to the heating probe. The model is adopted in this Chapter to account for vibro-bed phenomena and extended to predict

the effect of particle renewal parallel to the heating surface. It is shown that the model indicates the same experimental trends as those reported in the literature.

3.1 Dynamics of Vibro-beds

Most of the models for the dynamics of vibro-beds assume that the bed behaves like a single plastic body. The latter implies that when the bed of particles collides with the vessel base, there will be no rebound of the bed from the base. This assumption allows treating the bed as a rigid porous piston of constant porosity that follows the vessel trajectory, immediately after a bed-vessel collision, until the next bed lift-off occurs.

The plastic-body approximation is attractive due to enormous difficulties in describing the effect of local solid-solid and solid-fluid interactions in the bed, as well as the variations in solid-wall frictional forces over the height of the area of contact. Porosity variations, bed-compression effects, and variations in frictional forces between particles and vessel walls are discarded by assuming the bed to be sufficiently shallow.

Figure 30 on page 70 schematically represents the vibration of a rigid, porous piston, and shows the instantaneous displacement, velocity, and acceleration of a vessel over a single vibrational cycle when the vibrations are vertical and sinusoidal. Rigid porous-piston models of vibro-beds can be generally represented by the following equation:

$$M_b a = F_n - M_b g + \Sigma F_i \qquad [3.1]$$

In this equation, M_b is the mass of the porous piston, a is the acceleration of the center of mass of the rigid piston, F_n is the normal force exerted by the vibrating vessel at the bottom of the bed, g is the gravity acceleration, and ΣF_i is the sum of all other forces acting on the porous piston. Rigid

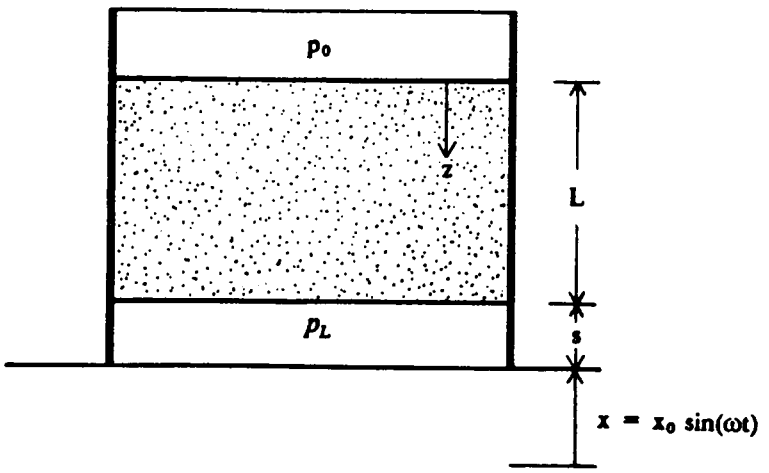

(a) Representing a vibro-bed

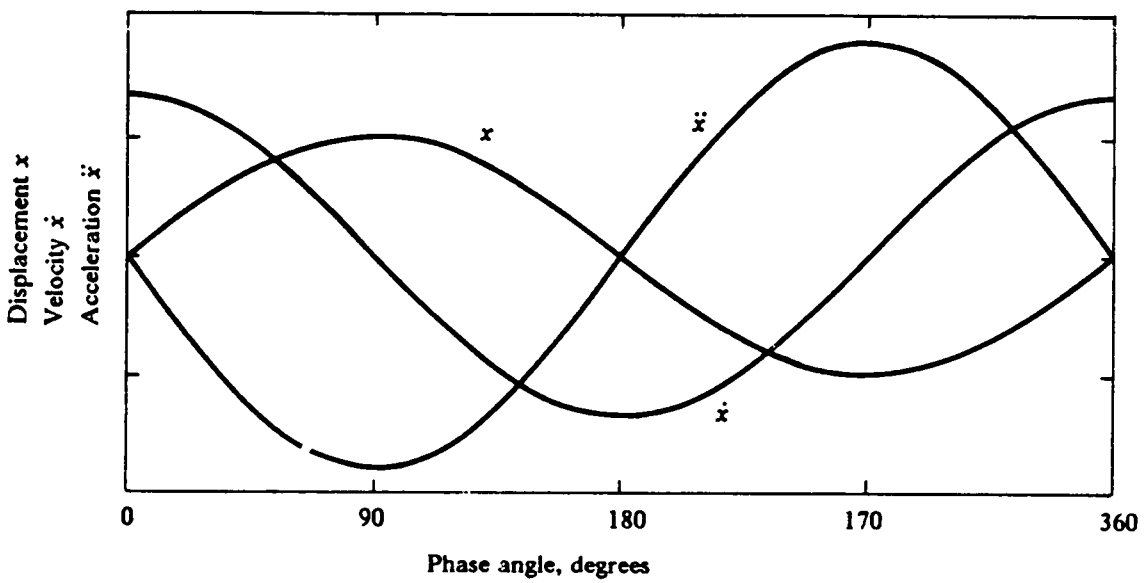

(b) Illustrating bed dynamics

Figure 30. Vibration of a bed of particles: Rigid porous piston of constant porosity. Notation: z = bed ordinate; L = bed depth; s = air-gap size; x = vessel displacement; x_0 = maximum vessel displacement; ω (= 2πf) = angular frequency; f = vibrational frequency; t = time; p_O = pressure above the bed; p_L = pressure below the bed.

Table 3 : Characteristics of vibro-bed dynamics models

Models	Forces on the vibro-bed		Remarks
	Flight period	Contact period	
Single-particle[4]	Gravitational	Gravitational Normal force at the lower bed boundaty	Equation [3.3] on page 71 Figure 31 on page 72 Air-gap size independent of particle diameter
Kroll[5]	Gravitational Drag	Gravitational Normal force at the lower bed boundary	Equation [3.14] on page 81 Figure 34 on page 79 Incompressible gas
Gutman[14]	Gravitational Drag	Gravitational Interparticle force at the lower bed boundary Drag	Equation [3.26] on page 92 Figure 39 on page 91 Compressible gas

porous-piston models do not account for the presence of any surface immersed into the vibrated bed.

Table 3 on page 71 summarizes the characteristics of the single-particle model, Kroll's model[5], and Gutman's model[14]. Differences among the models reside primarily in the types of forces existing in the system and their mechanical representations.

3.1.1 Single-particle model

3.1.1.1 Formulation

This model, first proposed by Bachman[4], treats the rigid porous piston as a single plastic particle subjected to vibrations on a vibrating plate. Neither wall-frictional forces nor drag forces are present. Such a representation is schematized in Figure 31 on page 73. Under these conditions, equation [3.1] is reduced to:

$$M_b a = F_n - M_b g \qquad [3.2]$$

Since no relative motion among particles is permitted, this equation describes the movement of any particle within the bed. Referring to the nomenclature presented in part (a) of Figure 30 on page 70, equation [3.2] can be rewritten as

$$\frac{d^2}{dt^2}(x + s) = \frac{F_n}{M_b} - g \qquad [3.3]$$

In this equation, $x = x_0 \sin(\omega t)$ is the sinusoidal displacement of the vibrating vessel, and s is the thickness of the gap that might form between the base plate and the lower boundary of the bed. The mass M_b of the bed can be represented as $AL\rho_b$, where A is the cross-sectional area of the bed and of the vessel, L is the depth of the bed, and ρ_b is its bulk density.

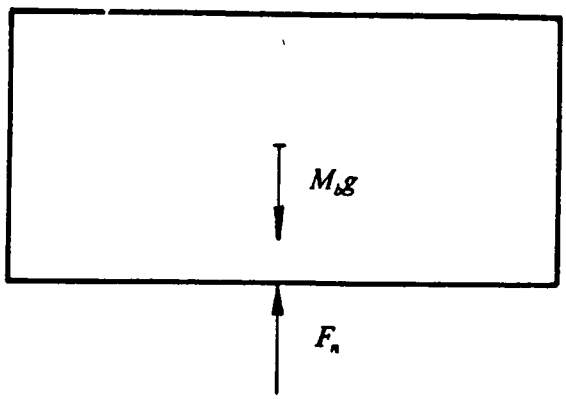

(a) Contact period

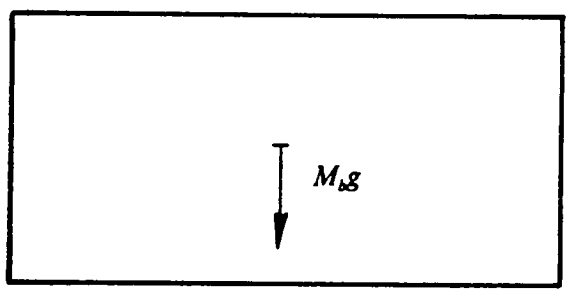

(b) Flight period

Figure 31. **Single-particle model:** Force balance on a vibrating rigid porous piston. Notation: g = gravitational acceleration; M_b = mass of the bed; F_n = Normal force at the lower boundary of the bed.

When the bed is in contact with the base plate, as shown in part (a) of Figure 31 on page 73, the gap thickness becomes zero. The resulting normal compression force per unit mass of particles exerted by the floor of the vessel on the lower boundary of the bed is given by

$$\frac{F_n}{AL\rho_b} = g\,[1 - K\sin(\omega t)] \qquad [3.4]$$

where

$$K = \frac{x_0\omega^2}{g} \qquad [3.5]$$

During the period of flight, as illustrated in part (b) of Figure 31 on page 73, the normal compression force at the bottom of the bed is zero and equation [3.3] becomes:

$$\frac{d^2}{dt^2}(x + s) = -g \qquad [3.6]$$

At bed lift-off time t_s, illustrated in Figure 33 on page 78, the normal force vanishes and the acceleration of the vessel equals gravity acceleration. The vessel is still in contact with the bed, and bed velocity and vessel velocity are the same. Thus, substituting $t = t_s$ into equation [3.4] gives

$$t_s = \frac{1}{\omega}\sin^{-1}\left(\frac{1}{K}\right) \qquad [3.7]$$

Also, at $t = t_s$, the initial conditions associated with equation [3.6] become:

$$x + s = x_s = x_0\sin(\omega t_s) \qquad [3.8]$$

$$\frac{d}{dt}(x + s) = \dot{x}_s = x_0\omega\cos(\omega t_s) \qquad [3.9]$$

Here, the subscript s indicates the evaluation of the variables at time t_s.

Solving equation [3.6] for the free-flight bed trajectory, one obtains the following expression:

$$(x + s) = x_s + (t - t_s)\left[-\frac{g}{2}(t + t_s) + \dot{x}_s + gt_s \right] \qquad [3.10]$$

3.1.1.2 Discussion

Despite the assumption of a rigid and porous piston, equation [3.4] can be used to predict the existence of compressive forces in a vibro-bed that lead to a reduction in bed porosity when the bed and vibrating vessel are in contact. The normal force per unit bed cross-sectional area, also called normal stress, becomes larger as the bed height and bulk density are increased. For a particular bed depth, the normal stress decreases from the lower boundary towards the upper boundary of the bed. As a consequence, a bed of particles should show compaction when subjected to vibrations, and this compaction should increase from the top towards the bottom. In the absence of other forces, the compaction effect should be larger for solids of high density than for those of low density.

Figure 32 on page 76 shows the calculated profiles of the normal force per unit of bed mass at the lower boundary of a vibrated bed for K = 0.5 and K = 1.0. The normal compression goes through a minimum at an angle of 90 degrees, where the vessel acceleration is also at its minimum value. This normal compression reaches a maximum at a phase angle of 270 degrees, where the vessel acceleration is maximum. Although the mean compression force per unit mass averaged over a vibrational cycle remains the same as K is increased, the maximum compression becomes larger and the minimum force smaller. At K = 1.0, the minimum normal force is zero at a phase angle of 90 degrees, indicating a tendency for bed lift-off that does not happen because the velocity of both the bed and vessel is zero as indicated in part (b) of Figure 30 on page 70. Any value of K greater than one causes the vertical normal compression to become negative, implying that the vessel detaches from the bed. According to the range of values the sine function can assume, and to the single-particle model, negative compression forces are present at phase angles less than 90 degrees. The greater the value of K, the smaller is the angle at which the bed and vessel separate from each other.

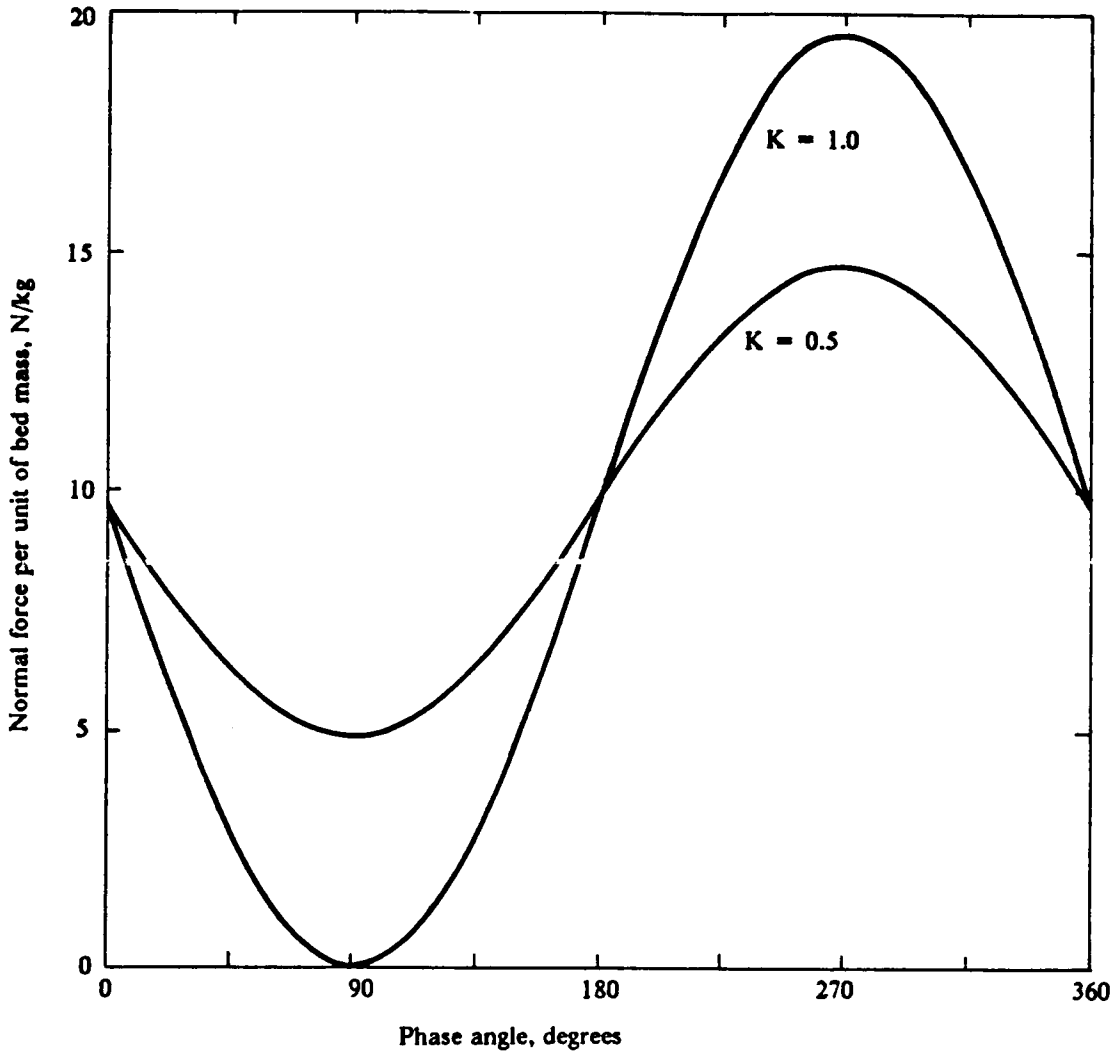

Figure 32. Normal force at the base of a vibro-bed: Single-particle model.

When K exceeds one and bed lift-off occurs, equation [3.4] still describes the motion of the bed during the fraction of the vibrating cycle in which the bed and vessel move together. However, during the period of flight when the normal compression force at the bottom of the bed is zero, the trajectory of the bed is governed by equations [3.6] through [3.10].

According to these equations, increasing K at a constant frequency (i) does not affect x_s, (ii) decreases the angle ωt_s at which the bed lift-off occurs, (iii) increases the lift-off velocity $\dot{x}_s$, and (iv) increases both the maximum height the bed is thrown and the maximum size of the air gap. At a constant K, increasing the frequency (i) does not change the lift-off angle ωt_s, (ii) decreases x_s , (iii) decreases bed velocity at the bed lift-off, and (iv) decreases both the maximum bed-throw height and maximum air-gap size.

These conclusions are valid as long as uniform bed trajectories are observed over each vibrational cycle. Both the bed trajectory and size of the air gap are independent of bed characteristics and particle properties, while the dynamics of the bed is affected only by vibrational conditions. Part (a) of Figure 33 on page 78 shows the predicted steady trajectories for a sufficiently low K-value, when the collisions between the bed and the floor of the vessel occur before the vessel passes again at the point defined by ωt_s, namely, the bed lift-off angle. Otherwise, trajectories become unsteady. They may change from cycle to cycle as illustrated in part (b) of the figure, and even skip whole vibrational cycles. In these cases, only trajectories beginning at ωt_s follow the conclusions described in the preceding paragraph.

Suzuki et al.[38] utilized the single-particle model to analyze the compaction of particles larger than 400 μm in vessels vibrated at frequencies between 20 and 70 Hertz and K-values ranging from one to four. Bed depth was fixed at 190 mm. They correlated the degree of bed compaction to the relative velocity between the bed and vessel at their collision divided by the velocity of the bed at lift-off. The correlation showed a good agreement with experimental results. The bed compaction increased up to K = 2.5, and then decreased again, but at a lower rate. Smaller vibrational frequencies were more effective below K = 2.5; above this value, the effect of the frequency on the compaction of the bed was not conclusive. The bed compaction was much more sensitive to the

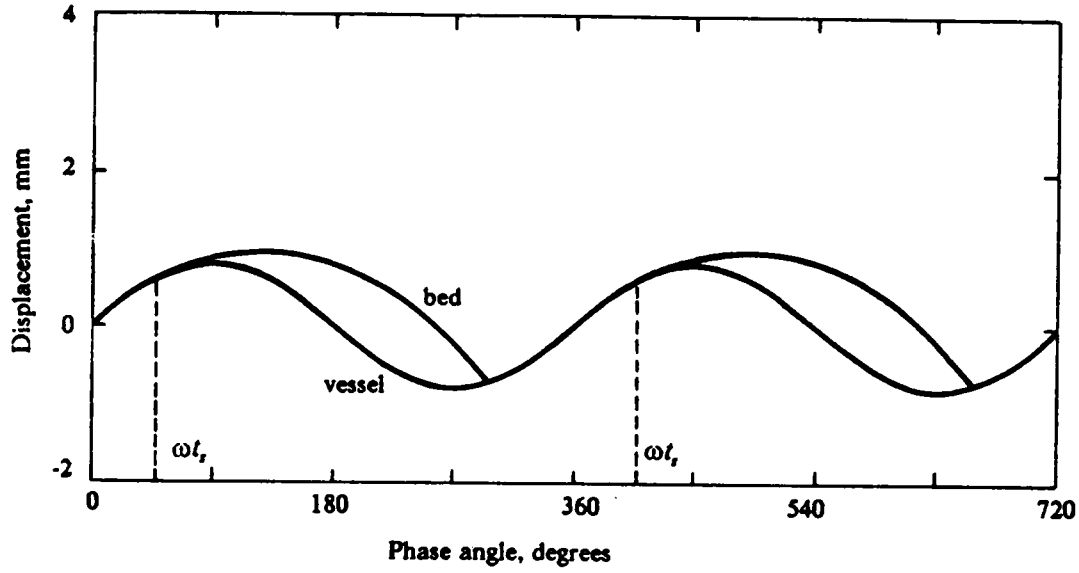

(a) K = 2

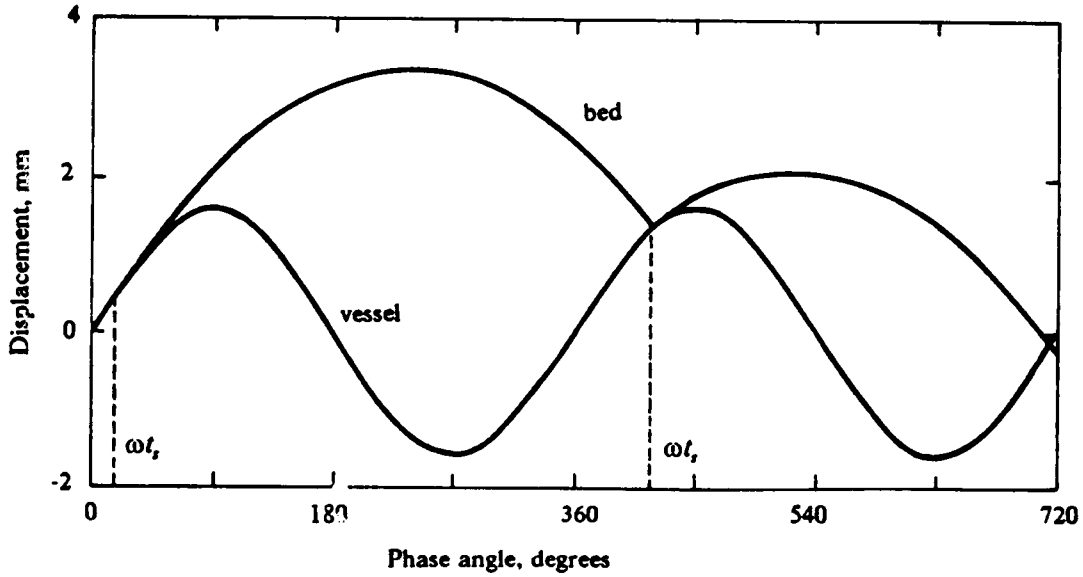

(b) K = 4

Figure 33. Bed trajectories according to the single-particle model.

particle density than to the vibrational frequency; heavy particles were observed to become more compacted than light particles.

Observations done by Gray and Rhodes[33] have confirmed the bed trajectories illustrated in Figure 33 on page 78. Using phosphor-bronze balls of 3-mm diameter, steady trajectories were observed at low K-values; at higher K-values, the unsteady trajectories shown in part (b) of the figure became usual. Further increasing K resulted in bed-vessel collisions at every two or three vibrating cycles. Skipping a whole cycle between collisions was even observed in beds of a 53-μm phosphor-bronze powder. However, the bed trajectories calculated from the single-particle model did not agree with the experimental results in any situation. The authors attributed the non-agreement between the model and the experiments to the presence of air-drag and frictional forces. They concluded that the single-particle model could only be applied to large, granular materials of high density when the effects of drag and frictional forces were minimal. Their experiments were performed with vibro-beds of about 150-mm depth.

3.1.2 Kroll's Model

3.1.2.1 Formulation

The model of Kroll[5] represents an improvement on the single-particle model. As seen in Figure 30 on page 70, when an air gap is formed, the detachment of the bed from the vessel produces a net suction action. Air is driven through the bed under the newly developed pressure differential. When the air gap closes, the pressure differential is reversed, and air is now expelled out of the bed. As discussed in secttions 2.1.1. and 2.1.4., this oscillatory air flow generates drag forces on the bed of particles, which affect bed dynamics.

Kroll introduced these phenomena in his model by assuming that the gas is incompressible. Thus, the model is also called an incompressible-gas model. Figure 34 on page 80 illustrates the

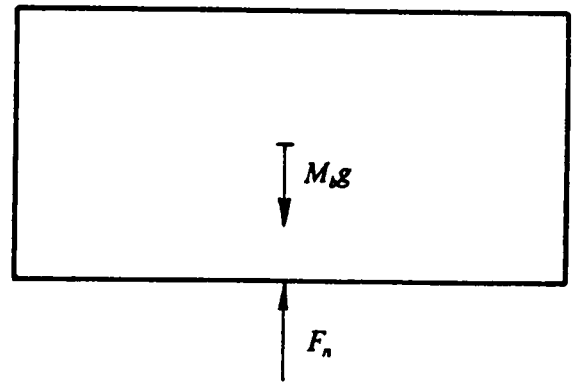

(a) Contact period

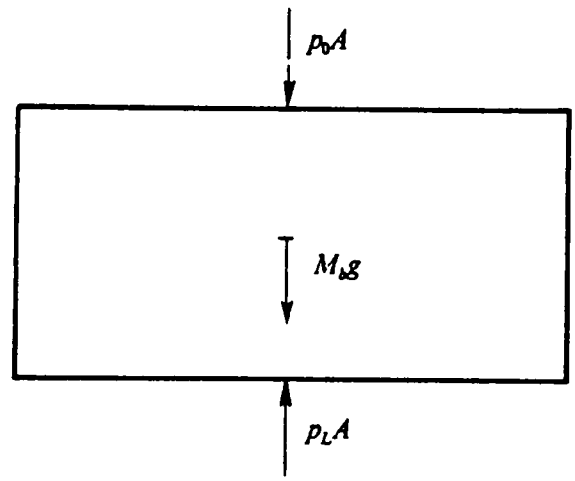

(b) Flight period

Figure 34. Kroll's model: Force balance on a vibrating rigid porous piston. Notation: g = gravitational acceleration; A = cross-sectional area of the bed; M_b = mass of the bed; F_n = normal force at the base of the bed; p_0 = pressure above the bed; p_L = pressure below the bed.

forces acting on a vibrating rigid porous piston according to Kroll's model. In the model, the gas velocity is assumed to be proportional to the pressure drop according to the well-known Darcy's law,

$$u = -\frac{\kappa\varepsilon}{p_0}\frac{dp}{dz} \qquad [3.11]$$

In this equation, u is the relative gas-solid superficial velocity, ε is the porosity of the bed, p is pressure, z is the bed ordinate as shown in Figure 30 on page 70, and κ is the bed premeability in m^2sec^{-1} as given by Carman-Kozeny's correlation,

$$\kappa = \frac{p_0}{1.8 \times 10^2 \mu}\left[\frac{d_p\varepsilon}{1-\varepsilon}\right]^2 \qquad [3.12]$$

where μ is the gas viscosity, and d_p is the particle diameter.

Other assumptions of the single-particle model were maintained. Thus, the bed behaves as a single rigid porous piston of a constant and uniform porosity, floor-bed collisions are instantaneous and inelastic, and wall frictional forces are negligible. As a consequence of these asumptions, the rate of change of the air-gap thickness can be expressed as:

$$\frac{ds}{dt} = u = -\frac{\kappa\varepsilon}{p_0}\frac{(p_L - p_0)}{L} \qquad [3.13]$$

As shown in Figure 30 on page 70, p_L is the pressure in the air gap, p_0 is the pressure above the bed of particles, and L is the bed depth.

Figure 34 on page 80 illustrates the forces acting on a vibrating rigid porous piston according to Kroll's model.

When no air gap exists, equation [3.4] is still applicable over the period of time in which the bed and vessel move together, or

$$\frac{F_n}{AL\rho_b} = g[1 - K\sin(\omega t)] \qquad [3.4]$$

Conclusions drawn for the single-particle model with respect to the compaction effects, bed lift-off angle, and K-dependence are valid.

During the flight period, however, equation [3.3] is modified to give

$$M_b \frac{d^2}{dt^2}(x + s) = A(p_L - p_0) - M_b g \qquad [3.14]$$

After evaluating the second-order derivative and rearranging this equation

$$\frac{\kappa\varepsilon\rho_b}{p_o}\frac{d}{dt}\left[\frac{p_L - p_o}{\rho_b L g}\right] + \frac{p_L - p_o}{\rho_b L g} = 1 - K\sin(\omega t) \qquad [3.15]$$

By substituting ωt for the independent variable t, and by defining a dimensionless group

$$N = \frac{\omega\kappa\varepsilon\rho_b}{p_o} \qquad [3.16]$$

one can find from equation [3.15] that

$$N\frac{d}{d(\omega t)}\left[\frac{p_L - p_o}{\rho_b L g}\right] + \frac{p_L - p_o}{\rho_b L g} = 1 - K\sin(\omega t) \qquad [3.17]$$

Based on the initial conditions that at bed lift-off time t_s , $p_0 = p_L$ and $s = 0$, the solution of equations [3.17] and [3.13] are:

$$\frac{p_L - p_0}{\rho_b L g} = \left[1 - \frac{K\sin(\omega t - \zeta)}{(1 + N^2)^{1/2}} - A_3 \exp\left(\frac{\omega t_s - \omega t}{N}\right)\right] \qquad [3.18]$$

and

$$\frac{s\omega^2}{g} = -N\left[\omega t - \omega t_s + \frac{K[\cos(\omega t - \zeta) - \cos(\omega t_s - \zeta)]}{(1 + N^2)^{1/2}}\right]$$

$$+ N^2 A_3\left[1 - \exp\left(\frac{\omega t_s - \omega t}{N}\right)\right] \qquad [3.19]$$

where

$$A_3 = \left[1 - \frac{K \sin(\omega t_s - \zeta)}{(1 + N^2)^{1/2}} \right] \qquad [3.20]$$

and

$$\zeta = \tan^{-1} N \qquad [3.21]$$

The dimensionlee group N defined by equation [3.16] does not have a straightforward physical interpretation. Considering the inverse of the permeability of the bed, $1/\kappa$, as a measure of the resistance of the bed to fluid percolation, the inverse of N can be interpreted as being proportional to the hydraulic resistance per unit of bed density. In this case, large values of N correspond to a low hydraulic resistance per unit of bed density, and vice-versa.

The identification and utilization of the dimensionless group N had not been reported in the vibro-bed literature.

3.1.2.2 Discussion

In equation [3.18], the left-hand side is the ratio of the pressure force to the gravitational force acting on the bed or the bed weight. This ratio can be defined as a dimensionless pressure difference. The left-hand side of equation [3.19], $s\,\omega^2/g$, is a dimensionless air-gap size. It can be interpreted as the "acceleration" of the lower boundary of the bed of particles with respect to the base plate of the vibrating vessel. Both the dimensionless pressure difference and the dimensionless air-gap size are dependent only on two parameters: the vibrational intensity parameter K and the dimensionless group N defined by equation [3.16].

Equations [3.18] and [3.19] show some characteristic features of the incompressible-gas model. At constant K and N, gauge pressures at the floor of the vibrating vessel are directly proportional

to the bed depth and to the bulk density of the bed, and the size of the air gap is inversely proportional to the square of the vibrational frequency.

Figure 35 on page 85 shows plots of those equations over a vibrational cycle, beginning at the bed lift-off time, for different values of the dimensionless group N at K = 4. Although no specific numerical values need be assigned to the parameters that form the dimensionless group N, the N-values shown in the figure correspond to a bed vibrated at 25 Hertz. The solid density is 3600 kg/m^3, and the average bed-porosity is 0.41. The increasing values of N are associated, respectively, with particle diameters of 0.05, 0.2, 0.5, and 1.0 mm.

In general, as N increases, the maximum amplitude of the pressure variations becomes smaller and the maximum size of the air gap larger. Increasing the vibrational frequency results in smaller pressure fluctuations and smaller air gap thicknesses. The net effect of utilizing particles of higher density is higher peak-pressure fluctuations, and larger air gaps. The air pressure p_0 above the bed does not affect the bed behavior as long as it does not change the viscosity of the gas. With increasing values of bed porosity, the amplitude of the floor-pressure oscillations and the size of the air gap decrease.

Figure 35 on page 85 also shows that as N increases, the period of time the bed spends in flight increases, the locations of the maximum air gap size and of the peak pressure move forward in the vibrational cycle. As a result the model description approaches that of the single-particle model. Thus, the effect of drag forces on bed behavior at constant K becomes continuously less important as the angular vibrational frequency, particle diameter, and bed porosity are increased, and as the gas viscosity is decreased.

At very small values of the dimensionless group N, it is possible to show that equation [3.18] is reduced to:

$$\frac{p_L - p_0}{\rho_b L g} = 1 - K \sin(\omega t) \qquad [3.22]$$

This equation establishes a limit on the maximum amplitude of the floor-pressure oscillations, and predicts that floor pressures generated by vibrations are sufficiently high to avoid the bed lift-

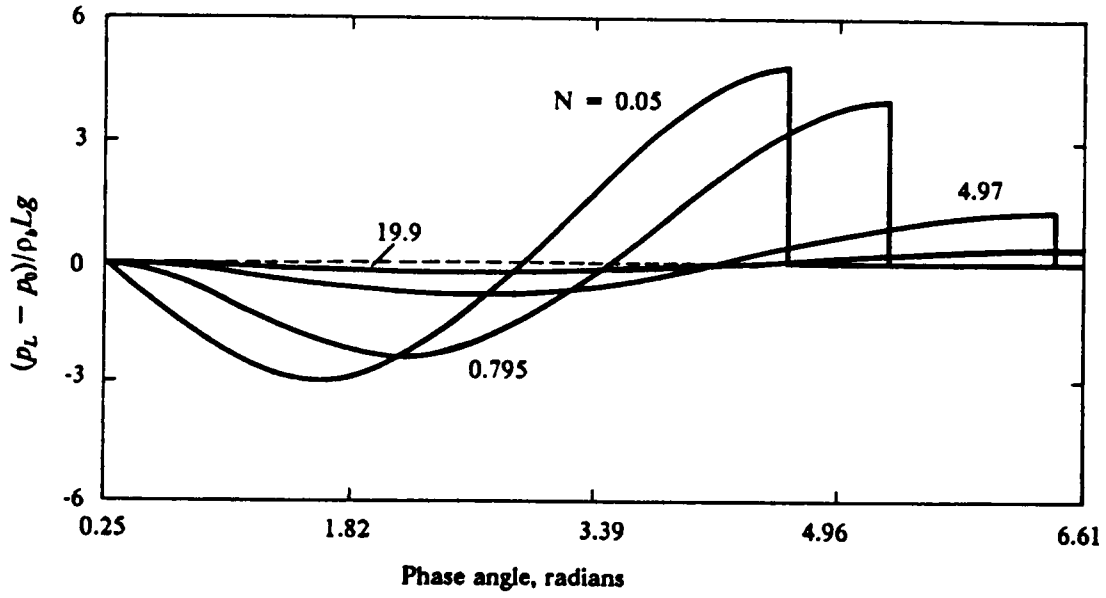

(a) Dimensionless floor pressure

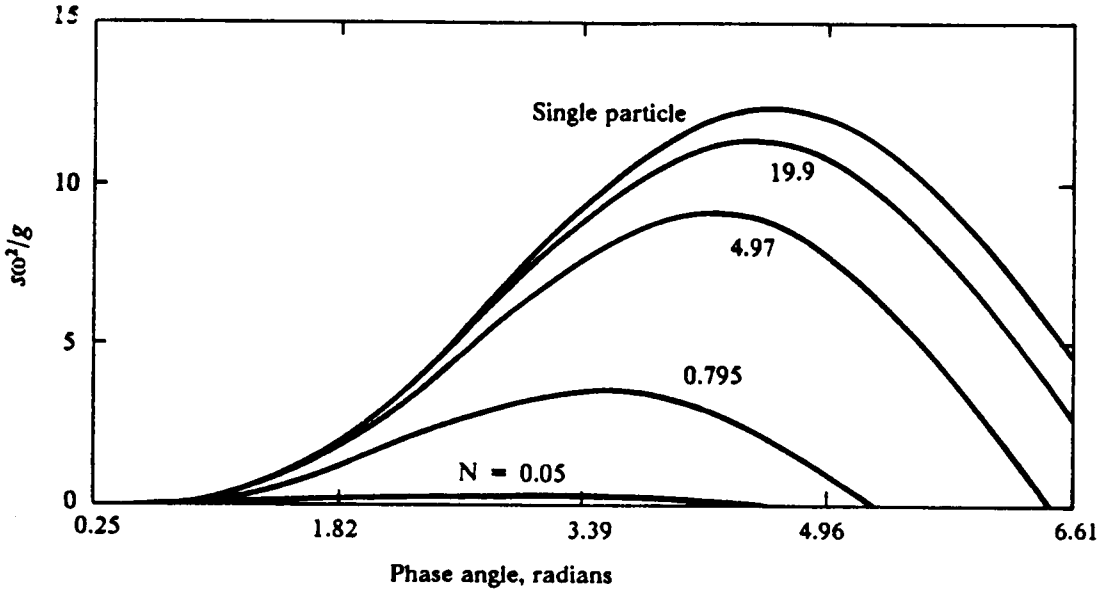

(b) Dimensionless air-gap thickness

Figure 35. **Dimensionless vibro-bed floor pressure and air-gap thickness:** Kroll's model. Layer of particles vibrated at K = 4. Notation: p_0 = pressure above the bed; p_L = pressure below the bed; ρ_b = bed bulk-density; L = bed depth; s = air-gap thickness; ω = angular frequency; g = gravitational acceleration; N = dimensionless parameter.

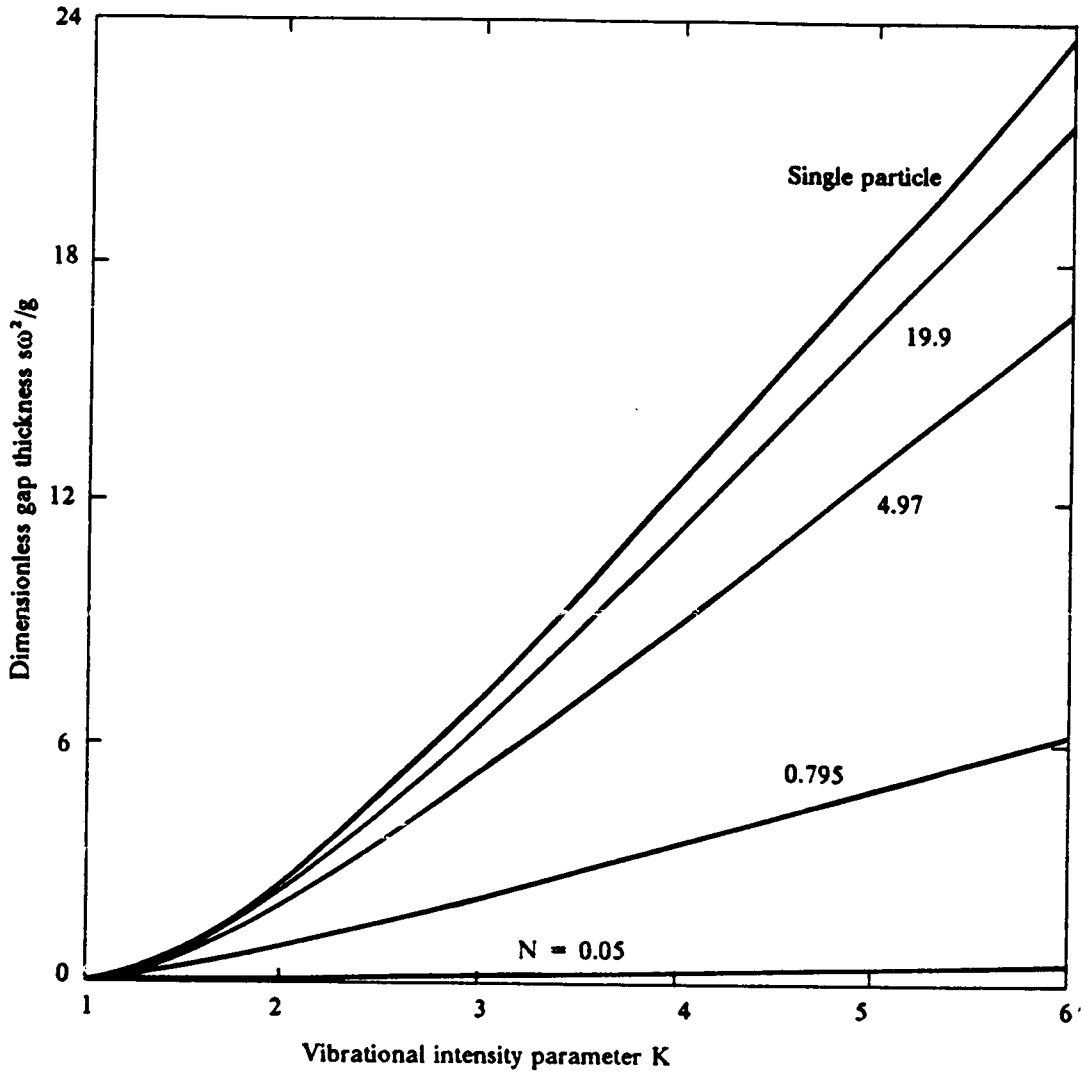

Figure 36. **Dimensionless maximum air-gap thickness in a vibro-bed:** Dependence on the vibrational intensity parameter K according to Kroll's model. Notation: s = air-gap thickness; ω = angular frequency; g = gravitational acceleration.

off. In this case, no air would flow into the bed, and pressure variations would solely be due to the compression and expansion of the gas within the bed. This description, however, would not be valid physically. It requires the expansion and compression of the vibrated bed, and would thus invalidate the basic incompressible-fluid assumption. Therefore, it seems plausible to expect the model to break down under these conditions due to gas-compressibility effects and/or variations in bed porosity.

The maximum gap-size dependence on the vibrational intensity parameter K is shown in Figure 36 on page 86. Kroll's model predicts a continuous growth of the size of the gap with increasing K-values. Except for K-values close to one, the relationship is nearly linear.

A comparison between theoretical predictions and experimental results is presented in the discussion of Gutman's model in section 3.1.3.2 of this Chapter.

3.1.2.3 Effect of gas compressibility

Kroll[6] observed the inability of his model to predict the actual bed behavior when the bed depth and vibrational frequency were increased, and when the particle size was decreased. He attributed this failure to gas compressibility-effects, and to variations in bed porosity. To demonstrate the importance of gas compressibility, Kroll analized the pressure profiles in a fixed bed subjected to a constant pressure at the upper boundary, and to a sinusoidal pressure oscillation at the lower boundary. The mass balance over a differential section of the bed led to:

$$\frac{\partial p}{\partial t} = \kappa \frac{\partial^2 p}{\partial z^2} \qquad [3.23]$$

By solving the differential equation, Kroll obtained the following expression for the pressure distribution within the fixed bed at the instant of time that a maximum suction pressure exists below the bed:

$$\frac{p - p_0}{p_L - p_0} = \frac{z}{L} - \frac{2}{\pi}\xi_K \sum_{n=1}^{\infty} \frac{(-1)^{n+1}}{n(n^4 + \xi_K)} \sin\left(n\pi\frac{z}{L}\right) \qquad [3.24]$$

where ξ_K is a dimensionless parameter defined by

$$\xi_K \equiv \frac{\omega^2 L^4}{\pi^4 \kappa^2} \qquad [3.25]$$

The notation in the above equations is the same as that used previously for vibro-beds. It is defined in Figure 30 on page 70.

Figure 37 on page 89 shows the dimensionless pressure distribution given by equation [3.24], which is dependent on the parameter ξ_K only. For sufficiently small values of ξ_K, the pressure distribution within the bed becomes linear, and Kroll's model is assumed to be valid as long as the other assumptions are satisfied. This is likely to happen at low vibrating frequencies and small bed depths, and at large bed permeabilities. For a 0.05-mm particle bed of a porosity of 0.41 vibrated at 25 Hertz, increasing values of ξ_K correspond to bed depths of 20, 30, and 50 mm.

Kroll considered the gas compressibility as the main cause for porosity variations within a vibro-bed. Since the greatest pressure gradients are located at the lower boundary of the bed, the bed expansion starts at that boundary and moves upward, but at a lower intensity. This follows because the pressure gradients decrease toward the top of the bed. Kroll compared the behavior to the response of a gas-fluidized bed to a sudden increase in the gas flow rate; the bed porosity propagates from the lower boundary towards the upper one. Following this interpretation, the expansion should start after the bed lift-off. When the gap closes and the air outflow increases, the bed expansion should continue towards the top of the bed. As a consequence, when the bed compacts after the collision between the lowest layer of particles and the base plate, the floor pressure may still increase and then eventually decrease. If the period of flight is sufficiently high, the bed compaction might not be complete, or the floor pressure might not be completely released before the regular lift-off point, thus causing irregular bed behavior.

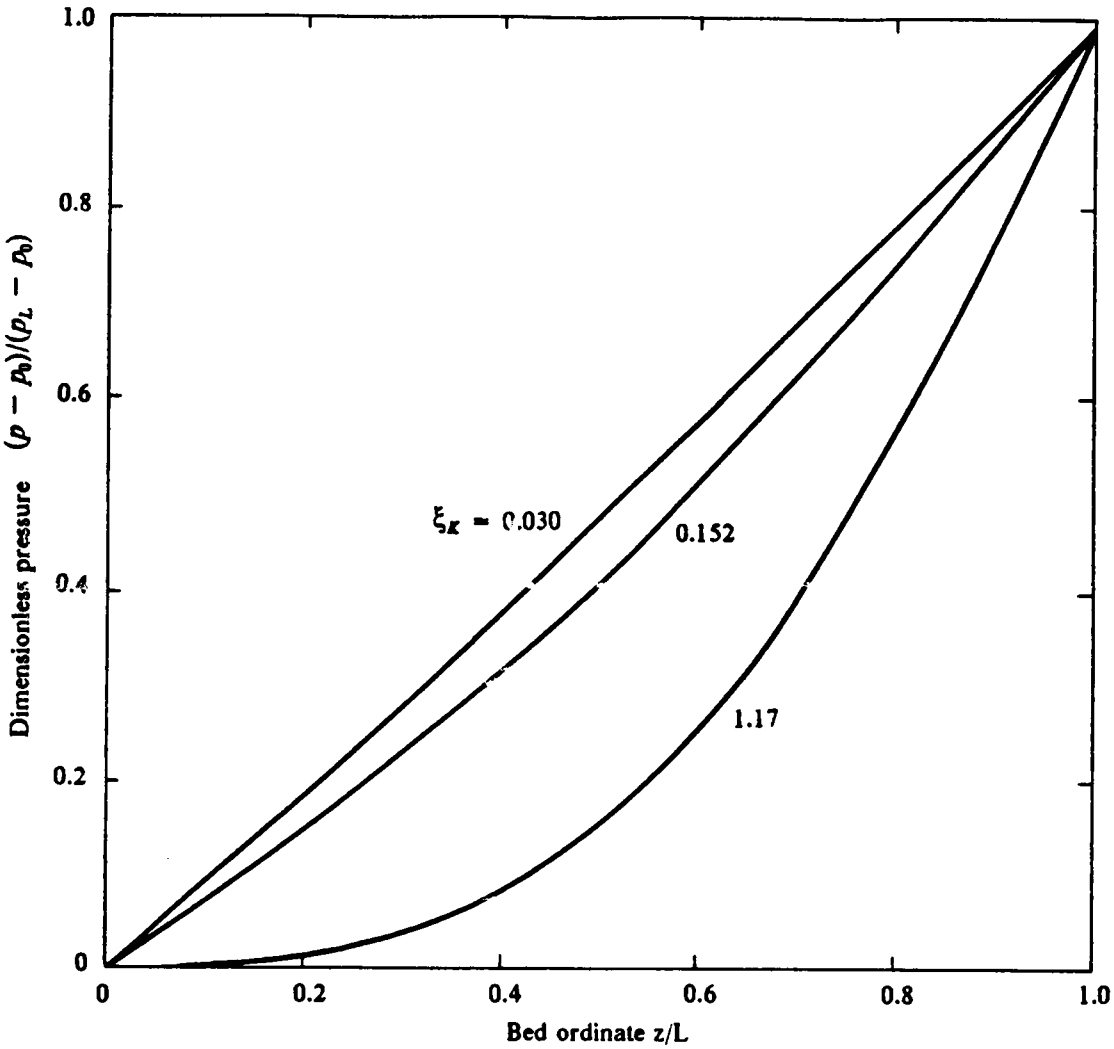

Figure 37. Gas-compressibility effect on the pressure profile in a fixed bed: Maximum negative pressure at the lower boundary of a bed subjected to a sinusoidal pressure oscillation. Notation: p = pressure in the bed at location z; p_0 = pressure above the bed; p_L = pressure below the bed; ξ_K = dimensionless parameter defined by equation [3.25]; L = bed depth.

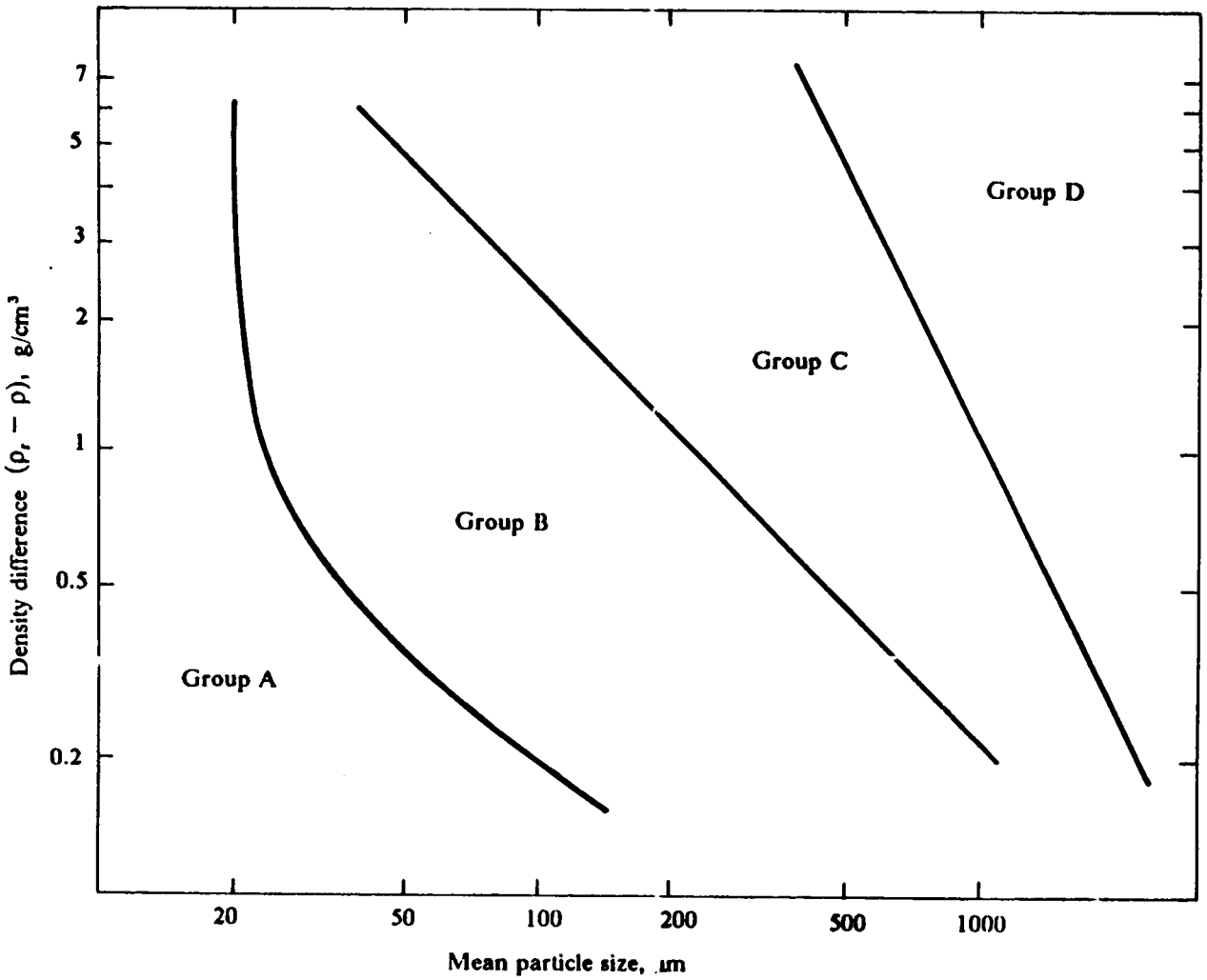

Figure 38. Powder-classification diagram for gas fluidization: Ambient conditions. (Geldart[39])

It is well-known that fixed beds become fluidized when the pressure drop across the bed equals the weight per unit cross-sectional area of the bed, and that the characteristics of gas-fluidized beds are strongly dependent on particle size. As shown in Figure 38 on page 90, the powder classification proposed by Geldart[39] is basically supported on the characteristic behavior of solids of different size and density when gas-fluidized. Type C is very difficult to fluidize; channelling is severe, or the bed lifts as a plug. As the particle size and/or density is increased from those of type A towards type D, the bed expansion and solid circulation before the formation of bubbles decrease, and the bed collapses faster when the fluidizing-gas supply is cut off. Kroll's observations[6] of vibro-bed behavior fit these characteristics: (i) no bed-expansion for large particles, (ii) considerable bed expansion for small particles, and (iii) gas channelling in beds of fine powders. Also, as shown in Figure 35 on page 85, the floor gauge-pressure per unit of bed weight becomes greater than one as the dimensionless parameter N is decreased. Therefore, there seem to exist certain conditions for fluidization to occur in a vibrated bed.

3.1.3 Gutman's Model

3.1.3.1 Formulation

Gutman[14 24] removed the assumption of gas incompressibility in Kroll's model, and proposed a model that allows the gas to expand and contract isothermally within a vibro-bed. This model is known as the compressible-gas model. Despite the allowance for air compressibility, the bed is still treated as a rigid porous piston of a constant porosity, and wall effects are negligible.

The forces acting on a rigid vibrated-bed during the flight and contact periods are schematically represented in Figure 39 on page 92. Because of the allowance for gas compressibility, the floor pressure might not fall instantaneously down to atmospheric pressure during the moment that the bed and vessel collide as predicted by Kroll's model. Thus, Gutman avoided using independent

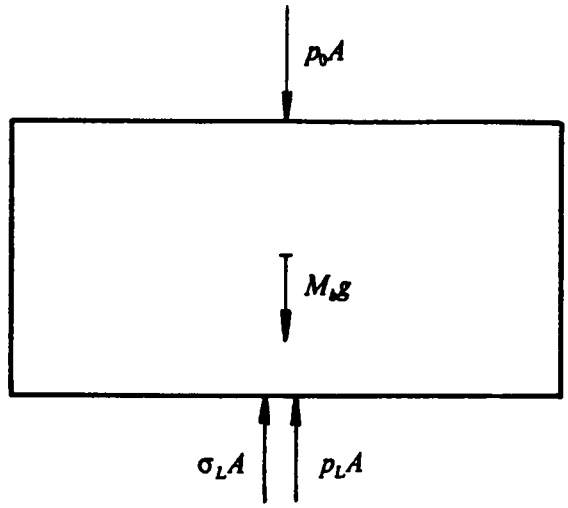

(a) Contact period

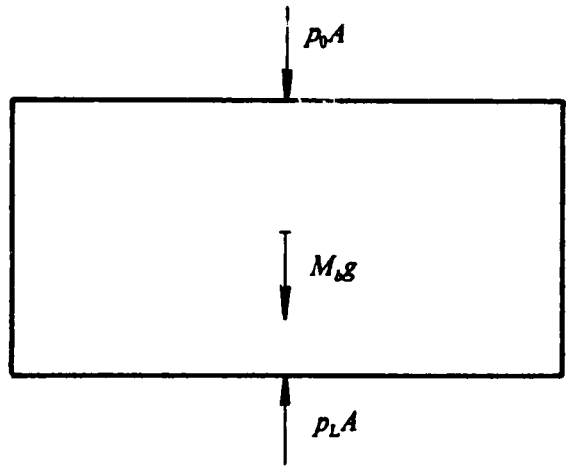

(b) Flight period

Figure 39. **Gutman's model:** Force balance on a vibrating rigid porous piston. Notation: p_0 = pressure above the bed; p_L = pressure below the bed; σ_L = normal interparticle stress at the bottom of the bed; g = gravity acceleration; A = bed cross-sectional area; M_b = bed mass.

equations for the flight period and for the contact period. The equation of motion of the bed can be written as:

$$M_b \frac{d^2}{dt^2}(x + s) = - M_b g + A (\sigma_L + p_L - p_0) \qquad [3.26]$$

In this equation, M_b is the mass of the bed, A is its cross-sectional area, and σ_L is the interparticle normal vertical stress at the base of the bed, which is zero when the bed is in flight.

Gutman assumed that the pressure and the interparticle stress at the bottom of the bed could be represented by the following Fourier series:

$$p_L = p_0 + a_0 + \sum_{m=1}^{\infty} a_m \sin(m\omega t + \gamma_m) \qquad [3.27]$$

and

$$\sigma_L = c_0 + \sum_{m=1}^{\infty} c_m \cos(m\omega t) + \sum_{m=1}^{\infty} d_m \sin(m\omega t) \qquad [3.28]$$

where a_m , γ_m , c_m , and d_m are constants to be determined.

The pressure variation within the bed is given by equation [3.23],

$$\frac{\partial p}{\partial t} = \kappa \frac{\partial^2 p}{\partial z^2} \qquad [3.23]$$

In this equation, κ is the bed permeability as defined by equation [3.12], and z is the vertical bed ordinate as defined in Figure 30 on page 70.

A material balance over the air gap yields:

$$\frac{d}{dt}(\rho s) = \rho \frac{ds}{dt} + s \frac{d\rho}{dt} = \rho u \qquad [3.29]$$

where ρ is the air density in the gap, s is the size of the air gap, and u is the gas velocity at the lower boundary of the bed.

Neglecting small air density changes and using Darcy's law, equation [3.29] is reduced to:

$$\frac{ds}{dt} = \dot{} - \frac{\kappa\varepsilon}{p_0}\left(\frac{\partial p}{\partial z}\right)_L \qquad [3.30]$$

Gutman solved equations [3.26], [3.23], and [3.30] by an iterative procedure.

3.1.3.2 Comparison with Kroll's model

Figure 40 on page 95 compares the air-gap thickness and floor pressures predicted by Kroll's model and by Gutman's compressible-gas model for a 40-mm bed of 100-μm glass particles vibrated at a frequency of 25 Hertz and an amplitude of of 0.50 mm. Particularly important is the effect of air compressibility on the release of the floor pressure after the bed and vessel collide. Kroll's model predicts an instantaneous drop of the pressure down to atmospheric pressure, while Gutman's model predicts a more modest decay by taking into account the compression that the gas may undergo when the bed is not very permeable to the gas flow. The discrepancy in the predictions of development and thickness of the air gap is significant. In this specific case, Gutman's prediction for the gap thickness is more than twice that of Kroll's prediction. Gutman did not present any explanation for this phenomenum.

Equation [3.30] shows that the rate of change of the gap size is directly proportional to the pressure gradient existing at the lower boundary of the bed of solids. As can be seen in Figure 37 on page 89, the pressure gradient increases as gas-compressibility effects become more intense. Therefore, the rate of change of the gap will be larger when the compressibility effect is significant, and so will the size of the gap. Figure 41 on page 96 presents predictions of both Kroll's and Gutman's models as a function of the vibrational intensity parameter K. As shown previously, the compressibility effect is independent of the vibrational amplitude. And thus the ratio of the predictions of Gutman's model to Kroll's model for the size of the air gap at a constant vibrational frequency is also independent of the vibrational intensity parameter K.

At a vibrational frequency of 20 Hertz, the compresibility effect is not important in a 40-mm deep bed of spherical glass beads for particle sizes greater than 100 μm.. Both models estimate

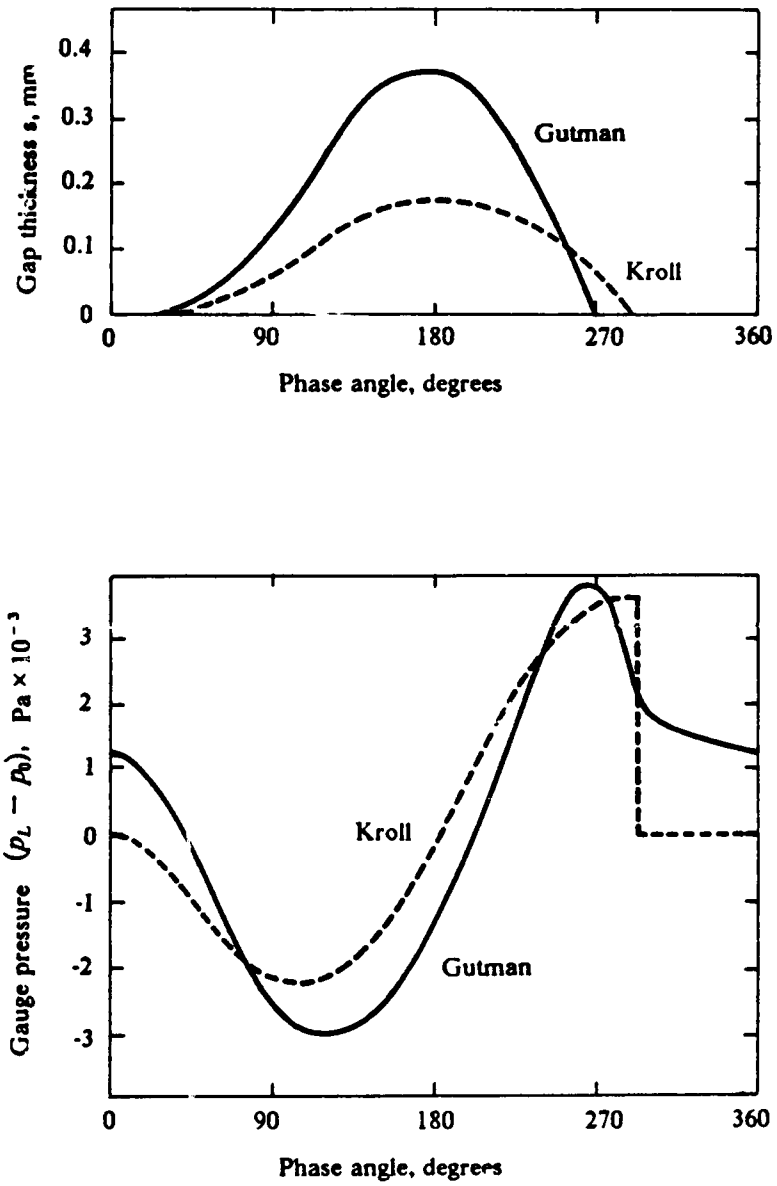

Figure 40. Theoretical floor pressure and air-gap thickness in a vibro-bed: 40-mm layer of 100-μm spherical glass particles. Vibrational frquency: 50 Hertz. Amplitude: 0.50 mm. (Gutman[14])

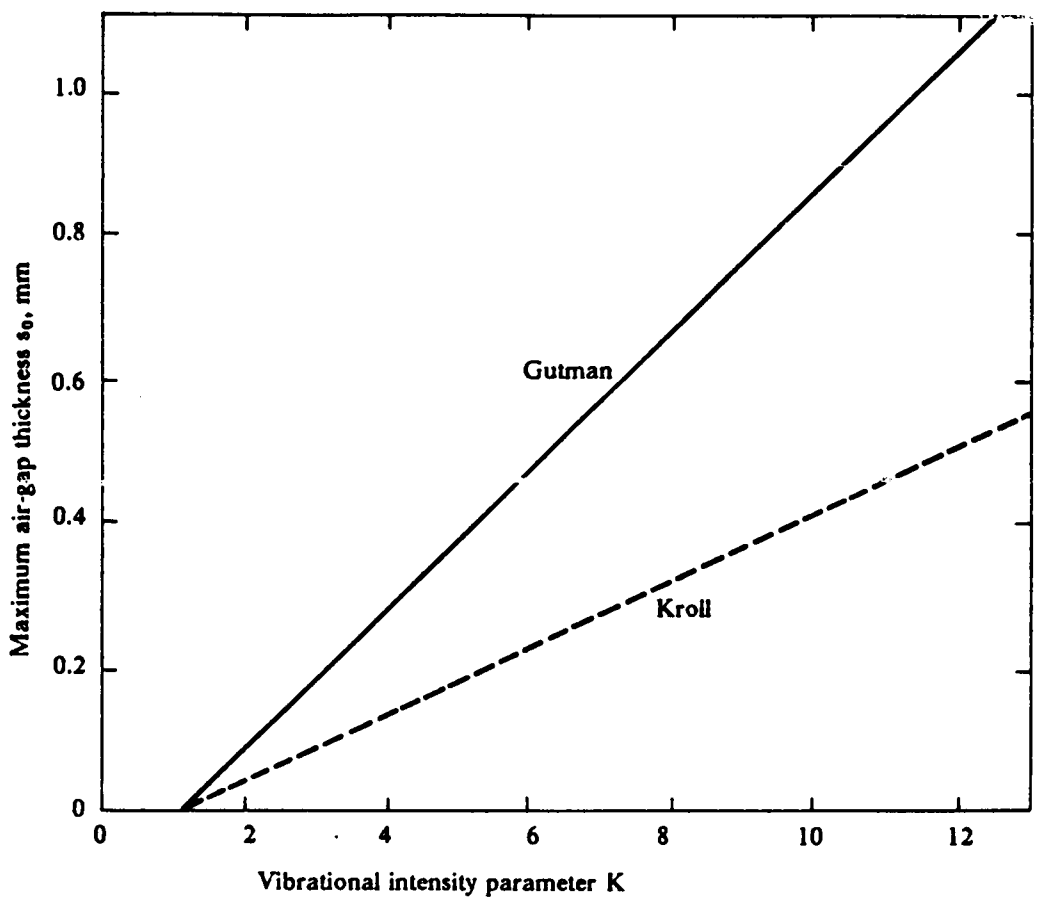

Figure 41. Theoretical variation of the maximum air-gap thickness with K: 40-mm layer of 100-μm glass particles vibrated at a frequency of 50 Hertz (Gutman[14]).

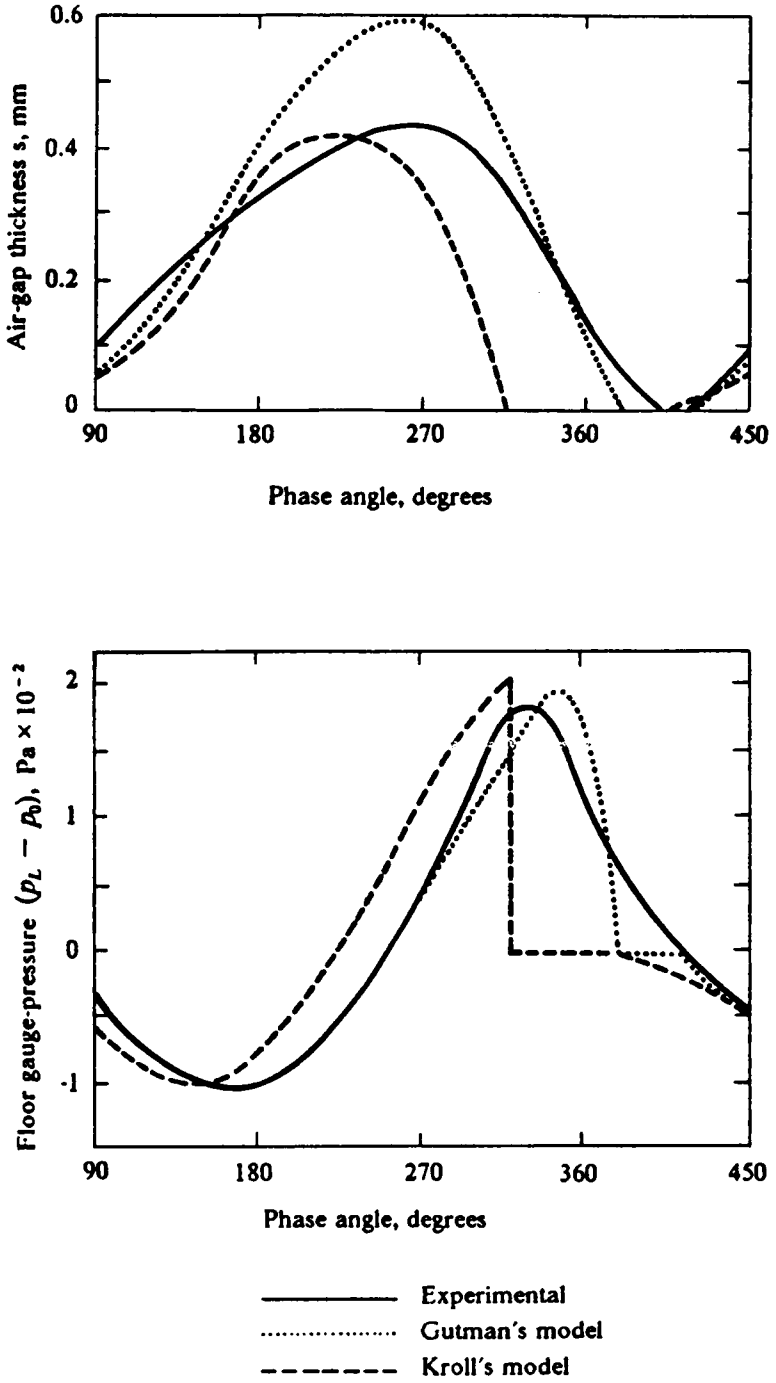

Figure 42. Air-gap thickness and floor pressure in a vibro-bed: 40-mm layer of glass particles of 710-850 μm in diameter vibrated at a frequency of 50 Hertz and an amplitude of 0.28 mm (Gutman[14]).

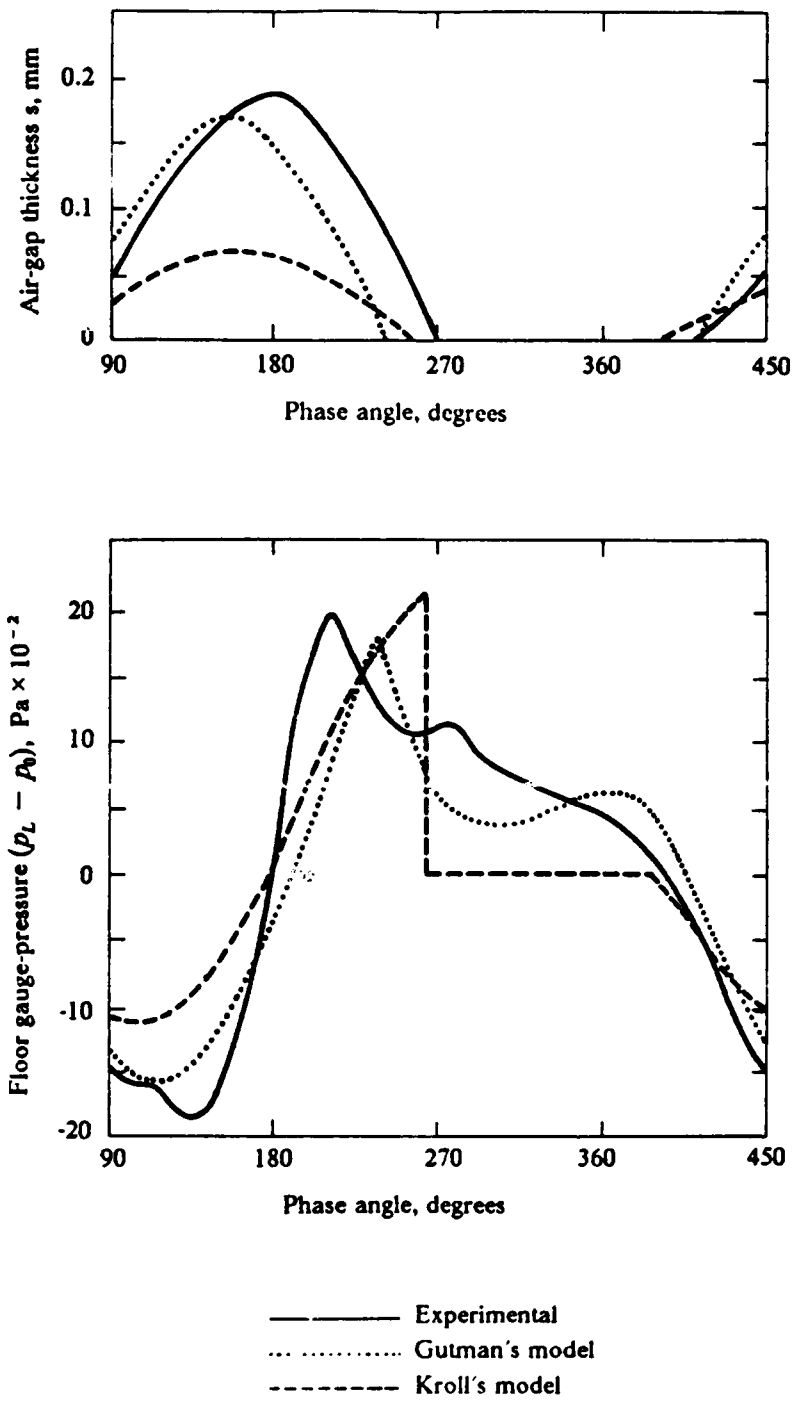

Figure 43. Air-gap thickness and floor pressure in a vibro-bed: 40-mm layer of glass particles of 89-124 μm in diameter vibrated at a frequency of 50 Hertz and an amplitude of 0.28 mm (Gutman[14]).

identical gap sizes and floor gauge-pressure magnitudes. At 50 Hertz, however, it seems that gas compressibility can no longer be neglected, even for particles as large as 800 μm.. Figure 42 on page 97 compares experimental results with the predictions of the two models for 800-μm glass beads, and Figure 43 on page 98 shows the similar comparison for 100 μm particles. For larger particles, Kroll's model appears to give a better estimate of the gap size; while for smaller glass beads, Gutman's model seems to work better. Gutman attributes the discrepancy in the estimate of his model for the larger particles to wall effects.

3.1.3.3 Limitations of the model

Gutman's model predicts that the maximum floor pressure increases linearly with bed depth for small depths, and then it slowly approches a limiting value. Gutman experimentally observed this behavior for beds of large particles. For small particles, however, the floor pressure reached a maximum value for bed depths of approximately 60 mm, and then it started to decrease. Such a behavior was related to tensile stresses caused by the non-linear pressure gradients within the bed, which can generate large porosity variations and thus invalidate the rigid-bed assumption. Based on the equation of motion of a section of bed between $z = 0$ and $z = z_1$, Gutman obtained the following expression for the interparticle stress during the flight period:

$$\sigma_{z1} = (p_L - p_0)\frac{z_1}{L} - (p_{z1} - p_0) \qquad [3.32]$$

In this equation, σ_{z1} is the interparticle stress at z_1. When the pressure gradient is linear within the bed, $\sigma_{z1} = 0$. However, when the gas-compressibility effect becomes important, the resulting pressure gradient is no longer linear, and $\sigma_{z1} < 0$. Tensile stresses set in and tend to cause porosity variations.

In discussing the application of Kroll's model and of his own model, Gutman presents experimental evidence of the validity of Darcy's law for vibrational frequencies up to 100 Hertz. Above

100 Hertz, gas-solid frictional forces are not solely controlled by viscous effects, and the dissipation of energy is mainly due to rapid changes in the gas momentum.

To determine the conditions under which the gas compressibility cannot be neglected, Gutman followed the same approach that Kroll[6] used. By analyzing the oscillating flow in a fixed bed, Gutman obtained the dimensionless group ξ_G.

$$\xi_G = \left[\frac{\omega}{2\kappa}\right]^{1/2} L \qquad [3.33]$$

in which ω is the angular vibrational frequency, κ is the permeability of the bed, and L is the vibro-bed depth. The dimensionless group ξ_G is almost identical to the group ξ_K defined by equation [3.25] and can also be identified from the dimensionless form of equation [3.23], that is,

$$\frac{\partial^2 P}{\partial Z^2} = \frac{\omega L^2}{\kappa} \frac{\partial P}{\partial(\omega t)} \qquad [3.34]$$

In this equation, $Z = z/L$ and $P = (p - p_0)/\rho_b g$. The presence of the group $\omega L^2/\kappa$ confirms the appropriateness of the dimensionless group in equation [3.33] to assess the significance of gas-compressibility effects.

Gutman suggested that the gas compressibility should be taken into account when $\xi_G > 0.5$. He reported that his model breaks down at $\xi_G \geq 2.0$.

The simplifying assumption that the air density in the air gap can be approximated by the density at the conditions existing at the upper boundary of the bed seemed to be adequate for Gutman's experimental conditions since the floor-pressure deviation was less than 5%. By using equation [3.29], density variations can be neglected if:

$$\frac{s}{\rho_0}\frac{d\rho}{dt} << \frac{ds}{dt} \qquad [3.35]$$

An analysis of the order of magnitude of the terms leads to $(\Delta\rho/\rho_0) = (\Delta p/p_0) << 1.0$. Deviations greater than 5% are likely to occur for beds of small, high-density particles vibrated at high frequencies.

3.1.4 Applicability of theoretical models

From a general perspective, the single-particle and Kroll's models may be considered a particular cases of Gutman's model. The single-particle model is valid if the effect of drag forces on the bed behavior is negligible. Kroll's model applies if drag forces are significant, but the effect of gas compressibility can be neglected. These considerations restrict the applicability of each model to specific ranges of experimental conditions.

Although not reported in the literature, it was shown in section 3.1.2 that a dimensionless analysis can be utilized to express the equations for floor pressures and air-gap sizes in dimensionless form. According to Kroll's model these dimensionless variables are dependent on two parameters only: the vibrational intensity parameter K, and a dimensionless group N that can be interpreted as the inverse of the bed resistance to gas percolation per unit bed-density. As N is increased, the vibrated bed approaches the single-particle behavior.

Gutman[14] suggested that the effect of gas compressibility is significant when the magnitude of the parameter ξ_G defined by equation [3.33] is larger than 0.5, and reported that his model breaks down for $\xi_G > 2.0$.

Figure 44 on page 102 maps on a two-dimensional graph regions of applicability of each model in terms of K- and N-values. It was assumed that the bed behavior could be described by the single-particle model when the effect of drag forces on the maximum air-gap size were less than 5%. The region of applicability of Gutman's model in this map is dependent on the vibrational frequency, bed depth and bed permeability. No theoretical model is available for very small values of the dimensionless parameter N.

Like Geldart's powder classification shown in Figure 38 on page 90, the mapping in Figure 44 on page 102 defines four different regions. Considering that drag forces in both vibrated and gas-fluidized beds significantly affect bed behavior, such similarity does not seem to be surprising.

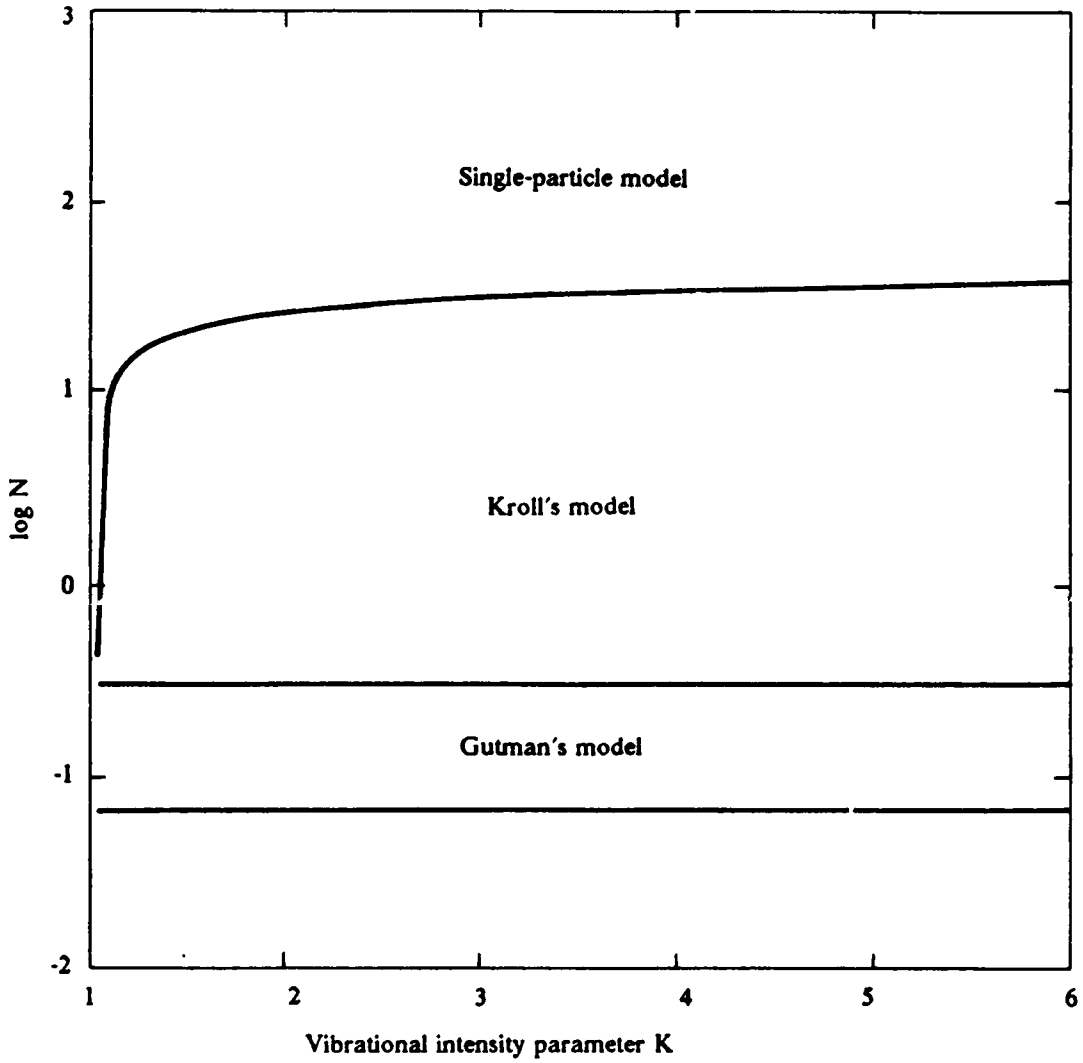

Figure 44. **Applicability of theoretical models for vibro-bed dynamics:** 50-mm bed of particles of density of 3600 kg/m^3 vibrated at a frequency of 25 Hertz. Bed porosity: 0.41. N is defined by equation [3.16], and it essentially represents the hydraulic resistance per unit of bed density. No theoretical models are available for very small values of N.

3.1.5 Summary

The effects of drag forces and gas compressibility account for the differences in the formulation of the single-particle, Kroll's, and Gutman's models. The analyses of the models yielded the following conclusions:

(1) The single-particle model predicts the bed compaction during the period of time that the bed and vessel stay together, and the formation of air gaps when the vibrational intensity parameter K exceeds one. At sufficiently high K-values, non-uniform bed trajectories should eventually occur at consecutive vibrational cycles, and the bed may even remain in flight over whole vibrational cycles. The disavantage of the model resides in its estimates of gap sizes and bed-flight periods, which are incorrectly independent of particle size and type.

(2) Kroll's model, in accounting for drag forces, allows estimates for the effect of bed and particle properties on the development of air gaps. The air-gap size and bed-flight period are reduced as the permeability of the bed to gas percolation is decreased.

(3) Gutman's compressible-gas model predicts that the size of air gaps should be larger than those estimated by Kroll's model. When the bed and vessel collide, the floor pressure does not decay abruptly to the pressure above the bed as predicted by Kroll's model. Gutman suggests that his model is appropriate for small particles.

All of the models assume that the bed behaves as a rigid porous piston. This assumption does not permit the utilization of any of the models for predicting solid-circulation rates and patterns, which knowledge is essential in designing and optimizing heat-transfer equipment.

3.2 *Heat Transfer in Vibro-beds*

As discussed in Chapter 2, previous work on heat transfer in vibro-beds indicated that heat-transfer coefficients were very dependent on the gas medium and on the solid-circulation pattern within the vibrated bed. Experimental results at very low absolute pressures demonstrated that heat transfer by solid-solid contact was very small. These observations suggested that the heat-transfer mechanism to be composed primarily of two consecutive steps: (i) transfer through the gas layer separating the particles and the heating surface, and (ii) transfer inside the layer of particles. This mechanism is very similar to that in gas-fluidized beds; differences are apparently related to the origin of solid circulation patterns, and to the nature of gas gaps around the heating surface. In gas-fluidized beds, the solid circulation and mixing is mainly induced by bubble activity; bubbles also interrup periodically the direct contact between particles and the heater. Since bubbles are not very frequent in vibro-beds of larger particles, the vibro-bed dynamics is governed by the oscillating gas flow and wall-friction forces induced by mechanical vibrations. Gas gaps, if existing, may periodically be formed around the heating surface by the relative motion between the bed and the vibrating vessel.

Several models have been proposed for heat transfer in vibro-beds. Ringer's[41] and Muchowski's[42] models account for heat tranfer in both the gas layer and the layer of particles. Gutman's[14,48] model assumes that the resistance to heat transfer is confined to the gas layer only. The model of Kalt'man and Tamarin[44] is an analogy with the packet model developed by Mickley and Fairbanks[49] for gas-fluidized beds. Only the models of Ringer and of Muchowski satisfy a two-step heat-transfer mechanism, but their applicability is restricted by the difficulty in determining the solid-circulation rates and patterns in vibro-beds.

Zabrodsky[18] made an analysis of the trends of heat transfer between a gas-fluidized bed and a heat-transfer surface placed within the bed by assuming that only the layer of particles located closest to the heating surface exchanges thermal energy with the surface. Renewal of particles in this layer was assumed to take place at directions normal to the surface. This model was developed

by Zabrodsky for a heat-transfer surface at constant temperature, and will be called the one-layer model for vibro-bed heat transfer below. Neither has Zabrodsky attempted to apply his model to vibro-bed heat transfer, nor was the application of the model considered in the published literature.

In what follows, Zabrodsky's model is adopted to examine the effects of several experimental variables and parameters on heat-transfer coefficients between a vibro-bed and a heating surface immersed into the bed. The model is also slightly modified to account for solid renewal parallel to the heat-transfer surface.

3.2.1 Formulation of the one-layer model

A schematic diagram of the one-layer model is shown in Figure 45 on page 106. Zabrodsky[18] made the following assumptions: (i) temperature gradients within solid particles are negligible when compared to the temperature difference between the surface of the heater and that of the particle, (ii) particles exchange the thermal energy acquired from the heater with the bulk of the bed before returning again to the layer nearest to the heating surface; (iii) the curvature of the heating surface is negligible; (iv) the local heat-transfer coefficient between the first layer of particles and the heat-transfer surface is constant during the particle-surface contact time: and (v) the temperature of the heating surface is constant.

The amount of heat absorbed by a single particle close to the heater during a differential period of time dt can be written as:

$$dQ = \frac{\lambda}{\delta_g} \frac{\pi d_p^2}{4} (T_h - T_p)\, dt = C_{ps}\rho_s \frac{\pi d_p^3}{6} dT_p \qquad [3.62]$$

In this equation, dQ is the amount of heat absorbed during time dt, λ is the thermal conductivity of the gas medium, δ_g is the average thickness of the gas layer between the particles and the heating surface, d_p is the particle diameter, T_h is the heating surface temperature, T_p is temperature of the particles in the first row, C_{ps} is the specific heat of the solid, and ρ_s is the density

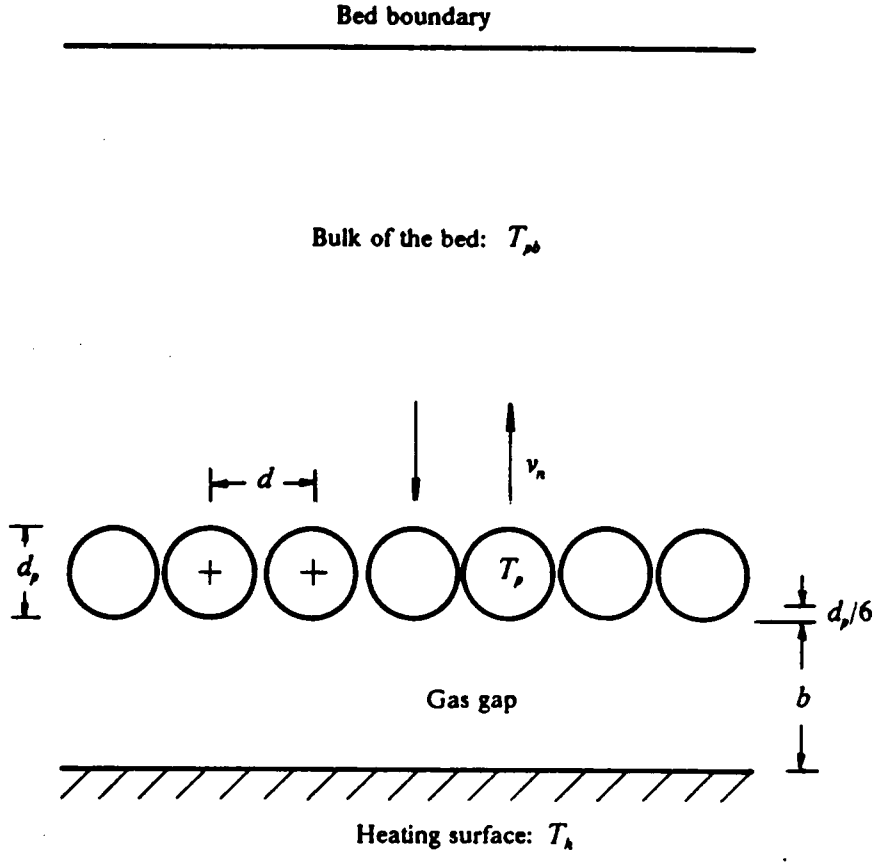

Figure 45. Zabrodsky's[18] one-layer heat-transfer model: Constant heating-surface temperature. Direction of solid renewal: normal to the surface. Notation: T_h = heating-surface temperature; T_p = particle temperature in the layer closest to the heat-transfer surface; T_{pb} = bulk bed-temperature; v_n = particle-velocity component that is normal to the surface; d_p = particle diameter; d = interparticle distance; $d_p/6$ = air sub-layer thickness; b = air-gap size.

of the solid. Since the average gas-layer thickness is used, the heat-transfer area is taken as the projection of the sphere of solid on the heat-transfer surface. The heating of the second row of particles is neglected.

Integrating equation [3.62] over the period of time that the particle remains close to the heating surface at a constant gas-layer thickness, and rearranging the result gives

$$T_p - T_b = (T_h - T_b)\left[1 - \exp\left[-\frac{1.5\lambda}{\delta_g C_{ps}\rho_s d_p}\tau\right]\right] \qquad [3.63]$$

where T_b is the temperature of the particles in the bulk of the bed, and τ is the the residence time of the particle in the first row near the heating surface. This residence time is also called the renewal time, and sometimes the contact time when particles are in direct contact with the surface.

The residence time was related to the particle spacing d,

$$d = d_p\left[\frac{1 - 0.476}{1 - \varepsilon}\right]^{1/3} = \frac{0.807\, d_p}{(1-\varepsilon)^{1/3}} \qquad [3.64]$$

and to the component of the particle velocity, v_n , that is normal to the heating surface by:

$$\tau = \frac{d}{v_n} = \frac{0.807\, d_p}{v_n (1-\varepsilon)^{1/3}} \qquad [3.65]$$

In equation [3.64], the standard particle spacing $d = d_p$ refers to a dense, cubical packing of spheres, for which the porosity is 0.476.

Defining n as the number of particles per unit area of the layer, the amount of heat exchanged per unit surface area during the renewal time is:

$$Q_\tau = \rho_s C_{ps}\frac{\pi d_p^3}{6} n (T_p - T_b) = \rho_s C_{ps}\frac{\pi d_p^3}{6 d^2}(T_p - T_b) \qquad [3.66]$$

By computing the heat flux per unit time, and by referring the heat transfer coefficient to the temperature difference between the surface of the heater and the bulk of the bed, one can obtain

$$h = \rho_s C_{ps} v_n (1 - \varepsilon) \left[1 - \exp \left[- \frac{1.2\lambda}{\delta_g \rho_s C_{ps} v_n (1 - \varepsilon)^{1/3}} \right] \right] \qquad [3.67]$$

The average gas-layer thickness is assumed to be given by

$$\delta_g = b + \frac{d_p}{6} \qquad [3.68]$$

where b accounts for any additional gap existing between the heater and the particles, like a gas gap in vibro-beds.

One must keep in mind that it is not possible to obtain experimentally a net particle velocity that is normal to the heating surface. Thus the velocity appearing in equation [3.67] actually represents a kind of diffusional velocity of fresh particles only. This diffusion can be caused by a process of random turbulent mixing, or by a lateral intermixing within an ordered stream of solid particles. As discussed in Chapter 2, both processes have been observed in vibro-beds, and determined to increase with the intensity of the vibration.

In the following discussion of the effects of experimental conditions on the behavior of heat-transfer coefficients in vibro-beds, the fluid medium is assumed to be air and the average temperature of the air layer is about 80°C.

3.2.2 Effects of particle renewal and bed porosity

Figure 46 on page 109 shows a plot of the heat transfer coefficient as a function of the product $\rho_s C_{ps} v_n$, which quantifies the thermal capacity of the flux of fresh particles arriving at the heating surface, for a bed of 0.2-mm particles and several bed porosities. Particles are assumed to be in contact with the heater; no additional air gaps are present. Lower porosities, or higher particle concentrations, yield greater heat transfer coefficients. The dependence of the coefficient on the thermal capacity of the stream of particles is very strong at the beginning, and then shows a tend-

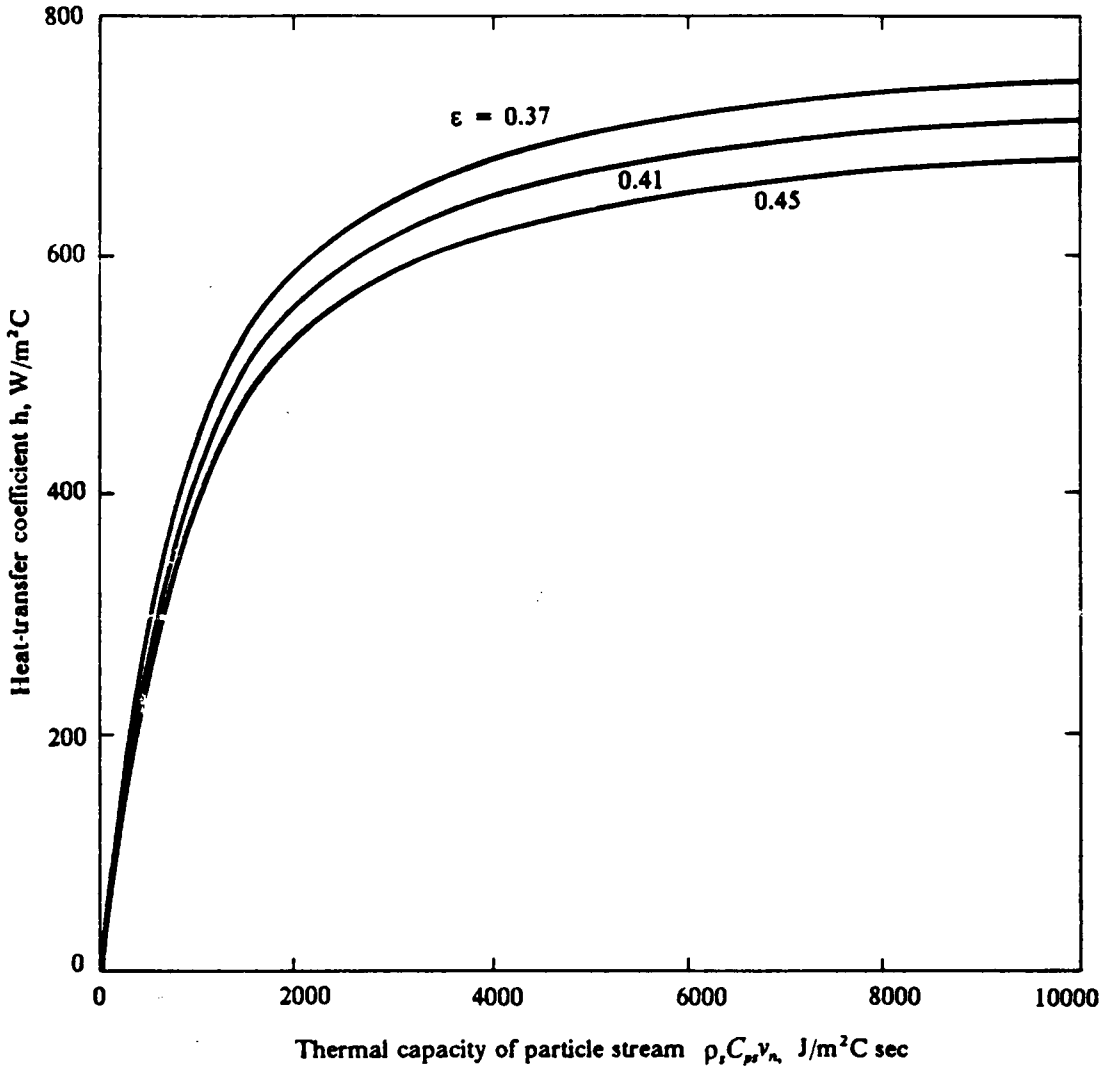

Figure 46. Effect of bed porosity on heat transfer in vibro-beds: Heat-transfer coefficients between a layer of 200-μm particles and a heating surface in the absence of air gaps as a function of the thermal capacity of the stream of solids arriving at the surface. Notation: ε = bed porosity; ρ_s = solid density; C_{ps} = solid specific heat; v_n = particle velocity normal to the heating surface.

ency to level out. For a particular type of solid, an increase in the normal velocity leads to a smaller contact time between particles and the heater, and thus to improved heat transfer coefficients as long as the porosity remains unchanged. Since greater particle velocities also cause the bed porosity to increase, there is a compromise between increasing the normal velocity of the solids and the associated effect of bed expansion, which is probably dependent on particle shape, roughness and density. According to Geldart[39], the expansion effect becomes less significant as the particle density is increased, and so one can expect porosity effects to be more serious for low-density solids. In any case, they seem more likely to occur in the region where the heat transfer coefficient levels out. This follows because a large increase in the normal velocity yields only very little improvement in heat transfer. Such a large increase in particle velocity might be accompanied by an appreciable bed expansion, which can offset any benefits from smaller contact times. In the absence of air gaps, this could explain the maximum observed in the curves of the heat-transfer-coefficients for vibrated beds when the vibrational intensity was increased.

The increase in the heat transfer coefficient with decreasing contact times can be easily justified through the following equation,

$$Q = h_p (T_h - T_p) = h (T_h - T_b) \qquad [3.69]$$

In this equation, the first term represents the actual heat transfer between particles in the first layer and the heater; and the second term defines the heat transfer coefficient in the vibro-bed. The coefficient h_p is dependent on the particle size and the gas thermal conductivity only. For constant bed and heating-surface temperatures, the thermal conductivity remains constant, and so does h_p. If the contact time of the particles with the heater is reduced, particles will leave the heater at a lower temperature. Therefore, the average temperature difference $(T_h - T_p)$ is higher for small contact times, resulting in greater rates of heat transfer. Consequently, the overall heat-transfer coefficient calculated from equation [3.69] increases as the contact time is decreased.

Figure 46 on page 109 also tells about the effects of particle density and specific heat of the solid on the heat transfer coefficient. At a constant contact time, the heat transfer coefficient increases with increasing thermal capacity, $\rho_s C_{ps}$, of the solids, and the dependence is stronger at low

values of the total thermal capacity of the stream of fresh particles. If the solid of higher thermal capacity is denser, the bed porosity is likely to be lower and thus favors that dependence. However, if the increase in the thermal capacity is accomplished by using a less dense solid, the benefit of achieving a higher heat-transfer coefficient might be offset by an undesirable bed expansion. This is again more likely to occur in regions where the heat transfer coefficient levels out. In general, in order to achieve comparable heat-transfer performance, particles of higher thermal capacities do not need to be renewed near the heating surface as frequently as particles of lower heat capacities.

Obviously, the heat transfer coefficient can not assume a zero value in the absence of solid circulation as shown in Figure 46 on page 109. The minimum value for the coefficient is limited by its value in a fixed bed of particles, and so the values of heat-transfer coefficients below that in a fixed bed are physically meaningless. Muchowski[42] and Gutman[50] have measured fixed-bed coefficients in the range of 25 to 50 W/m^2K in the absence of any additional air gaps. In terms of the model, a zero coefficient indicates only that after an infinite contact time, the temperature of the first layer of particles has reached the temperature of the heating surface. In other words, since the particle velocity is zero, a zero coefficient suggests that no thermal energy is exchanged with the bulk of the bed.

The predicted normal-to-the-heater component of the particle velocity for heat transfer coefficients of about 500 W/m^2C does not seem to be very high. For corundum particles with a density of 4,000 kg/m^3 and a specific heat of 760 J/kg.K, this normal velocity component is approximately $4.7x10^{-4}$ m/s, or 0.47 mm/s. The corresponding contact time between particles and the heater is 0.41 seconds. If the heat capacity of the solid is lower, higher velocities will be necessary for achieving comparable heat-transfer performance.

3.2.3 Effect of air gaps

In case the particles do not touch the heating surface, an additional air layer will be present; the factor b in equation [3.68] accounts for this effect. The air layer may be generated by large

particle velocities, which require large gas velocities. It may also be generated by a relative velocity between the vibrating vessel and the bed of particles, which corresponds to an air gap.

The dependence of the heat transfer coefficient on the thickness b of the additional gas layer is shown in Figure 47 on page 113 for a bed of particles of 200 μm in diameter. A layer thickness of about 50 μm reduces the coefficient to less than half of its original highest value, and to only about 10% of the original value if the thickness is increased to 500 μm. When compared to the average thickness of the air sub-layer when the particles are in contact with the heating surface, which is $d_p/6$ or about 30 μm, those values for the thickness of the additional gas layer are very large. Therefore, for constant heater and bed temperatures, the heat transfer through the gas gap to the vibro-bed of 200-μm particles becomes negligible during the period of time that the gap is greater than 500 μm. During this period of time, the heating-surface area covered by the gap is lost for heat transfer purposes, no matter how fast the the particle renewal rate might be. Since the reduction in the heat transfer coefficient is dependent on the relative size of the gas gap with respect to the particle diameter, gaps are more unforgiving when they are present in beds of small particles. Fortunately, as discussed in the preceding section, under identical vibrational conditions, the maximum size of the gap decreases as the particle size is decreased. For vertical flat heaters and in the absence of air gaps, thin gas layers that might originate from increased solid activity will also be more unforgiving as the particle size is reduced.

Kal'tman and Tamarin[44], and Zabrodskii et al[43] have reported higher heat transfer coefficients as the temperature in a vibro-bed and in an gas-fluidised bed, respectively, was increased. Kal'tman and Tamarin utilized vibro-beds of corundum particles. The trend can be analized in terms of the plots presented in Figure 47 on page 113 by observing that an increase in the thermal conductivity of the gas affects heat transfer just oppositely as does an increase in the size of the gas gap. Thus, if the same temperature difference between the bed and heater is kept at higher bed temperatures, the heat transfer coefficient will be enhanced for the same solid velocity. An increase in temperature of 200 degrees above ambient temperature increases the thermal conductivity of air by about 50%. Within the same range of temperatures, the thermal conductivity of corundum decreases to half of its value at ambient temperature. The latter observation seems to validate the assumption that the

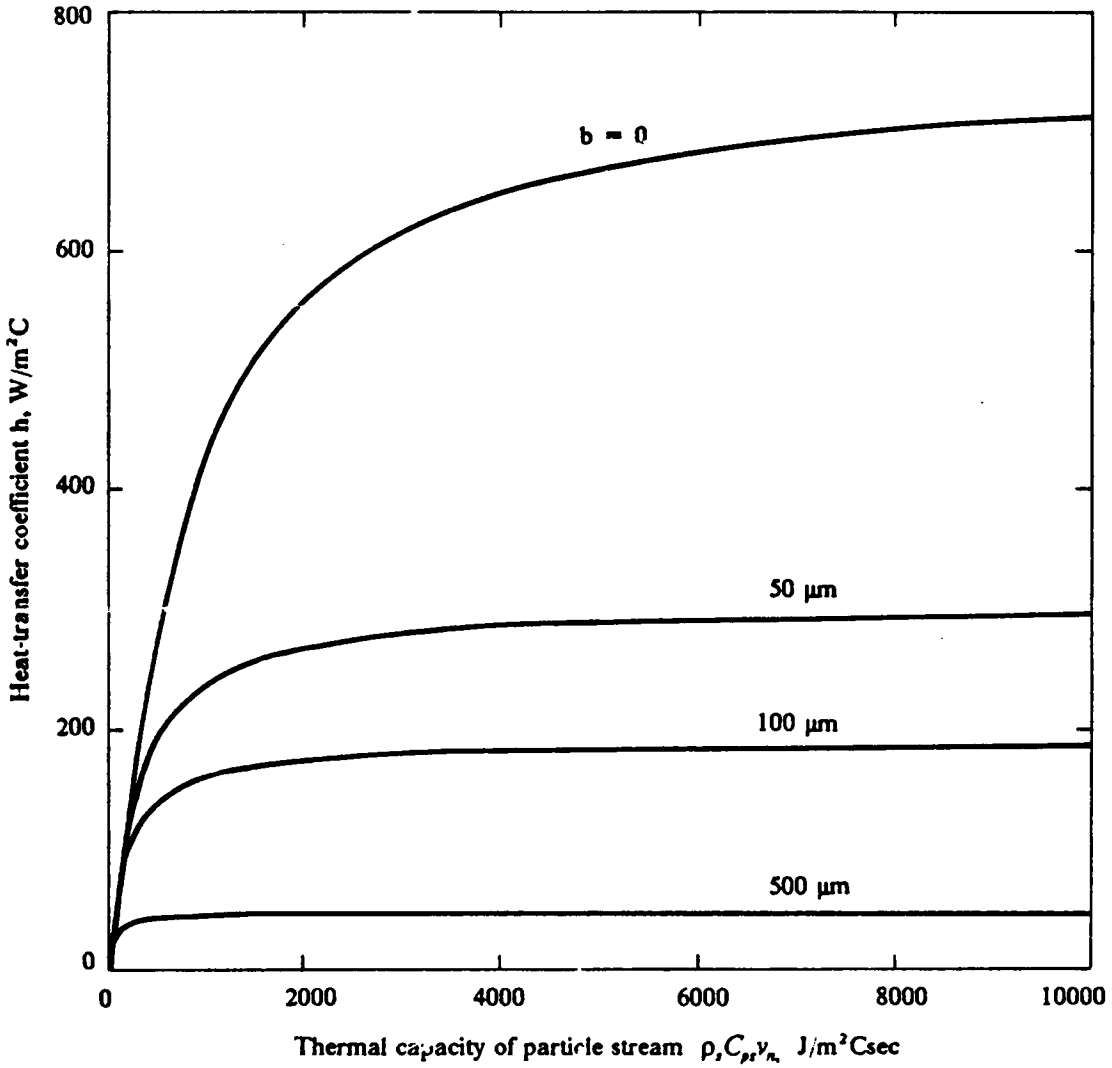

Figure 47. **Effect of air-gap size on heat transfer in vibro-beds:** Heat-transfer coefficients betwwen a layer of 200-μm particles and a heating surface as a function of the thermal capacity of the stream of particles arriving at the surface. Bed porosity: 0.41. Notation: b = air-gap size; ρ_s = solid density; C_{ps} = solid specific heat; v_n = particle velocity normal to the heating surface.

solid thermal conductivity is not an important parameter in heat transfer between a vibro-bed and an immersed heating surface.

The rapidly increasing character of the heat-transfer coefficient observed with increased thermal capacities of the incoming stream of fresh particles follows the experimental findings discussed in Chapter 2. In general, as the vibrational intensity is increased, the solid activity is intensified, and the heat-transfer coefficient increases. The maximum in the heat-transfer coefficient that is eventually reached seems to be caused by the negative effects of increased bed expansion and air gap sizes.

As shown in Figure 47 on page 113, the heat-transfer coefficient levels out at lower particle velocities, or higher contact times, as the size of the air gap increases. These results refer to a constant gap size, and cannot be directly applied to vibro-beds. In vibro-beds, the formation of the air gap is periodic, and thus equation [3.62] must be integrated with respect to the air-layer thickness as a function of time, not over a single vibrational cycle, but over the period of time that the particle resides in the first row of solids, even if the particles are not in direct contact with the heating surface. In this case, one must be careful with the concepts of contact time and renewal time. The renewal time is independent of the presence of air gaps, and is inversely proportional to component of the particle velocity that is normal to the heater. The contact time of a particle with the heating surface is dependent on the period of time that the heater is covered by an air gap. Both periods of time are extended over several vibrational cycles if the renewal time is greater than the duration of one vibrational cycle. However, the heat-exchanging power is very much reduced during the period of time that the heating surface is partially or totally covered by an air gap. Now, since less heat is absorbed when gaps are present, less particles are needed to remove that smaller amount of heat. Thus, the renewal time can be lower than if no gap is present. In general, the heat transfer coefficient at a specific location on the heating surface is not constant, but varies over the vibrational cycle as the size of the gap changes.

An interesting situation arises if the heat transfer during the presence of the gap can be neglected. From Figure 47 on page 113, a particle velocity of 0.47 mm/s is required in a bed of 0.2-mm corundum particles to achieve a heat-transfer coefficient of 500 W/m^2K in the absence of an air gap.

If a gap is present and assuming that the surface is in contact with the bed during 3/8 of the vibrational cycle, it can be calculated that the heat transfer coefficient during the time of contact increases to about 640 W/m^2C for the same particle velocity. The reason is that for the same renewal time, the contact time is reduced by the presence of the gap. In this situation, it clearly is the contact time, and not the renewal time, that controls the heat-transfer coefficient during the period of time that thermal energy exchange takes place. The contact time, which can here be thought as an effective renewal time, was reduced by the gap to about 38% of its value without the gap, but the heat flux still accounted for about 48% of the flux in the absence of the gap. The preceding percentages are not the same. This is because the heat-transfer coefficient is increased over the reduced period of time that the bed and heater remain in contact. Therefore, the reduction in the average heat-transfer coefficient over a vibrational cycle is not in general directly proportional to the reduction in the time of contact between the heater and bed of particles.

The preceding example might explain the observed dependence of the heat-transfer coefficient on the vibrational conditions and the appearance of a maximum heat-transfer coefficient at higher vibrational intensities. Initially, as the intensity of vibrations is increased, heat transfer is increased by an improvement in solid circulation, resulting in a higher heat-transfer coefficient over the period of time the bed is in contact with the heating surface. As shown in Figure 47 on page 113, this fact is large at low particle velocities and overcomes any negative effect due to an increase in the size of the air gap. Eventually a stage is reached when no sensible improvement can be achieved by increasing the normal velocity of the particles, and the reduction of heat transfer by increased gap sizes predominates. The resulting average heat transfer coefficient passes through a maximum and then decreases. If higher solid renewal rates lead to a sensible porosity increase around the heater, it will enhance the negative effect of the gap size.

3.2.4 Effect of particle size

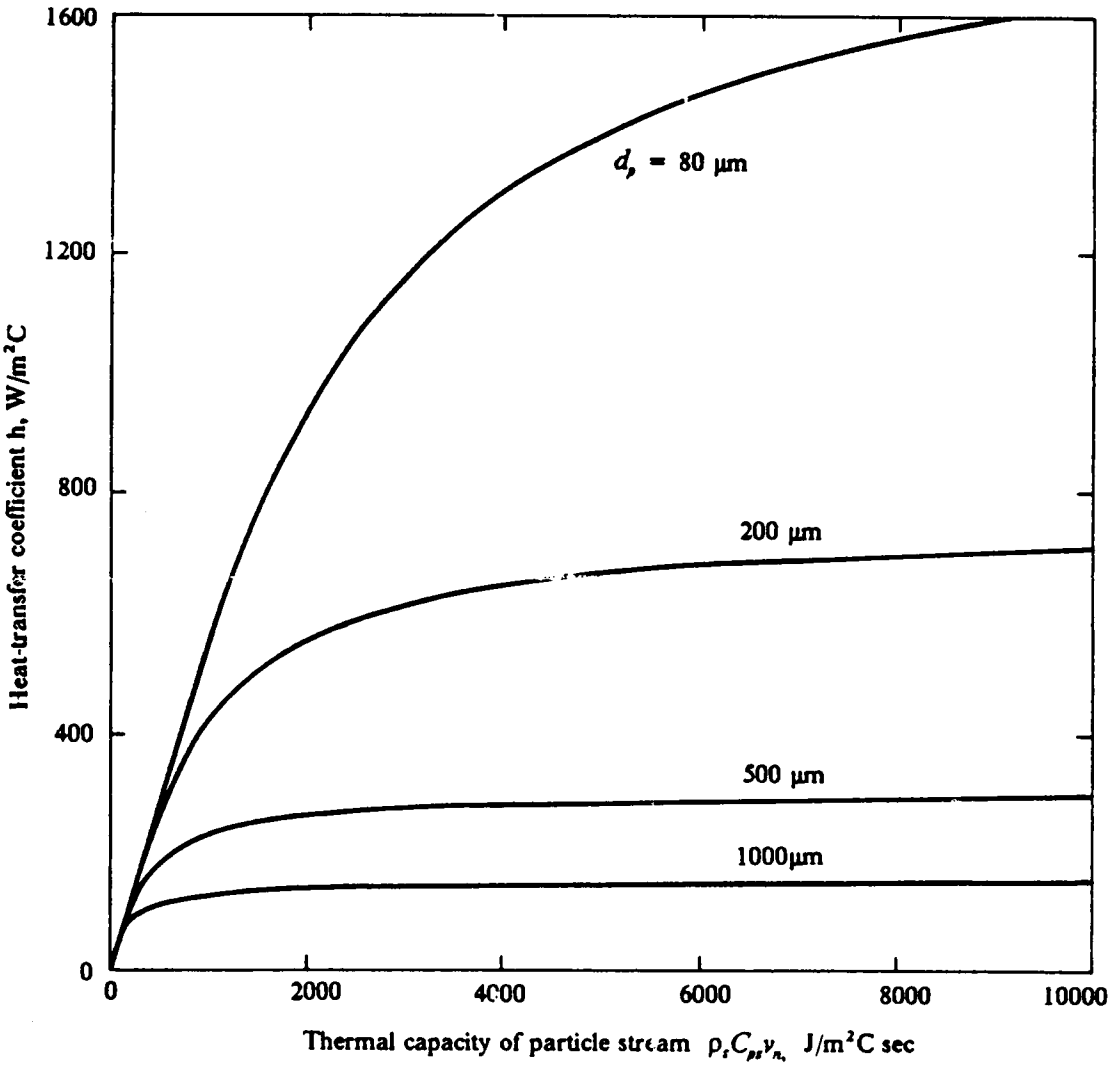

Figure 48. **Effect of particle size on heat transfer in vibro-beds:** Heat-transfer coefficients between a layer of particles and a heating surface in the absence of air gaps as a function of the thermal capacity of the stream of solids arriving at the surface. Bed porosity: 0.41. Notation: d_p = particle diameter; ρ_s = solid density; C_{ps} = solid specific heat; v_n = particle velocity normal to the heating surface.

The dependence of the heat-transfer coefficient on the particle size is shown in Figure 48 on page 116. Particles were assumed to be in contact with the heating surface in the absence of an air gap. As the particle size is increased, a sharp reduction in the heat-transfer coefficient occurs. The reduction is a consequence of the increased average size of the air sub-layer between the surface of the heater and the particles in contact with the heater. The average size of that sub-layer is $d_p/6$, and the increased thickness of the air sub-layer has the same effect as increasing the air gap at a constant particle size. Thus, for large particles, heat transfer can only be moderately improved and over a very limited range of particle velocities. As the particle size is reduced, and so is the average size of the gas sub-layer, higher heat-transfer coefficients can be achieved by improving the solid circulation. Heat transfer in beds of small particles becomes very large in the range of small renewal times. It was shown in previous sections that as the the particle size is reduced at constant vibrational conditions, the maximum size of the gas gap in vibro-beds decreases, and that the air gap covers the heat-transfer surface during a smaller fraction of the vibrational cycle. Therefore, higher heat-transfer coefficients can be obtained in beds of small particles than in beds of large particles. This is because the reduction in particle-heater contact time per cycle is lower, and because the thickness of the gas layer between the particles and heater is smaller. That behavior also suggests that the maximum heat-transfer coefficient for vibrated beds of large particles can be attained at less intense vibrational conditions than the maximum for small particles.

3.2.5 Limiting cases

The exponential term appearing in equation [3.67] for the heat-transfer coefficient introduces the possibility of two limiting situations. In the first case, when the component of the particle velocity that is normal to the heater surface, v_n, is very low, the equation is reduced to:

$$h = \rho_s C_{ps} v_n (1 - \varepsilon) \qquad [3.70]$$

The solid circulation is less intense, and heat transfer is independent of the resistance in the gas layer. At the same particle velocity, the magnitude of the heat-transfer coefficient is defined by the heat capacity of the solid. A layer of particles of a high heat capacity can absorb the same amount of thermal energy with a smaller increase in its temperature than a layer of particles of a low heat capacity.

The second limiting situation corresponds to high solid-circulation rates, and the equation for the heat-transfer coefficient becomes:

$$h = \frac{1.2\lambda(1-\varepsilon)^{2/3}}{\delta_g} \qquad [3.71]$$

Thus, for small renewal times, the heat transfer coefficient is explicitely independent of all particles properties. Physically, it means that the temperature increase of the first row of particles is negligible when compared to the temperature difference between the bed and the heater. The magnitude of the coefficient is uniquely defined by the resistance in the gas layer and by bed porosity. The thickness of the gas and the bed porosity determine the maximum value of the heat-transfer coefficient that can be obtained for a certain particle size.

Both limiting cases and the transition between these cases for a bed of 200-μm particles are illustrated in Figure 49 on page 119. By comparing this figure to Figure 48 on page 116, one can observe that the transitional region between the two limiting cases occurs over wider ranges of values of the thermal capacity of the stream of fresh particles as the particle size is decreased. This result is significant when considering the tendency of small particles to require higher vibration intensities in order to obtain comparable solid-circulation and mixing rates. Wider transition ranges between the limiting cases suggest that small particles can show a stronger dependency on particle properties than large particles. In beds of large particles, the transition is very rapid at small solid velocities, which is enhanced by the presence of large air gaps.

The applicability of the one-layer model increases as the particle size is increased. It can be explained physically by the fact that the heating area covered by a single particle increases with the square of its diameter, but its volume increases with the cube of the diameter. In addition, the re-

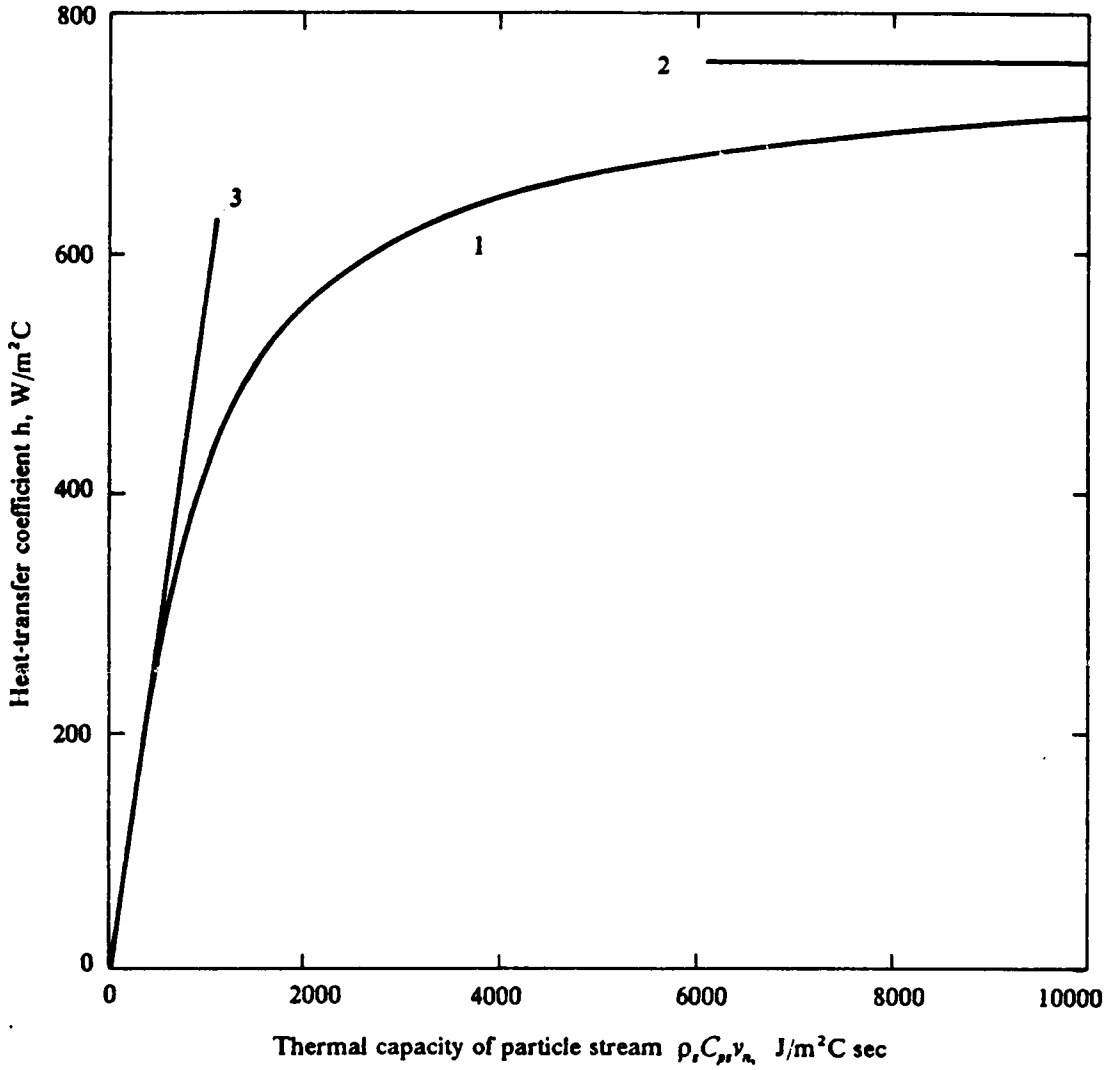

1 - Full model, eqn. 3.67
2 - High solid-circulation rate, eqn. 3.71
3 - Low solid-circulation rate, eqn. 3.70

Figure 49. Limiting cases of heat tranfer in vibro-beds: Heat-transfer coefficients between a layer of 200-μm particles and a heating surface in the absence of air gaps as a function of the thermal capacity of the stream of particles arriving at the surface. Bed porosity: 0.41. Notation: ρ_s = solid density; C_{ps} = solid specific heat; v_n = particle velocity normal to the heating surface.

sistance to heat transfer of the air layer also increases with the diameter of the particle. Consequently, since large particles absorb less heat and have a higher thermal capacity, the temperature increase is not as large as that for small particles.

The effect of air gaps on the increase in the temperature of a particle can be exemplified for a vibro-bed of 200-μm corundum particles analyzed previously in section 3.2.3.. In the absence of an air gap and for a heat-transfer coefficient of 500 W/m^2K, the calculated increase in the temperature of the particle is about 60% of the temperature difference between the bulk of the bed and the heating surface. In the presence of an air gap, the corresponding increase is reduced to about 29%. Under the same conditions, these values are greater for smaller particles and smaller for larger particles. Therefore, the need of a multi-layer heat-transfer model becomes noticeable as both the particle size and particle velocity are decreased.

3.2.6 Maximum heat-transfer coefficients

The strong effect of particle size on the maximum heat-transfer coefficient at small particle renewal times is illustrated in Figure 50 on page 121. In the absence of air gaps, the maximum coefficient increases as the particle size is decreased. Smaller bed porosities yield improved heat transfer. The effect of an additional gas gap between the layer of particles and the heater becomes more pronounced as the particle diameter is decreased, and is far more significant than any porosity changes in the vibro-bed.

The presence of air gaps in vibro-beds and the occurrence of a maximum heat-transfer coefficient as the intensity of vibrations is increased may be interpreted as the gas resistance controlling the mechanism of heat transfer at that limiting value. In this situation, since bed porosity and air-gap size are dependent on the particle size and density, equation [3.71] is reduced to some kind of correlation among the heat-transfer coefficient and the thermal conductivity of the gas, the diameter of the particles, as well as the density of the solid. The form of such correlation can apparently be determined experimentally. That is probably why Zabrodskii et al[43] were able to obtain very good

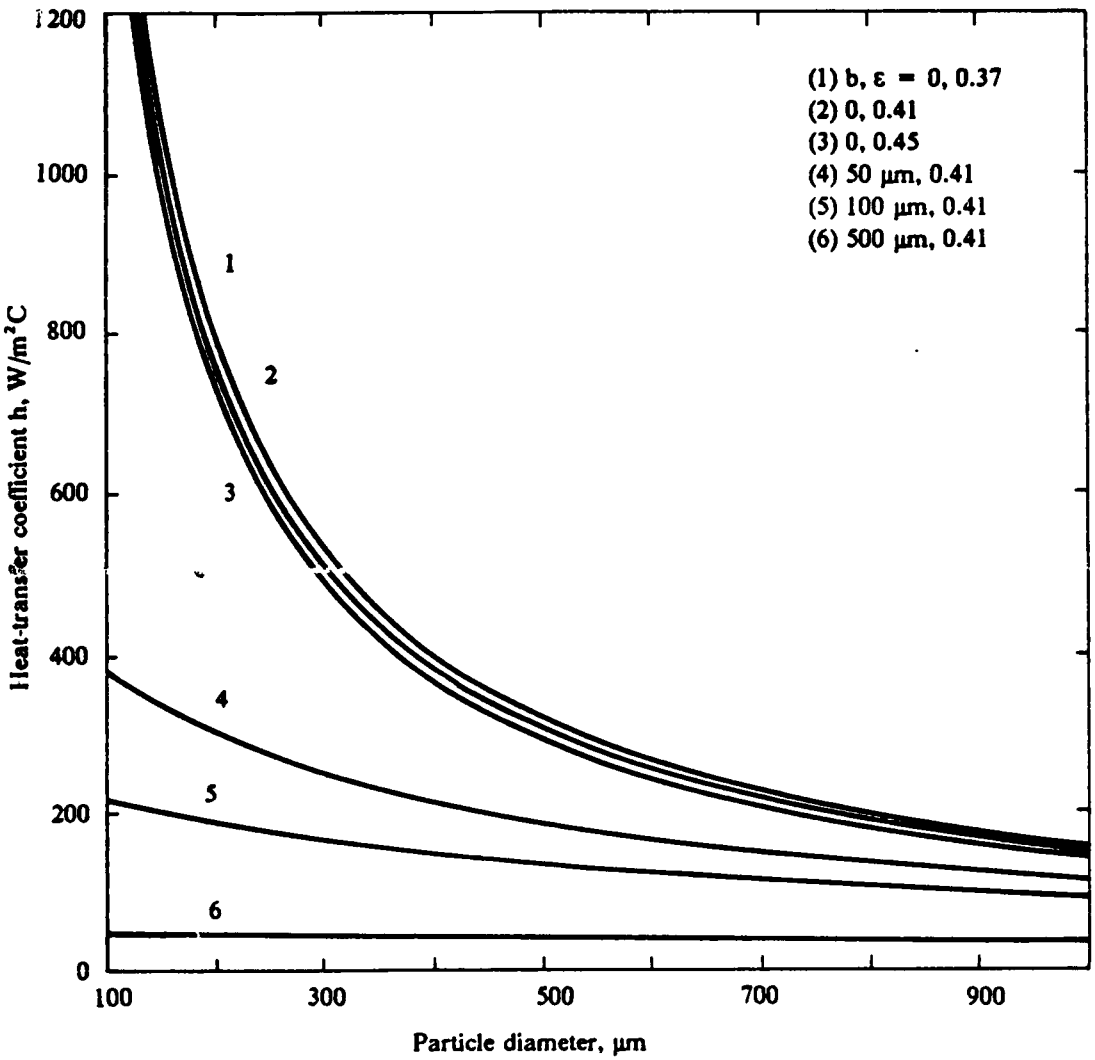

Figure 50. Effect of particle size on maximum heat-transfer coefficient in vibro-beds: Resistance in the air layer controls heat transfer. Parameters: b = air-gap thickness, ε = bed porosity.

results in correlating their experimental data when plotting the group $h_{id}/\lambda^{0.6}\rho_s^{0.2}$ against the particle diameter as shown in Figure 17 on page 43.

3.2.7 Solid renewal parallel to the heat-transfer surface

Zabrodsky[18], defined the renewal time in terms of the particle-velocity component that is normal to the heating surface, and neglected any solid renewal by the parallel component of the velocity. That seems to be appropriate for gas-fluidized beds, in which solid mixing is mainly caused by the action of raising gas bubbles. However, as discussed in Chapter 2, solid-flow patterns in vibro-beds consist mostly of well-ordered streams. This behavior introduces some new aspects to heat transfer in vibro-beds. For an ordered flow of particles parallel to the heating surface, the renewal time is given by:

$$\tau = \frac{L_h}{v_p} \qquad [3.72]$$

In this equation, L_h is the heating-surface dimension in the direction of solid flow, and v_p is component of the particle velocity parallel to the surface. Thus, the particle renewal time is directly proportional to the dimension of the heating-surface parallel to the solid flow. The heat-transfer surface should be oriented so that the solid stream follows the shortest dimension of the surface. From a practical point of view, it is more convenient to adopt the design of the heating surface to induce certain bed dynamics than to do it in the opposite way.

Figure 51 on page 123 illustrates the effect of the characteristic dimension of the heating surface on the heat-transfer coefficient when the particle renewal is due to the parallel component of the particle velocity. The characteristic dimension of the heater is here supposed to be the dimension parallel to the direction of solid flow. For particles of 0.2 mm in diameter, a very sensible decrease in the heat-transfer coefficients occurs as the characteristic dimension of the heater is increased from 10 to 20 to 40 mm. Differences in heat-transfer coefficients become smaller as the

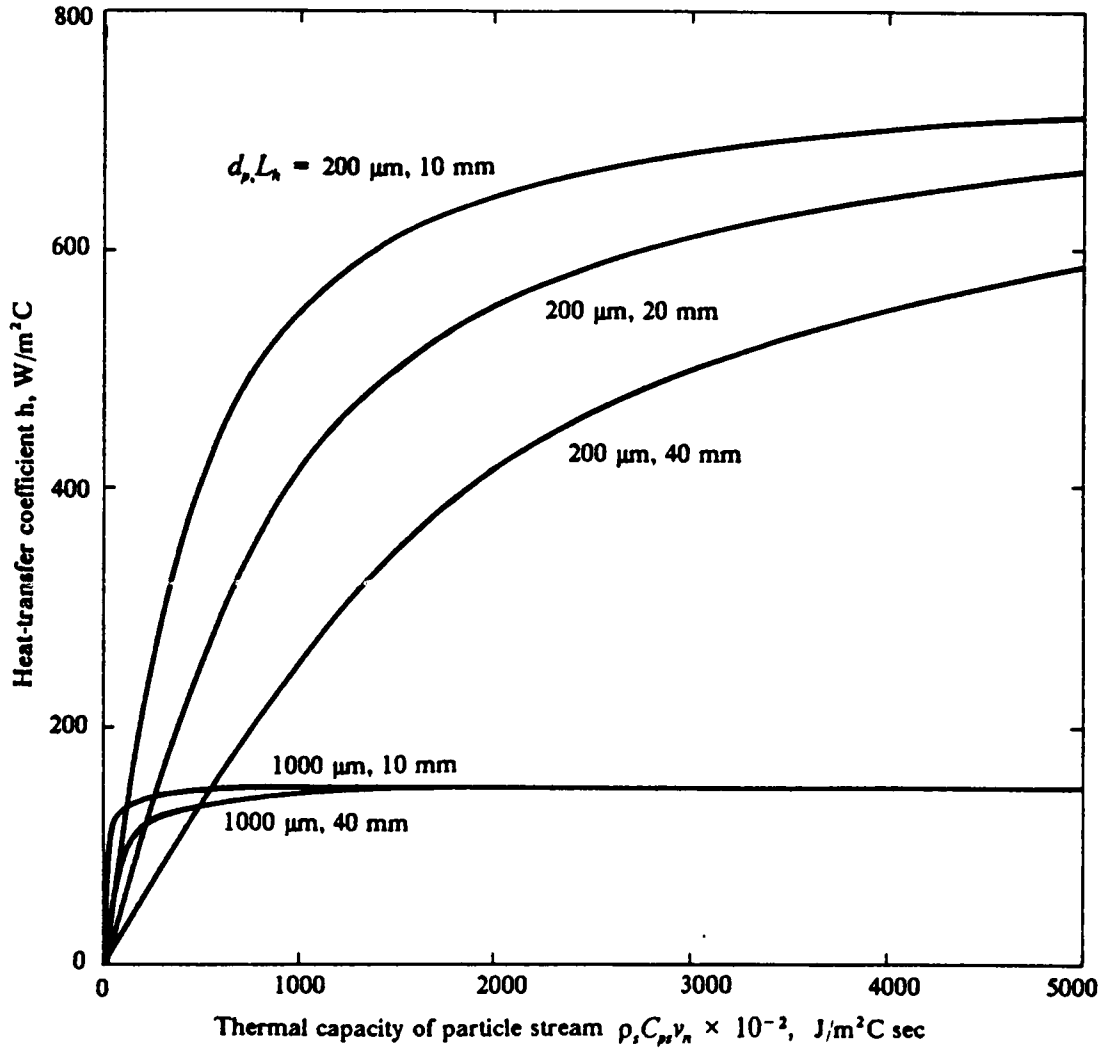

Figure 51. **Effect of heater length on heat transfer in vibro-beds:** Heat-transfer coefficients between a layer of particles and a heating surface in the absence of air gaps as a function of the thermal capacity of the stream of particles arriving at the surface. Notation: d_p = particle diameter; L_h = heater length; ρ_s = solid density; C_{ps} = solid specific heat; v_n = particle velocity parallel to the heating surface.

particle velocity is increased. For particles of 1.0 mm in diameter, only minor effects occur at small particle velocities when the characteristic dimension is changed from 10 to 40 mm. The behavior is again related to the resistance to heat transfer; since the resistance over most of the range of particle velocities is the layer of air, large particles heat up less than small particles, and so the rate of heat transfer is not affected very much by an increase in heater dimensions. To obtain the maximum values for the heat-transfer coefficients illustrated in Figure 51 on page 123, particle velocities of about 170 mm/s, or renewal times of 0.06 seconds, are required in beds of corundum particles. Gutman[14] has observed particle velocities of the order of 10 mm/s at the walls of vibro-beds of glass beads. Assuming this value as representative of solid flow, the corresponding heat transfer coefficient in the absence of air gaps would be approximately 300 W/m^2K for a heating surface with a characteristic dimension of 10 mm. This value is well below the reported values discussed in Chapter 2, which are of the order of 450 W/m^2K.

3.2.8 Summary

The trends in vibro-bed heat-transfer behavior predicted by the one-layer model showed good agreement with the experimental results discussed in Chapter 2. These trends can be summarized as follows:

(1) Heat-transfer coefficients increase as the particle-renewal rate at the heating surface is increased. At sufficiently high particle-renewal rates, the heat-transfer coefficient reaches a maximum value.

(2) An increase in bed porosity lowers the heat-transfer coefficient. This effect is small when compared to the decrease in the heat-transfer coefficient caused by the presence of air gaps between the bed and the heating surface.

(3) At identical solid-circulation rates, the heat-transfer coefficient increases as the particle size is decreased. The maximum heat-transfer coefficient occurs at lower solid-circulation rates in beds of large particles than in those of small particles.

(4) Increasing the thermal capacity of the solid increases the heat-transfer coefficient. This effect is more pronounced at smaller solid-circulation rates. The maximum heat-transfer coefficient is affected by the properties of the solid only to the extent that these properties might change the porosity of the bed or the size of the air gap.

(5) In vibrated beds, both the solid-circulation rates and the size of air gaps increase as the vibrational intensity is increased. The maximum heat-transfer coefficient occurs when the size of the air gap becomes sufficiently large to offset the benefit of an increased solid-circulation rate.

(6) The heat-transfer coefficient is decreased by an increase in the size of heater when solid renewal is due to a component of the particle velocity that is parallel to the heater. If solid renewal is achieved by a component that is normal to the heater, the heat-transfer coefficient is independent of the dimensions of the heating surface.

4.0 Experimental Investigation on Vibro-Bed Dynamics

4.1 Scope of Experimental Investigations

As discussed in previous chapters, solid circulation and solid mixing constitute important factors in heat transfer between a vibro-bed and an immersed heating surface. Particles act as heat carriers between the bulk of the bed and the surface of an immersed heater. The solid activity is generated either by mechanical vibrations alone, or by the combined effect of vibrations and gas currents induced within the bed. In general, higher gas-percolation rates lead to an improvement in the solid activity and to an increase in the bed porosity because drag forces on the particles become more significant.

The formation of regions of high porosity or gas gaps between the base plate of the vibrating vessel and the bed of particles has been reported since the pioneering work of Bachman[4] and Kroll[5-6]. The negative effects of air layers between a heating surface and a moving stream of particles is well-known. Air gaps around cylindrical heating surfaces placed horizontally within a *non-aerated* vibrated bed have either not been studied, or simply not been reported. Malhortra and

Mujumdar[37] described the existence of air gaps on the top and at the bottom of horizontal, cylindrical heating surfaces immersed in *aerated vibrated beds.*

In this chapter, experimental results concerning several aspects of shallow vibro-bed dynamics are reported. These results include:

(i) Configurations assumed by the surface of vibrated beds.

(ii) Solid-circulation patterns within the bulk of the bed and around a horizontal, cylindrical surface immersed into the bed.

(iii) Formation of air gaps at the vessel floor and the surface of a dummy probe immersed in the bed.

(iv) Magnitude of pressure oscillations at different locations on the floor of the vibrating vessel.

It is intended to establish general patterns of shallow-vibro-bed behavior in terms of particle properties and vibrational conditions. The relationship between the observed phenomena and the forces present in vibro-beds is discussed. The Chapter ends with a summary of relevant conclusions, and suggestions for further research.

4.2 Experimental Apparatus and Conditions

Table 4 on page 128 lists the types of solids used as bed materials in the present investigation. These solids were selected because they cover a wide range of densities. Most of the research was conducted in beds of Master Beads. For comparison, high-density and low-density glass beads were also utilized in experiments.

As will be described in Chapter 5, the utilization of vibro-beds of Norton "Master Beads" resulted in very high heat-transfer coefficients. "Master Beads" contain mainly aluminum oxide, about 86%,, and other constituents including 2-4% silica, 6-8% iron oxide, and 4-5% titania. Its density is 3680 kg/m^3. These particles are easily found on the market, are fairly inexpensive and substantially spherical. Both high body-strengh for impact and high wear-resistance make Master

Table 4 : Experimental conditions for vibro-bed dynamics studies

Item	Condition
A. Average particle diameter, μm	
ASTM mesh -20 + 30	707
-30 + 40	500
-70 + 100	177
-140 + 200	88
B. Particle density, kg/m^3	
Soda-lime silica glass beads[1]	
(Low-density glass)	2500
Master Beads[2]	3680
Barium-titanate glass beads[1]	
(High-density glass)	4490
C. Static-bed height, mm	30
D. Vibrational Conditions	
Frequency, Hertz	25
Vibrational intensity parameter K	2-6

[1] Made by Potter Industries
[2] Made by Alcoa Company

Beads an almost ideal solid for vibro-bed applications. Such characteristics favored Master Beads as the natural selection for the heat-recovery system illustrated in Figure 2 on page 7.

This heat-recovery system consists of a vibrating trough containing a shallow bed of particles. Although the definition of what constitutes a shallow bed is not clear, it was assumed that a bed depth of 30 mm would be appropriate to simulate the bed behavior of the vibrating trough. Therefore, the experimental program was developed with vibro-beds of average static-bed depth of 30 mm.

A single vibrating frequncy of 25 Hertz was used in all experiments. Lower and higher frequencies introduced severe distortions in the vibratory motion of the vibrating system.

The vibrating system is illustrated in Figure 52 on page 130. It has a length of 0.91 m, a width of 0.61 m, a height of 0.51 m and a weight of about 180 kg. Vessels of different geometries could be attached to a vibrating table, which consisted of a massive steel plate and a titanium plate. The purpose of the steel plate was to increase the weight of the table, and thus reduce distortions caused by periodic collisions between the bed and the base plate of the vibrating vessel. It also assures a uniform field of vibrations when the load of particles was not uniformly distributed over the floor of the vessel. Several sets of blue tempered steel leaf-springs were used to connect the vibrating table to a cylindrical steel support. A long, thin drive shaft transmited the vibrations of an electromagnetic vibrator, model VG 100 from Vibration Test Systems, to the vibrating table. The whole system was supported on a cement block, which was separated from the floor of the building through a wooden skid.

The vibrator was connected to a vacuum cooling vent and driven by a sinusoidal signal generated by a Signal Generator and amplified by a 300-Watt Crown Amplifier. Vibrational intensities were determined by measuring the instantaneous acceleration of the vibrating table through the use of an accelerometer attached to the table. The output signal from the accelerometer was displayed on the screen of an oscilloscope.

Vibro-bed dynamics were studied in two different vessel geometries: cyclindrical and rectangular. The rectangular vessel consisted of a two-dimensional vessel with a rectangular cross section. Further details of the vibrating vessels are given in the following sections.

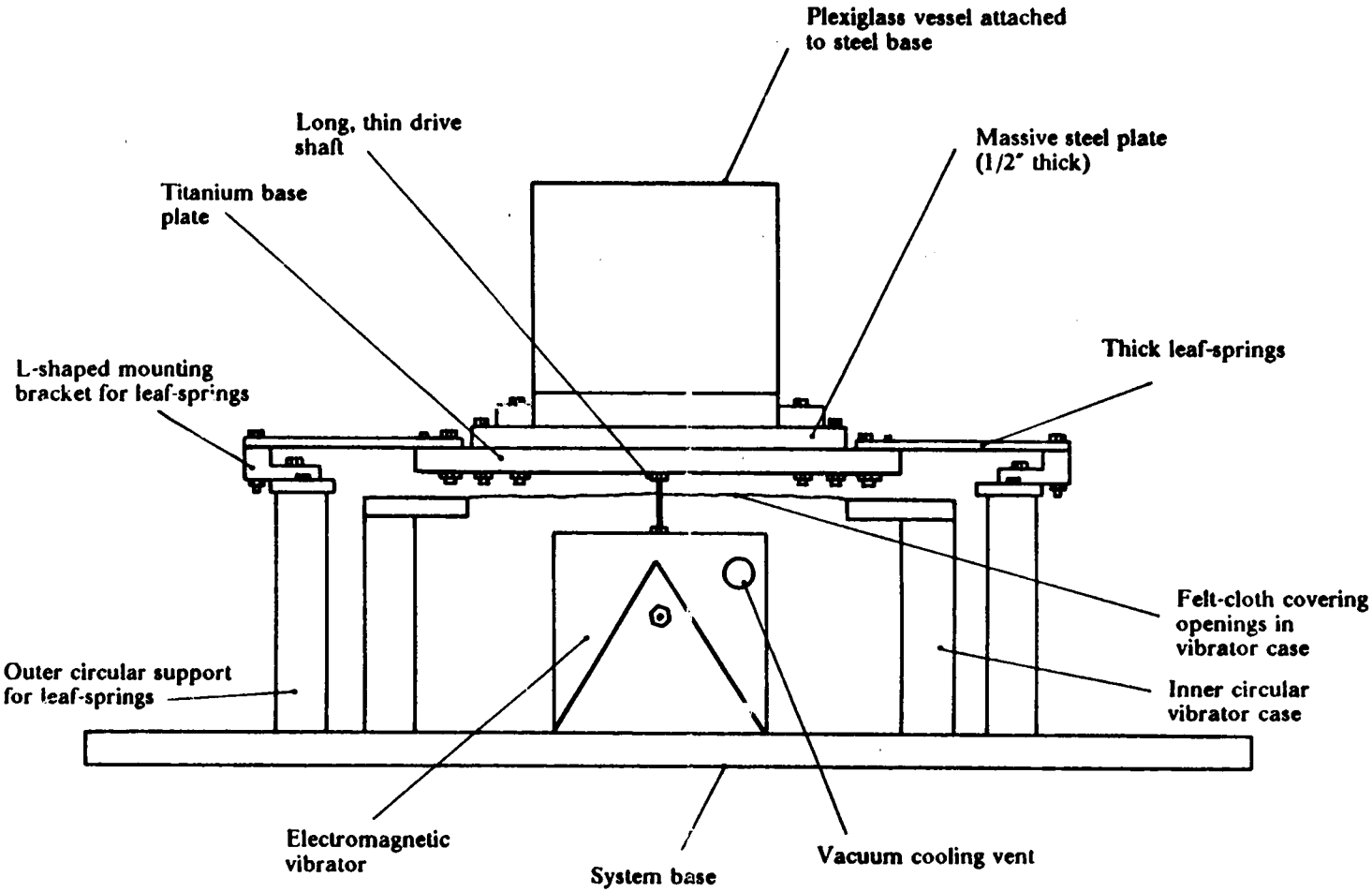

Figure 52. Schematic diagram of a vibrated-bed system: Cylindrical Plexiglass vibrating vessel (Thomas et al.[51]).

4.3 *Dynamics in Cylindrical Vessels*

4.3.1 Experimental procedure

A cylindrical, plexiglass vessel of 170 mm in diameter had a horizontal, 12.7-mm cylindrical heating surface fixed 20 mm above the floor of the vessel. The latter was attached to a vibrating table and filled with Master Beads up to a height of 30 mm. For each size range of particles, the bed was vibrated at different vibrating amplitudes and a constant frequency of 25 Hertz.

The most interesting features of beds of Master Beads vibrated in cylindrical vessels were related to the bed-surface shape and to the flow of solid particles on the surface of the bed and at the walls of the vessel. These features were found to be very dependent on particle size and on the vibrating conditions.

4.3.2 Master Beads of 0.088 mm in diameter

With exception to a slight compaction of the bed of particles, no bed activity was observed for K-values below one. When K exceeded one, the solid actitvity started slowly, and became more intense as K was increased. For similar initial static-bed configurations, it took more time to reach the final vibrated-bed configuration at lower K-values.

Figure 53 on page 132 shows final vibro-bed configurations for Master Beads (-140+200 mesh), corresponding to a geometrically average particle diameter of 88 μm. In the figure, arrows indicate direction of solid flow on the surface of the bed and circular parts represent a top view of the bed. Either the symmetrical or the wall-piling configuration could be obtained at a parallel or normal orientation with respect to the cylindrical heating surface. Thus, in case of the wall-piling configuration, the solid flow on the surface could be parallel to the heating surface or normal to the

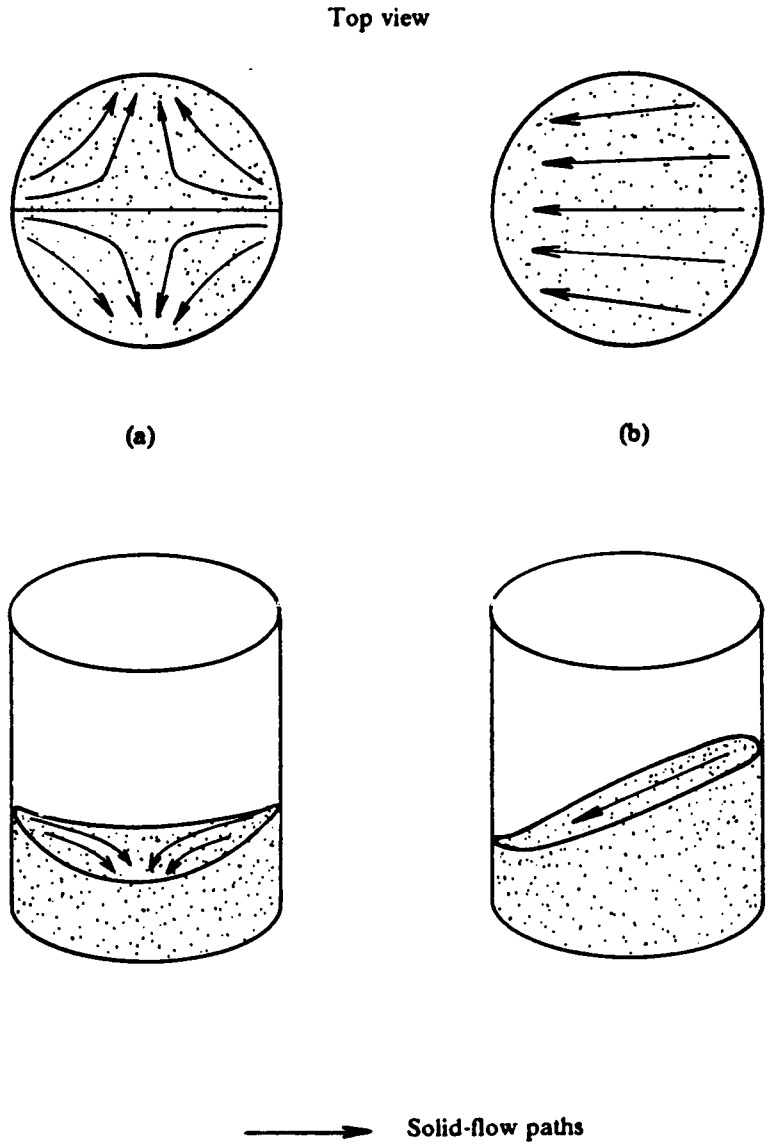

Figure 53. Vibro-bed configurations of 88-μm Master Beads: Cylindrical vessel vibrated at a frequency of 25 Hertz. Notation: (a) Symmetrical configuration; (b) Wall-piling configuration.

heating surface. The symmetrical configuration resembled a mixed-flow pattern. Since the bed configurations were stable, the solid flow in the opposite direction should exist within the bulk of the bed.

All vibrated-bed configurations presented an irregular surface shape as a consequence of the non-uniform distribution of particles over the base plate of the vibrating vessel. The tendency to form deeper and shallower regions of particles within the vessel was observed immediately after the vibrations had been applied. Vibrated beds with flat horizontal surfaces could not be obtained.

Under most vibrational conditions investigated, the initial static-bed structure proved to be a critical factor in defining the final vibrated-bed configuration. Starting with a horizontal static-bed surface, seldom could the final shape of the vibrated bed-surface be predicted. Any of the final configurations shown in Figure 53 on page 132 could be obtained by making little holes on the surface of a static bed. When applying vibrations, the shallowest part of the bed would develop at the location of the hole. Similarly, solid piles could be moved around the vibrated bed to obtain any of those configurations.

The effect of vibrational conditions on bed configurations was more pronounced at high K-values. The symmetrical configuration in Figure 53 on page 132 became unstable for K greater than 4. At K-values above 5, final stable configurations could no longer be mantained. The flow of solids on the surface of the bed was always directed from the deepest part toward the shallowest part of the bed.

The appearance of the surface of the vibro-bed and the solid velocity were dependent on the acceleration of the vibrating vessel. The solid flow rate seemed to increase continuously as K was increased. The flow of particles was very low at K-values up to two. Between K-values of 2 to 3, a remarkable bed expansion took place with an increase in the surface solid-flow. The appearance of the bed surface was very smooth for K-values up to four, after which a major change was observed. The surface became very active, resembling a spouting bed at $K = 5$ and above.

Observations of the solid behavior at the vessel walls showed that the direction of flow of particles was not exclusively down towards the base plate. Although this pattern was determined to exist at shallower regions of the vibrated bed, the wall-flow was observed to be also horizontal

or upwards at other locations. Close to the bed surface, a thin layer of high bed porosity was detected at K-values greater than 3. Inside this layer, the flow was parallel to the surface and directed toward the shallowest parts of the bed. This layer became thicker at increasing K-values.

4.3.3 Master Beads of 0.177 mm in diameter

Beds of Master beads of 177-μm in diameter (-70 + 100 mesh), presented some similarities with the behavior of smaller particles. Final flow configurations for this particle size are shown in parts (a) and (b) of Figure 54 on page 135. The shape of the bed surface was not as curved as that for smaller particles. Although the surface was still inclined, it was flatter, and so only cross-sections normal to the heating surface were illustrated in the diagrams of the figure. In general, configurations with solid-flow patterns parallel to the heating surface were not as stable as the normal patterns.

Configuration (a) was actually a slight variation of the mixed-flow pattern observed in beds of 88-μm particles. Both surface-flow patterns were symmetric in relation to the axis of the horizontal, cylindrical heating surface, and the deepest region of particles was located above the heating surface. But the surface of the deepest region of solids in the bed of smaller particles was not as uniform as that in beds of 177-μm particles. As a result, different solid-flow patterns were generated on the surface of the bed; in contrast to a mixed-flow pattern, the flow was predominantly normal to the heating surface on both halves of the bed of 177-μm particles.

Configuration (b) of Figure 54 on page 135, with the shallowest region located the wall of the vessel differed a little from the corresponding configuration for 88-μm shown in Figure 53 on page 132. In the bed of larger particles, the shallowest region was located at the vessel wall opposite to the pile of solids; while for smaller particles, it was located a little away from the wall.

For 177-μm particles, vibro-beds with flat horizontal surfaces could not be obtained, and the initial static-bed structure was found to be critical in determining the vibro-bed behavior. The di-

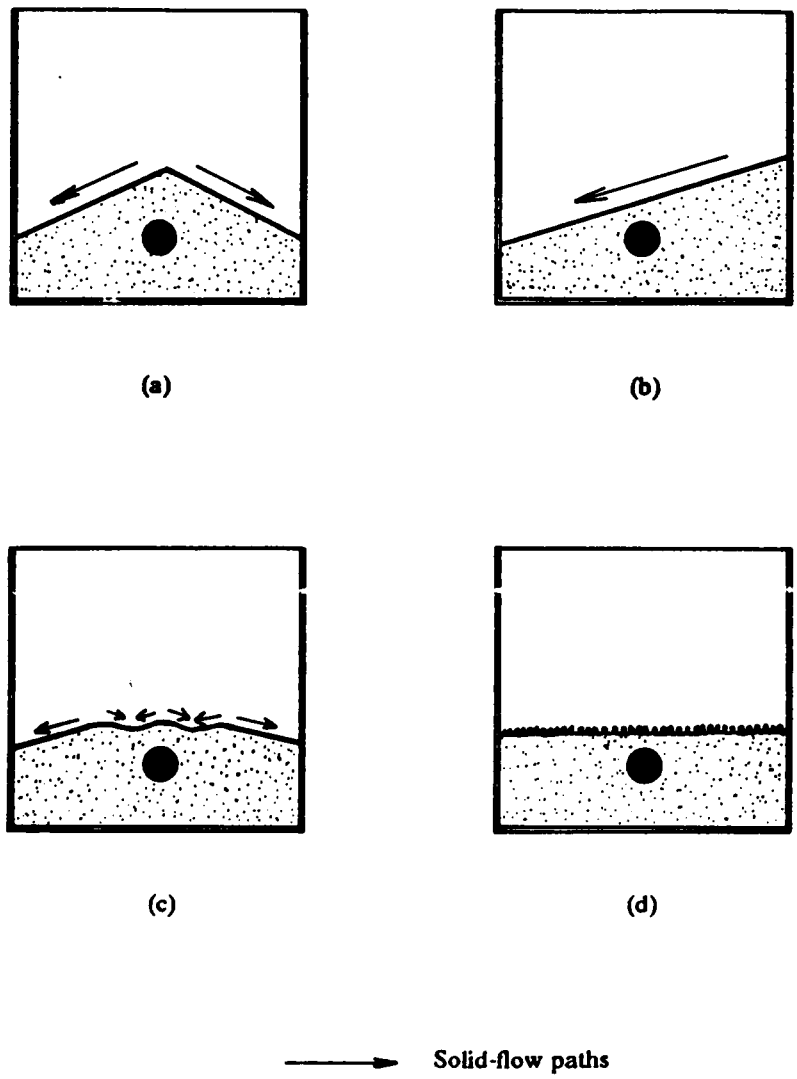

Figure 54. Vibro-bed configurations of 177- and 707-μm Master Beads: Cylindrical vessel vibrated at a frequency of 25 Hertz. Notation: (a) Symmetrical configuration, dp = 177 μm. (b) Wall-piling d_p = 177 μm; (b) Wall-piling configuration, d_p = 177 μm; (c) Configuration for K < 5, d_p = 707 μm; (d) Configuration for K ≥ 5, d_p = 707 μm.

rection of solid flow on the surface was always down-the-hill, and the solid flow near the wall was not solely downward the base plate of the vibrating vessel.

At K-values up to 4, configurations (a) and (b) of Figure 54 on page 135 could be observed initially in vibro-beds of 177-μm particles. Thereafter, the configuration with the solid pile at the wall of the vessel was no longer stable. No matter what was the initial static-bed structure, the final structure at high K-values would tend to the symmetrical configuration shown in diagram (a). In general, the inclination of the surface of the bed was steeper at low values of K, and decreased as K was increased. Both the solid flow and solid activity on the surface became more intense as K was increased.

When the vibrational intensity was increased, two major changes in bed behavior were again noticed. At K-values between 2 and 3, the bed seemed to expand and the solid circulation to increase remarkably. At K-values between 4 and 5, the surface of the bed lost its smoothness, with solid activity getting much more intense. During this second change, a layer of high porosity became very visible at the surface of the bed. This layer seemed less expanded than that observed in beds of Master Beads of 88 μm in diameter.

4.3.4 Master Beads of 0.707 mm in diameter

The behavior of vibro-beds of 707-μm Master Beads (-20+30 mesh), was different from smaller particles, yielding basically just one final bed configuration. As shown in diagrams (c) and (d) of Figure 54 on page 135, the shape of the bed surface was not as irregular as that for smaller Master Beads.

Configuration (c) was observed for lower K-values. This configuration underwent only minor changes when K was increased up to values little above 4; the shallowest regions at the walls of the vessel tended to flatten out. Three little bumps have been observed on the bed surface, with one appearing right above the heating surface, and the other two located each side of the heater, about halfway between heater and vessel wall. These bumps looked like sources of particles being circu-

lated on the surface of the bed, while the shallower regions at vessel walls and between the bumps seemed to function as particle sinks. The solid flow on the vibro-bed surface was again down-the-hill with its origin at the top of the bumps. However, at the wall, the flow of particles was now consistently directed downwards everywhere around the perimeter of the cylindrical vessel.

As shown in diagram (d) of Figure 54 on page 135, the bumps on the surface of the bed were no longer distinguishable at K = 5, and the surface became horizontal. A very large number of particle sources and sinks were apparently distributed all over the bed surface, resembling a spray-like behavior. But no net solid surface-flow appeared to exist in any direction, and the wall-flow seemed to loose its consistent downward character.

At K = 2, the particle activity was very small in the vibrated bed, and solid circulation was barely visible. Increasing K-value did increase the solid circulation both on the bed surface and at the vessel wall. It did also intensify a non-uniform spray of particles observed on the surface of the bed, mainly at the bumps. That spray did not resemble a coherent expanded layer as was observed for smaller particles, even though it covered almost uniformly the whole bed surface at K = 5. Air gaps seemed to form between the vessel-base plate and the bottom of the bed of particles at larger K-values.

4.4 Vibro-bed Dynamics in Two-dimensional Vessels.

4.4.1 Experimental investigation

Figure 55 on page 138 presents a schematic diagram of a rectangular, two-dimensional vessel utilized for the investigation of vibro-bed dynamics. The vessel base and the side walls were made of rectangular aluminum bars, and both the front and the back walls were made of Lexan plates. The rectangular cross-section of the vessel had a length of 162 mm, and a width of 25.4 mm. A

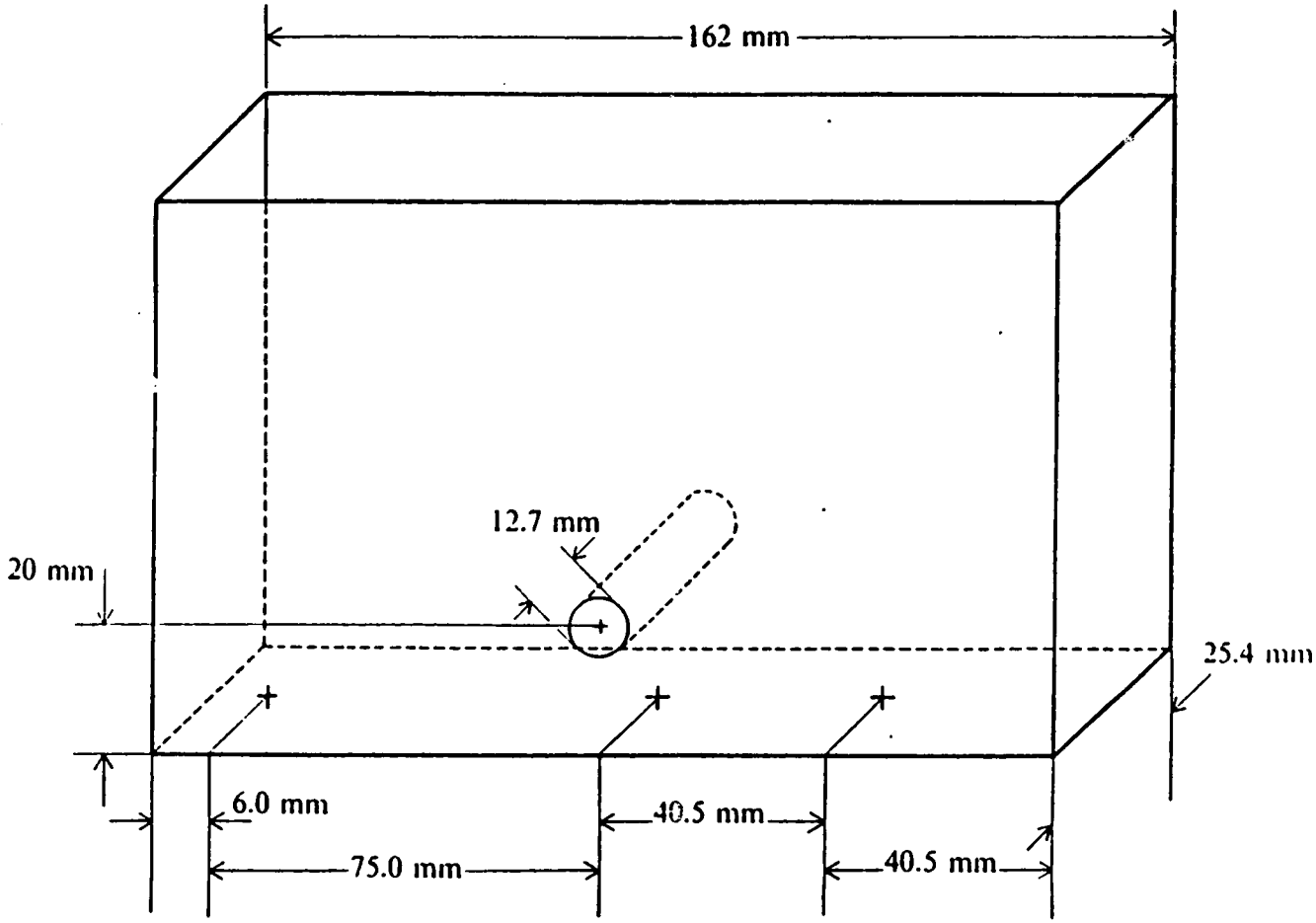

Figure 55. Diagram of a rectangular two-dimensional vibrating vessel: The schematic diagram shows a dummy heat probe and location of pressure transducers (indicated by "+") for measurements of instantaneous floor pressures.

cylindrical aluminum rod of 12.7 mm in diameter was fixed between the Lexan walls, parallel to the floor of the vessel. The distance between the axis of the rod and the floor of the vessel was 20 mm. The three crosses on the floor of the vessel indicate the locations where instantaneous floor-pressure measurements were performed.

This two-dimensional vessel was designed to simulate a slice of the cylindrical vibrating vessel that is normal to the heating surface. The cylindrical aluminum rod acted as a dummy heating surface, or dummy heating probe, and was assumed to affect solid-circulation patterns in approximately the same way that the true heating surface changed flow patterns within the cylindrical vessel. Wall effects might, however, be a little greater than in a cylindrical vessel. Transparent Lexan walls allowed characterization of flow patterns at the walls, observation of bed expansion, and identification of air gaps at the vessel floor and around the dummy heating probe.

A graduated glass cylinder was used to measure the volume of solids that constituted the vibro-bed. To obtain an average static-bed height of 30 mm, the vessel was filled with 125 ml of slightly compacted particles. That volume was kept constant for all particle sizes and types. In a loosened state, the actual bed depth could be a little greater than 30 mm.

Most of the observations concerning vibro-bed dynamics were performed for symmetrical bed-configurations. As shown previously in Figure 53 on page 132 and Figure 54 on page 135, such configurations are characterized by solid "bunkering" above the heating probe. "Bunkering" is an alternate way of expressing the formation of solid piles at a specific bed location. Symmetrical configurations were observed in beds of all particle sizes and types, thus allowing interpretation of the results under similar conditions.

Configurations others than the symmetrical one could only be obtained for beds of particles of 88 and 177 μm in diameter. Figure 56 on page 140 shows comparative diagrams for different bed configurations obtained in beds of those small particles. Solid arrows indicate simplified flow paths observed at the wall of the two-dimensional vessel and on the surface of the bed. Diagram (a) refers to the symmetrical flow configuration. The trapezoidal region below the dummy probe illustrates what might be called a segregated or dead region. The solid circulation within this region, and solid interchange with the rest of the bed were very dependent on particle size and the intensity

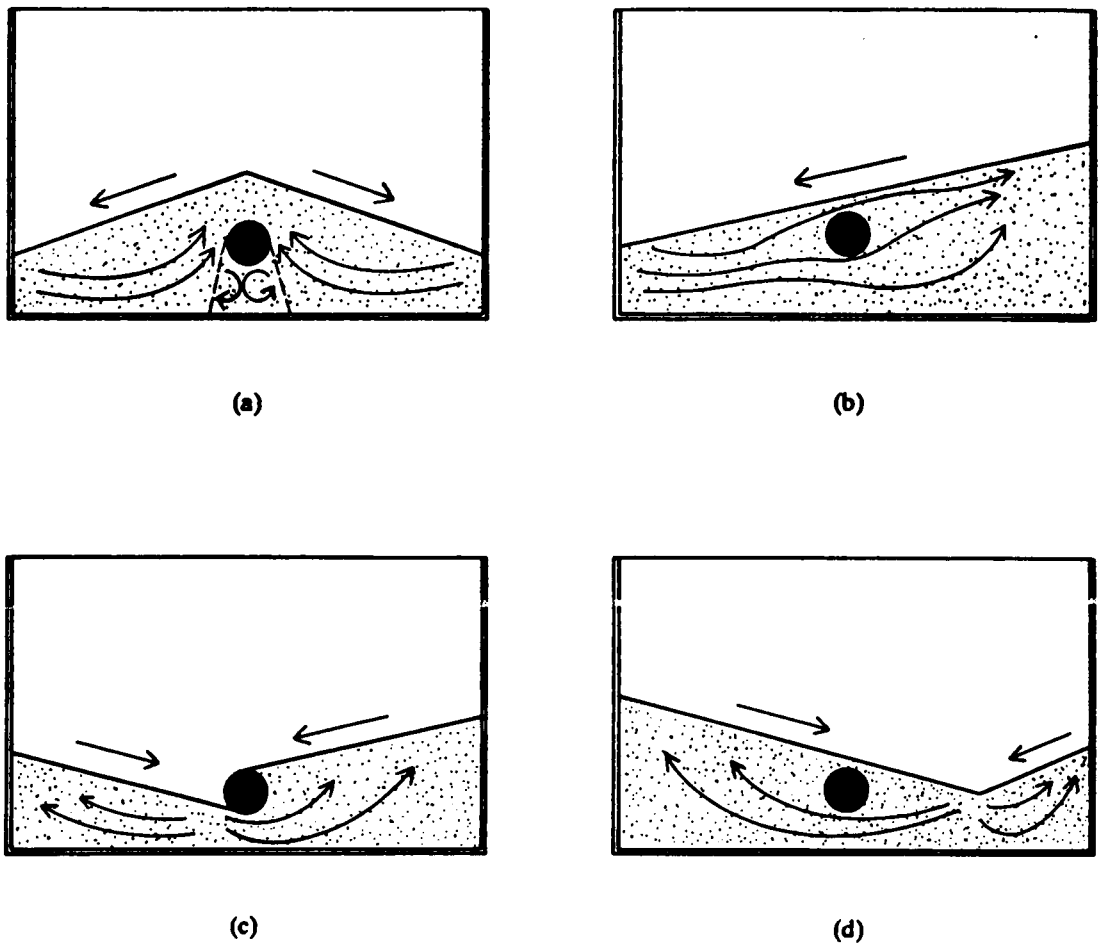

Figure 56. Bed configurations in a two-dimensional vibrating vessel: Layers of 88- and 177-μm Master Beads vibrated at 25 Hertz. Bed configurations: (a) Symmetrical; (b) Shallowest region at a side-wall; (b) Shallowest region at the probe; (d) Shallowest region between the probe and side-wall. Configuration (a) shows a segregated region of particles below the dummy heat probe.

of the vibrations. Such large dead regions were absent from the other bed configurations due to the kind of flow path existing around the dummy probe. From the point of view of heat transfer, the symmetrical configuration can be expected not to yield the best heat transfer coefficients.

All of those bed configurations had, however, some common features. The mean path of the flow of particles within the bulk of the bed was always directed from the shallowest parts of the bed toward the deepest ones, while the back flow in the opposite direction took place within a thin layer of particles near the bed surface. Bunkering was more severe at low K-values, and became less pronounced as K was increased. However, the rate of solid circulation became faster with increasing K-values.

Differences in behavior with respect to the bed stability were noticed at values of K above 4. For smaller 88-μm particles, configurations (c) and (d) were more stable than the symmetrical configuration; for 177-μm particles, the opposite was true.

Configurations of beds of particles vibrated in two-dimensional vessels appeared, therefore, to be very similar to those configurations observed in beds vibrated in cylindrical vessels as illustrated in Figure 53 on page 132 and Figure 54 on page 135. Bed characteristics such as surface shape, bunkering of particles, increased solid activity with stronger vibrating conditions and their dependence on particle size followed the same trends in both types of vibrating vessels. These similarities suggested that solid-circulation patterns determined in two-dimensional vessels would constitute a good approximation to those actually existing in beds contained in cylindrical vessels.

4.4.2 Solid circulation

Solid-circulation patterns were observed in two ways. A small amount of tracer particles colored differently from the rest of the bed was placed within the bed and the movement of the tracers observed visually and/or recorded by a video-camara. This method indicated the circulation paths for solids at the vessel walls and within the bed. It also showed up "segregated zones" or "segregated regions" within the bed, in which there was either little particle circulation or little particle inter-

change with the rest of the bed. The term "segregated region" was used interchangeable with the term "dead region" in this work.

In the second way, solid-circulation patterns were observed by using small rubber "markers". Two markers were used in the observations: one of about 3 mm in diameter, and a second one, of about 1.5 mm in diameter. Both visual observation and video-recording showed that the markers quickly "discovered" a major solid circulation path, and took up "residence" therein. These markers were seen to repeatedly enter the bed at a particular location on the bed surface. They remained out of view for a short period of time, and then appeared again at a second particular location. Finally, the markers slided along the bed surface from the second to the first location, where they re-entered the bed.

4.4.2.1 Effect of vibrational conditions

Diagrams of solid-flow patterns for Master Beads og 177 μm in diameter are shown in Figure 57 on page 143 for several K-values. In these diagrams, solid arrows represent the path followed by the colored particles. Since the configuration of the bed was symmetrical, flow patterns were sketched at only half of the bed. Colored particles placed at the side wall initially traveled on the vessel floor towards the dummy probe, and from locations near the probe up and to the surface of the bed. The back flow on the surface toward the side-walls of the vessel was restricted to a thin surface layer.

Three different flow regions were identified. Below the dummy probe, a segregated region contained two circulation loops. At the bed surface, a thin expanded layer was apparently responsible for all the flow of particles away from the probe. And the third, the bulk region, was spreading over the rest of the bed. The solid activity within each of these regions improved when the vibrational intensity was increased.

At K = 2, a tiny fraction of the colored particles in the bulk region shown in Figure 57 on page 143 was continuously diverted into the circulation loops. The rate of interchange of particles

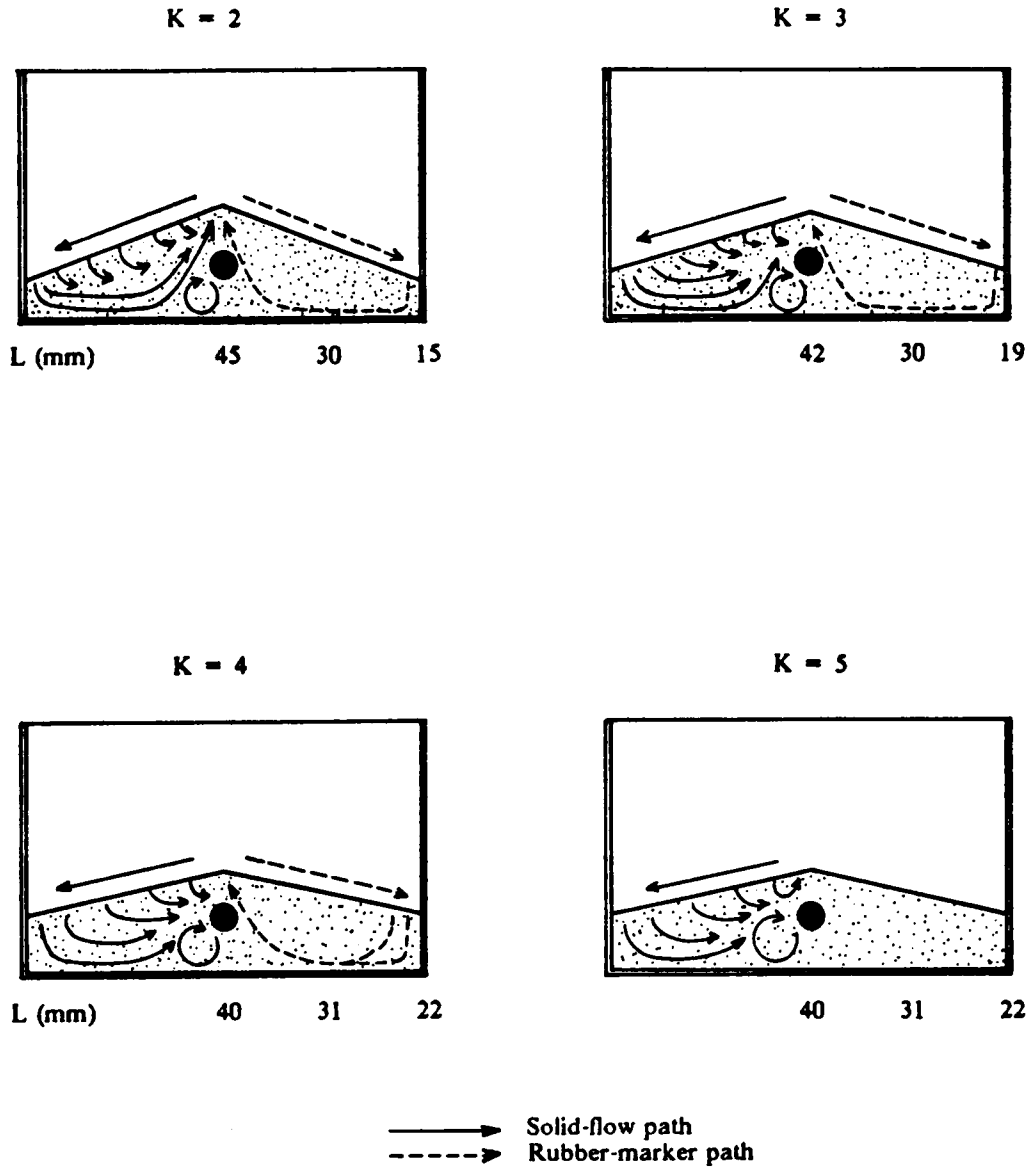

Figure 57. Effect of the K-value on solid-circulation patterns in vibro-beds: Layer of 117-μm Master Beads vibrated at a frequency of 25 Hertz in a two-dimensional vessel. Notation: K = vibrational intensity parameter; L = bed depth.

between the bulk region and the circulation loops seemed to be very small. As K was increased, the solid flow in each of the regions became faster, and so also the rate of interchange of particles between the bulk region and the circulation loops. Thus, the renewal rate of particles in the loops improved, but the particles entrained by the bulk flow were apparently not immeadiately carried away from the probe. Instead, they seemed to remain in contact with the probe while the bulk stream was moving upwards to the surface of the bed.

The solid velocity within the thin surface layer was the fastest among the velocities in the three regions. As illustrated in Figure 7 on page 20, particles moving on the bed surface toward the side walls of the vessel were entrained along their way by the bulk region. This entrainment became stronger as K was increased, and its path was always directed towards the heating probe. Such effect would eventually equalize the concentration of colored particles in the bed half in which the particles had been introduced; the process was slower at low vibrational intensities than at high intensities. The solid mixing between bed halves was very poor.

Particle velocities within the bulk region were not uniform. The vertical velocity near the side walls of the vessel was very high. The velocity of particles following any specific flow path continuously decreased along the path. In general, the velocity became smaller from the base plate toward the bed surface, and from the vessel side-wall toward the heating probe.

Figure 57 on page 143 shows that the surface of the bed initially became less inclined as K was increased. A strong tendency to form circulation loops above the heating probe was noticed. These loops were clearly identified at K = 5. Loops below the probe became larger, and did extend deeper into the bulk region. Fresh particles were continuously fed into the loops above and below the probe; but the renewal rates in the upper loops were apparently faster due to the back flow of particles within the thin surface layer. At K = 3.5, tracer particles placed near the vessel side-wall took about 26 seconds to reach the bed surface above the heating probe. At K = 4, this time was reduced to only 6 seconds. However, the particle homogeneity was still reached faster in the bulk region than within local loops below the dummy probe.

Dashed arrows in Figure 57 on page 143 indicate the path of the rubber markers introduced into the bed. Small sections of the markers could be identified "floating" in the lower boundary of

the vibrated bed towards the heating probe during the fraction of time that the air gap between the base plate and the bed was open. Other times, the marker followed a path close to the Lexan walls; it would sink at the side walls of the vessel, move horizontally along the base plate, and then slide close to the heating probe toward the surface of the bed. This behavior was very consistent at lower K-values, but would become random at K-values above 4.

Table 5 on page 146 presents the measured periods of time that the markers of 1.5 and 3 mm in diameter stayed out of sight within the bulk of the bed. They were observed to disappear close to the side wall of the vessel, and reappear later on the bed surface above the dummy probe. The period of time decreased from about 63 seconds at K = 2 to about 16 seconds at K = 3. The values for both the small marker and the large one were virtually identical. At K = 4, not only were the values different, but the markers also did not disappear regularly at the same locations as those for smaller K-values. This irregular pattern was particularly noticeable for the 1.5-mm marker, which would seldom slide back to the side-wall of the vessel after reappearing on the surface of the bed. On its way down the bed-surface, the small marker could disappear into the bed at any surface position. Sometimes, the marker did reappear on the surface at an location other than the top of the solid pile accumulated above the probe. The frequency of disappearance and reappearance of the smaller marker could not be measured. The pattern followed by the larger rubber marker was more consistent with respect to its reappearance on the top of the pile, but the marker could sometimes be entrained by the bed at a location a little away from the vessel side-wall, as illustrated in Figure 57 on page 143. It stayed out of sight longer than the smaller marker, about 7 seconds. This behavior was attributed to the larger mass and size of the 3-mm marker, making it less susceptible to changes in flow direction. At values of K above 4, it was no longer possible to follow the circulation patterns of any of the markers.

These observations clearly demonstrated that the solid circulation increased rapidly with increasing values of the vibrational intensity parameter K. Colored particles seemed to follow a well-ordered flow-circulation pattern with little interaction between neighboring streams of particles. The same was true for the rubber markers at low K-values. At higher K-values, the behavior of the markers suggested a sensible degree of intermixing between different streams of particles.

Table 5 : Estimated solid-circulation times in vibro-beds between the vibrating vessel side-wall and the dummy probe.

Particle size and type	Estimated circulation times, seconds			
	K = 2.0	K = 2.5	K = 3.0	K = 4.0
d_p = 88 μm				
Master Beads		69 ± 2	40 ± 1	11 ± 1
d_p = 177 μm				
Low-density glass beads	95 ± 5	37 ± 2	17 ± 2	11 ± 1
Master Beads	63 ± 2	26 ± 1	16 ± 1	7 ± 2
High-density glass beads	110 ± 5	31 ± 1	21 ± 2	15 ± 4
d_p = 500 μm				
Master Beads		25 ± 1		5 ± 1

4.4.2.2 Effect of particle size

88-μm Master Beads: As shown in Figure 58 on page 148, a small change in the shape of the bed surface was observed for Master Beads of 88 μm in diameter. In addition to a notable particle bunkering at the center of the bed, the bed also showed a weaker bunkering effect at both side walls of the vibrating vessel. As a consequence, the shallowest regions of the bed were displaced a little away from the side walls. The particle activity in the solid piles at the walls was very low. In the rest of the bed, regions of flow similar to those shown in Figure 57 on page 143 for 177-μm particles were detected. At K = 5, the symmetrical bed configuration became unstable, and major bunkering occurred at one of the side walls.

Very little solid activity was noticed within a trapezoidal region below the probe, even at K = 4. Two local circulation loops were present, but their circulation speeds and rates of solid interchange with the bulk region could virtually be neglected. The solid activity was practically restricted to the bulk region and to a thin layer of high porosity near the bed surface. Within these regions, the solid flow did increase when vibrations were intensified.

Although some solid activity existed at K = 2 for small 88-μm Master Beads, only higher vibrational intensities were explored. As seen in Figure 58 on page 148, colored particles showed that the solid flow was highly non-uniform over the depth of the bed. In contrast to the pattern observed for 177-μm particles, Figure 57 on page 143, little solid entrainment from the thin surface layer to the bulk region occurred during the down-the-hill flow of particles on the bed surface. Particles were primarily dragged into the bed at the shallowest zone, and they followed along the floor toward the dummy probe, and then would be carried toward the surface and back to the shallowest part of the bed again. In the bulk of the bed between the surface layer and a flowing layer near the vessel base, the velocity of the stream of particles was low.

Experiments conducted with rubber markers showed that the periods of time in which the markers stayed out of view within the bed was lower than those discussed in the preceding section for 177-μm particles. As shown in Table 5 on page 146, this period of time was about 69 seconds

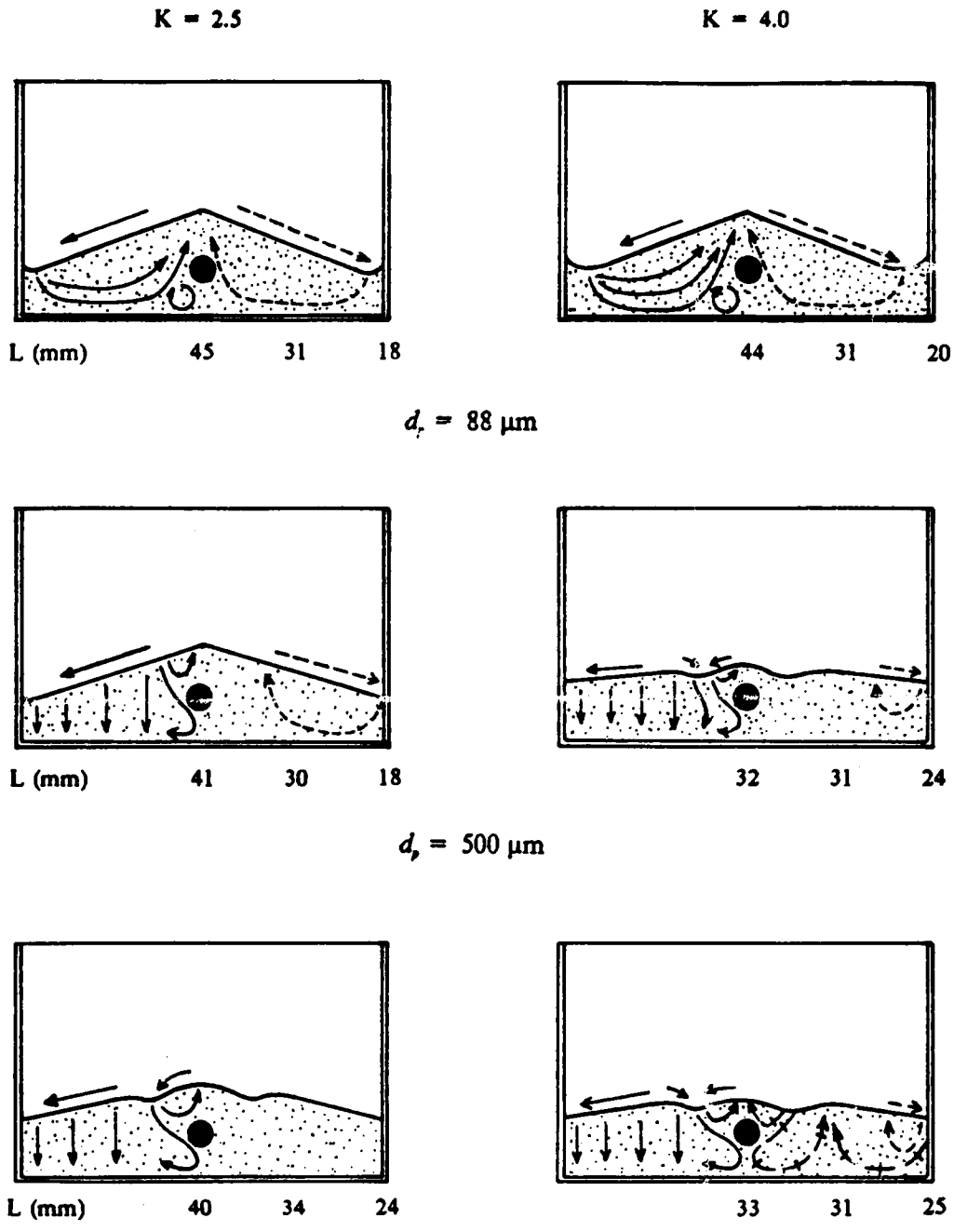

Figure 58. Effect of the particle size on solid-flow patterns in vibro-beds: Layers of Master Beads vibrated at a frequency of 25 Hertz in a two-dimensional vessel. Notation: K = vibrational intensity parameter; d_p = particle diameter; L = bed depth.

at K = 2.5. It was reduced to about 11 seconds at K = 4. Thus, besides the heterogeneous character of the flow pattern, circulation in beds of 88-μm Master Beads was less intense than that for 177-μm particles at the same symmetrical bed configuration.

Figure 58 on page 148 reveals that no tendency to the formation of circulation loops above the heating probe at K = 4. Instead, both rubber markers and colored particles were noticed to reappear on the bed surface over a small region around the top of the solid pile, and not just at the top of the pile. Particle streams did not converge towards the heating probe as illustrated in Figure 57 on page 143 for the 177-μm particles. The upstream of particles near the probe was spreading deeper into the bulk of the bed.

500- and 707-μm Master Beads: Figure 58 on page 148 illustrates that major changes in solid-circulation patterns occurred at the Lexan walls of the vibrating vessel and in the bulk of the vibrated bed when Master Beads of diameter larger than 177 μm were utilized as the bed material, For Master Beads of 500 μm and 707 μm in diameter, solid-circulation paths developed at the lexane walls of the vessel were, in general, no longer representative of the circulation paths followed by particles in the bulk of the bed. Except for the region near the dummy heating probe, circulation paths at the Lexan wall were preferentially directed vertically from the bed surface toward the base plate of the vessel. In the bulk of the bed, the flow patterns could not be determined accurately.

As shown in Figure 58 on page 148, the shape of the bed surface went through some kind of transition and depended on the vibrational conditions, as the particle size was increased. For beds of 500-μm Master Beads, the shape of the surface at lower K-values was identical to the one observed for 177-μm particles. Strong bunkering occurred above the heating probe, and the shallowest regions developed at the side-walls of the vessel. When K was increased to 4, however, the surface showed a tendency to become horizontal, and three little bumps appeared at locations near the center of the bed. One was located exactly above the dummy probe, and the other two were developed near the bump above the probe, one on each side. This configuration persisted up to K-values slightly above 5. At K = 6, the bed surface became horizontal, a very intense solid activity evolved within the bed and on its surface, and the bumps could no longer be localized. This ex-

treme behavior was also observed in beds of 707-μm particles, but it set in at a K-value of K = 5. At K-values below 5, all bed configurations of 707-μm particles showed three characteristic bumps on the bed surface.

Small amounts of colored particles placed at one of the side-walls of the two-dimensional vessel disappeared within the bulk of the bed, and later reappeared on the surface of the bed. In beds of 500-μm Master Beads vibrated at K = 2.5, colored particles reappeared on the bed surface at a location about halfway between the side-wall and the heating probe after staying approximately 16 seconds in the bulk of the bed. Some of the particles would then flow downward the lexane walls, while the remaining particles would slide on the surface back to the side wall. Particles were observed to appear on the bed surface at the top of the solid pile above the probe 37 seconds after they had been placed at the side-wall of the vessel. Solid-circulation paths in the bulk of the bed were, therefore, not the same as those at the walls of the vessel that are illustrated in Figure 58 on page 148.

As K was increased to 4, colored particles placed at the side wall of the vibrating vessel did not flow toward the dummy probe as fast as at K = 2.5. It took some minutes until colored particles were first observed on the bed surface at the bump near the dummy probe. The bed region below this bump seemed to offer a large resistance to particle transfer toward the probe. As shown in Figure 58 on page 148, solid-flow paths at the vessel wall close to the probe also displayed a pattern different from that in the remaining of the bed. The vertical paths became curved.

Figure 58 on page 148 also shows that rubber markers placed at the side wall of the vessel were never observed to follow any path that led to the bed surface above the dummy probe. The circulation paths of markers were restricted to regions close to the side walls of the vessel. Therefore, the circulation times reported in Table 5 on page 146 are not representative of solid interchange between the bulk of the bed and the surface of the dummy probe. When the markers were placed on the bed surface above the probe, they were observed to be entrained by solid-circulation loops existing above the probe and to stay therein.

As shown in Figure 58 on page 148, solid-circulation patterns in beds of 707-μm Master Beads were very similar to those for 500-μm particles. Solid circulation in the horizontal direction was,

however, less intense in the beds of 707-μm Master Beads. At K = 5, the bed surface displayed a spray-like nature and solid-flow patterns at the vessel walls became random in character. The solid mixing within the bed resembled a random turbulent type of mixing.

The experimental observations in beds of 500- and 707-μm Master Beads suggest that solid-flow patterns in the bulk of these beds can be represented as sketched in Figure 58 on page 148 at the right half of the diagram relative to 707-μm particles vibrated at K = 4. In this case, the particle flow can be considered partially ordered within each circulation loop, but random mixing is required to interchange particles at boundaries of the loops.

4.4.2.3 Effect of particle density.

Bed configurations and solid-flow patterns for three different types of particles are presented in Figure 59 on page 152. Low-density glass spheres, Master Beads, and high-density glass spheres of the same size, 177 μm in diameter, were utilized in the observations. As shown in Table 4 on page 128, Master Beads have an intermediate density between low-density and high-density glass beads. Symmetrical bed configurations for low-density glass spheres and for Master Beads were stable over the investigated range of vibrating conditions. For high-density glass spheres, however, that configuration became unstable at K = 5. The bunkering of particles took place at both side-walls of the vibrating vessel, and the shallowest part of the bed was displaced toward the dummy probe location.

The bunkering was more severe for the low-density glass beads, and decreased as the density of the particles increased. It was also more severe at low K-values than at high values. The intensity of particle bunkering could not be directly related to the intensity of solid circulation within the bed.

The solid-circulation patterns observed at the vessel walls were affected by the solid density. At K = 2, the circulation for low-density glass beads started primarily at the side-walls of the two-dimensional vessel, and moved toward the dummy probe and then upward to the bed surface.

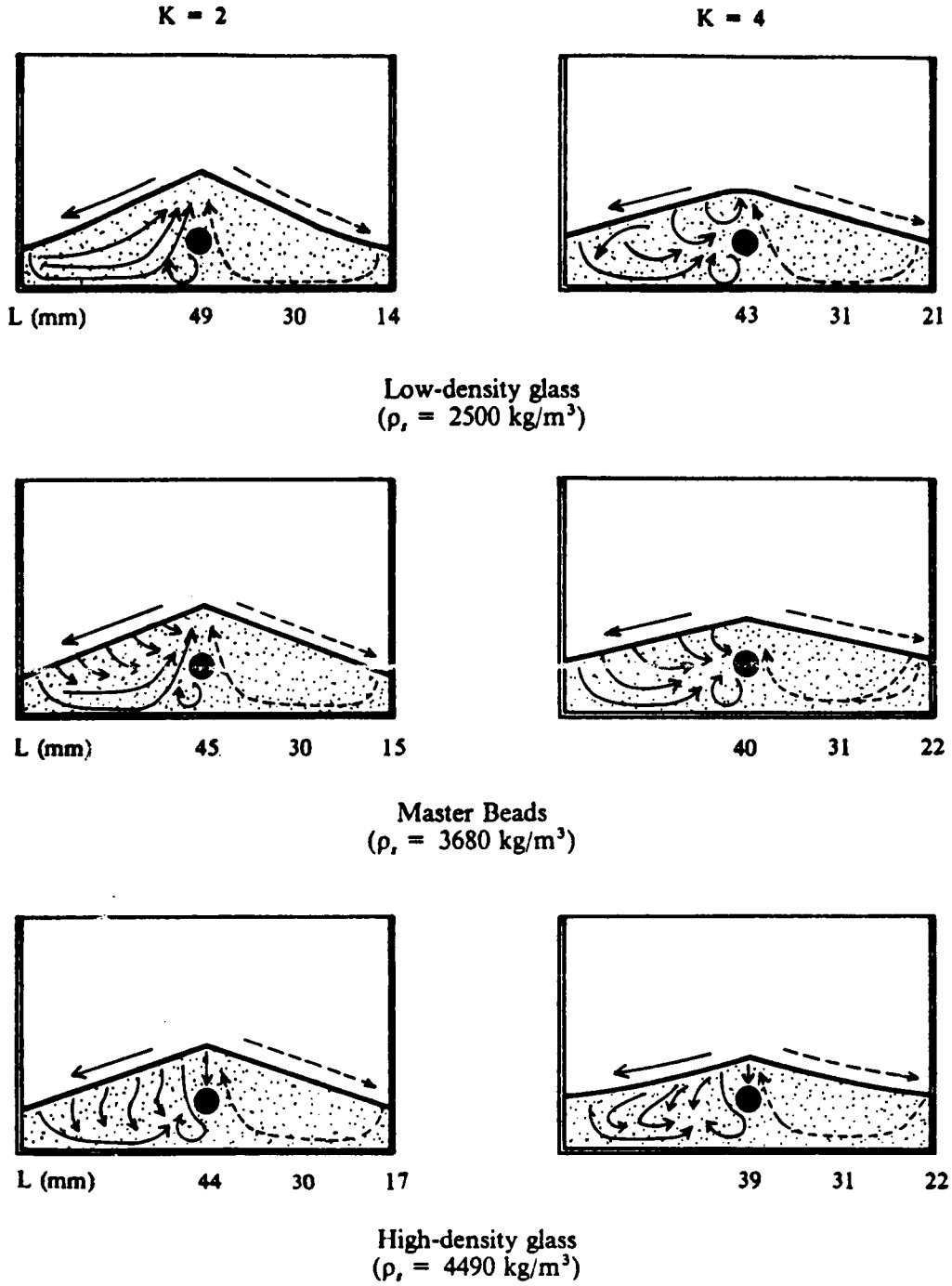

Figure 59. Effect of the particle density on solid circulation in vibro-beds: Layer of 177-μm particles vibrated at a frequency of 25 Hertz in a two-dimensional vessel. Notation: K = vibrational intensity parameter; L = bed depth; ρ_S = solid density.

The velocity of the streams was higher near the base plate, and decreased vertically toward the bed surface. As illustrated in Figure 59 on page 152, the origin of solid streams in beds of Master Beads was distributed over the bed surface, but streams initially existing near side walls were faster than those at other surface locations. The velocity of each stream decreased along its path toward the probe.

The solid velocity within circulation loops detected below the dummy probe seemed to be lower for the low-density beads. Wall-flow patterns in beds of high-density glass spheres showed a high degree of vertical particle displacement, except in the region near the base plate where the flow was clearly in the horizontal direction. For these high-density particles, the direction of solid streams near the dummy probe was downward. On the bed surface, for all types of solids, particles were observed to slide down the surface from the top of the solid pile toward the side wall.

Periods of time that rubber markers stayed out of sight within the bulk of the bed are presented in Table 5 on page 146. The results indicated that markers in beds of Master Beads found their way toward the dummy probe faster than markers in beds of either low-density or high-density glass beads. With exception to K = 2.5, the circulation speed of markers was higher in beds of low-density glass spheres than in beds of high-density glass spheres.

Solid-circulation patterns within the bulk of the bed seemed to be identical to those observed at the Lexan wall, with exception to those in beds of high-density glass particles. For these particles, rubber markers clearly indicated an upward path of particles near the dummy probe despite the opposite direction observed in the wall pattern.

Effects of utilizing particles of higher density in vibrated beds were observed to be similar to those of increasing the size of the bed material. In light of Geldart's powder classification[39], which was originally derived for gas-fluidized beds as discussed in Chapter 3, such similarities were likely to be expected. According to this classification, bed expansion and drag forces excerted by the gas on the bed material decrease as either the particle size or density is increased. When either reducing the particle size or increasing the particle density in vibro-beds under identical bed configurations and vibrational conditions, it was determined that there were optimal size and density for which particle circulation was most intense.

The observation that solid circulation was less intense when substituting high-density glass beads for Master Beads does not imply that heat-transfer performance is deteriorated in beds of high-density glass particles. Since the density of these particles is higher, their thermal capacity $\rho_s C_{ps}$ might offset any reduction in particle renewal rates at the heating surface, thus resulting in higher heat-transfer coefficents than for Master Beads.

4.4.2.4 Renewal of particles at the heating surface

The determination of the renewal time of particles near the heating surface was not feasible with the current experimental system. In fact, renewal times were observed to be dependent on which location on the heating probe was considered. For all particle sizes, particle-renewal rates were apparently higher at the lateral surfaces of the cylindrical dummy probe. The particle-renewal rate at the top of the probe relative to the one at the bottom of the probe seemed to be dependent on the particle size and vibrational conditions. The formation of circulation loops at those locations limited the renewal of particles. Despite the fact that under some conditions, the loops presented great rotational velocities, particles within the loops would return to the surface of the probe before being mixed with the bulk of the bed. For these reasons, the determination of particle velocities around the heating surface may not give a reliable quantification of the renewal rate of particles at the heating surface.

For the same reasons, the determination of the time that particles spent out of sight within the bulk of the bed, as reported in Table 5 on page 146, cannot be considered a measure of the renewal time. At the best, it represented a measure of the degree of solid interchange between the probe surface and the bulk of the bed.

The results obtained so far show only that at identical vibrational conditions, the particle-renewal rate first increases as the particle size is reduced, goes through a maximum for 177-μm Master Beads, and then decreases. For 177-μm particles, either increasing or decreasing the particle density results in smaller renewal rates than those in beds of Master Beads. The experimental ob-

servations also suggest that particle renewal is performed by ordered streams of particles at low K-values, but that at sufficintly K-values intermixing between streams and random turbulent mixing become important.

4.4.3 Air gaps

4.4.3.1 Experimental procedure

The previous discussion considered the solid circulation in vibro-beds primarily as a stedy-state phenomenon. In reality, the particle dynamics is the net result of cyclic transient phenomena taking place over repeating vibrational cycles. When placing a normal light bulb behind the two-dimensional vessel and iluminating the vibrating bed, permanent air gaps were observed at the vessel floor and at the top and bottom of the dummy probe.

Observations of the dynamical behavior of air gaps in vibro-bed were performed by placing a stroboscopic light behind the two-dimensional vessel. By darkening the room and by setting the flashing frequency of the stroboscope a little below the vibrational frequency of the vessel, the instantaneous development of air gaps could be observed. Since the strobe light flashed once during each vibrational cycle at increasingly larger phase angles from cycle to cycle, the characteristics of bed and vessel dynamics could be followed in slow motion. The procedure permitted the observation of the development of air gaps as well as the identification of the approximate vessel location in the vibrational cycle relative to air-gap formation.

4.4.3.2 Formation of air gaps

A schematic representation of the development of air gaps in a vibro-bed of 177-μm Master Beads is shown in Figure 60 on page 156. Each diagram in this figure refers to an approximate

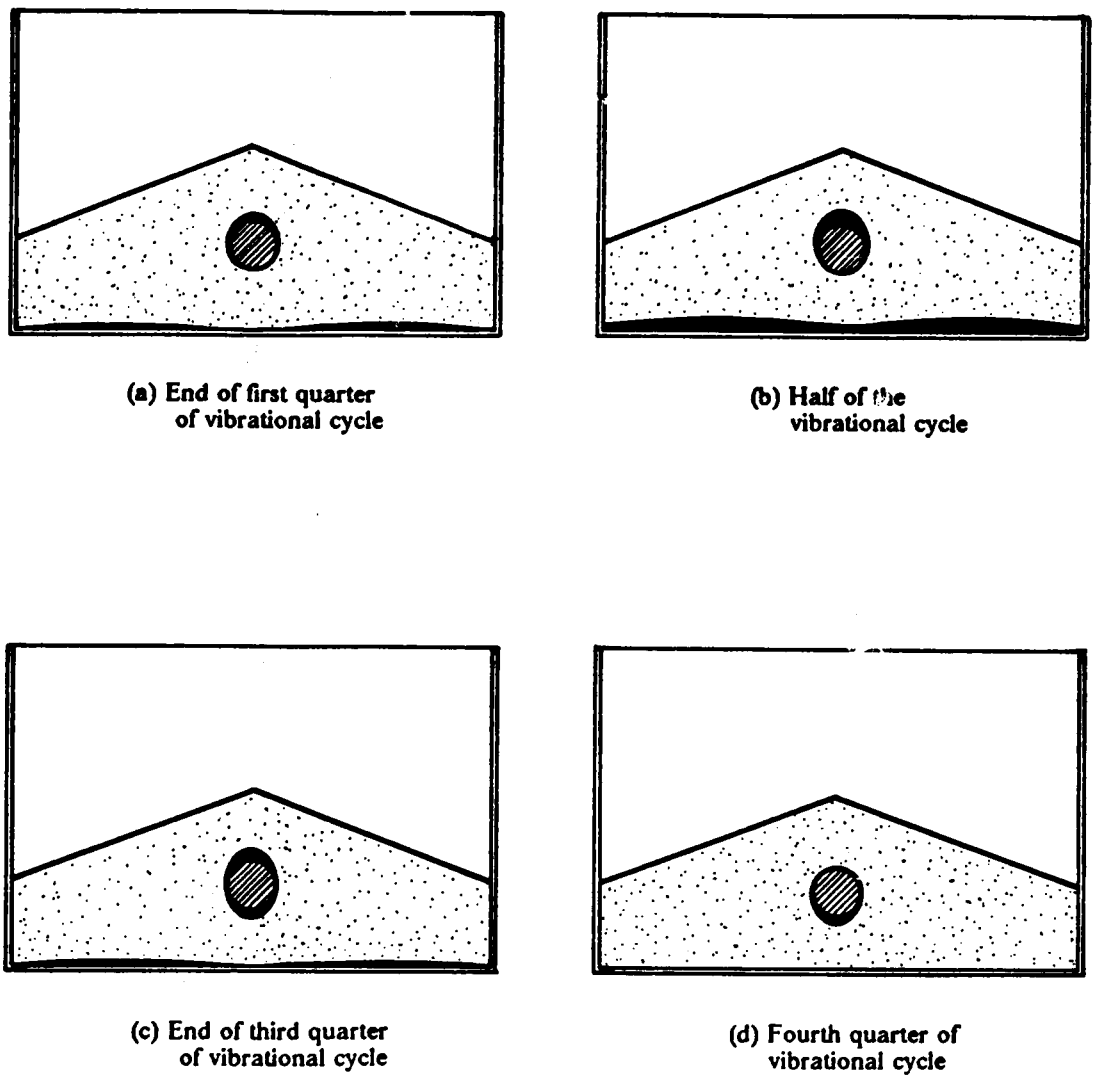

(a) End of first quarter of vibrational cycle

(b) Half of the vibrational cycle

(c) End of third quarter of vibrational cycle

(d) Fourth quarter of vibrational cycle

Figure 60. Air-gap formation in a vibro-bed of 177-μm Master Beads: Layer of particles vibrated at a frequency of 25 Hertz and K = 4. Air gaps are represented by the dark regions at the vessel floor and the dummy probe.

position of two-dimensional vessel within the vibrational cycle. The dark regions at the vessel plate and at the probe represent the observed air gaps. The vessel was vibrated at a frequency of 25 Hertz and K = 4.

The air gaps started to form at the base plate and at the top of the probe at the end of the first quarter of the vibrational cycle. As seen in Figure 60 on page 156, the gap at the base plate did not develop uniformly along the floor of the vibrating vessel. The floor gap was first observed to form halfway between the probe and the side wall of the two-dimensional vessel. As the vessel moved downward, the gaps grew in size and seemed to reach their maximum thickness at a about half of the vibrational cycle. They then started to disappear, and a new gap was forming at the bottom of the probe. Before the end of the third quarter of the cycle, the floor gap had already closed below the probe. The figure shows that only the gap at the bottom of the probe was still existing during the last quarter of the vibrational cycle. This gap would close before the next bed lift-off.

The formation of air gaps in vibrated beds was observed to be dependent on the vibrational intensity parameter K. No gaps were detected in the vibro-bed up to K-values of 2.5. At K = 2.5, tiny air gaps formed at the top and bottom of the dummy probe. Floor gaps were first seen to develop at K = 3. At this K-value, however, the floor gaps formed halfway betweem the probe and the vessel wall only, as illustrated in Figure 60 on page 156 by diagram (a). As K was further increased, the gap thicknesses and the period of time that the gaps remained open became larger.

The formation of the floor gaps is governed by the relative motion between the vessel and the bed of particles. Gaps at the dummy probe develop because of the relative motion beween the particles and dummy probe. At the beginning of a vibrational cycle when the vibrating vessel is moving upward, the deceleration of the vessel and the probe become larger than the deceleration of particles. Both the vessel floor and the upper surface of the probe detach from the bed of particles, and air gaps are formed. Particles below the probe are retarded by the deceleration of the probe and tend to prevent the formation of the floor gap at that location.

When the vessel and probe start their downward motion in the vibrational cycle, the bed of particles is still moving upward and the size of the gaps increases. Particles below the probe are

pressed downward by the motion of the dummy probe. As shown in Figure 30 on page 70, the motion of the probe and vibrating vessel is again decelerated between 180 and 270 degrees. In this part of the vibrational cycle, the deceleration of the probe will eventually become larger than that of particles. As a consequence, an air gap forms at the bottom of the dummy probe.

The relative motion between the probe and particles seemed also to be responsible for the formation of the local circulation loops existing below the probe, as shown in Figure 57 on page 143. When the bed lifts off the base plate of the vessel and the floor gap is formed, particles move upward faster than the vessel and probe. Particles below the probe are retarded by the probe, and may eventually have their motion reversed when the probe moves downward. Since particles away from the probe follow their upward movement, a certain amount of angular momentum will be imparted on the particles at both sides below the probe. This angular momentum creates and sustains the local circulation loops existing below the dummy probe.

4.4.3.3 Effect of particle size

88-μm Master Beads: No air gaps were observed to develop at either the dummy probe or the vessel floor in beds of 88-μm Master Beads up to K-values of 4. The symmetrical flow configuration became unstable at K-values above 4.

The absence of air gaps suggested that the relative motion between the probe and the bed of particles was not as fast as for 177-μm Master Beads. Under this circunstance, less angular momentum would be transmitted to the particles below the dummy probe. Therefore, the particle speed within the local circulation loops should be very small. As discussed in section 4.4.2.2, this trend was verified experimentally.

500- and 707-μm Master Beads

As the particle size was increased, the maximum gap thicknesses and the period of time that the gap remained open increased. Figure 61 on page 159 illustrates the gap developments in a bed

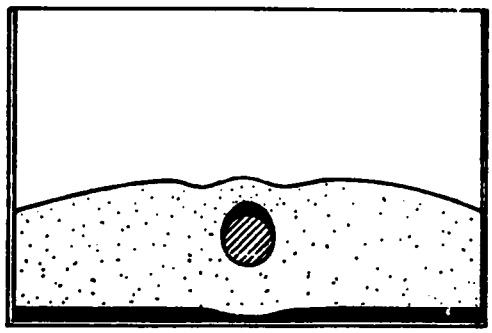

(a) End of first quarter of vibrational cycle

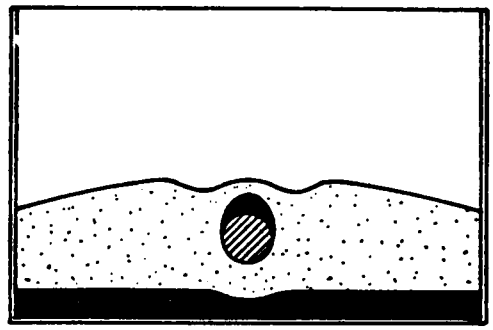

(b) Half of the vibrational cycle

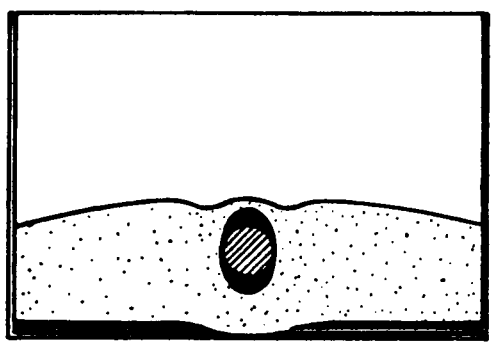

(c) Beginning of fourth quarter of vibrational cycle

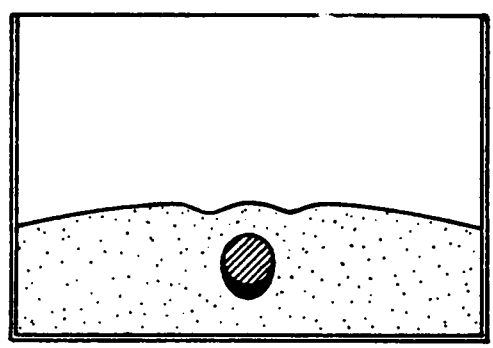

(d) End of vibrational cycle

Figure 61. Air-gap formation in a vibro-bed of 707-μm Master Beads: Layer of particles vibrated at a frequency of 25 Hertz and K = 4. Air gaps are represented be dark regions at the vessel floor and at the dummy probe.

of 707-μm Master Beads vibrated at a frequency of 25 Hertz and K = 4. Each diagram in the figure refers to an approximate vessel position within a vibrational cycle. Air gaps are represented by dark regions at the vessel floor and at the surface of the dummy probe.

As shown in Figure 61 on page 159, the floor gap develops uniformly along the base plate, except for the region below the dummy probe. In this region, the effect of the motion of the probe results in smaller thicknesses and earlier disappearance of the floor gap. Air gaps at the base plate and at the top of the dummy probe develop at smaller and disappear at larger phase angles than those in beds of 177-μm particles. In beds of 707-μm particles, these gaps disappear during the fourth quarter of the vibrational cycle, when the vibrating vessel and probe are again moving upward. The presence of the air gap at the bottom of the probe extends over to the beginning of the next vibrational cycle.

Air gaps at the vessel floor and the top of the probe started to form at K = 2. Their thicknesses increased quickly with increasing K-values. At K = 5, the floor gap below each bed half resembled an overlaping image of two gaps of different thicknesses. During a vibrational cycle, the surface of one bed half was always at a higher position than the other. The two bed halves seemed to be vibrating independently of each other.

As shown in Figure 61 on page 159, air gaps at the vessel base and the top of the probe were observed to disappear during the last quarter of the vibrational cycle. During this quarter, the bed of particles moved downward while the probe was moving upward. This relative motion imparts angular momentum on the particles above the probe, and creates the two local solid-circulation loops as illustrated in Figure 58 on page 148. The circulation loops below the probe shown in this figure are created and sustained during the first half of the vibrational cycle.

4.4.3.4 Effect of particle density

The procedure used for the observation of air gaps was not sufficiently accurate to determine the effect of particle density on the thickness of air gaps and on the period of time that they re-

mained open. The pattern of gap development for 177-μm low-density and high-density glass beads was, however, identical to the one illustrated in Figure 60 on page 156 for 177-μm Master Beads.

4.4.4 Floor pressures.

4.4.4.1 Characteristics of the pressure-measuring system

A pressure-measuring system was built to determine the instantaneous pressure fluctuations at different locations on the floor of the vibrated bed.

Pressure transducers were installed underneath the base plate of the two-dimensional vessel as illustrated in Figure 62 on page 162. The tip of each transducer, which contained the actual pressure sensor, was imbedded into a hole that was drilled into the base plate. Pressure fluctuations at the floor of the vessel were transmitted to the transducer through a small channel, of about 0.8 mm in diameter, connecting the housing of the transducer to the interior of the vessel. The channel and upper part of the housing were loosely packed with steel wool to avoid solids from slipping into the pressure-sensor chamber. The output voltages of transducers were fed to an analog-to-digital converter board, and collected by an IBM PC for further treatment.

Solid-state pressure transducers, model 14PC01 made by Honeywell, were used in the investigation. The transducers had a full range of ± 6.895 kPa, and were driven by a constant-voltage supply of 8 Volts, which also provided a virtual ground to shift the transducers output to ± 2.5 Volts. The typical noise of a pressure transducer was within ± 10 Pascal. The response time was rated as one millisecond. The calibration of the transducers was performed statically by using an oil made by Merriam Instrument. This oil, denoted as Merriam 827, had a specific gravity of 0.827. The results of the calibration showed that the response of the transducers was linear without any hysteresis effect. Zero drifts of a few millivolts per hour were determined under ambient conditions present in the laboratory. Because the collection of each set of pressure data lasted only a fraction

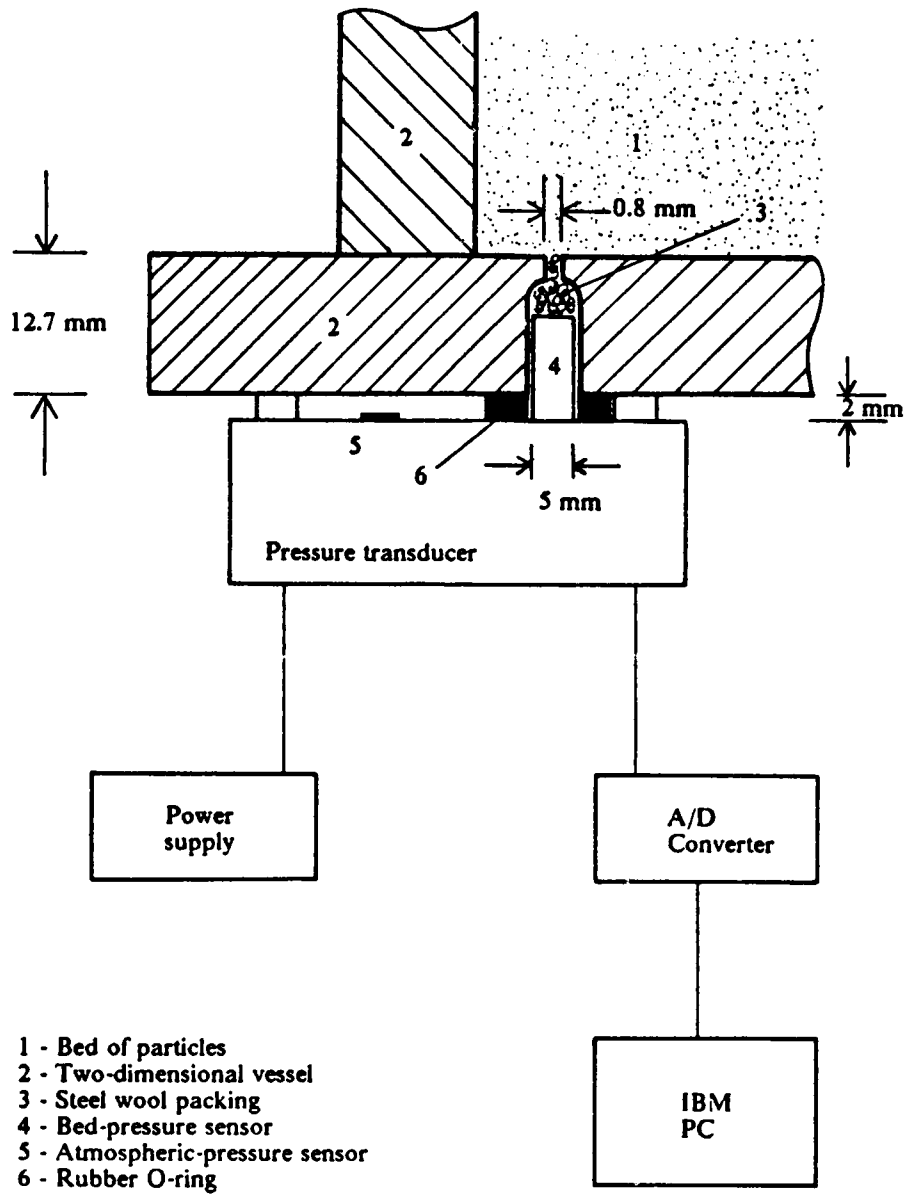

Figure 62. Schematic diagram of a pressure-measuring system: Two-dimensional vibrating vessel.

of a second, such little a variation could be neglected. Any drift existing at the beginning of each sampling period was assumed constant over the whole period, and accounted for during later treatment of the data.

The analog-to-digital (A/D) converter board was designated as model DT2801 made by Data Translation. It could incorportate programmed software, and could collect data at a maximum rate of 13,000 Hertz. The gain for the pre-amplifier was fixed at 8 in order to obtain a resolution of 1.7 Pa in the conversion process. Pressure data at each floor location were collected at a rate of 2,500 Hertz, which was also the collection rate for the instantaneous vibrational acceleration. The total sampling rate of 10,000 Hertz was made possible by using the direct-memory-access feature of the IBM PC. BASIC language was used to program tha computer and the A/D converter board.

As shown in Figure 55 on page 138, the floor pressures were measured at three different locations along the base plate of the two-dimensional vessel. One pressure tap was situated about 6 mm away from one of the side walls of the vessel, a second one being halfway between the side wall and the probe, and the third one being exactly below the dummy probe. Since bed configurations were symmetric with respect to the probe, pressures at equivalent locations in the two bed halves were assumed to be the same.

Phase angles were determined from the sampling rate and the vibrational acceleration of the vessel. At a vibrational frequency of 25 Hertz, one hundred samples of the instantaneous vibrational acceleration were taken during each cycle. A new vibrational cycle began after each set of 100 data points.

4.4.4.2 Effect of vibrational conditions.

Figure 63 on page 164 shows instantaneous floor-gauge pressures for a bed of 177-μm Master Beads vibrated at a frequency of 25 Hertz and K = 4. The curves are similar to those obtained by Gutman[14], particularly the pressure variation at the floor halfway between the side wall and the dummy probe. Floor pressures become negative over the first part of the vibrational cycle and then

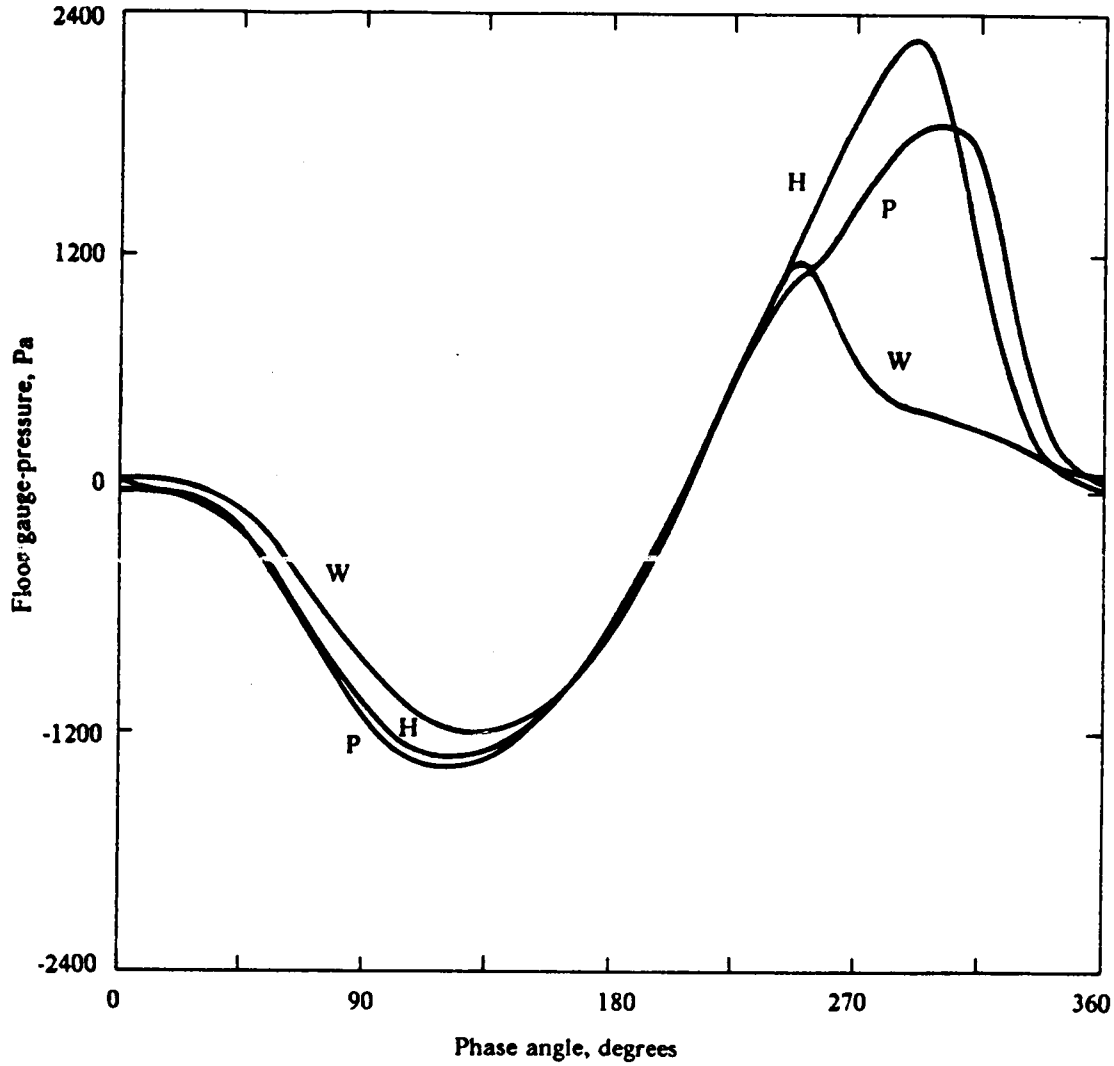

Figure 63. Floor pressures in a vibro-bed of 177-μm Master Beads: Gauge pressures at the base of a layer of particles vibrated at 25 Hertz and K = 4. Notation: W - At the side wall; P - Below the dummy probe; H - Halfway between probe and side wall.

positive during the second part of the cycle. This indicates a suction action at the base plate during the first part of the cycle. It also corresponds to an air expansion when the pressure is negative and an air compression when the pressure is positive at the base plate.

Air flows into the bed during the fraction of the vibrational cycle that Figure 63 on page 164 shows the floor pressure as being negative. The inflow of air generates drag forces on the particles. Drag forces retard the upward motion of particles and thus tend to reduce the instantaneous thickness of the air gap at the floor of the vibrating vessel. During the fraction of the cycle that the pressure is positive, the air flow is reversed and tends to retard the closing of the floor gap.

If the floor pressure at each location on the base plate were independent of the other locations, pressures during the suction period would be proportional to the bed depths shown in Figure 57 on page 143. The bed depth located halfway between the side wall and the probe is approximately 40% larger than the depth at the side wall of the vessel. As seen in Figure 63 on page 164, however, the absolute negative pressure halfway between the side wall and the probe is at most 20% higher than that at the side wall. The instantaneous pressures at these locations become equal late in the second quarter of the vibrational cycle. These observations indicate that (i) air flows from the region of higher pressure at the side wall toward regions of lower pressures below the dummy probe, and (ii) the vertical pressure difference per unit bed depth is greater at the side wall than halfway between the wall and the probe. The latter causes drag forces on the particles to be larger at the side walls. Consequently, as illustrated in Figure 60 on page 156, the air-gap thickness is smaller at the side wall than halfway between the probe and the side wall.

During the fraction of the vibrational cycle in which air compression occurs, the maximum positive pressure at the side wall is larger than halfway between the probe and the side wall because the air-gap thickness at and the bed depth are smaller at the side wall. The latter observations are illustrated in Figure 60 on page 156 and Figure 57 on page 143, respectively. They result in the later disappearance of the air gap located halfway between the probe and the side wall and in the earlier occurrence of the maximum positive pressure at the side wall.

Figure 63 on page 164 shows that the positive floor pressure below the dummy probe tends to decrease at approximately the same phase angle as the floor pressure at the side wall does before

continuing to grow until a maximum value is eventually reached later in the vibrational cycle. As shown in Figure 60 on page 156, only the particles below the probe compact on the base plate when the air gap closes. Particles at the laterals and above the dummy probe are still in flight. As these particles compact, the floor pressure below the probe resumes its growth until reaching a maximum value. It is therefore the presence of the probe that results in the abnormal behavior in the growth of the floor pressure below the dummy probe.

Figure 64 on page 167 presents the maximum negative and positve floor pressures measured at the base plate of the vibrating vessel as a function of the vibrational intensity parameter K. The maximum pressure increases with increasing K-values. Since higher K-values mean larger vibrational accelerations, the acceleration of the vessel when the bed is in flight increases with respect to the gravity acceleration of the particles as K is increased. Thus, when the vessel tends to separate from the bed at the beginning of the vibrational cycle, the suction created at the floor of the vessel is larger at higher K-values because of the faster separation between the bed and the vessel. This results is lower floor pressures and larger air gaps. When the gap disappears, the opposite occurs, that is, the bed and vessel approach each other faster as K is increased. Air compression is thus larger, resulting in higher maximum positive floor pressures at greater K-values. Consequently, since the pressure differential is proportional to the magnitude of drag force, the drag force on the particles also increases with increasing K-values.

The K-dependence of the average floor pressures at the base of the vessel over a vibrational cycle is shown in Figure 65 on page 168. The absolute value of the average floor pressures increases with increasing K-values. Average floor pressures are positive below the probe as well as halfway between the probe and the side wall. They are negative at the wall, except for K = 2. Gutman[14] reported that average floor pressures were always positive. He, however, did not measure the floor pressure at the wall of the vibrating vessel. As seen in Figure 65 on page 168, the highest average floor pressure was determined halfway between the probe and the side wall. At this location, the air gap was also the thickest.

When reporting the solid circulation in beds of 177-μm Master Beads, section 4.4.2.1 of this Chapter, the local solid-circulation loops below the dummy probe shown in Figure 57 on page 143

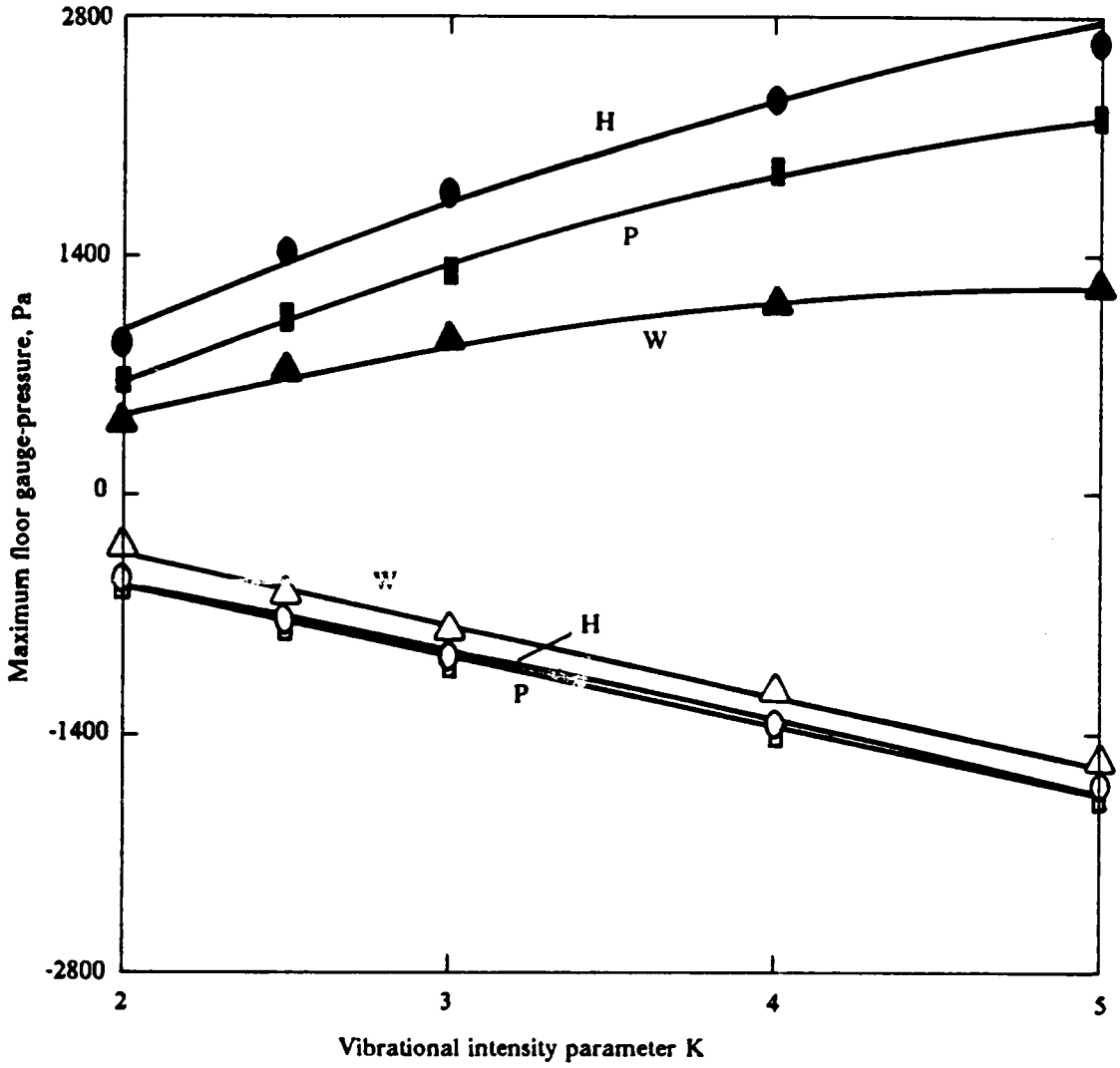

Figure 64. **K-dependence of floor pressures in a vibro-bed of Master Beads:** Maximum floor gauge-pressures at the base of a layer of 177-μm particles vibrated at 25 Hertz and K = 4. Notation: W - At the side wall; P = Below the dummy probe; H - Halfway between probe and side wall.

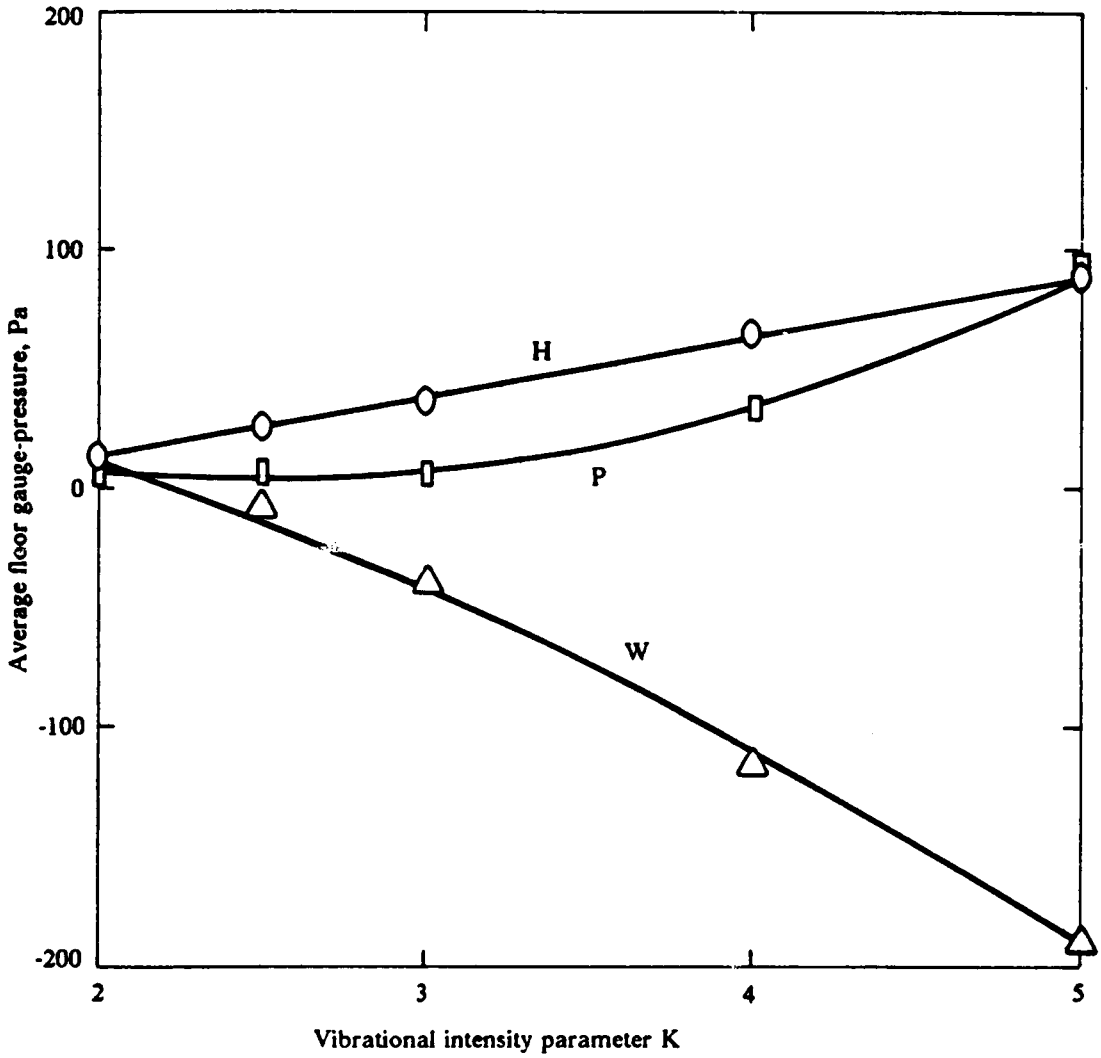

Figure 65. Average floor-pressures in a vibro-bed of 177-μm Master Beads: Gauge pressures at the base of a layer of particles vibrated at 25 Hertz and K = 4. Notation: W - At the side wall; P - Below the probe; H - Halfway between probe and side wall.

were attributed to the relative motion between the dummy probe and the bed of particles. The physics that generate the solid-flow patterns in the bulk of the bed toward the dummy probe was not discussed. According to Gutman[14], the difference in the levels of particles contained in an U-tube subjected to vibration is caused by a difference in the mean air pressures at the bottom of the two limbs of the tube. Figure 65 on page 168 shows that the average floor pressure in beds of 177-μm Master Beads was highest halfway between the probe and side wall. Following Gutman's interpretation, the observed average floor-pressure difference would generate gas and particle flows toward the side walls of the vibrating vessel. Since the actual particle flow in the bulk of the bed was in the opposite direction, the average floor-pressure difference cannot be the origin of the observed solid-circulation patterns in vibrated beds of 177-μm Master Beads.

The solid-circulation patterns illustrated in Figure 57 on page 143 for beds of 177-μm particles are generated by horizontal and vertical components of a gas flow that is induced by the instantaneous pressure field existing in the vibro-bed. Above the bed, the pressure is atmospheric. Figure 63 on page 164 shows that the instantaneous pressure below the bed decreases from the side wall toward the dummy probe during the fraction of the vibrational cycle that the floor pressure is negative. When the floor pressure is positive, the pressure at the side wall becomes smaller than the one located halfway between the probe and the side wall after the air gap at the side wall disappears. These observations indicate that instantaneous pressures change in both the vertical and horizontal directions within the vibro-bed. However, air flows able to entrain particles toward the dummy probe are induced only during the period of time that the floor pressure is negative.

As discussed in section 4.4.3, the development of air gaps at the top of the dummy probe follows the same mechanism as that for the formation of air gaps at the floor of the vessel. This suggests that the same suction action present at the base plate should be present at the top of the probe and reduce the local air pressure. The resulting pressure difference between the top of the probe and its neighborhood would generate gas currents toward the dummy probe. Particles entrained by these gas currents seemed to explain the convergence of the solid-circulation paths toward the dummy probe as illustrated in Figure 57 on page 143.

It was concluded that the solid-circulation patterns shown in Figure 57 on page 143 were induced by instantaneous pressure differentials existing in the vibrated bed when both the base plate and the dummy probe tend to separate from the bed of particles. This explanation confirms the assumption of Buevich et al[28] that particle entrainment by gas currents is allowed only during the fraction of the vibrational cycle in which the bed is not compacted onto the base plate of the vibrating vessel.

4.4.4.3 Effect of particle size.

88-μm Master Beads

Figure 66 on page 171 shows the floor-pressure variation over a single vibrational cycle in a bed of 88-μm Master Beads vibrated at 25 Hertz and K = 4. Although the general form of the pressure curves is the same as that for 177-μm Master Beads in Figure 63 on page 164, some differences are apparent. For 88-μm Master Beads, the maximum negative pressures are larger and occur slightly earlier in the vibrational cycle, and the maximum positive pressures are of approximately the same magnitude as the absolute negative pressures. Also, the maximum negative pressures and the switching from negative to positive floor pressures occur slightly earlier in the vibrational cycle than for 177-μm particles.

Higher floor pressures in beds of 88-μm Master Beads indicate larger drag forces exerted by air currents on the solid particles than in beds of 177-μm Master Beads. This results in a faster deceleration of 88-μm particles when the instantaneous acceleration of the vessel becomes larger than the gravity acceleration of the particles at the beginning of the vibrational cycle. Since no air gaps were observed in beds of 88-μm Master Beads, these beds did not behave as a rigid porous piston. As discussed in section 3.1.2.2, floor-pressure variations in the absence of air gaps require bed expansion and compression. Figure 58 on page 148 shows that the horizontal solid-circulation paths in beds of 88-μm Master Beads are confined to the lower portion of the bed near the base

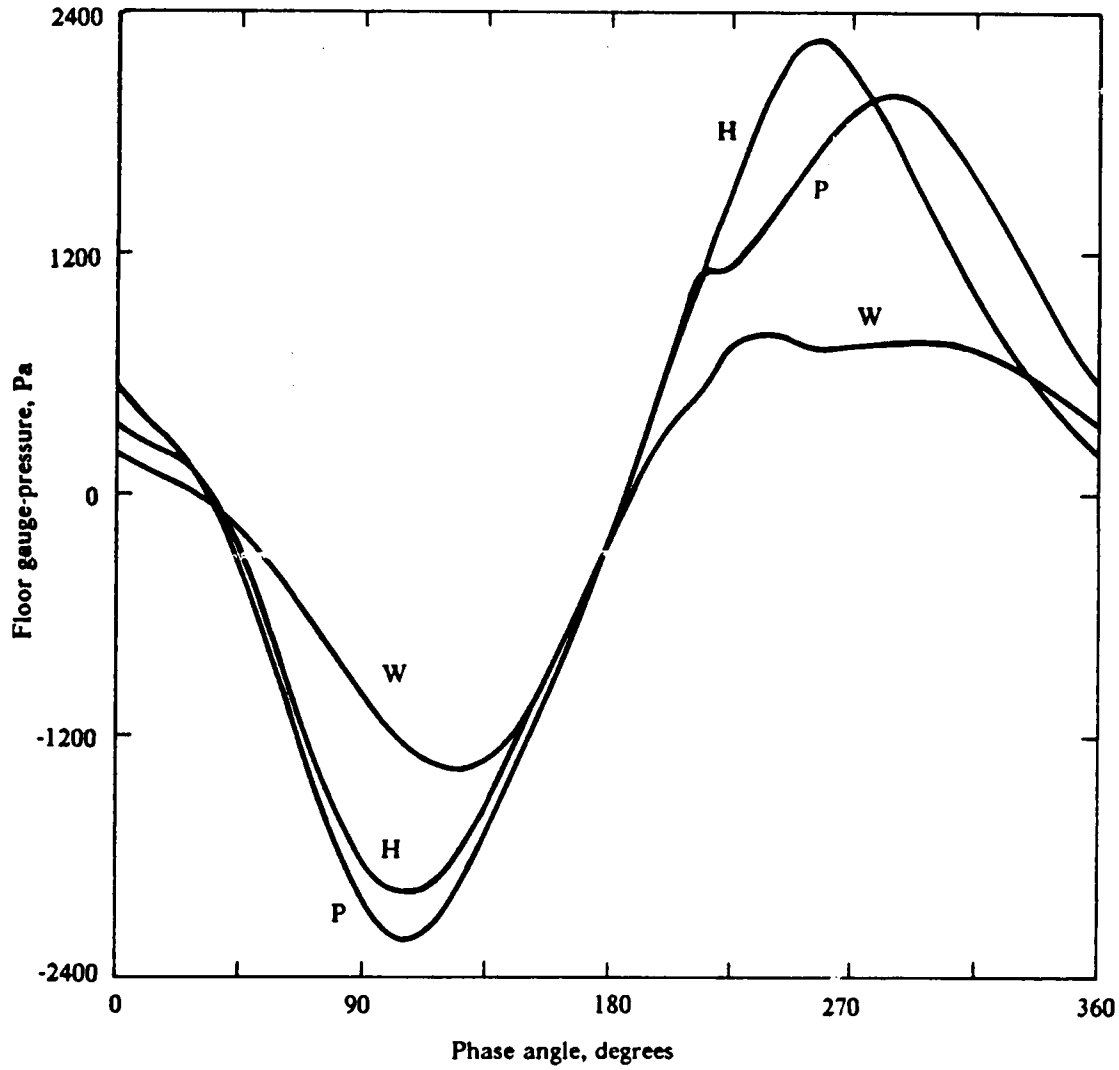

Figure 66. Floor pressures in a vibro-bed of 88-μm Master Beads: Gauge pressures at the base of a layer of particles vibrated at 25 Hertz and K = 4. Notation: W - At the side wall; P - Below the dummy probe; H - Halfway between probe and side wall.

plate of the vibrating vessel. This observation suggested that bed expansion occurred primarily in the lower layers of particles.

Since particles are deaccelerated faster in beds of 88-μm Master Beads, the maximum negative pressures and the switching from negative to positive floor pressures occur earlier in the vibrational cycle than for 177-μm Master Beads as shown in Figure 63 on page 164 and in Figure 66 on page 171. The compression of the air at the base of the bed begins earlier for 88-μm Master Beads. For these particles, air compression is promoted by the compaction of the bed of solids. The faster deacceleration of 88-μm particles implies that the relative motion between the bed and the dummy probe is smaller than in beds of 177-μm particles. This imparts less angular momentum to the local solid-circulation loops existing below the probe in beds of 88-μm Master Beads as shown in Figure 58 on page 148. Their circulation speed is, therefore, very low.

Solid-circulation rates in beds of 88-μm Master Beads were observed to be lower than in beds of 177-μm Master Beads as reported in Table 5 on page 146. The larger floor-pressure gradients in beds of 88-μm particles shown in Figure 66 on page 171 were insufficient to obtain higher solid-circulation rates. The high permeability of beds of small particles and the confinement of bed expansion to the lower layers of particles led to less solid circulation as the particle size was reduced.

500- and 707-μm Master Beads

Figure 67 on page 173 and Figure 68 on page 174 show the instantaneous floor pressures in beds of 500- and 707-μm Master Beads, respectively, vibrated at a frequency of 25 Hertz and $K = 4$. These figures together with Figure 63 on page 164 for 177-μm Master Beads and Figure 66 on page 171 for 88-μm Master Beads indicate that maximum positive and negative floor pressures decrease as the particle size is increased. The observation tells that the drag forces exerted on the solids decrease with increased particle diameter.

The thickness of the air gaps in beds of 707-μm Master Beads was observed to be smaller than in 177-μm beds. These observations are illustrated in Figure 60 on page 156 and Figure 61 on page 159. The smaller drag forces on larger particles resulted in less deacceleration of the bed of particles after the vessel has separated from the bed. Consequently, as seen in Figure 63 on page 164,

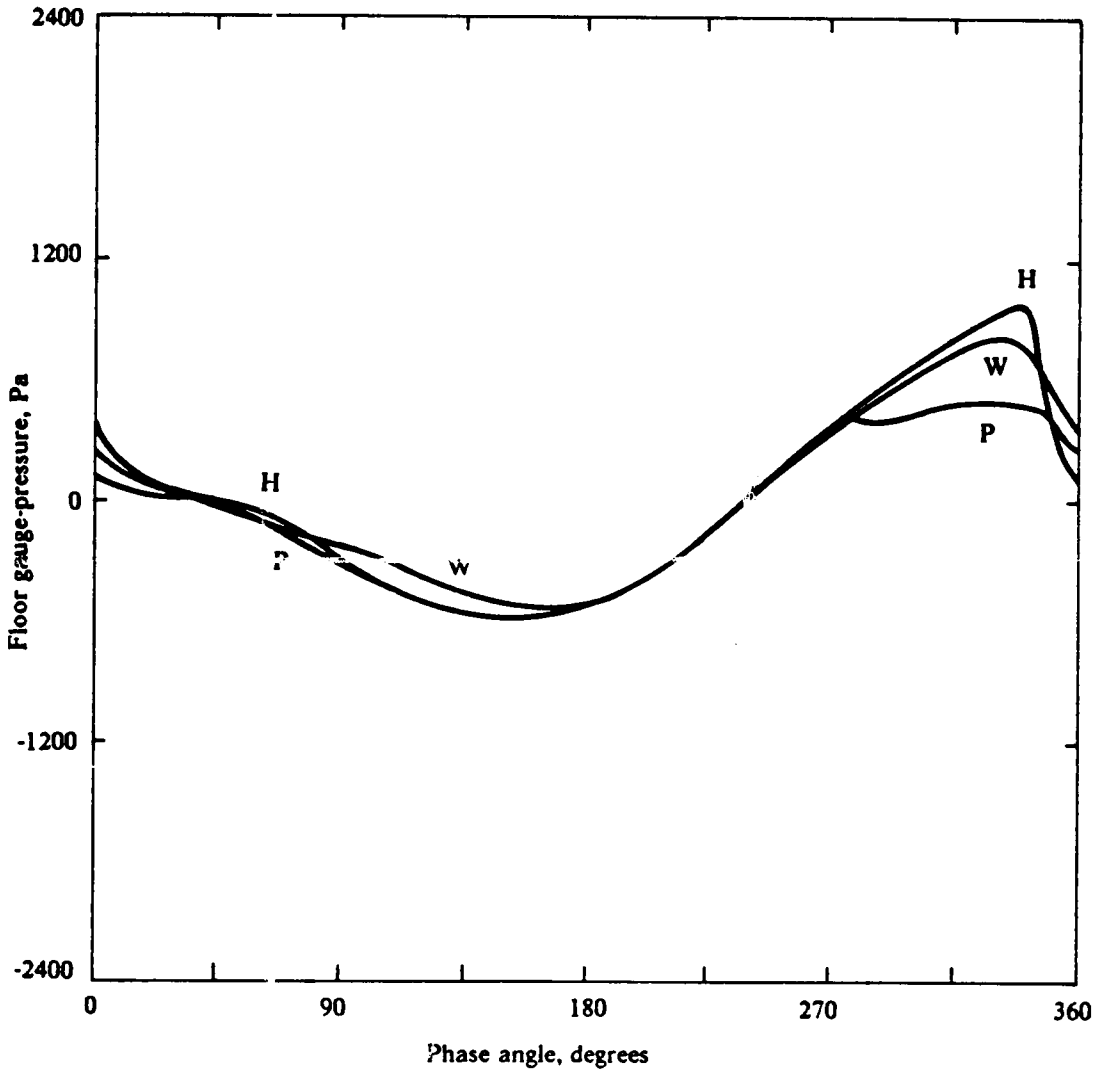

Figure 67. Floor pressures in a vibro-bed of 500-μm Master Beads: Gauge pressures at the base of a layer of particles vibrated at 25 Hertz and K = 4. Notation: W - At the side wall; P - Below the dummy probe; H - Halfway between probe and side wall.

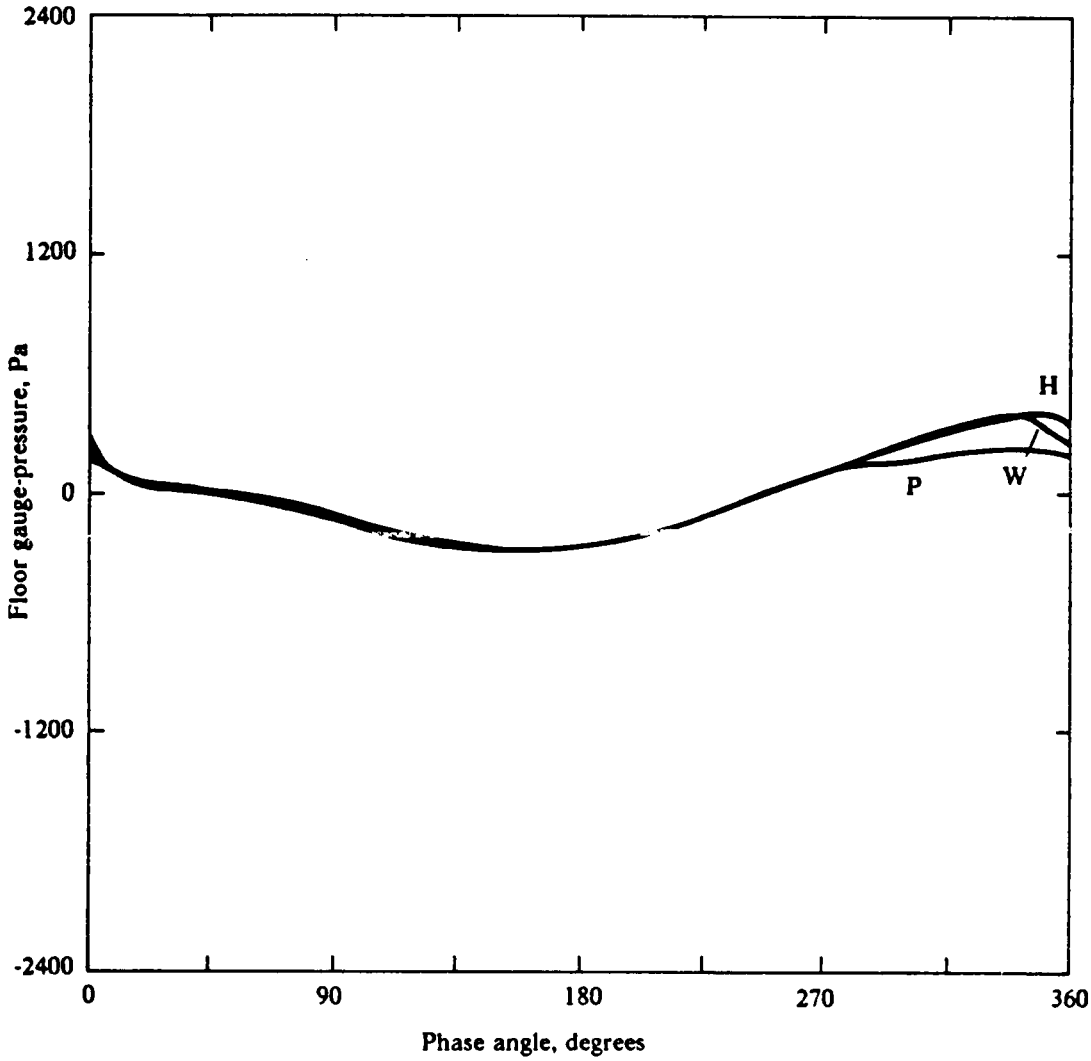

Figure 68. Floor pressures in a vibro-bed of 707-μm Master Beads: Gauge pressures at the base of a layer of particles vibrated at 25 Hertz and K = 4. Notation: W - At the side wall; P - Below the dummy probe; H - Halfway between probe and side wall.

Figure 67 on page 173, and Figure 68 on page 174, the maximum negative pressures and the switching from negative to positive floor pressures occur later in the vibrational cycle than for smaller 177-μm Master Beads.

Smaller drag forces in beds of large particles also reduce the intensity of solid circulation as the particle size is increased. As discussed in section 4.4.2.2 and shown in Figure 58 on page 148, the intensity of solid circulation decreased and the solid-flow paths at the vessel wall approached vertical with increased particle diameter.

4.4.4.4 Effect of particle density

Figure 69 on page 176, Figure 70 on page 177, and Figure 63 on page 164 illustrate the effect of particle density on the instantaneous floor pressures in a bed vibrated at a frequency of 25 Hertz and K = 4. The densities of low- and high-density glass beads and of Master Beads are reported in Table 4 on page 128. Increasing the particle density resulted in higher maximum negative and positive floor pressures. The maximum negative floor pressure in the bed of low-density glass beads occurred a little earlier in the vibrational cycle than those for high-density glass beads. The switching from negative to positive floor pressures also occurred a little later in the bed of high-density beads. These observations suggested that the air-gap size was smaller in the bed of low-density glass beads, but the difference in air-gap thickness could not accurately be detected with the technique of stroboscopic lighting described in section 4.4.3.

The instantaneous pressure differentials along the base plate when the floor pressures are negative indicate that solid circulation should be directed from the side wall toward the dummy probe. As shown in Figure 69 on page 176 and Figure 70 on page 177, these floor pressures decrease from the side wall in direction to the probe. The pressure differentials however, cannot explain the distinct characteristics of the solid-flow patterns shown in Figure 59 on page 152. The solid-circulation paths in beds of high-density glass beads displayed some trend toward vertical paths in the upper half of the bed. The circulation paths for low-density glass beads were not as

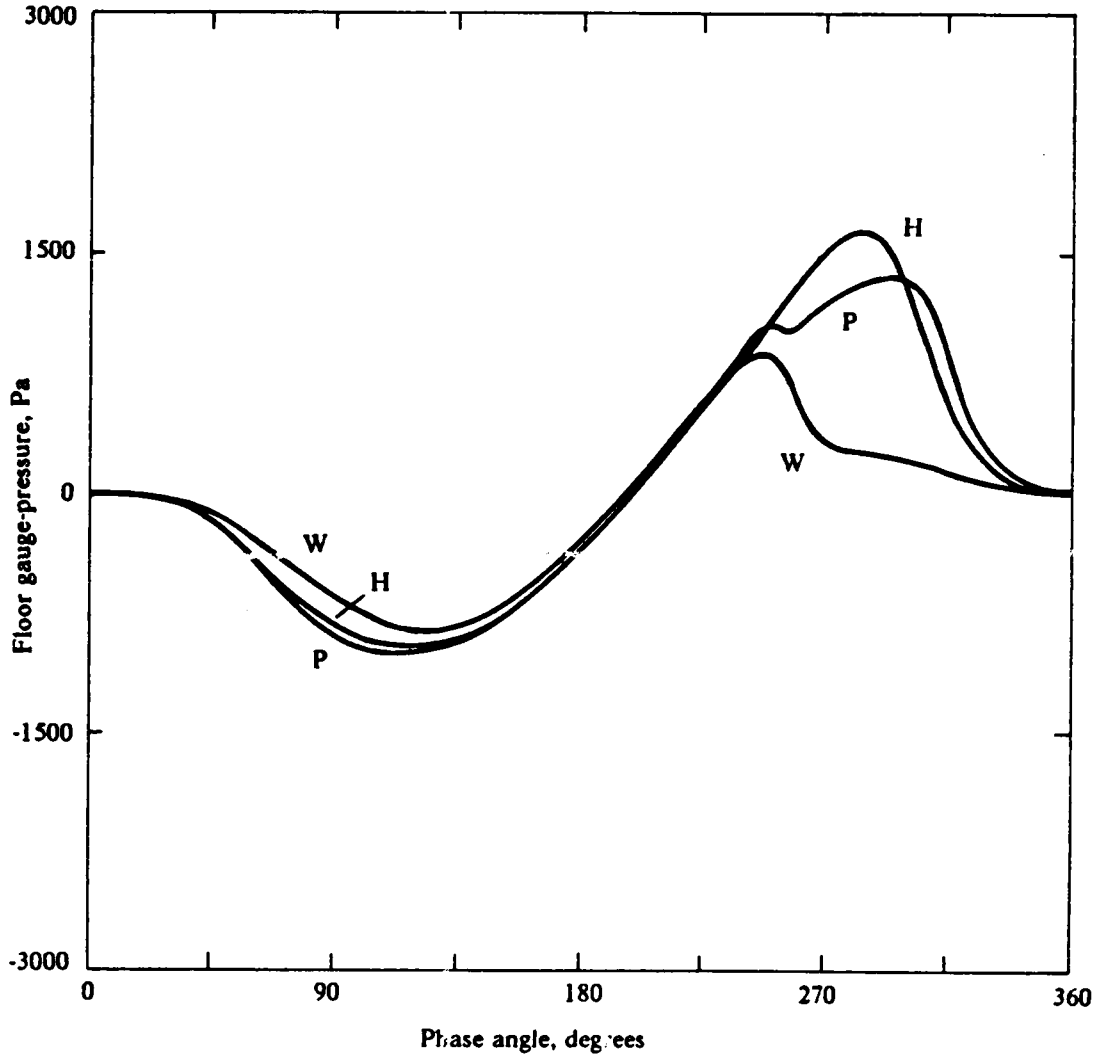

Figure 69. Floor pressures in a bed of 177-μm low-density glass beads: Instantaneous gauge pressures at the base of a layer of particles vibrated at 25 Hertz and K = 4. Notation: W - At the side-wall; P - Below the dummy probe; H - Halfway between probe and side wall.

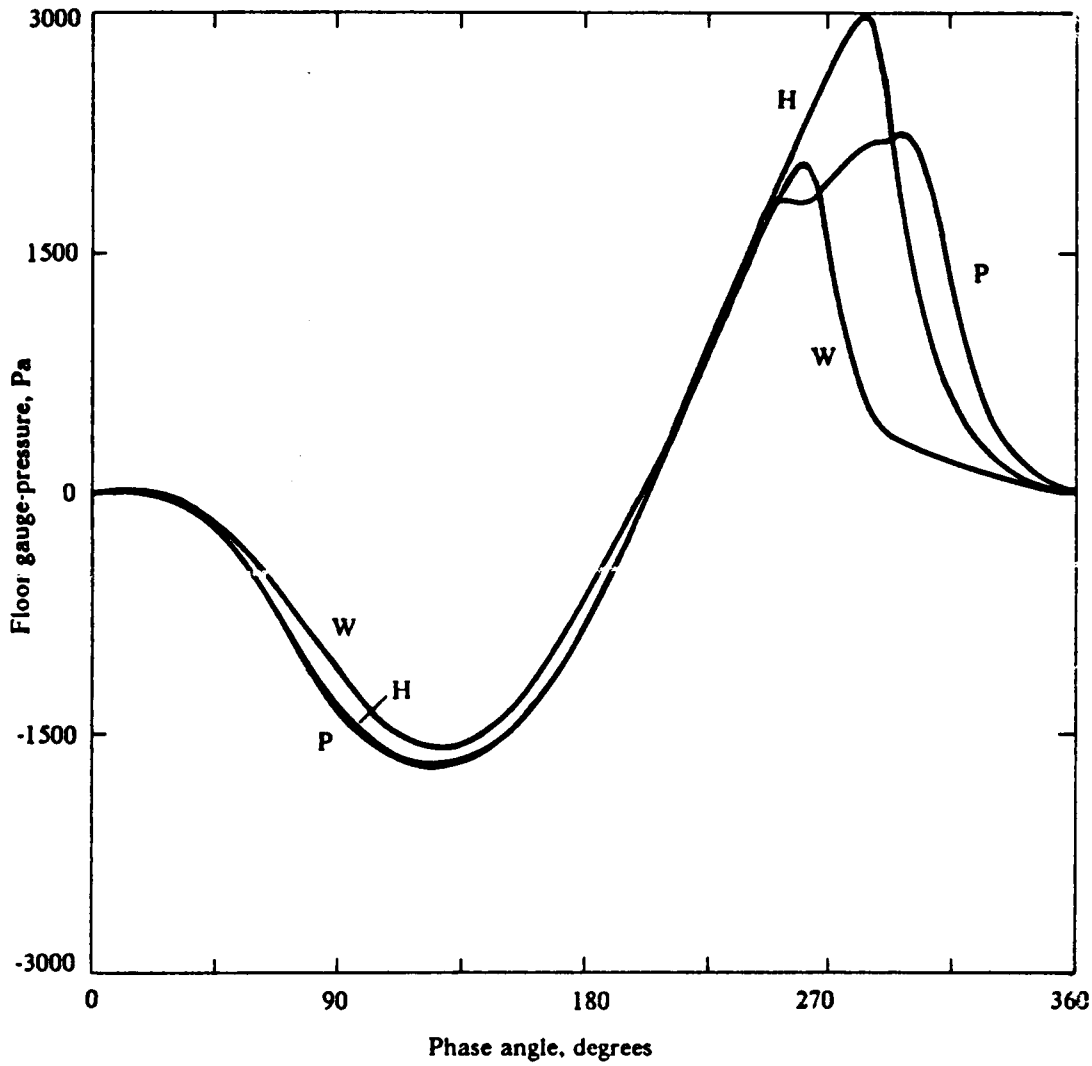

Figure 70. **Floor pressures in a bed of 177-μm high-density glass beads:** Instantaneous gauge pressures at the base of a layer of particles vibrated at 25 Hertz and K = 4. Notation: W - At the side-wall; P - Below the dummy probe; H - Halfway between probe and side wall.

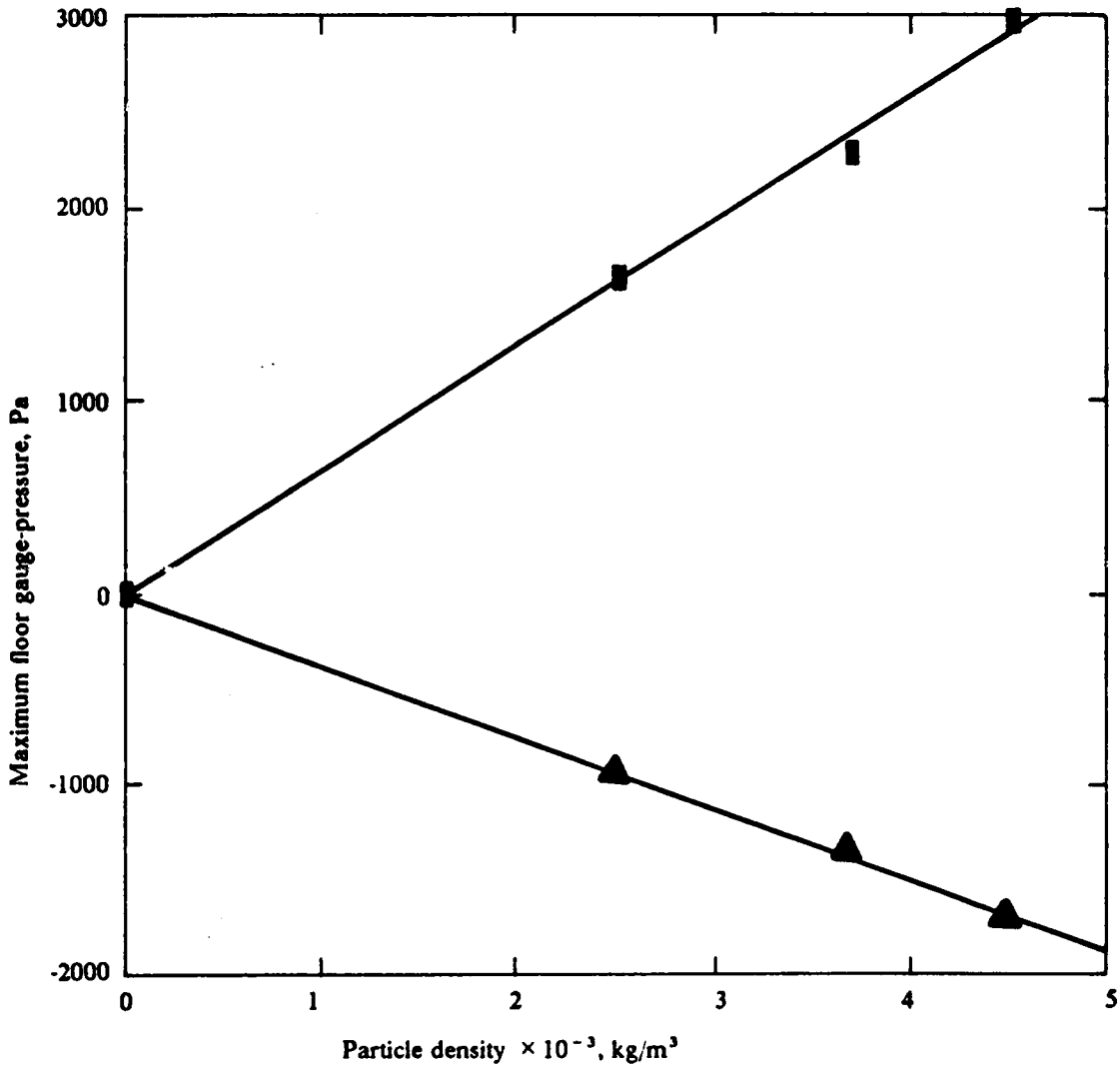

Figure 71. Dependence of maximum floor pressures on particle density: Gauge pressures halfway between the probe and the side wall at the base of a bed of 177-μm particles vibrated at 25 Hertz and K = 4.

well-ordered as those for Master Beads. Also, the pillaring of solids above the probe became more severe as the particle density was decreased. These phenomena were similar to those observed in beds of Master Beads when changing the particle size. Table 5 on page 146 shows that solid-circulation times first decreased and then increased as the particle size was increased. The table indicates the same pattern for increased particle density. It suggested that the effect of increasing the particle density was equivalent to that of increasing the particle size. This equivalence was, however, not observed in relation to the instantaneous floor pressures. As Figure 71 on page 178 illustrates, the magnitude of the absolute negative and positive floor pressures is directly proportional to the particle density. Increasing the particle density has the opposite effect on the floor pressure as increasing the particle size.

4.4.4.5 Theoretical predictions

Theoretical models for vibro-bed dynamics presented in Chapter 3 were developed for rigid porous beds of constant porosity. No allowance was made for any bed internals, or for non-uniform bed depths. Such conditions have not been observed in the present investigation, and thus those models can not be expected to be very accurate in predicting actual bed behavior. In addition, the experimental determinations discussed in this Chapter were not sufficient for fully testing the different models. For example, gap-size measurements were not made.

The applicability of existing models to the present experimental conditions is discussed first. Then, Kroll's model is utilized to compare theoretical floor-pressure estimates to actual measured values.

Applicability of existing models: The graph in Figure 44 on page 102 maps regions of applicability of vibro-bed dynamics models in terms of the vibrational intensity parameter K and the dimensionless group N defined by equation [3.16]. As shown in section 3.1.2.1, the group N was

obtained by expressing Kroll's equation in a dimensionless form. The criteria used to establish the applicability of the models are discussed in section 3.1.4.

Figure 72 on page 181 shows a mapping of the regions of applicability of (i) the single-particle model, section 3.1.1.1, (ii) Kroll's model, section 3.1.2.1, and (iii) Gutman's model, section 3.1.3.1, for beds of Master Beads vibrated at 25 Hertz. This mapping is valid for beds of 40-mm in depth and average porosity of 0.41. The locations corresponding to different particle sizes of Master Beads were marked in the figure.

Figure 72 on page 181 indicates that the single-particle model is not applicable even for large 707-μm Master Beads. Since drag forces cannot be neglected, Kroll's model should be used in calculations involving the behavior of beds of 707- and 500-μm Master Beads. Gas-compressibility effects become important in beds of 177-μm and smaller Master Beads. For these particles, Gutman's model should give better estimates of bed behavior.

The significance of drag forces and gas compressibility was qualitatively identified in the present investigation. Drag forces induced solid bunkering and horizontal particle circulation, and resuslted in a reduction in the the air-gap thickness as the particle size was decreased. The former two phenomena are illustrated in Figure 57 on page 143 and Figure 58 on page 148. The latter is shown in Figure 60 on page 156 and Figure 61 on page 159.

Prediction of Kroll's model

Figure 73 on page 182, Figure 74 on page 183 and Figure 75 on page 184 compare experimental instantaneous floor pressures in beds of Master Beads with estimates from using Kroll's model. An average bed porosity of 0.41 was utilized in the calculations for all particle diameters. It was assumed that the bed depth determined after external vibrations had been stopped was a good approximation for the actual depth of the vibro-bed. The sudden decrease of the estimated positive floor pressure shown in these figures reflects the absence of pressure forces during the period of time bed and vessel are in contact as illustrated in Figure 34 on page 80.

The maximal negative pressures predicted by Kroll's model at the floor near the side walls of the vibrating vessel were smaller than the actual pressures for all particle sizes. But the predicted

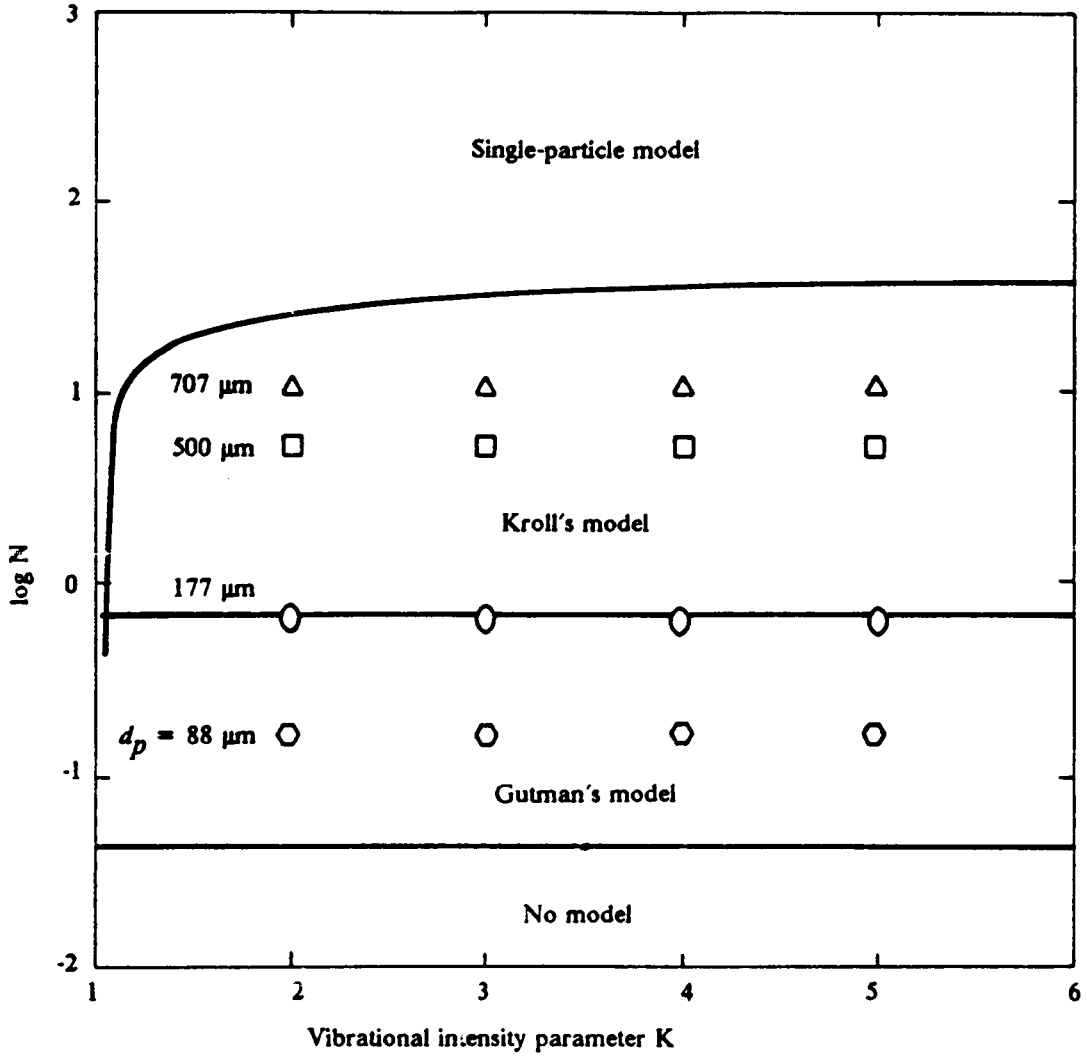

Figure 72. Applicability of theoretical models for vibro-beds of Master Beads: 40-mm layers of particles vibrated at 25 Hertz. Bed porosity: 0.41. N is the dimensionless parameter defined by eequation [3.16] and represents the hydraulic resistance per unit of bed density.

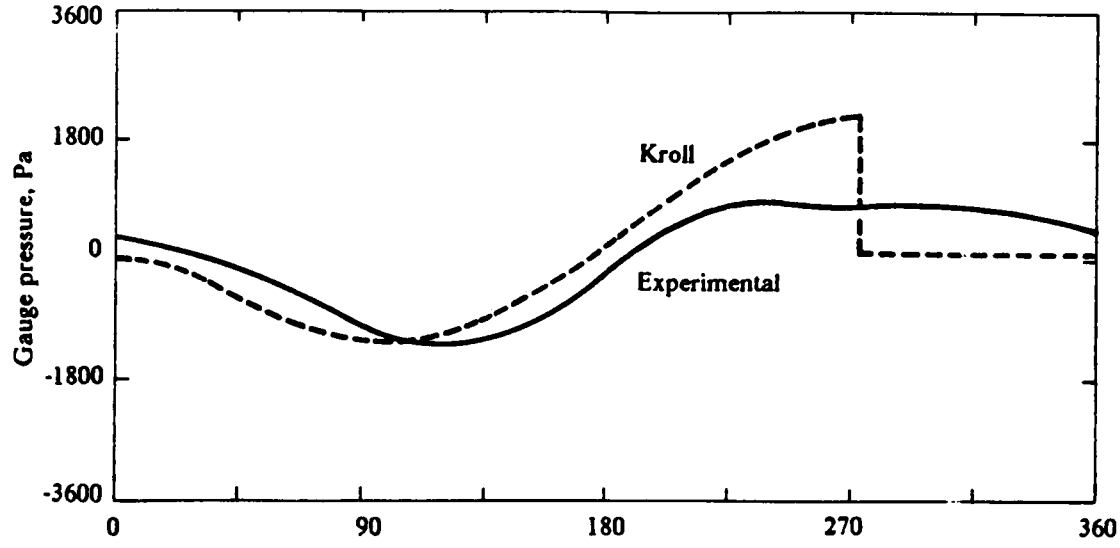

(a) At the side wall

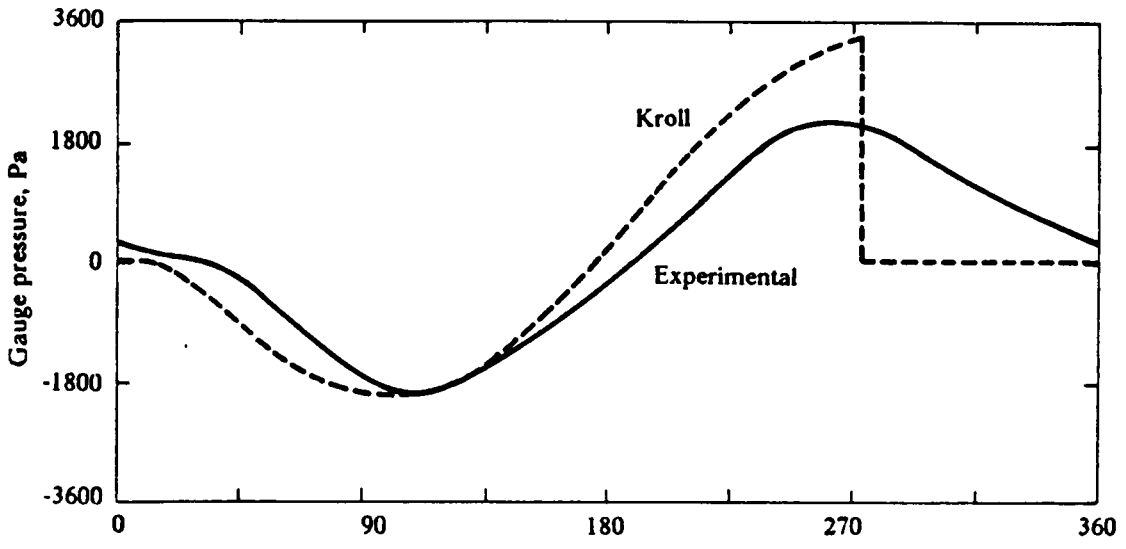

(b) Halfway between probe and side wall

Figure 73. Kroll's floor-pressure estimates in beds of 88-μm Master Beads: Comparison with experimental floor pressures in a bed vibrated at 25 Hertz and K = 4.

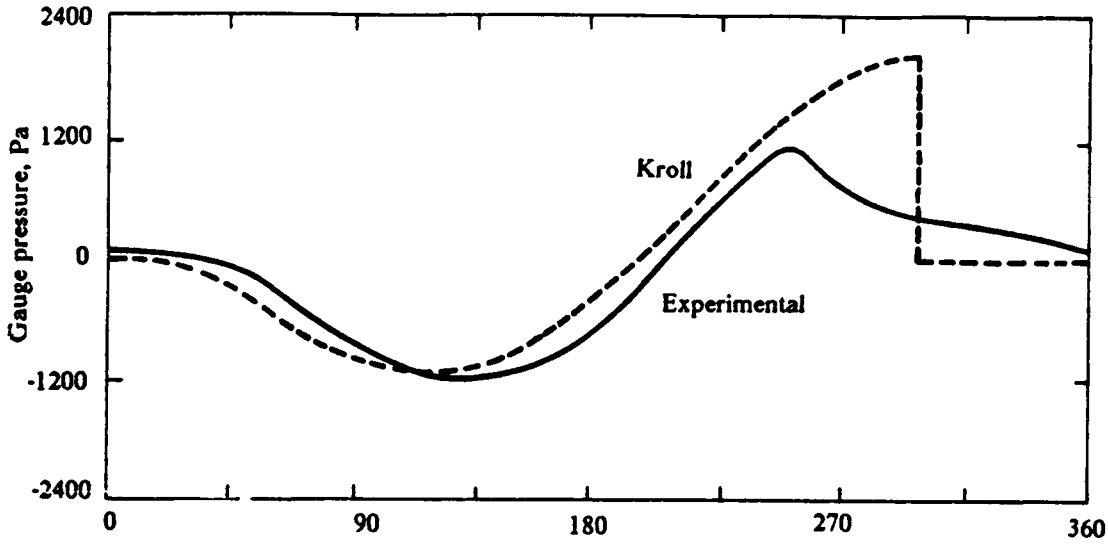

(a) At the side wall

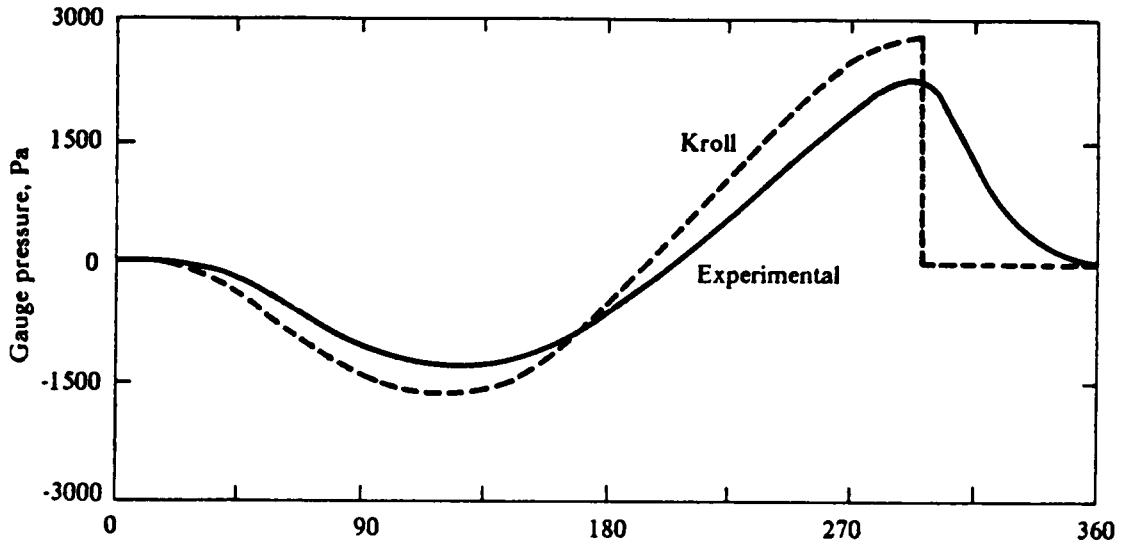

(b) Halfway between probe and side wall

Figure 74. Kroll's floor-pressure estimates in beds of 177-μm Master Beads: Comparison with experimental floor pressures in a bed vibrated at 25 Hertz and K = 4.

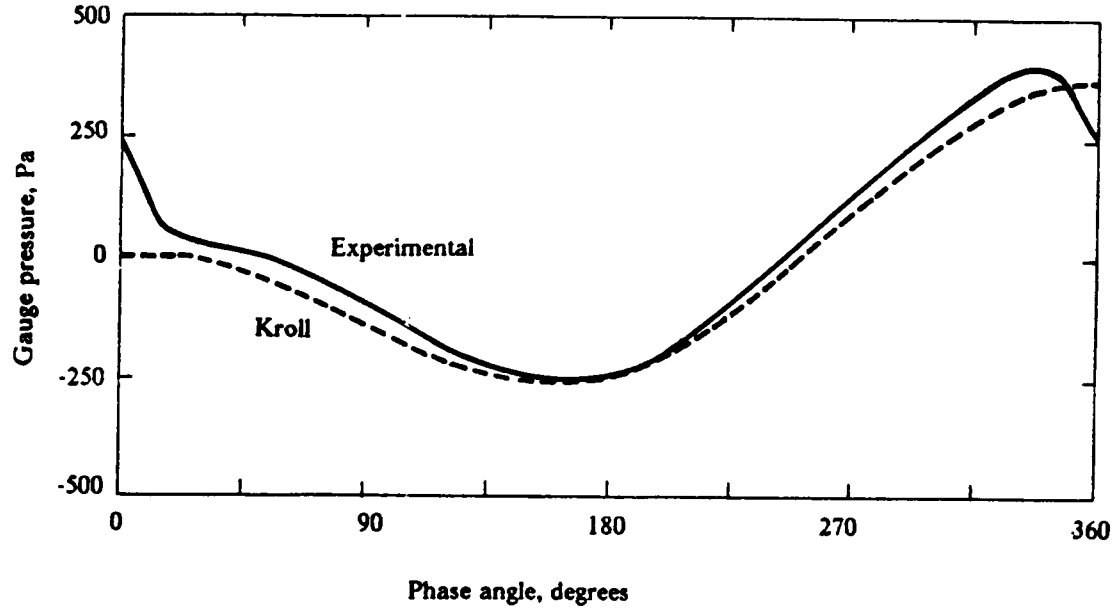

(a) At the side wall

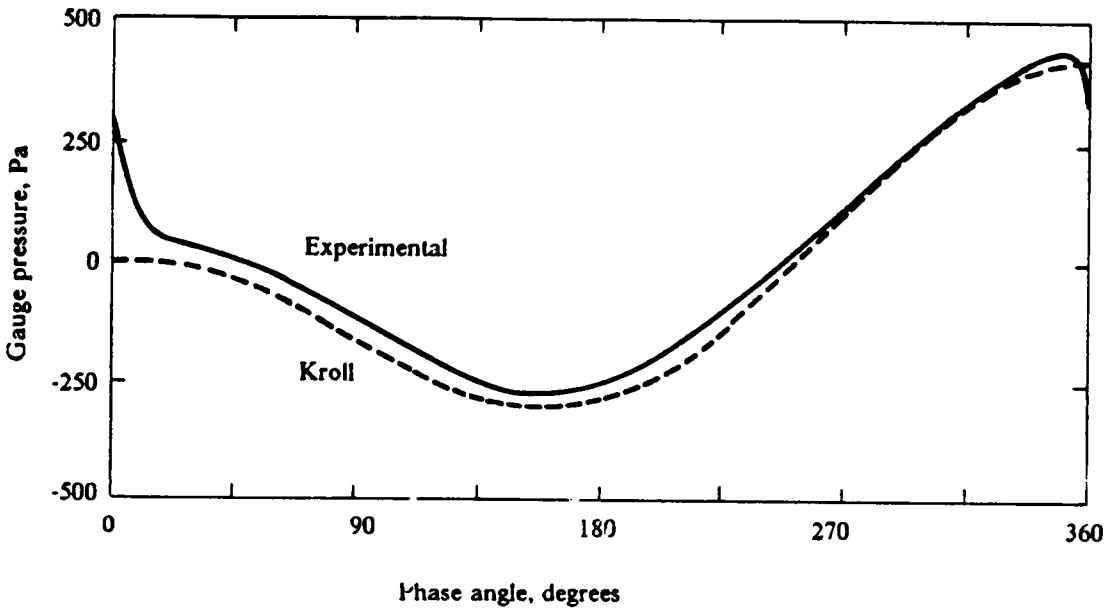

(b) Halfway between probe and side wall

Figure 75. **Kroll's floor-pressure estimates in beds of 707-μm Master Beads:** Comparison with experimental floor pressures in a bed vibrated at 25 Hertz and K = 4.

maximal negative pressures located halfway between the probe and side walls were always larger than the actual ones. Air flow from the side walls toward the dummy probe would cause the actual pressure at the walls to decrease below its ordinary value, while increasing the actual pressure located halfway between the walls and probe.

The maximal pressures during the compression period did not present such a consistent trend between the actual and predicted values. Figure 73 on page 182 and Figure 74 on page 183 show that for Master Beads of 88 and 177 μm in diameter, respectively, predicted pressures were always higher than actual measured values. Figure 75 on page 184 illustrates that for Master Beads of 707 μm in diameter, the predicted values were in aggreement with the actual values.

Figure 40 on page 95 and Figure 42 on page 97 illustrate the effect of gas compressibility by comparing estimates from using Kroll's and Gutman's model. Instantaneous pressures predicted by Kroll's modell always trail those by Gutman's model over the whole vibrational cycle. The switching from negative to positive floor pressures occurs earlier in the cycle according to Kroll's model. This behavior was observed for 88- and 177-μm Master Beads as illustrated in Figure 73 on page 182 and Figure 74 on page 183, respectively. It seems, therefore, appropriate to attribute the discrepancy between experimental pressures and estimates by Kroll's model to gas-compressibility effects.

In summary, floor pressures predicted by Kroll's model were observed to be more accurate for vibro-beds of large particles. Small discrepancies seemed to be caused by air currents between different locations along the base plate. As the particle size is reduced, discrepancies between theory and experiment were observed to increase. Gas-compressibility effects appear to be the major cause.

4.5 *Conclusions*

The behavior of beds of different particle types and sizes vibrated at a frequency of 25 Hertz was investigated. The vibrational intensity parameter K was varied between 1 and 6. Vessel geometry was changed by utilizing two types of vibrating vessels: a cylindrical vessel, and a rectangular, two-dimensional vessel. Master Beads, low-density glass beads and high-density glass beads were used as the bed material. Beds of Master Beads had the following size ranges expressed in ASTM mesh: -20+30, -30+40, -70+100, and -140+200. The respective geometrically-averaged diameters were 707 μm, 500 μm, 177 μm, and 88 μm. Beds of glass beads were restricted to one average particle size, 177 μm. The average static bed height was kept constant at 30 mm. Unless otherwise stated, the conclusions assume solid bunkering at the center of the vessel above the horizontal, cylindrical dummy heating surface.

4.5.1 Experimental data

Based on the experimental data obtained in this investigation, the following conclusions can be made:

Instantaneous floor pressures were, in general, not uniform along the base plate of the vibrating vessel at the same phase angle. The average floor pressure was lower at locations of the base plate at which the bed was shallowest.

(ii) Solid bunkering, which is an alternate way of expressing the formation of solid piles at specific bed locations, is caused by local bed nonuniformities that induce lower floor pressures at locations where the bed is less permeable to air. The probability of solid bunkering decreased as either the particle size of K was increased.

(iii) Solid circulation in the bulk of vibro-beds was induced by the instantaneous pressure differentials that developed along the vessel base during the fraction of vibrational cycle that the floor

pressure was negative. Solid-circulation paths were directed from the shallowest toward the deepest region of the vibrated bed. The rate of solid circulation was low in vibro-beds of large 707-μm particles. As the particle size was reduced, the solid-circulation rate was initially increased. Highest circulation rates were observed in beds of 177-μm Master Beads. Further decreasing the particle size resulted in a lower solid-circulation rate. For beds of 177-μm particles, increasing or decreasing the density of solids decreased the rate of solid circulation.

(iv) Local solid-circulation loops developed in pairs above and below the heating probe when solid bunkering occurred above the dummy heater. Loops above the probe disappeared as the particle size or the K-value was reduced. The loops were destroyed by horizontal streams of particles when bunkering was allowed at side walls of the vibrating vessel in beds of small particles. The circulation loops were generated by the relative motion between the bed and vessel, which imparted angular momentum to the particles above and below the probe.

(v) Solid interchange between local solid-circulation loops and the bulk of the bed was low at small K-values. The interchange increased as K was increased.

(vi) Air gaps tended to develop at the top and bottom of the dummy probe when the absolute acceleration of the vibrating vessel became larger than the gravitational acceleration of the particles in the first and third quarters of the vibrational cycle, respectively. The size of these gaps increased as either the particle size or the K-value was increased. No air gaps were formed in beds of 88-μm Master Beads.

4.5.2 Comparison with theoretical models

Based on the comparison of experimental data with available models, the following conclusions can be reached:

(i) Drag forces are considerable for 707-μm Master Beads, the largest particles utilized in the experimental program. Thus, the single-particle model is not applicable.

(ii) According to Gutman's criterion for the relevance of air-compressibility effects, Kroll's model does not give accurate estimates of floor-pressure variations and air-gap sizes in beds of 177-μm and smaller particles.

(iii) Kroll's model yielded good estimates of floor-pressure variations in beds of 707-μm Master Beads. As the particle size was decreased, discrepancy between estimates and experimental values increased. Besides gas-compressibility effects, air currents in the horizontal direction were also responsible for this discrepancy.

4.6 Recommendations

(i) The investigation on vibro-bed dynamics was performed at constant vessel and bed dimensions. Varying bed depth as well as probe height and diameter may affect the characteristics of solid-circulation loops that develop above and below the probe in symmetrical bed configurations. The length of the two-dimensional vessel and the diameter of the cylindrical vessel, may change the pattern and the intensity of overall solid circulation. Such variations in the system parameters may result in improved solid renewal rates at the dummy heating surface and should be investigated.

(ii) In a semi-continuous system, in which a constant flow rate of supernatant gas is in contact with a vibrated batch of solid particles, the bunkering effect found in beds of smaller particles might vary considerably with the relative dimensions of the vibrating trough. This dependence should be determined in order to optimize solid circulation and the orientation of the heating surface.

(iii) In continuous systems, as well as in each of the heat-exchange cells in the semi-continuous system illustrated in Figure 2 on page 7, the presence of baffles and the solid flow induced by the inclination of the trough or by the horizontal component of the vibrations can be expected to affect the circulation patterns generated by drag forces, and the circulation loops around the probe. The non-vertical character of vibrations might also affect the development and size of air gaps on the

top and at the bottom of horizontal, cylindrical heating surfaces. Again, such effects should be determined to optimize the solid circulation and orientation of the heating surface.

(iv) It was shown that, when utilising sufficiently small particles, solid circulation within the vibro-bed became appreciably deteriorated at mild vibrational conditions because the low permeability of the bed led to considerable porosity variations. It would be of practical interest to investigate the possibility and feasibility of utilizing controlled bed aeration at particular sections of the base plate of the vessel in order to induce favorable solid circulation patterns within the bed.

5.0 Experimental Investigation on Vibro-Bed Heat Transfer.

The experimental investigation on heat transfer in vibrated beds was primarily aimed at evaluating a bed of Master Beads as the heat-transfer medium between a hot supernatant gas and cooling surfaces placed within a vibrated bed of particles. Such an evaluation was performed by determining heat-transfer coefficients between beds of Master Beads and a horizontal, cylindrical heating surface placed within the vibrated bed, as well as the dependence of the coefficients on particle size, vibrational conditions, and solid-flow patterns. Some experimental results were also obtained for beds of different types of solids in order to compare the performance.

Emphasis is placed on the physical phenomena affecting the heat-transfer process. The experimental results on bed dynamics discussed in Chapter 4 are used in the interpretation of the heat-transfer performance. The experimental results on heat transfer are also compared with theoretical estimates from the one-layer model of Zabrodski[18] discussed in section 3.2.

The Chapter ends with a summary of the conclusions obtained from the experimental investigation, and with recommendations for further research in vibro-bed heat transfer.

5.1 Experimental System and Conditions

5.1.1 Experimental system

Figure 76 shows a schematic diagram of the experimental system utilized in this investigation. The vibrating vessel consisted of a cylindrical glass vessel of 170 mm in diameter supported on a stainless-steel base plate, which was attached to the vibrating system illustrated in Figure 52 on page 130. The cylindrical heating surface was suspended into the vessel through two steel rods of approximately 4 mm in diameter that were fixed to a strong steel frame attached to the vibrating table. The elevation of the axis of the heating surface from the floor of the vibrating vessel was kept constant at 20 mm.

As shown in Figure 77 on page 192, at the center of the heating surface (Huang[52]) was an electrical cartridge heater, having a diameter of 6.4 mm and total length of 73.4 mm. The surface of the cartridge was covered by a tightly fitted cylindrical copper surface that is 3.35-mm thick. The surface contains grooves that are 2.6-mm wide and 1.42-mm deep for housing thermistor-type temperature-sensing elements and their leading wires. A total of three thermistors was utilized to measure the temperature of the heating surface. These included one at the bottom of the surface near its left boundary, and the other two at the laterals of the surface halfway between its boundaries. At the boundaries, the heating probe was isolated from the metallic support through 5-mm-wide asbestos rings. In order to protect the thermistors, the heating surface was wrapped with an aluminum foil.

A separate temperature probe that could be inserted at any position within the bed was used to monitor the bed temperatures. Temperature readings were displayed on an indicator. Bed temperatures were measured at six different locations, three at each side of the heating probe. The values of these temperatures were within $\pm 2\ ^{0}C$, and thus their arithmetic average was used in the computation of heat-transfer coefficients.

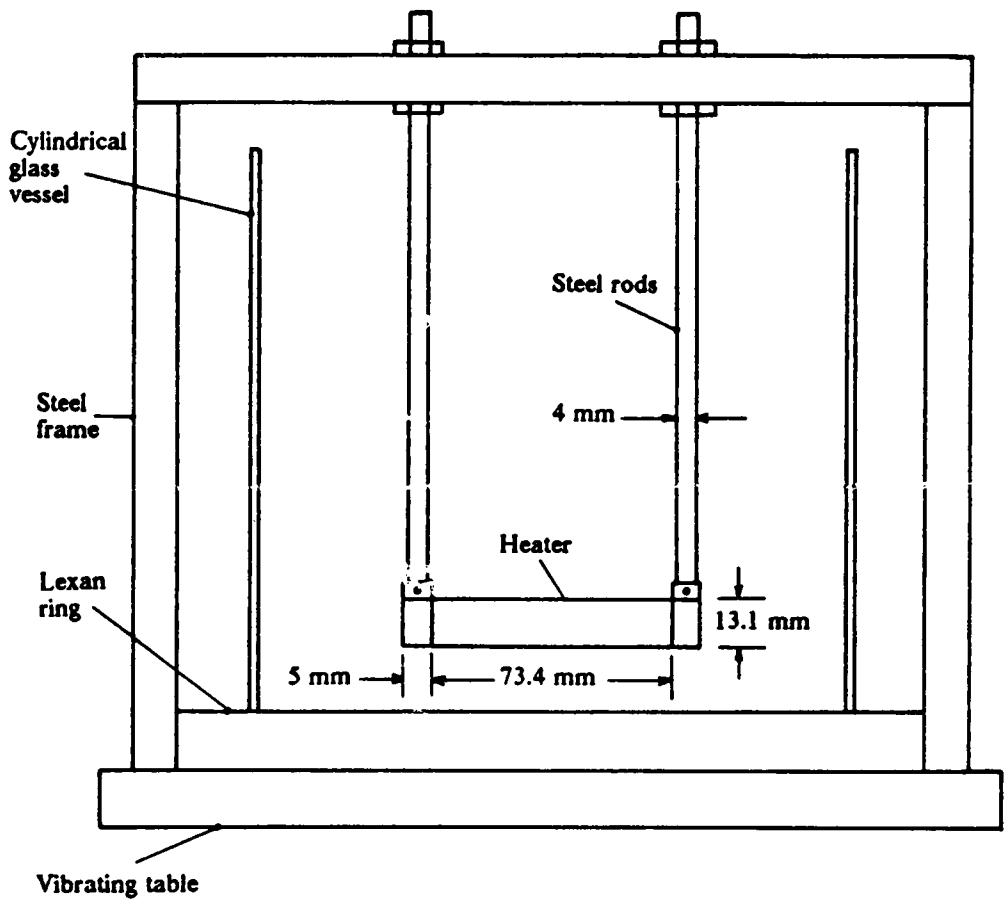

Figure 76. **Schematic diagram of the experimental heat-transfer system:** Cylindrical heating surface of 13.1 mm in diameter suspended 20 mm above the floor of a cylindrical glass vessel of 170 mm in diameter.

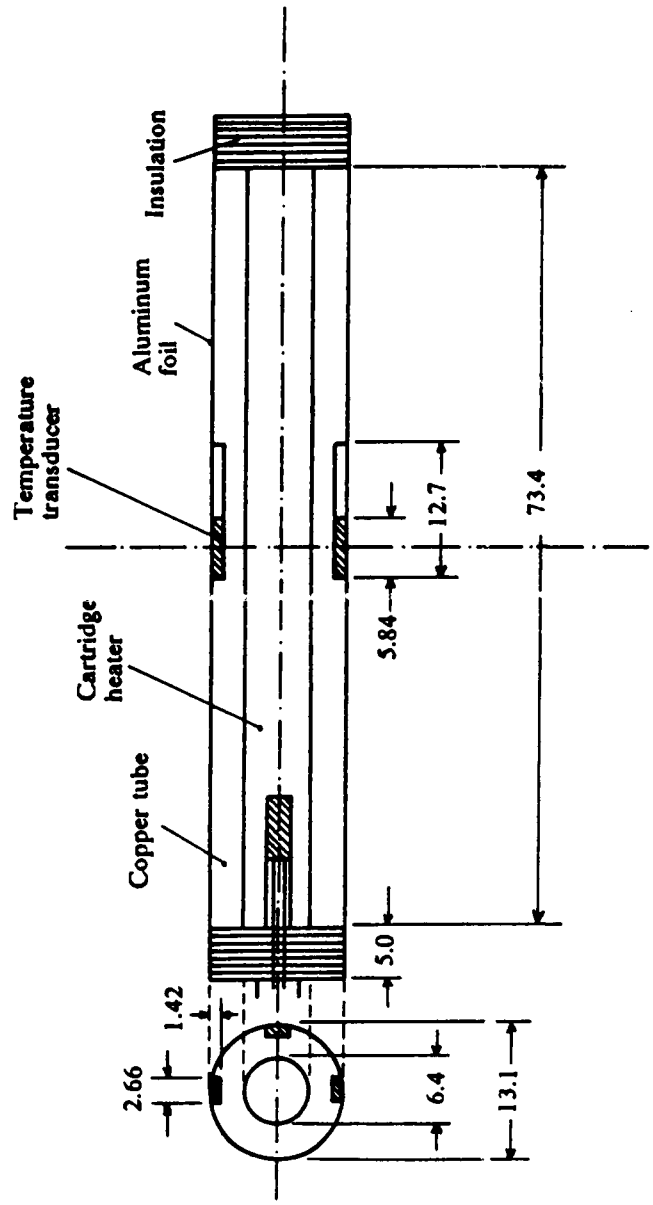

Figure 77. Diagram of a cylindrical heat-transfer surface: Units in mm (Huang[32]).

Differences between the heating-surface temperatures at the bottom and at the laterals of the probe were dependent on the vibrational intensity parameter K and on the particular solid-flow pattern. Since these temperature differences were within a few degrees, average values were used in heat-transfer calculations also.

The accuracy of the experimental system was quantitatively estimated in terms of two sources of error: (i) the error due to heat losses to the asbestos rings at the boundaries of the probe, and (ii) the error introduced by the grooves that housed temperature-sensing elements and their leading wires.

The surface area of the asbestos rings at the ends of the heating surface represent about 15% of the area of the heating probe. It was assumed that the temperature difference between the surface of the rings and the vibrated bed is less than half the difference between the probe and the bed. Then, for identical heat-tranfer coefficients, the asbestos rings transfer to the bed less than 8% of the total heat generated by the probe. The heat-transfer coefficient based on the area of the heating probe would, therefore, be about 8% higher than the actual heat-transfer coefficient.

The maximum error in the determination of heat-transfer coefficients caused by the presence of grooves on the heating surface can be estimated by making some assumptions. The grooves introduce an air layer betweem the floor of the grove and the aluminum foil that covers the heating probe. If it is assumed that this air layer totally insulates the floor of the groove from the aluminum foil, heat transferred from the foil to the bed above the location of the groove must be supplied to this region through conduction in the foil from the neighbor regions. Since the thermistors have an insulating layer at the opposite side of the sensing surface, identical process of heat conduction in the aluminum foil should also occur above the thermistors. For a maximum heat-transfer coefficient between the probe and the bed of 500 $W/m^2.K$, the maximum temperature difference on the foil between either the center of the groove or the center of the thermistor and the remainder of the heating surface was calculated as being 3 ^oC. Since this number represents about 10% of the measured temperature difference between the heating surface and the vibrated bed, the actual heat-transfer coefficient should be about 10% lower than the computed value.

Considering these two sources of error, the actual heat-transfer coefficients are at most 18% lower than the computed values. This discrepancy is dependent on the magnitude of the coefficients. The error is reduced as the coefficient decreases. For a heat-transfer coefficient of 250 $W/m^2.K$, the temperature difference on the aluminum foil computed in the previous paragraph drops to 1.5 ^0C, and the total error to 13%.

As shown in Figure 76 on page 191, the power- and thermistor leading-wires leaving the heating probe at its boundaries, due to their assymmetrical configuration, may introduce additional effects on the solid-circulation patterns in the vibrated bed. These effects could not be determined.

Despite the above inaccuracies, the relative magnitudes of the measured heat-transfer coefficients were considered representative of changes in bed and vibrational parameters.

5.1.2 Experimental conditions

Table 6 summarizes the experimental conditions used in this investigation. Three different types of solids were utilized in the determination of heat-transfer coefficients in vibro-beds: low-density glass beads, Master Beads, and glass nodules filled with CO_2. Glass nodules have a very low density, about 450 kg/m^3, and also a very low heat capacity. Their low density makes them very sensitive to drag forces.

Particle sizes ranged from 114 μm to 1190 μm. For the smaller sizes, the effects of solid bunkering and solid-circulation patterns on the heat-transfer coefficient were determined. The static bed-depth was kept constant at 30 mm in the experimental investigation.

The vibrational intensity parameter K was varied by using different vibrational amplitudes at a constant vibrational frequency of 25 Hertz. Heat-transfer coefficients were measured for K-values between 2 and 7.

Table 6 : Experimental conditions for heat-transfer studies

Item		Condition
A. Average particle diameter, μm		
Low-density glass beads		
ASTM mesh	-16 + 25	1190
	-20 + 30	707
	-40 + 50	353
	-100 + 140	125
Master Beads		
ASTM mesh	-20 + 40	674
	-60 + 100	235
	-100 + 200	114
CO_2-filled glass nodules		
ASTM mesh	-20 + 40	594
B. Particle density, kg/m^3		
Low-density glass beads		2500
Master Beads		3680
CO_2-filled glass nodules		450
C. Static-bed height, mm		30
D. Vibrational Conditions		
Frequency, Hertz		25
Vibrational intensity parameter K		2-7

5.2 *Experimental Results*

Heat-transfer coefficients were calculated from equation [2.1]:

$$Q = h A_h (T_h - T_b) \qquad [2.1]$$

In this equation, Q is the total heat input to the vibro-bed, A_h is the surface area of the heating probe, T_h is the average heating-surface temperature, T_b is the average bed temperature, and h is the heat-transfer coefficient between the heating surface and the vibrated bed.

Figure 78 shows the dependence of the heat-transfer coefficient on the vibrational intensity parameter K for beds of several particle sizes and types. For 125-μm and 353-μm low-density glass beads, and for 114-μm Master Beads, solid bunkering was observed at the wall of the cylindrical vibrating vessel. Solid-circulation in the bulk of these beds of particles followed a cross-flow pattern in relation to the probe, from the shallowest part toward the deepest part of the vibrated bed. For the remaining particle sizes and types, solid bunkering ocurred above the heating probe and yielded a symmetrical bed configuration.

The effect of solid-flow patterns on the heat-transfer coefficient in beds of small particles is presented in Figure 79 on page 198. Three different flow patterns with respect to the heating surface were investigated: (i) cross flow, (ii) parallel flow, and (iii) symmetrical flow. The latter is characterized by solid flow from the wall of the vessel toward the probe on both sides of the heating surface.

5.2.1 Effect of vibrational conditions

There appears a common trend on the dependence of the heat-transfer coefficient on the vibrational conditions, as characterized by the vibrational intensity parameter K. Heat-transfer performance is first improved when K is increased. Eventually, a maximum is reached, after which

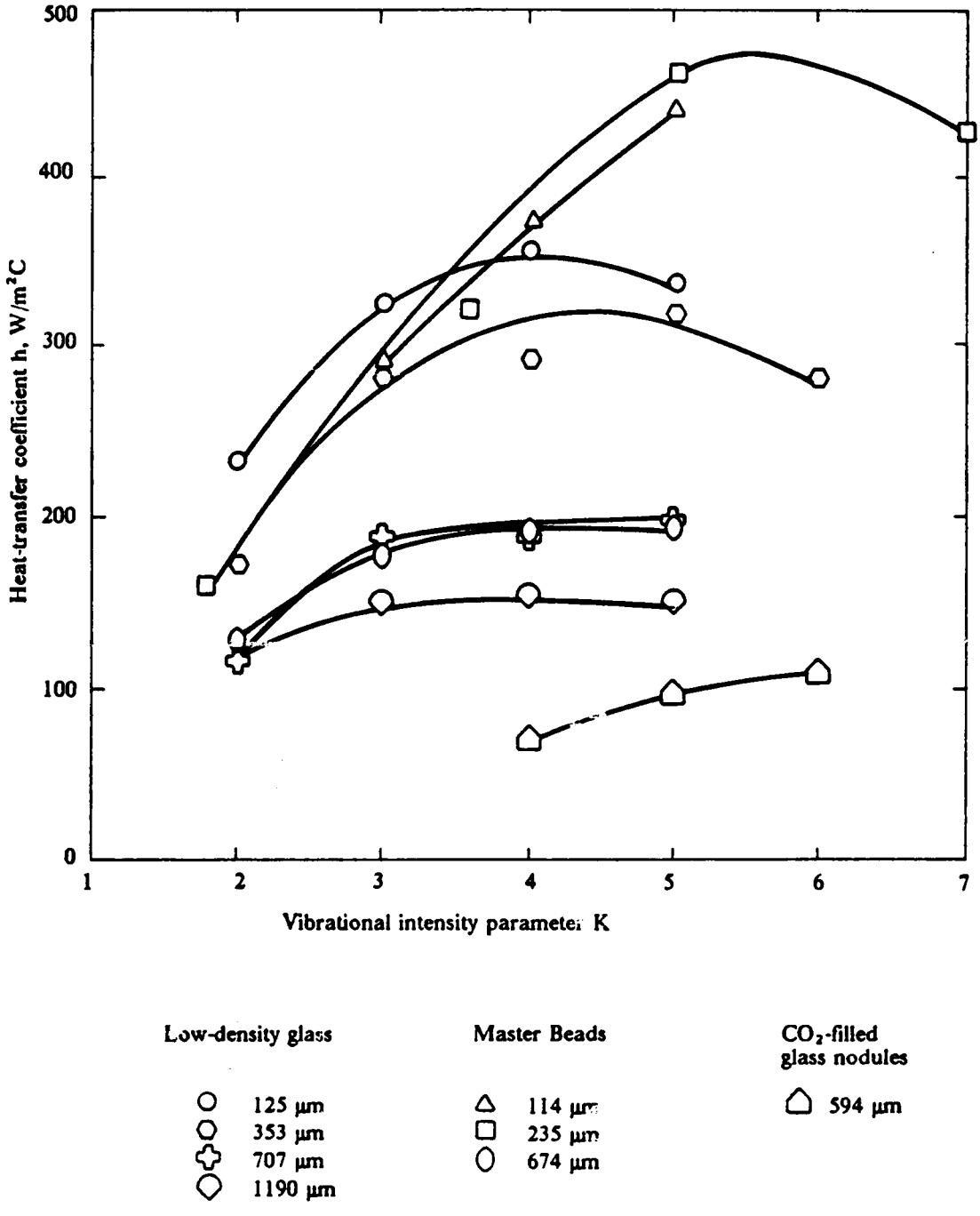

Figure 78. Effect of particle size and density on heat transfer in vibro-beds: Heat-transfer coefficients between a horizontal cylindrical heating surface and a layer of particles vibrated at a frequency of 25 Hertz.

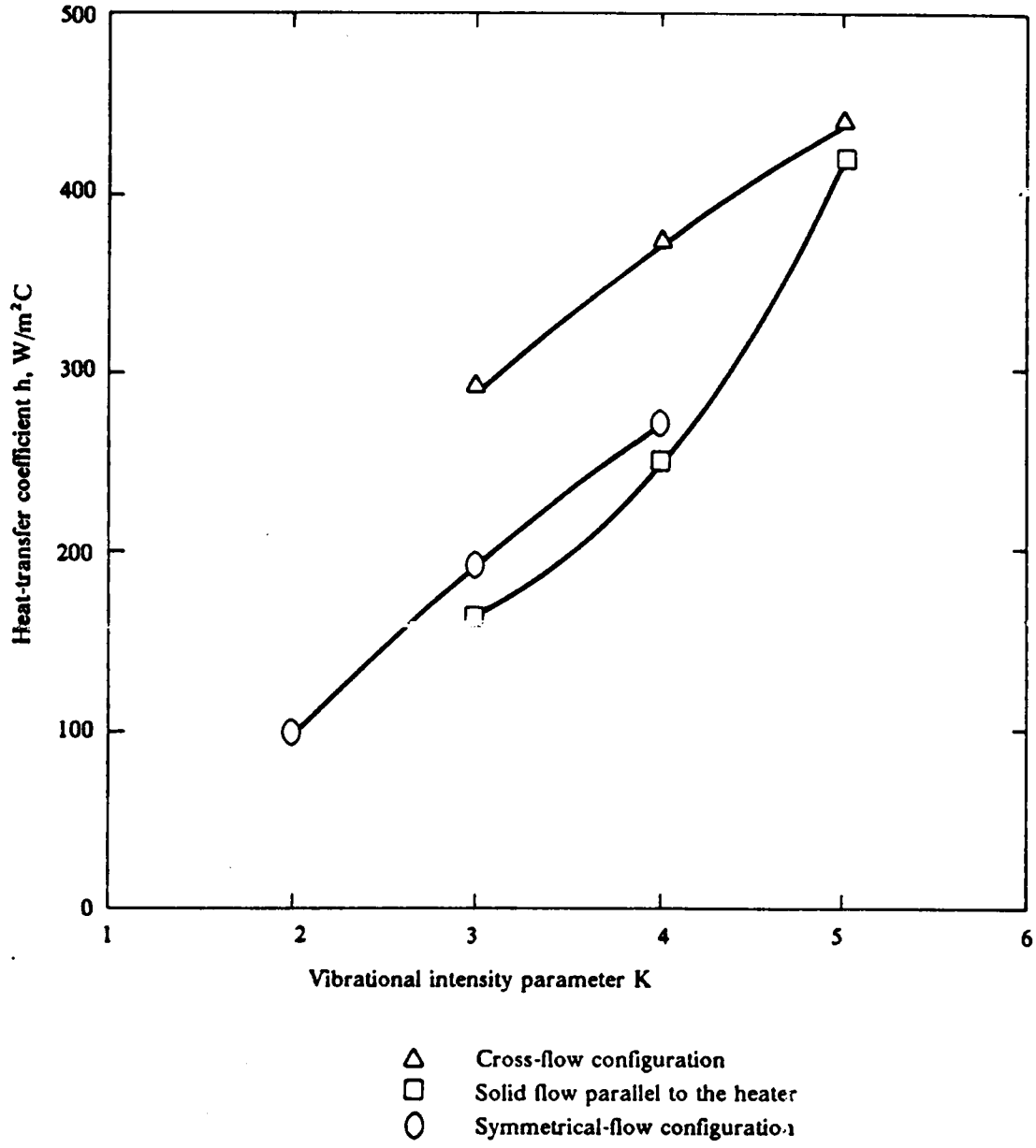

Figure 79. Effect of solid circulation on heat transfer in vibro-beds: Heat-transfer coefficients between a horizontal cylindrical heating surface and a layer of 114-μm Master Beads vibrated at a frequency of 25 Hertz.

the heat-transfer coefficient either decreases or levels off. The particular K-value at which the maximum coefficient appears is affected by the particle diameter and by the type of solid. In general, the maximum in the heat-transfer coefficient is displaced toward higher K-values as the particle size is reduced.

The effect of the K-value on the heat-transfer coefficient appears to be stronger below K = 3 than at higher values, and to decrease as the particle size is increased.

5.2.2 Effect of particle size

As shown in Figure 78 on page 197, the heat-transfer performance in beds of low-density glass beads increases continuously as the particle size is reduced. The maximum heat-transfer coefficient ranges from about 140 $W/m^2.K$ for 1130-µm particles to about 330 $W/m^2.K$ for 125-µm particles.

Beds of Master Beads yielded higher heat-transfer coefficients of approximately 460 $W/m^2.K$ for 235-µm particles. The particle-size dependance shows, however, a distinct behavior. On decreasing the particle size, a maximum heat-transfer coefficient was found for 235-µm particles. Further decreasing the particle size reduced the heat-transfer coefficient. The coefficient for the small 114-µm particles was, however, still increasing at K = 5.

The increase in the maximum heat-transfer coefficient obtained by reducing the particle size requires a larger vibrational-power input to the system. Beds of smaller particle sizes must be vibrated at higher K-values in order to achieve high heat-transfer coefficients. For the smallest Master Beads, however, larger power inputs does not seem to give better heat-transfer coefficients in the range of K-values investigated.

5.2.3 Effect of solid type

Low-density glass beads are less dense and have a lower volumetric heat capacity, ρC_p, than Master Beads. The values of the volumetric heat capacity, based on specific heats reported by Incropera and De Witt[53], are, respectively, 1875 kJ/m^3.K and 2815 kJ/m^3.K. Glass nodules are comparatively much lighter; by assuming the same C_p-value as for soda-lime glass, they have a volumetric heat capacity of only 338 kJ/m^3.K.

Figure 78 on page 197 shows that heat-transfer coefficients become more sensitive to the type of bed material as the particle size is reduced. Master Beads of 235-μm diameter yield higher heat-transfer coefficients than the smaller 125-μm low-density glass beads at K-values above 3. Below K = 3, however, these beds of glass beads present poorer heat-transfer performance than beds of 114-μm and 235-μm Master Beads.

For a particle size of about 700 μm, heat-transfer coefficients in beds of low-density glass spheres and of Master Beads are virtually identical at all K-values. Differences in solid density and in volumetric heat capacity seem not to be sufficiently high to affect heat-transfer performance. But coefficients in beds of 594-μm glass nodules, which have a much lower density and volumetric heat capacity, are considerably lower than those for either low-density glass spheres or Master Beads.

5.2.4 Effect of solid-circulation patterns

Distinct solid-circulation patterns could only be obtained in vibro-beds of small particles. Beds of particles of diameter above 500 μm allowed only one bed configuration, which was characterized by weak bunkering of solids above the heating surface.

The effect of solid-circulation pattern with respect to the cylindrical heating probe on the heat-transfer coefficient is illustrated in Figure 79 on page 198 for a vibro-bed of 114-μm Master

Beads. The best heat-transfer performance is obtained when bunkering occurs at the wall of the vibrating vessel and solid circulation is normal to the heating surface. In contrast to this cross-flow configuration, solid circulation parallel to the heating surface yields the lowest heat-transfer coefficients.

When bunkering is allowed above the heating surface, heat-transfer coefficients are lower than for the cross-flow configuration and slightly higher than those for the parallel-flow configuration. In this situation, solid circulation is also normal to the probe, but particles reach the probe from both sides of the surface and do not correspond to a cross-flow situation. Local solid-circulation loops form below the heating surface.

Heating-surface temperatures were very stable for K-values up to 3. At K = 4, little variations in these temperatures were detected. Variations of the order of $\pm 5\ ^{o}C$ were measured at K = 5, and were larger at the laterals of the heating-surface than below it. This behavior closely followed the degree of turbulence observed in the bed. which also increased as K was increased. At K = 6, solid-circulation patterns could no longer be controlled, and deepest and shallowest regions in the bed switched their locations very rapidly. This behavior was also observed in beds of 125-μm low-density glass beads. Bed instability, however, occurred at K = 5.

5.3 Comparison of Experimental Results with the One-layer Model

Sprung et al.[50] and Thomas et al.[51] investigated the effects of solid circulation and air gaps on heat-transfer rates in shallow beds of Master Beads. As shown in Figure 80, these heat-transfer studies consistently covered a wide range of particle sizes, including those used in the experimental investigation in vibro-bed dynamics described in Chapter 4 of this dissertation. Since the vibrational conditions and the bed depth were also the same as those utilized in this dissertation,

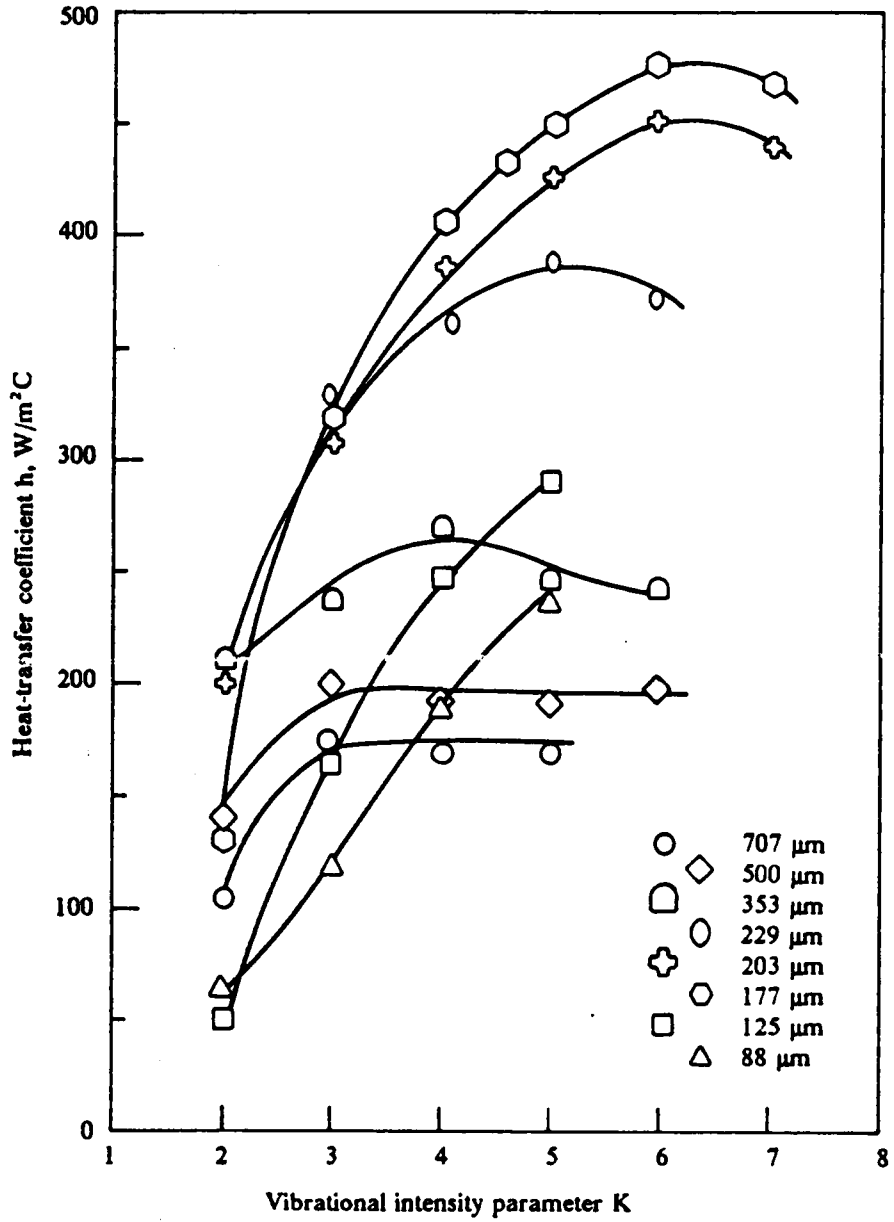

Figure 80. **Heat-transfer coefficients in vibro-beds of Master Beads:** 30-mm layer of particles vibrated at a frequency of 25 Hertz (Sprung et al.[50] and Thomas et al.[51]).

the results reported by Sprung et al. and Thomas et al. are included in this discussion of the one-layer model. The aim is to increase the accuracy in assessing the factors that affect the heat-transfer mechanism in shallow vibro-beds. The range of particle sizes for the heat-transfer coefficients presented in Figure 78 on page 197 and Figure 79 on page 198 is not the same as that used in the studies of bed dynamics reported in Chapter 4 of this dissertation.

5.3.1 The physics of heat transfer in vibro-beds

5.3.1.1 Solid circulation

The fact that vibro-beds display much higher heat-transfer coefficients than fixed beds suggests itself that the motion of particles induced by vibrations causes an improvement in heat-transfer performance. Figure 48 on page 116 illustrates the effect of the solid-circulation rate on the magnitude of the heat-transfer coefficient for different particle sizes according the one-layer model of Zabrodsky[18]. For a given particle size, the heat-transfer coefficient increases as the particle-velocity component that is normal to the heating surface is increased. In this case, the heat-transfer coefficient is independent of the heating-surface dimensions and of the orientation of the surface with respect to the particle flow. As seen in Figure 51 on page 123, the coefficient is dependent on the dimension and orientation of the probe when the particle velocity is parallel to the heating surface.

The significance of the effect of solid-circulation pattern on the heat-transfer coefficient in vibro-beds is illustrated in Figure 79 on page 198. Diagrams (a) and (b) of Figure 56 on page 140 show, respectively, the symmetrical and cross-flow solid-circulation patterns. When the particle flow is parallel to the cylindrical heating surface, the vibro-bed configuration is similar to diagram (b) of that figure. The longitudinal axis of the probe is, however, parallel to the solid-circulation path.

The experimental data in Figure 79 on page 198 demonstrate that particle renewal at the heating surface at lower K-values is predominantly caused by a particle-velocity component that is parallel to the heating probe. The highest coefficients were obtained for the cross-flow configuration. The parallel-flow configuration yielded the poorest heat-transfer performance. The local solid-circulation loops existing below the heating surface for the symmetrical-flow configuration reduce considerably the heat-transfer coefficients with respect to those for the cross-flow configuration. As discussed in section 4.4.2.2, particle interchange between the bulk of the bed and the local solid-circulation loops is very poor.

Figure 79 on page 198 shows that the difference in the magnitude of the heat-transfer coefficients for parallel- and cross-flow configurations decreases and tends to disappear. This observation indicates that the solid renewal at the heating surface becomes less dependent on the orientation of the surface as K is increased. According to the one-layer model for heat transfer, the particle-velocity component that is normal to the heating surface controls the process of solid renewal. The heating-surface temperature variations reported in section 5.2.4. seem to confirm this change in the mechanism of particle renewal at the heating surface.

The experimental observations on solid circulation described in section 4.4.2.2. of Chapter 4 indicated that the intensity of solid circulation increased as either the K-value was increased or the particle size reduced. In the range of experimental conditions investigated, the highest solid-circulation rates were observed in beds of 177-μm Master Beads. Further decreasing the particle size, reduced the circulation rates. Increasing the K-value was, therefore, equivalent to increasing the intensity of solid circulation in the vibrated bed.

Figure 78 on page 197, Figure 79 on page 198 and Figure 80 on page 202 show that, for any particle size, the heat-transfer coefficient first increases as the vibrational intensity parameter is increased. For most of the particle sizes, the coefficient reaches a maximum value, indicating that the vibrational intensity parameter (and hence the solid-circulation rate) alone cannot explain the experimental results and that the resistance of air gaps to heat transfer should be considered. The form of the curves in those figures is similar to that predicted by the one-layer model as illustrated in Figure 48 on page 116. This latter figure also shows that higher solid-renewal rates are needed

in order to achieve optimum heat-transfer performance as the particle size is reduced. Such a prediction was confirmed by the experimental behavior of the heat-transfer coefficient. The maximum heat-transfer coefficient occurred at higher K-values for small particles than for the large ones. In beds of Master Beads of diameter below 177-μm, the heat-transfer coefficient was still increasing at K = 5.

5.3.1.2 Air layers

Figure 48 on page 116 illustrates the dependence of the heat-transfer coefficient on the particle diameter according to the one-layer model. As the particle diameter is decreased, the maximum heat-transfer coefficient obtainable in a vibro-bed is reduced. This results from the decreasing nature with decreased particle diameter of the gas sub-layer between the heating probe and the first layer of particles. As seen in Figure 47 on page 113 and Figure 50 on page 121, the presence of air gaps reduces the maximum heat-transfer coefficient. The air gaps also cause the maximum heat-transfer coefficient to occur at lower solid-circulation rates than in the absence of gaps. Consequently, air gaps control the heat-transfer process at sufficiently high solid-circulation rates.

The initial growth of the heat-transfer coefficient with increasing vibrational intensities, independent of particle size and type, indicates that the corresponding increase in the air-gap size is not the limiting factor in heat-transfer performance. As shown in Figure 80 on page 202, heat-transfer coefficients for low K-values in beds of small particles are even lower than those in beds of large particles. This contrasts the behavior suggested by the size of air gaps, which increase as the particle diameter is increased. At low K-values, therefore, solid circulation seems to be the main factor in controlling the heat-transfer performance.

However, as K is increased, and so is the intensity of solid circulation, the heat-transfer coefficient approches larger values as the particle size is reduced. Such a behavior reflects the effect of the increased air-layer size on the magnitude of the heat-transfer coefficient as the particle size decreased.

The studies on bed dynamics reported in section 4.4.3.3 revealed that, at the same K-value, the size of air gaps at the heating-surface and the fraction of the vibrational cycle that the gaps remain open decrease, as the particle size is decreased. Since the air sub-layer also decreases with decreased particle size, heat-transfer coefficients are higher in beds of small particles than in beds of large particles.

As shown in Figure 80 on page 202, the beds of two smallest sizes of Master Beads do not display a maximum in the heat-transfer coefficient at K-values up to 5, and show poorer heat-transfer performance than beds of larger particles. Since no air gaps were observed in beds of small particles, the controlling factor of heat transfer could not have been the size of the air gaps at the heating surface. The intensity of solid circulation was observed to be poor in beds of small particles. As discussed in section 4.4.2.2, almost-dead regions of particles were identified below the heating-surface, covering about half of the probe area.

5.3.1.3 Gas convection

The experimental data do not allow a critical assessment of the contribution by gas convection to heat transfer. Heat transfer by gas convection is not taken into account by the one-layer model. The observed dynamical behavior of vibrated beds yields, however, some trends about the effect of gas convection.

Gauge pressures measured at the floor of the vibrating vessel were either lower below the heating-surface than or of the same magnitude as halfway between the probe and the side wall of a two-dimensional vibrated bed. The former case, which is typical of small particles, results in air-convective currents from the bulk of the bed toward the heating surface but not in the opposite direction. In the latter case, no horizontal gas-convection currents are present. These observations suggest that heat transfer by gas convection can be neglected in shallow vibrated beds.

5.3.1.4 *Particle properties*

The observation that heat-transfer performance in vibrated beds is strongly affected by the rate of particle renewal at the heating-surface immediately implies that the heat capacity of particles should also be significant in determining the magnitude of heat-transfer coefficients. Figure 48 on page 116 illustrates the effect of the solid heat capacity on the heat-tranfer coefficient as predicted by the one-layer model. For identical solid-renewal rates, beds of particles of higher heat capacity yield higher heat-transfer coefficients because these particles can absorb the same amount of thermal energy with a lower temperature increase than particles with a lower heat capacity.

The volumetric heat capacities of low-density glass spheres, Master Beads, and CO_2-filled glass noddles are, respectively, 1875 kJ/m^{3}K, 2815 kJ/m^{3}K, and 338 kJ/m^{3}K. The heat-transfer coefficients in beds of Master Beads and low-density glass spheres of particle diameter greater than 594 μm are considerably higher than the coefficients in a bed of 594-μm CO_2-filled glass noddles. These noddles displayed a greater solid activity, but had a much lower heat capacity because of their extremely low density.

5.3.1.5 *Summary*

The experimental heat-transfer coefficients in shallow vibro-beds could be qualitatively interpreted in terms of a heat-transfer mechanism composed of two steps: (i) the transfer of thermal energy through the gas layer existing between the bed of particles and the heating surface, and (ii) the absorption of heat by the streams of particles that transport the energy from the heating surface to the bulk of the bed.

In beds of large particles, the gas layer becomes very thick and is present during a considerable fraction of the vibrational cycle. The resulting low heat-transfer coefficients do not require large solid-circulation rates to transfer the thermal energy to the bulk of the bed. As the particle size is

reduced, and the size of the air layer is decreased, the increased heat-transfer coefficients require greater solid-circulation rates.

Higher rates of solid circulation are obtained by increasing the vibrational intensity parameter K. As K is increased, the thickness of the gas layer and the fraction of the vibrational cycle the probe is covered by air gaps become sufficiently large to overcome the benefits of improved solid-circulation rates. This effect was not observed under current experimental conditions in the beds of the smallest particles used in the investigation.

The dependence of the heat-transfer coefficient on the bed porosity could not be directly assessed from the experimental data. The contribution of the gas-convective component to heat transfer, however, seems to be negligible in terms of experimental results on bed dynamics that were described in Chapter 4.

In the range of the experimental conditions investigated, Master Beads yielded the highest heat-transfer performance. Beds of smaller density and heat capacity yielded lower heat-transfer coefficients.

5.3.2 Quantitative predictions

Since the actual air-gap size and particle-renewal time at the heating surface are unknown, comparison of experimental heat-transfer coefficients with those predicted by the one-layer model is not possible. The one-layer model permits, however, estimating the maximum heat-transfer coefficient in the absence of air gaps.

Figure 81 compares the theoretical estimates of the maximal heat-transfer coefficients by the one-layer model in the absence of air gaps to the maximal experimental heat-transfer coefficients determined in beds of Master Beads. The actual heat-transfer coefficients were smaller than the estimates because of the presence of air gaps around the surface of the heating probe. But the trend of the dependence of the coefficients on the particle size is closely followed by the experimental data.

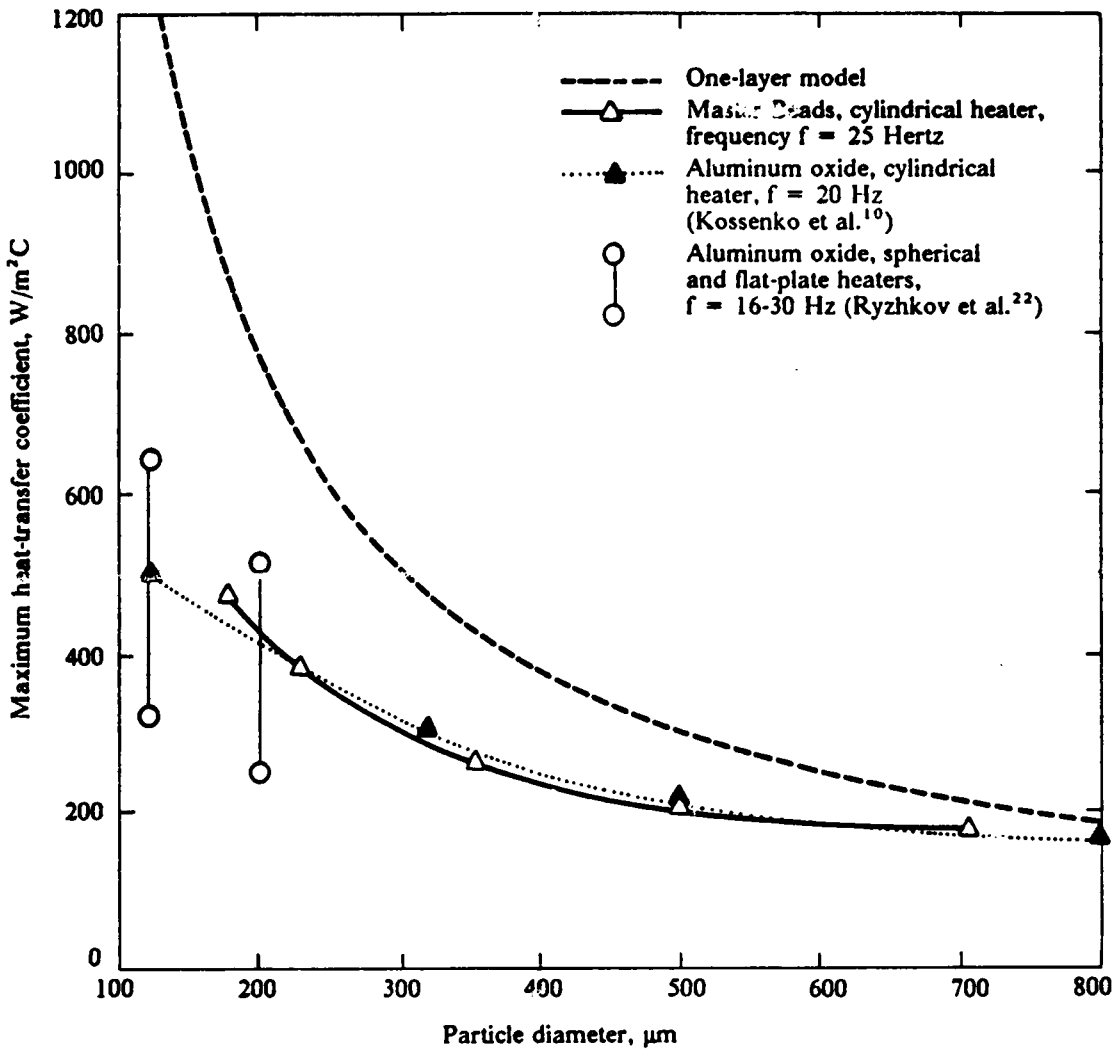

Figure 81. Theoretical and experimental maximum heat-transfer coefficients: Comparison of the maxima experimental heat-transfer coefficients with estimates from the one-layer model for vibro-beds of Master Beads vibrated at 25 Hertz.

As illustrated in Figure 81, the experimental heat-transfer coefficients in beds of Master Beads (86% of aluminum oxide) show good agreement with those obtained by Kossenko et al.[10] and Ryzhkov et al.[22] in vibro-beds of aluminum-oxide particles. Kossenko et al.[10] utilized a single row of horizontal, cylindrical heating surfaces immersed in beds of particles vibrated at a frequency of 20 Hertz. Ryzhkov et al.[22] obtained their data by using spherical and flat-plate heaters immersed in beds vibrated at frequencies between 16 and 30 Hertz.

The ratio of the actual heat-transfer coefficient in a bed of Master Beads to the theoretical estimate by using the one-layer model is plotted in Figure 82 against the particle size. It can be seen that the experimental value approaches the theoretical value as the particle diameter is increased. Since the air-gap size increases as the particle diameter is increased, one could have expected an opposite trend. The results suggest that the presence of air gaps is more effective in reducing heat-transfer coefficients in beds of small particles than in beds of large particles. As shown previously in section 3.2.3. of Chapter 3, a gap of 50 μm at a heating surface immersed in a bed of 200-μm particles decreases the coefficient by more than half of its value in the absence of a gap. Compared to the thickness of the air sub-layer, which was assumed as $d_p/6$ (d_p = particle diameter), such a gap size is proportionally greater for small particles when compared to large particles. As a consequence, the presence of smaller air gaps in beds of small particles may be more detrimental to heat transfer than the presence of larger gaps in beds of large particles. The one-layer model seems to establish a limit for the heat-transfer coefficient obtainable in vibro-beds.

5.4 Conclusions

Heat-transfer coefficients were determined between a horizontal, cylindrical heating surface and vibro-beds of Master Beads, and low- and high-density glass spheres, and CO_2-filled glass nodules. Beds were 30-mm deep and vibrated at a frequency of 25 Hertz. The vibrating vessel had a cylindrical geometry, and its diameter was 170 mm. The average size of particles ranged from 88 to 1190

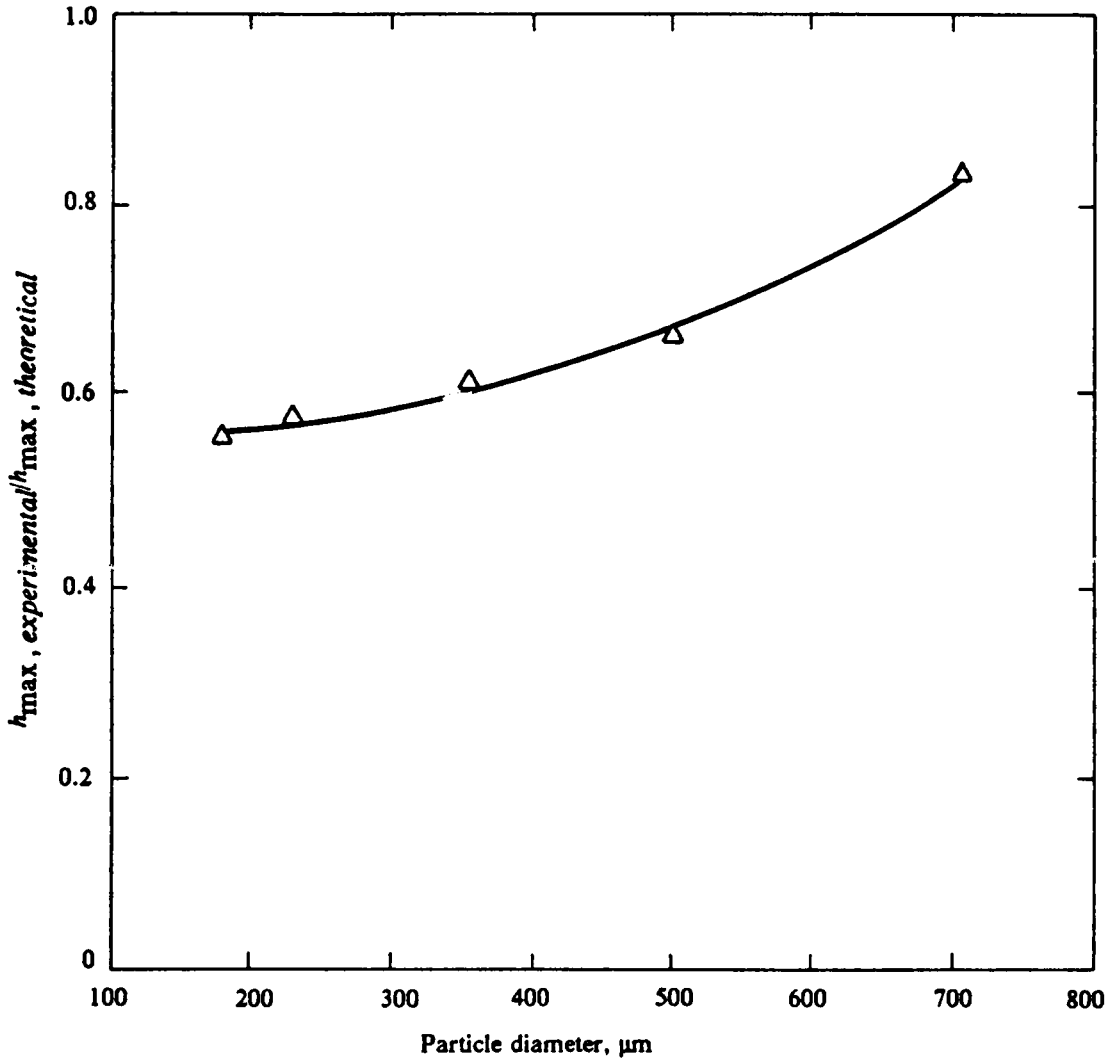

Figure 82. Ratio of maximum heat-transfer coefficients: Experimental-to-theoretical values. Theoretical estimates by the one-layer model for vibro-beds of Master Beads. Vibrational frequency: 25 Hertz.

μm. The temperature difference between the heating surface and the vibrated bed of solids was 30 ^{0}C. Conclusions were obtained from experimental results, and from their comparison with data reported in the literature and with theoretical models.

5.4.1 From experimental results

The analysis of the experimental results obtained in this investigation yielded the following conclusions:

(i) Beds of Master Beads present good heat-transfer performance when compared to lower-density materials. Decreasing the density of the bed material with respect to Master Beads reduces the magnitude of the heat-transfer coefficient.

(ii) At a constant particle size, the heat-transfer coefficient increases as the vibrational intensity is increased. For large particles, the heat-transfer coefficient attains a maximal value and then either decreases or approaches a constant value. For small particles, no maximum was detected under the present experimental conditions.

(iii) The heat-transfer coefficient is strongly dependent on the size of the bed material. The maximal value of the coefficient increases as the particle size is reduced.

(iv) In beds of small particles, the highest heat-transfer coefficients were obtained when the solid-flow path was normal to the axis of the cylindrical heating surface.

(v) As the vibrational intensity was increased, both solid-circulation rates and air-gap sizes increased. Initially, the positive effect of increased circulation rates offset the negative effect of larger air gaps. Eventually the gap size and the fraction of the vibrational cycle that the gap remained open compromised any increase in solid circulation. Further increasing the vibrational intensity led to a decrease in the heat-transfer coefficient because of the decreased contact between the particles and heating surface.

(vi) In beds of particles smaller than 177 μm, no air gaps were detected, but the rate of solid circulation decreased as the particle size was reduced. In the region below the heating probe, the

activity of particles became very poor, and their renewal almost inexistent. Thus, despite the absence of air gaps, heat-transfer coefficients decreased.

(vii) In beds of large particles, small circulation loops were observed above and below the probe. The detrimental effect of these loops on solid renewal at the heating surface does not severely limit the magnitude of the heat-transfer coefficient because of the large air-gap resistance to heat transfer.

5.4.2 From theoretical models

Based on the comparison of experimental data with available models, the following conclusions can be reached:

(i) The one-layer model, despite its simplicity, correctly predicts the relative effects on the heat-transfer coefficient of increasing the solid-circulation rates and air-gap sizes, and of changing the particle size, density and heat capacity.

(ii) The one-layer model, which assumes that the process of heat transfer is restricted to the first layer of particles, estimates upper bounds for the maximum heat-transfer coefficient if the presence of air gaps is neglected. It also predicts the trend of the dependence of the maximum coefficient on the size of bed material.

(iii) The discrepancy between the estimates of the one-layer model and the actual maximal heat-transfer coefficient decreases as the particle size is increased. This circunstance might reflect that air gaps are more effective in reducing the heat-transfer coefficient for the small particles than for larger ones.

5.5 *Recommendations.*

(i) The effects of varying bed depth, distance of the heating probe from the floor of the vessel, and diameter and geometry of the vibrating vessel on the magnitude of the heat-transfer coefficients should be investigated. Such variations might affect solid-flow patterns, and improve solid renewal at the heating surface.

(ii) In a continuous or a semi-continuous system, bunkering of solids might lead to bed dynamics distinct from batch systems. Such changes in solid behavior might affect the magnitude of the heat-transfer coefficient. Variations in trough dimensions and in the orientation of the heating surface should be considered in the investigation of continuous systems.

(iii) For continuous systems in which the conveying of solids is achieved by the inclination of either the trough or the vibrational force, the convective solid flow is expected to interfer with solid-circulation patterns induced by drag forces and with the development of air gaps. These effects on the heat-transfer coefficient should be experimentally investigated.

(iv) In applications involving the utilization of small particles, the absence of air gaps might impair the forced convection of the bed material through the trough. Controlled bed aeration at specific locations of the base plate might induce solid-circulation patterns favorable to heat-transfer purposes and to the conveying process. The feasibility and the effect of such an aeration could have practical interest, and should be included in an experimental program.

Part II: Synthesis of Silica Catalysts

6.0 Background and Objectives

6.1 Introduction

Much attention has been foccused on synthesis of zeolite catalysts over the past few decades. Zeolites are crystalline aluminosilicates whose structure contains a network of pores and cages. The total surface area of a zeolite is composed of: (i) the external surface area of the crystal, and (ii) the internal surface area of pores and cages. Dwyer[55] estimated that the internal surface area of a 1-μm zeolite crystal corresponds approximately to 99.5% of its total surface area. Catalytic applications of zeolites take advantage of the large internal surface area, but are limited to reactions involving molecules sufficiently small to diffuse into and out of the pore network. The maximum pore size of zeolites is of the order of 9 Å.

Some materials like clays and silicas have a layered structure and are, therefore, called layered materials. Each layer is a few atoms thick, but consists of an infinite two-dimensional network of atoms. A "crystal" of a layered material is composed of layers linked together by either van der Waals forces, or hydrogen bonds, or electrostatic forces between layers and cations present in the interlayer space. As in zeolites, the internal interlayer surface area is much larger than the external area of the material. In general, however, the layer separation is not sufficiently large to allow dif-

fusion of molecules into and out of the interlayer space. Expansion of the interlayer space could result in catalytic materials with pore sizes larger than those in zeolites.

The second section of this Chapter presents a review of some of the applications of layered compounds as catalysts. The third section reviews the techniques that have been utilized to expand the interlayer spacing of clay materials. Properties of a layered silica and its parent silicate, which could be used as supports for catalytic materials, are discussed in the fourth section. The fifth section describes the bonding of organosilicon compounds containing silanol groups to silica surfaces. The final section summarizes the results of the literature review, and presents the objectives of the studies on expansion of silica interlayer separation described in Chapter 7.

6.2 Layered Compounds as Catalysts

As schematically illustrated in Figure 83, layered compounds are characterized by their two-dimensional structure. In the case of montmorillonite, a natural clay, each layer consists of two arrays of silicon ions separated by a central array of aluminum and magnesium ions. Each silicon ion is coordinated to four oxygens; while each aluminum or magnesium ion, is coordinated to four oxygens and two hydroxy groups. The presence of magnesium ions in the aluminum positions results in a net negative electrical charge within the layers that is neutralized by alkali metal ions in the interlayer space. A net negative electrical layer-charge results also when aluminum ions occupy positions of silicon ions. Water molecules adsorbed into the interlayer space increase both interlayer spacing and distance. The interlayer distance is here defined as the distance between the centers of adjacent layers and the interlayer spacing as the distance between the surfaces of adjacent layers.

Natural clays were extensively used as cracking catalysts until the mid-1960s. The catalyst was prepared by acid treatment of montmorillonite, halloysite, or kaolinite[56]. Surface areas of montmorillonite determined by nitrogen adsorption (BET method) are of the order of 15-30 m^2/g,

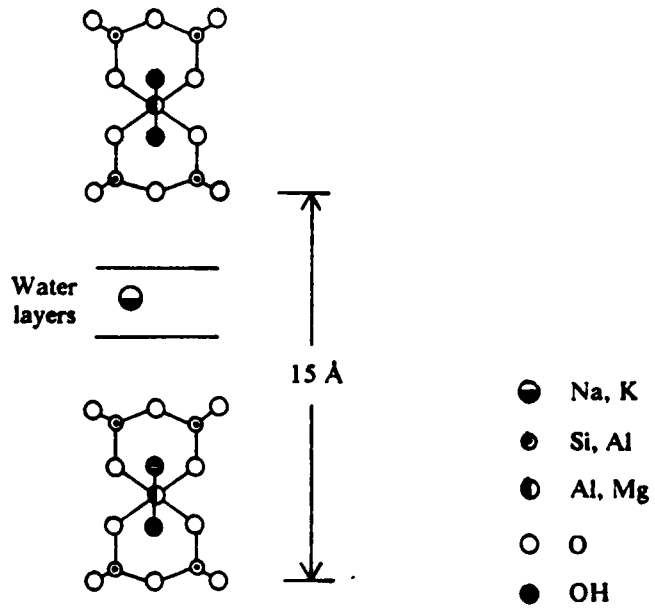

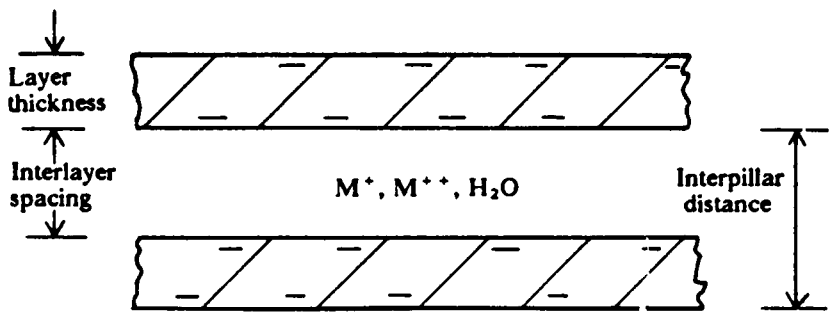

Figure 83. Schematic representation of two-dimensional compounds: (a) Layer structure of montmorillonite (Greenwood and Earnshaw[55]); (b) Layered material.

and do not include the large internal interlayer areas. Rupert et al.[56] reported surface areas by water adsorption in excess of 600 m^2/g. In contrast to nitrogen, water can penetrate the interlayer space of montmorillonite. Since cracking activity correlated well with surface areas determined by nitrogen adsorption, they concluded that the interlayer area was not involved in the cracking process.

Acid-treated montmorillonite was also utilized as a support for the production of hydrocracking catalysts. Thomas[57] described hydrocracking processes developed with tungsten, iron and nickel as the active catalytic phases. In both cracking and hydrocracking, however, natural clays have been replaced by synthetic amorphous silica-alumina and zeolite catalysts.

The utilization of synthetic clay-like materials as catalysts was reviewed by Swift[58] and Rupert et al.[56]. The synthesis of smectites was described by Granquist[59], and their cracking properties were reported by Cappell and Granquist[60]. As in montmorillonite, the layers of synthetic smectites consist of separate arrays of silicon and aluminum ions. In the silicon array, however, some of these ions are substituted by aluminum ions. The substitution confers to the layers a net negative electrical charge that is neutralized by ammonium ions present in the interlayer space. Calcination of the product at approximately 600 ^{0}C yields a catalyst whose cracking activity is comparable to commercial zeolites. The catalyst is thermally stable up to 900 ^{0}C, and its surface area as determined by nitrogen adsorption is 104 m^2/g.

Substitution of aluminum by nickel ions in synthetic smectites resulted in a hydroisomerization catalyst. The synthesis of this catalyst was discussed by Granquist[61], and its evaluation was described by Black and Swift[62]. Surface areas were dependent on the nickel content and ranged from 199 to 332 m^2/g. For hexane hydroisomerization, the hexane conversion increased from 45 to 86% but the selectivity to isomerized products decreased from 99 to 73% as the nickel content was increased.

According to Swift[58].synthetic clay-like materials have two advantanges: (i) the interlayer space allows synthesis of large molecules that would not fit in the cylindrical pore structure of zeolites; and (ii) the variety of ions that can be substituted for aluminum and silicon in the layers is wider than that in zeolites.

Layered materials that contain only silicon ions within the layers do not have a net negative electrical layer-charge. Within the layers, each silicon ion is coordinated to four oxygens, and each oxygen shared by two silicon ions. At a layer surface, terminal oxygen ions may be bonded either to metal ions or protons. In the present work, materials having metal ions bonded to surface oxygens will be called as metal polysilicates or simply metal silicates. If protons are bonded to surface oxygens, the material will be identified as a polysilicic acid, or a silic acid, or simply a layered silica. The utilization of layered silicas and silicates as catalytic materials or support for catalytic materials has not been reported in the literature.

6.3 Intercalation, Pillaring and Cross-Linking

Intercalation, pillaring, and cross-linking are terms used in the literature with layered compounds to describe processes that involve the introduction of chemical species into the interlayer space. There is no clear distinction among the concepts of intercalation, pillaring and cross-linking. Whittingham[63] defines "intercalation" as the reversible insertion of guest species into a layered or laminar host structure with maintenance of the structural features of the host. Rupert et al.[56] seem to reserve the term "clay pillaring" to the reversible or irreversible insertion of guest cations that expand the interlayer space of clays, creating a permanent porosity and allowing adsorption of other species. Thus, "swelling" or layer separation of clays by a swelling solvent like water is not considered a pillaring process. "Cross-linking" requires guest species to be chemically bonded to both of the surfaces that define the interlayer space, resulting in a rigid layer separation. In this dissertation, both cross-linking and pillaring are considered intercalation processes whether they are reversible or irreversible.

Interest in pillaring processes has been motivated by the potential utilization of pillared materials in catalytic processes that require catalysts with large pore size. Pore diameters in zeolites are limited to approximately 9 Å, which restricts the application of zeolites to reactions involving small

molecules. Pillaring of layered materials introduced the possibility of designing catalysts with a larger pore size by controlling the size of and the distance between the pillars.

Barrer and McLeod[64] were first in demonstrating the concept of the pillaring of clays. They utilized tetraalkylammmonium ions to increase the interlayer spacing of montmorillonite by approximately 4.5 Å. Barrer[65] reported surface areas by nitrogen adsorption as high as 180 m^2/g for montmorillonites pillared with monoalkylammonium ions. Figure 84 shows a schematical diagram of a pillared compound. By changing the type of ion and size of the alkyl chain of the ammonium ion, Barrer was able to obtain pillared compounds with different interlayer and interpillar spacings. The pillars, however, collapsed at temperatures of 200 to 250 ^0C. Barrer discussed the potential utilization of these compounds as molecular sieves.

Brindley and Sempels[66] utilized hydroxy-aluminum cations to pillar montmorillonite, obtaining interlayer spacings of 7.5 Å and surface areas of approximately 400 m^2/g. The cations were prepared by base hydrolysis of aluminum chloride in aqueous solutions and by reacting aluminum metal powder with an aqueous solution of aluminum chloride. Thermally stable materials were obtained upon calcination of the pillared compound at temperatures of 500 to 600 ^0C, where the hydroxy-aluminum cation was converted into its oxide form. Lussier et al.[67] presented pilot-plant catalytic-cracking data for the pillared clay and a conventional zeolite catalyst. The octane ratings of gasoline were the same, but the yield of gasoline from the pillared clay was approximately 10% lower than that for the zeolite. By using this same technique, pillared montmorillonites were prepared with hydroxy-zirconium[68], hydroxy-chromium[69], and hydroxy-titanium[70] cations. Surface areas ranged from 200 to 500 m^2/g.

Endo et al.[71,72] reported a technique for inserting pillars of silicon atoms in the interlayer space of montmorillonite, vermiculite and hectorite. Tris(acetylacetonato)silicon(IV) cations were intercalated in the clay materials, which were then calcined in air at 500 ^0C to remove the organic ligands. The resulting materials had surface areas up to 200 m^2/g, interlayer distances of 12.6 Å, and interlayer spacings of 3 Å. Endo et al. concluded that clay layers were separated by pillars of a single silicon atom. Despite the thermal stability of these materials, interlayer distances up to 18

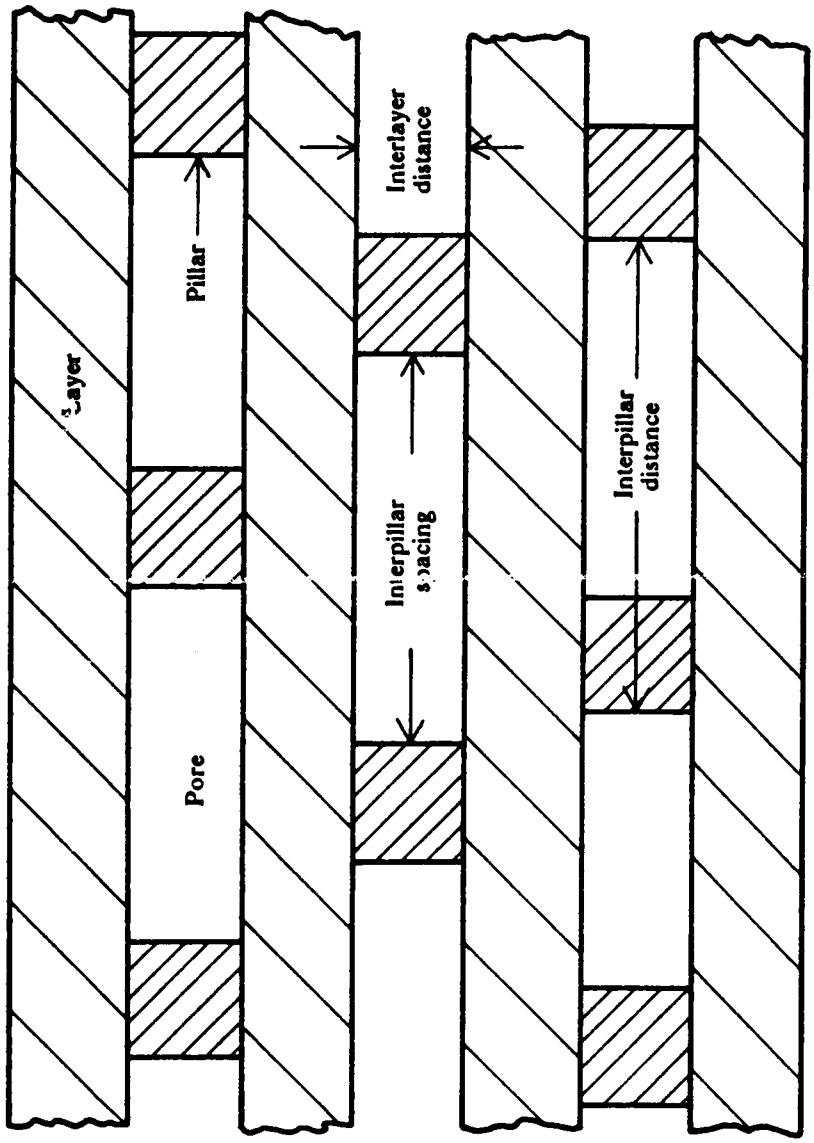

Figure 84. Schematic diagram of a pillared compound

Å were obtained by adsorption of glycerol and pyridine, indicating the absence of cross-linking. Also, no Lewis acidity was observed in the pillared hectorite.

Lewis et al.[73] described clays pillared by polyhedral, three-dimensional silica structures, resulting in clay layers separated by at least two silicon atoms. The three-dimensional silica structures were obtained by cyclic polymerization of monoorganyltrichlorosilanes and intercalated into the clay mineral. Calcination of the intercalated clay in air or steam at temperatures between 400 and 650 °C, resulted in pillared materials with surface areas of 150 to 400 m^2/g and interlayer spacings of 6 to 10 Å. Lewis et al. presented examples to demonstrate the utilization of the pillared clays as cracking catalysts and as supports for platinum in hydroisomerization reactions.

6.4 Na- and H-Magadiite

As previously mentioned, the catalytic applications of layered silicas and silicates have not been reported in the literature. The presence of terminal Si-OH groups on the surface of the layers seems, however, to provide favorable conditions for cross-linking of the layers by silicon pillars. In this section, some of the properties of a layered silica and the parent silicate are discussed.

The discovery of natural Na-Magadiite at Lake Magadi, Kenya, was reported by Eugster[74] in 1967. The synthesis and properties of synthetic Na-Magadiite were discussed by Lagaly and Beneke[75,76]. Hydrated Na-Magadiite is a layered silicate of composition $Na_2Si_{14}O_{29}.11H_2O$ and interlayer distance of 15.6 Å. The unit cell ($Na_2Si_{14}O_{29}.11H_2O$), which is defined as the smallest part of the structure that repeats itself, has a basal area (internal interlayer surface area) of approximately 54.7 $Å^2$. Na-Magadiite was transformed into quartz at 500 °C and into tridymite at 700 °C. The sodium ion can be exchanged with a variety of organic cations. Interlayer distances as high as 64 Å were obtained by intercalation of alkylammonium cations. Potentiometric titration of Na-Magadiite with HCl resulted in H-Magadiite, a layered silica with surface silanol groups (Si-OH).

The properties of H-Magadiite were reported by Lagaly and Beneke[77] as well as by Lagaly[78]. The composition and interlayer distance of hydrated H-Magadiite were determined as being $H_2Si_{14}O_{29}.5.4H_2O$ and 13.2 Å, respectively. When the layered silica was dehydrated at 300 °C, the interlayer distance decreased to 11.2 Å. Heating above 400 °C induced condensation of silanol groups with formation of siloxane bonds (Si-O-Si) between the layers.

Lagaly[78] found that H-Magadiite formed intercalation compounds with different kinds of organic compounds of high dipole moment and strong acceptor sites for hydrogen bonds. Intercalation was easier with hydrated rather than dehydrated H-Magadiite. Intercalated dimethylsulfoxide (DMSO) increased the interlayer distance to 15.8 Å. Further treatment of this intercalation compound with alkylamines expanded the interlayer distance up to approximately 65 Å. The capability of forming intercalation compounds was lost when H-Magadiite was heated to 400-600 °C because of cross-linking betweeen the layers by siloxane bonds.

Lagaly[78] found that exchange of silanol protons by organic cations was not feasible without first exchanging the protons by metal ions. The exchange of sodium ions for protons was very pH-dependent. At a pH of 6.0, only 15 % of the protons were exchanged. The percentage increased to 90 % at pH = 8.0. Complete exchange was attained at pH = 10.0. The surface acidity of H-Magadiite was very low when compared with that of an acid-treated clay catalyst[55]. The reactivity to Hammet indicators resulted in values of H_0 of 1.2-1.5 and < -8.2 for H-Magadiite and the clay catalyst, respectively. The higher the value of H_0, the lower is the acidity of the solid surface. Values of H_0 for H-Montmorillonite ranged from -5.6 to -8.2[55].

The nature of the silanol groups in H-Magadiite was studied by Rojo et al.[79]. IR spectra of H-Magadiite dehydrated at 150 °C showed a band at 3620-3640 cm^{-1} and another one at 3480 cm^{-1}, indicating different silanol environments. By comparison with the band of a free silanol group (3750 cm^{-1}), the band at 3480 cm^{-1} was attributed to groups involved in strong hydrogen bonds between adjacent layers of H-Magadiite. This latter band disappeared when H-Magadiite was heated up to 500 °C. Rojo et al. obtained a value of 3.5 Si-OH groups per 100 $Å^2$ for the silanol surface-density. The surface area of H-Magadiite was determined by adsorption of polar organic molecules as being 750 m^2/g.

The discussion in the preceeding paragraphs suggests that the surface acidity of H-Magadiite is not sufficiently strong for catalytic-cracking applications. However, the condensation of silanol groups at high temperatures seems to indicate favorable conditions for cross-linking of silicon derivatives containing silanol groups. Such a pillared material could be utilized as a support for catalytic materials.

6.5 *Coupling of Silicon Compounds to Silica Surfaces*

Arkles[80] discussed the coupling of organic groups to a silica surface by the utilization of trimethoxy-organosilanes ($RSi[OMe]_3$, where R is an organic ligand and Me is a methyl group). The procedure is schematically illustrated in Figure 85. A trimethoxy-organosilane is dissolved in ethanol containing a small amount of water. By hydrolysis, the methoxy groups are substituted by silanol groups. The resulting organo-trisilanol molecules ($RSi[OH]_3$) then condense and form oligomers that are called siloxanes. By adding silica particles to the solution, the silanol groups of the siloxanes and silica particles form hydrogen bonds. In the final step, the solids are separated from solution and heated to approximately 110 ^{0}C in order to bond the siloxane molecules to the silica surface.

This procedure suggests an alternate approach for the pillaring of layered silicas. Instead of a trimethoxyorganosilane, a siloxane compound with two methoxy groups, one at each of the extremities of the molecule, could be used for pillaring of H-Magadiite. Two possible reaction schemes are illustrated in Figure 86 on page 227: (i) the methoxy groups would react directly with the silanol groups of the silica surface, and (ii) the methoxy groups would be hydrolized, and the resulting silanol groups condense with those of the silica surface.

As discussed in section 6.3, Lewis et al.[73] described a procedure for the pillaring of clay materials by polyhedral, three-dimensional silicon structures, which are called oligosilsesquioxanes. Figure 87 on page 228 shows a single oligosilsesquioxane molecule and a diagram of the pillared

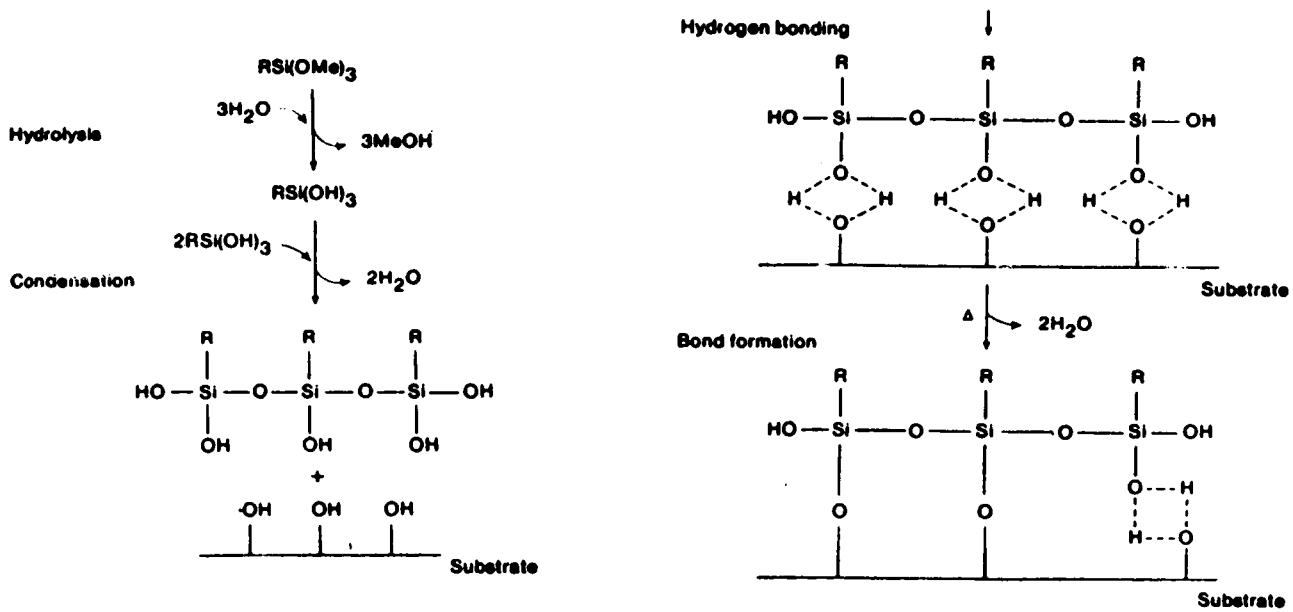

Figure 85. Coupling of organic groups to a silica surface: Schematic representation (Arkles[80]).

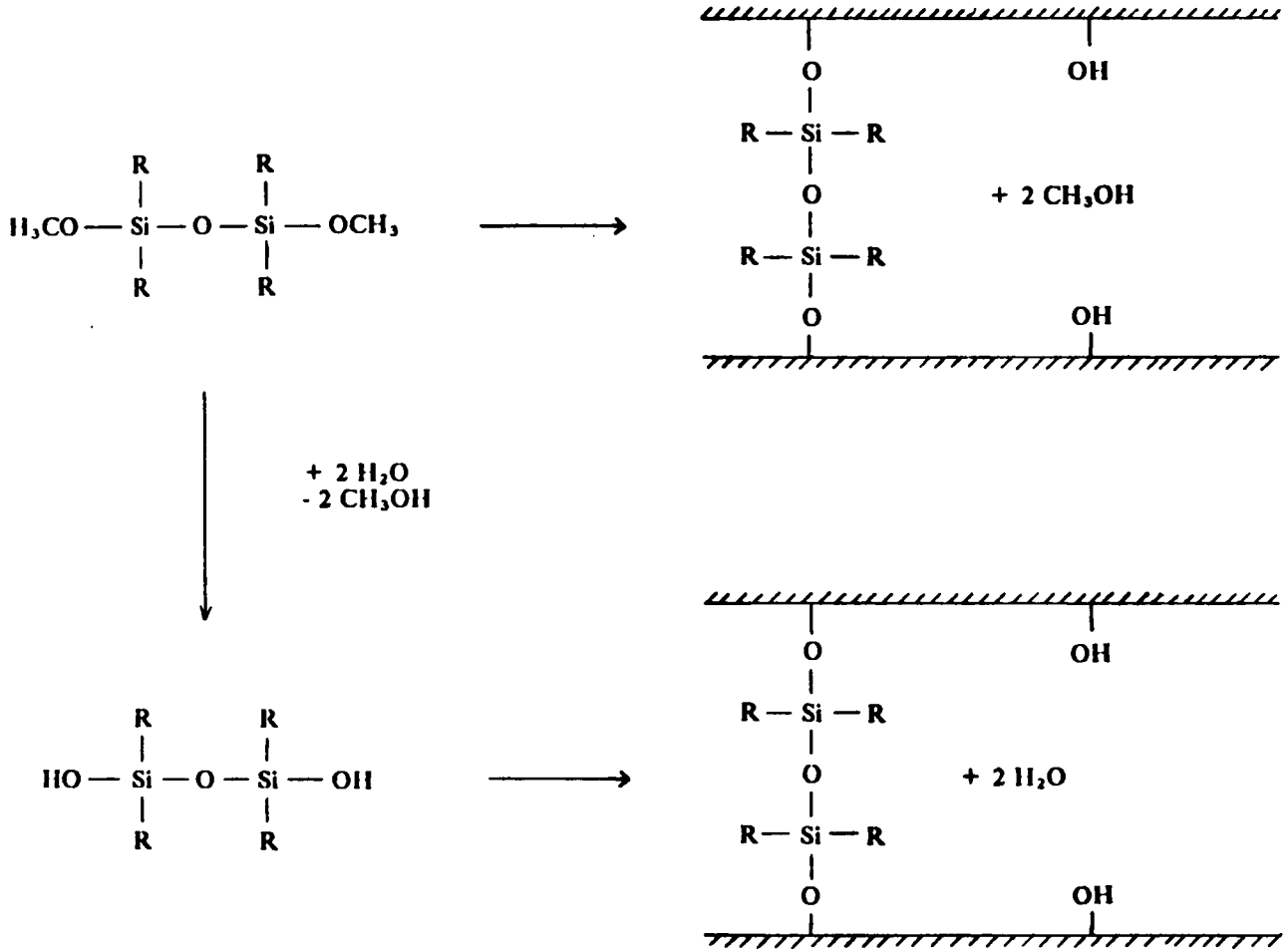

Figure 86. Schemes for pillaring of H-Magadiite: Utilization of a dimethoxytetraorganodisiloxane.

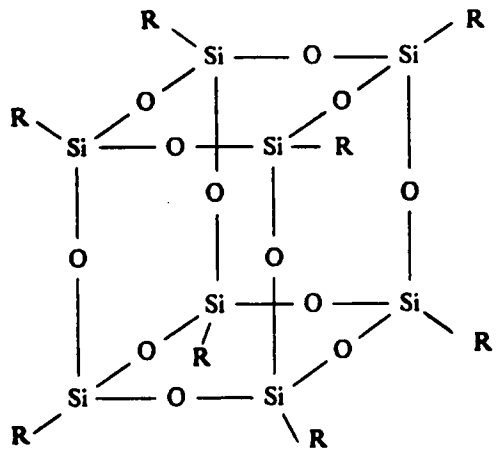

Figure 87. Pillaring of clays with oligosilsesquioxanes: (a) An oligosilsesquioxane molecule; (b) Representation of the pillared clay (Lewis et al.[73]).

clay. When a clay suspension was treated with a oligosilsesquioxane solution, the oligosilsesquioxanes would diffuse into the interlayer space. Lewis et al. reported that, depending on the nature of the organic ligands in the oligosilsesquioxane molecule, the oligosilsesquioxane could be bound to the surface of the clay by: (a) physical adsorption (van der Walls forces or hydrogen bonds) for ligands containing, for example, amine groups; and (b) ionic bonding for ligands containing cationic groups such as an ammonium cation. In the latter case, the oligosilsesquioxane would be exchanged for the interlayer cations of the clay. The calcination of such an intercalated clay at 100-800 ^{0}C for removing the organic ligands resulted in pillared materials of surface areas and interlayer spacings up to 400 m^2/g and 10 Å, respectively. Lewis et al. have not discussed the bonding between the three-dimensional silicon structure and the clay surface after calcination.

Lewis et al.[73] synthesized oligosilsesquioxanes by polymerization or condensation of trichloroorganosilanes in either polar or nonpolar organic solvents. As shown in Figure 88, condensation of trichlorosilanes may lead to oligosilsesquioxanes or large two- and three-dimensional oligomers. Lewis et al. reported that the formation of oligosilsesquioxanes is favored in dilute solutions of the tricholoroorganosilane and in the presence of acid and base catalysts. Low temperatures are preferred.

A procedure similar to that of Lewis et al. seems to be applicable to layered silicas, for example H-Magadiite. Oligosilsesquioxanes as well two- and three-dimensional oligomers (Figure 88) could be inserted into the interlayer space of H-Magadiite. During calcination of the resulting material, cross-linking between the silicon of the oligomer and the silica surface by siloxane bonds is likely to occur. This should result in pillars whose structure is similar to and as stable as H-Magadiite.

6.6 Summary and Proposed Investigation

The reported experimental results on the modification of layered compounds for catalytic purposes can be summarized as follows:

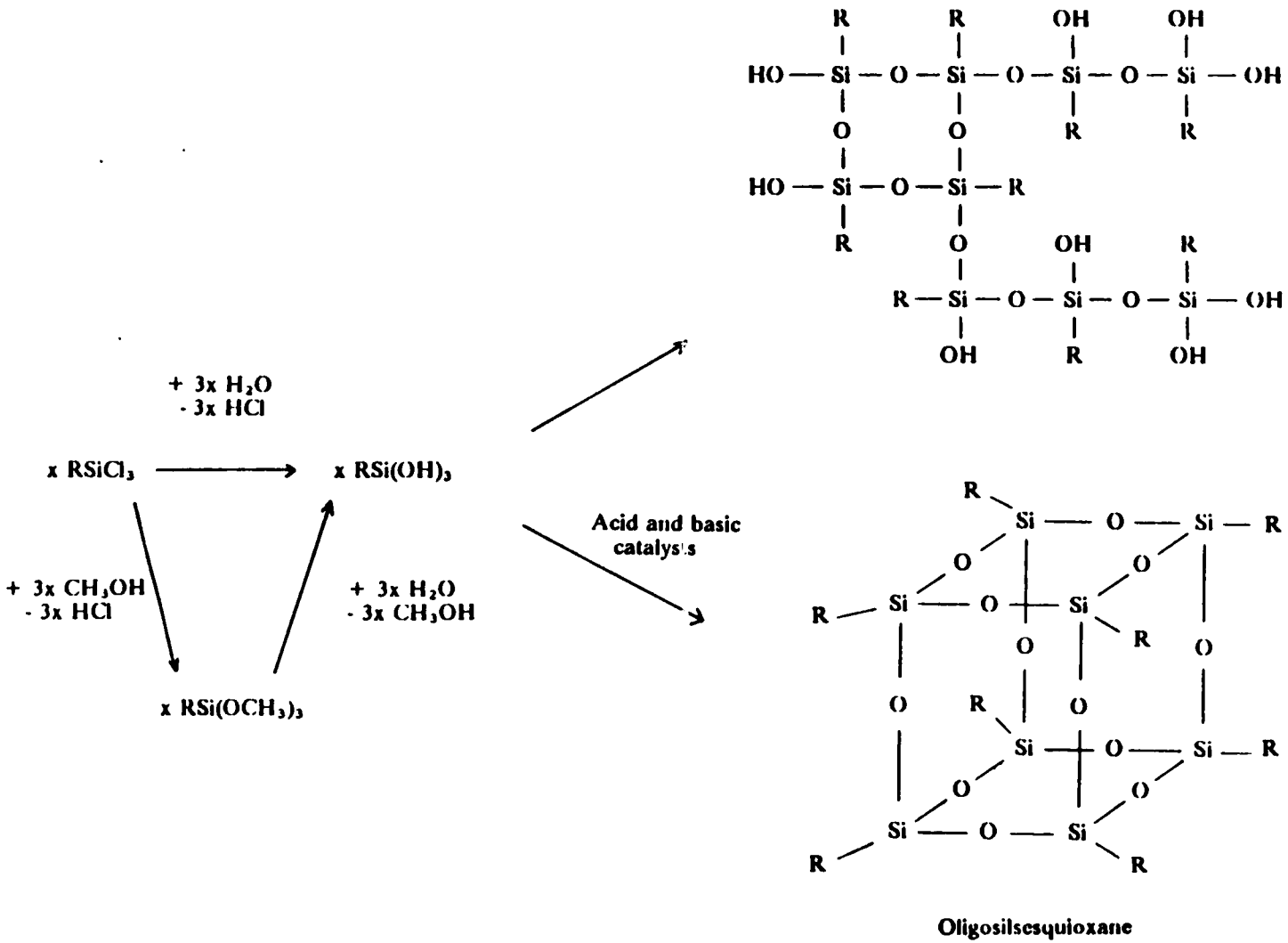

Figure 88. Polymerization of trichloroorganosilanes

(1) Intercalation, pillaring and cross-linking techniques are aimed at developing catalysts with large pore size and surface area;

(2) Application of these techniques has been restricted to the modification of clay-like materials;

(3) Organo-silicon compounds containing silanol groups have been bonded to silica surfaces;

(4) The presence of silanol groups on the interlayer surfaces of H-Magadiite suggests that silica pillars containing silanol groups can be used to cross-link the surfaces of the layers of H-Magadiite by the formation of siloxane bonds;

(5) The resulting layered compounds could be utilized as supports for catalytic materials.

The work reported in the following Chapter of this dissertation is intended to demonstrate the feasibility of the expansion of the interlayer spacing of H-Magadiite by introducing pillars which contain silicon atoms. In order to accomplish this objective, the work undertaken was divided into the following steps:

(i) Synthesis of Na- and H-Magadiite;

(ii) Intercalation of siloxanes and oligosilsesquioxanes into the interlayer space of H-Magadiite; and

(iii) Characterization of the resulting materials.

7.0 Experimental Results

The first section of this Chapter describes the experimental procedures utilized in the synthesis and preparation of layered materials and their intercalation compounds. This section presents procedures for the synthesis of Na-Magadiite, preparation of H-Magadiite, and intercalation of organosilicon compounds into H-Magadiite. Na-Magadiite, the parent material in the investigation, is a layered silicate which was synthesized at two different reaction conditions. H-Magadiite is a layered silicic acid derived from Na-Magadiite by exhanging protons for the sodium ions.

In the second section, the intercalated compounds are discussed in terms of the characteristics of the intercalation procedures and of the properties of the synthetic materials as determined by X-ray diffraction, thermal analysis, infrared absorption, and scanning electron microscopy. Surface areas and adsorption data as well as ion-exchange properties are also reported.

7.1 Experimental Procedures

7.1.1 Synthesis of Na-Magadiite

Na-Magadiite from three different sources was utilized in the experimental program described in this Chapter: (i) samples provided by Dow Chemical Company, (ii) Na-Magadiite synthesized in the Catalysis Laboratory before the beginning of the experimental program, and (iii) Na-Magadiite synthesized during the execution of the experimental program. During the execution of the experimental program, Na-Magadiite was synthesized by the two procedures described below: (1) Procedure A, which was developed by Saldarriaga[81], and (2) Procedure B, which is a modification of the experimental conditions of Procedure A. The initial molar composition of the reacting mixture was the same in both procedures: $Na_2O : 5SiO_2 : 122H_2O$.

7.1.1.1 Procedure A[81]

1.72 g of NaOH (Fisher Scientific) was dissolved in 34.6 g of deionized water. The solution was added to 15.0 g of colloidal silica (Ludox HS-40, Dupont De Nemours) and stirred for one hour for homogenization. Teflon-lined steel-bomb reactors were filled with the resulting mixture and placed in an oven whose temperature was 175 ^{0}C. After a reaction time of 21.5 hours, the reactors were taken out of the oven and quenched with tap water. The contents of the reactors were filtered, and the cake washed with small amounts of deionized water. The product was then air-dried at 100 ^{0}C for 2 hours.

7.1.1.2 Procedure B

4.08 g of NaOH (Fisher Scientific) was dissolved in 86.4 g of deionized water, and the resulting solution added to 37.6 g of Ludox HS-40 (Dupont De Nemours). After stirring for one hour, the mixture was transferred to a Teflon vessel, and the vessel hermetically closed. The mixture was allowed to react at a temperature of 97 °C for 49 days. The vessel was then quenched in tap water, the contents of the vessel filtered, and the solid product air-dried at 100 °C for 2 hours.

7.1.2 Preparation of H-Magadiite

H-Magadiite was prepared according to a procedure reported by Lagaly and Beneke[76,77].

A suspension of 20 ml of deionized water per 1.5 g of Na-Magadiite was stirred for one hour for homogenization. This suspension was titrated with a 0.1 N aqueous solution of HCl up to a pH of 2.0 over a period of 24 hours. The suspension was kept at the same pH and under continuous stirring for another 24 hours. The suspension was then filtered, and the cake washed with small amounts of deionized water. The product was vacuum-dried for at least 8 hours.

7.1.3 Intercalation of organo-silicon compounds into H-Magadiite

Intercalation experiments were performed with: (i) 1,1,3,3,5,5-hexamethyldiethoxytrisiloxane, and (ii) organyltrichlorosilanes (phenyltrichlorosilane and cyclohexyltrichlorosilane). All of the organo-silicon compounds were provided by Petrarch Systems, Inc.. Table 7 and Table 8 on page 237 summarize, respectively, experimental conditions utilized in the intercalation of trisiloxane and tricholorosilanes into H-Magadiite. A typical experimental procedure of each of the two sets of intercalation experiments reported in these tables is described below.

Table 7 : Experimental conditions for reaction with trisiloxane

Experiment	Reactants	Solvent	Reaction time, hrs	Parent Na-Magadiite
SLX1	0.5 g H-Magadiite 0.6 ml trisiloxane	4 ml DMSO[1] 4 ml ethanol	44	Dow Chemical
SLX2	0.51 g H-Magadiite 0.6 ml trisiloxane	8 ml ethanol	48.5	Dow Chemical
SLX3	0.50 g H-Magadiite 0.6 ml trisiloxane	8 ml ethanol	120	Dow Chemical
SLX4	0.50 g H-Magadiite 0.6 ml trisiloxane 0.4 ml water	8 ml ethanol	120	Dow Chemical
SLX5	1.18 g H-Magadiite 1.4 ml trisiloxane 0.95 ml water	19 ml ethanol	96	Catalysis Lab-VPI
SLX6	0.4 g H-Magadiite 0.6 ml trisiloxane 0.4 ml water	8 ml DMSO[1]	144	Dow Chemical
SLX7	0.5 g H-Magadiite 0.6 ml trisiloxane	8 ml ethanol	288	Synthesized at 175 °C
SLX8	1.00 g H-Magadiite 1.2 ml trisiloxane	16 ml hexane	32	Synthesized at 175 °C
SLX9	0.83 g H-Magadiite 0.4 ml trisiloxane 1 ml water	24 ml ethanol	40	Synthesized at 175 °C
SLX10	0.93 g H-Magadiite 0.3 ml trisiloxane	16 ml ethanol	24	Synthesized at 100 °C

Table 7 : Continued

Experiment	Reactants	Solvent	Reaction time, hrs	Parent Na-Magadiite
SLX11	1.00 g II-Magadiite 0.3 ml trisiloxane	16 ml ethanol	24	Synthesized at 100 °C
SLX12	1.00 g II-Magadiite	16 ml ethanol	24	Synthesized at 100 °C
SLX13[2]	1.50 g II-Magadiite 0.5 ml trisiloxane 1 ml water	19 ml ethanol	24	Synthesized at 100 °C
SLX14[3]	1.00 g II-Magadiite 0.9 ml trisiloxane 0.3 ml water 0.2 ml conc HCl	7 ml ethanol 12 ml water	3	Synthesized at 100 °C

[1] Dimethylsulfoxide
[2] pH adjusted from 3.9 to 6.8 with concentrated NH_4OH
[3] Same experimental procedure as that for trichlorosilane

Table 8 : Experimental conditions for reaction with trichlorosilanes

Experiment	Intercalating solution	H-Magadiite suspension	pH	Parent Na-Magadiite
SLN1	0.7 ml phenyltrichlorosilane 6.3 ml methanol 0.4 ml water	1.5 g H-Magadiite 18 ml water	6.6[1]	Synthesized at 100 °C
SLN2	0.7 ml cyclohexyltrichloro-silane 6.3 ml methanol 0.4 ml water	1.2 g H-Magadiite 15 ml water	6.7[1]	Synthesized at 100 °C
SLN3	0.7 ml phenyltrichlorosilane 6.3 ml methanol 0.4 ml water	1.2 g H-Magadiite 15 ml water	6.7[2]	Synthesized at 100 °C
SLN4	1.0 ml phenyltrichlorosilane 9.0 ml methanol 0.6 ml water	2.1 g H-Magadiite 25.2 ml water	6.3[3]	Synthesized at 175 °C
SLN5	1.0 ml phenyltrichlorosilane 9.0 ml methanol 0.6 ml water	2.1 g H-Magadiite 25.2 ml water	---[4]	Synthesized at 175 °C

[1] pH adjusted with concentrated NH_4OH during reaction.
[2] 0.3 ml concentrated NH_4OH added to intercalating solution. Final pH adjusted during reaction.
[3] pH adjusted with 50 water-50 conc NH_4OH during reaction.
[4] No addition of NH_4OH; pH very low, not measureable.

7.1.3.1 Typical experimental procedure for trisiloxane (SLX3)

0.6 ml of 1,1,3,3,5,5-hexamethyldiethoxytrisiloxane was mixed with 8 ml of anhydrous ethanol and 0.4 ml of deionized water. The resulting mixture was transferred to a Teflon vessel containing 0.5 g of H-Magadiite. The suspension was allowed to react at room temperature (22-25 ^{0}C) and under continuous stirring for 120 hours. The solid product was separated by filtration, washed with small amounts of ethanol, air-dried at 130-150 ^{0}C for one hour, and weighed.

7.1.3.2 Typical experimental procedure for trichlorosilanes (SLN1)

Step 1: 0.4 ml of deionized water was added to a solution of 0.7 ml of phenyltrichlorosilane ($[C_6H_5]SiCl_3$) in 6.3 ml of methanol contained in a Teflon vessel that had been immersed in an ice bath (T = 0.5 ^{0}C). The mixture was stirred for one hour while the temperature was maintained between 0.5 and 3 ^{0}C.

A suspension of 1.5 g of H-Magadiite in 18 ml of deionized water was at the same time stirred at room temperature during 45-50 minutes for homogenization. The pH of the suspension was measured as being 4.2, and the vessel containing the suspension placed into the ice bath.

Step 2: The mixture containing phenyltrichlorosilane was rapidly poured into the suspension of H-Magadiite. The extremely low pH of the resulting mixture was not measurable with the pH-meter. The pH of the mixture was adjusted to 6.6 by adding concentrated ammonium hydroxide (NH_4OH - Mallinckrodt) over a period of 45 minutes. Approximately 0.9 ml of ammonium hydroxide were needed to reach the final pH. The mixture was then maintained under stirring and at a temperature of 0.5-3 ^{0}C for 75 minutes. The total reaction time was 2 hours.

The final suspension was filtered and the filtration cake washed with small amounts of deionized water. The solid product was vacuum-dried at room temperature for approximately 20 hours and weighed.

7.1.4 Calcination of intercalated compounds

Intercalated compounds obtained by the preceeding procedures were calcined in ambient air and at two different temperatures: 470 and 650 °C. For calcination at 470 °C, the solid sample was heated up to the calcination temperature over a period of 1.5 hours and then maintained at this temperature for one hour. For calcination at 650 °C, the temperature of the solid sample was raised to 650 °C in 2 hours and kept at this value for one hour.

7.2 Results and Discussion

Experiments listed in Table 7 on page 235, which correspond to the intercalation of trisiloxane into H-Magadiite, resulted in materials of the same interlayer distance as that for the material intercalated with ethanol in the absence of trisiloxane (SLX12 in Table 7 on page 235). After dehydration at high vaccum and a temperature of 300 °C, the surface area of the intercalated compounds was identical to that of H-Magadiite, indicating no expansion of the interlayer spacing. Because of these observations, the discussion of the experimental results concerned with trisiloxane intercalation was not included in the following sections of this dissertation.

The discussion of experimental results was divided into the following topics:

(a) Intercalation and calcination;

(b) X-ray diffraction analysis;

(c) Thermal analysis;

(d) Infrared spectra;

(e) Surface area and adsorption data;

(f) Ion exchange; and

(g) Scanning electron microscopy

7.2.1 Intercalation and calcination

Intercalation experiments with trichlorosilanes are listed in Table 8 on page 237. Experiment SLN1 resulted in a sticky product that was not dry after approximately 18 hours of vacuum-drying at room temperature. The material was ground and returned to the drying oven for two additional hours. The amount of dry product was about 25 wt% larger than that of H-Magadiite at the beginning of the experiment. This yield was identical to those of intercalation experiments SLN4 and SLN5. Experiment SLN5, however, resulted into a non-sticky intercalated compound that was easily ground. No ammonium hydroxide was utilized in this latter experiment.

The second step of the experimental procedure described in section 6.2.3.2, which concerns the intercalation of trichlorosilane into H-Magadiite at temperatures of 0.5 to 3.0 °C, was performed at room temperature (22-25 °C) in experiments SLN2 and SLN3. At the end of these experiments, a considerable fraction of the solid product was literally glued to the magnetic stirring bar and the walls of the Teflon vessel. The recovered amount of product was less in weight than the initial amount of H-Magadiite.

In experiment SLN3, approximately 0.3 ml of concentrated ammonium hydroxide was added to the phenyltrichlorosilane solution before its addition to the H-Magadiite suspension. On adding the ammonium hydroxide to the phenyltrichlorosilane solution, a white solid was observed to immediately precipitate out of solution. The solid was identified as ammonium chloride by X-ray diffraction, indicating that part of the HCl present in the solution had been neutralized by the hydroxide.

In a separate experiment, the pH of a phenyltrichlorosilane solution was adjusted to 8.5 with concentrated ammonium hydroxide. Solids precipitated out of solution, and large amounts of a very dense and sticky material deposited on the surfaces of the vessel wall and magnetic stirring bar. The quantity of ammonium hydroxide added to the solution was approximately 25% larger than that theoretically needed to neutralize all of the HCl produced by hydrolysis of the trichlorosilane.

As reported in section 6.5, the formation of oligosilsesquioxanes is favored by either acid of base catalysts as well as by low temperatures and concentrations of the trichlorosilane. Since an oligosilsesquioxane like that illustrated in Figure 87 on page 228 and Figure 88 on page 230 cannot polymerize into larger compounds because of the organic ligands linked to Si atoms, the observations described in the preceeding paragraphs suggest that large amounts of oligomers other than oligosilsesquioxanes were present in the reaction system. In this situation, the utilization of higher temperatures in experiments SLN2 and SLN3 as well as the neutralization of HCl by additon of ammonium hydroxide, most probably induced further polymerization of the oligomers. Eventually the oligomers will become very large and can deposite on the magnetic stirring bar, vessel walls, and surface of the particles. Apparently, the concentration of trichlorosilane used in the experiments was not sufficiently low for inducing the formation of oligosilsesquioxanes.

The presence or absence of ammonium hydroxide in the intercalating solution seemed to also determine the color of the intercalated compound calcined at a temperature of 470 °C. Except for the white color of the calcined product of experiment SLN5, the color of the calcined products of the remaining experiments was orange-brown. The darkness of the calcined products increased in the following order: SLN3, SLN1, and SLN2. The intercalated compound of experiment SLN4 was not calcined.

Calcination of the compounds at 650 °C resulted in solids light-grey in color. This color was attributed to carbon residues from incomplete oxidation of the organic ligands of the parent trichlorosilane.

7.2.2 X-ray diffraction (XRD) patterns

XRD analysis was utilized to determine the interlayer distance of the intercalated compounds and to characterize Na- and H-Magadiite. The interlayer distance can be calculated from a XRD pattern by using Bragg's law:

$$\lambda = 2d \sin \theta$$

In this equation λ is the wavelength of the radiation, d is the distance between atomic layers, and θ is the angle of reflection of radiation. The XRD patterns presented below were obtained at a wave length of 1.5418 Å.

7.2.2.1 Na-Magadiite

Figure 89 illustrates the characteristic XRD pattern of Na-Magadiite. The interlayer distance was determined by the sharp reflection at $2\theta \cong$ 5.6 degrees. By using Bragg's law, the interlayer distance was calculated as being 15.78 Å. This value compares well with the distance of 15.6 Å reported by Lagaly and Beneke[76]. The pattern shown in Figure 89 was determined for Na-Magadiite synthesized in this laboratory. The synthesis temperature was 100 °C.

7.2.2.2 H-Magadiite

The XRD pattern shown in Figure 90 on page 244 corresponds to H-Magadiite obtained from Na-Magadiite synthesized at a temperature of 100 °C, and resulted in an interlayer distance of 13.6 Å. The multiple sharp reflections that characterize the structure of Na-Magadiite at 2θ-values between 24 and 30 degrees (Figure 89) were not present in the XRD pattern for H-Magadiite. For H-Magadiite, the XRD pattern shows strong reflections at 2θ -values of approximately 6.5, 12.5, 24.5, and 26.5 degrees. These reflections are broader than those of Na-Magadiite in Figure 89. Lagaly and Beneke[77] reported similar observations, and attributed the phenomenon to distortions in the structure of Magadiite caused by the substitution of H for Na.

Brindley[82] analysed XRD patterns of Na-Magadiite at different states of hydration. In vacuum, the interlayer distance of Na-Magadiite was reduced to 13.5 Å. Reflections were also present at 2θ-values of 13.2, 24.9 and 26.9 degrees, which are approximately the same as those shown in

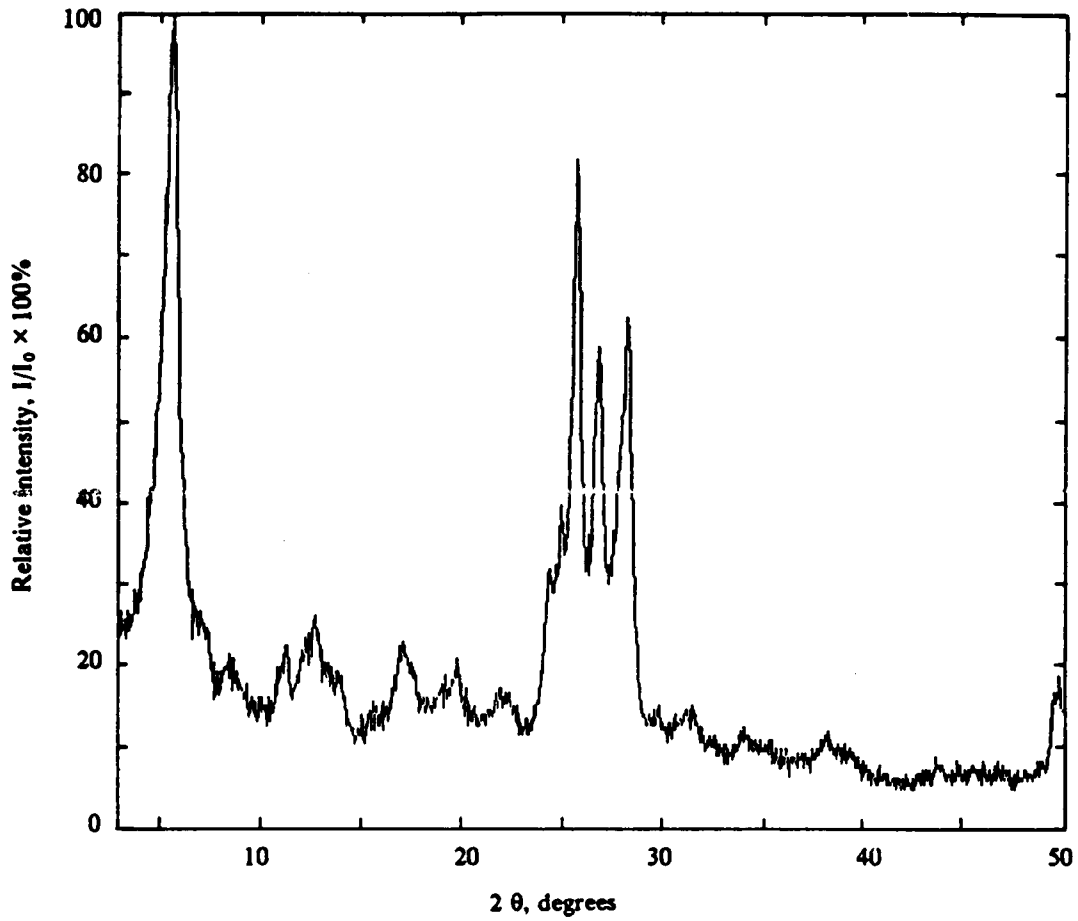

Figure 89. X-ray diffraction pattern of Na-Magadiite: Material synthesized and air-dried at 100 °C.

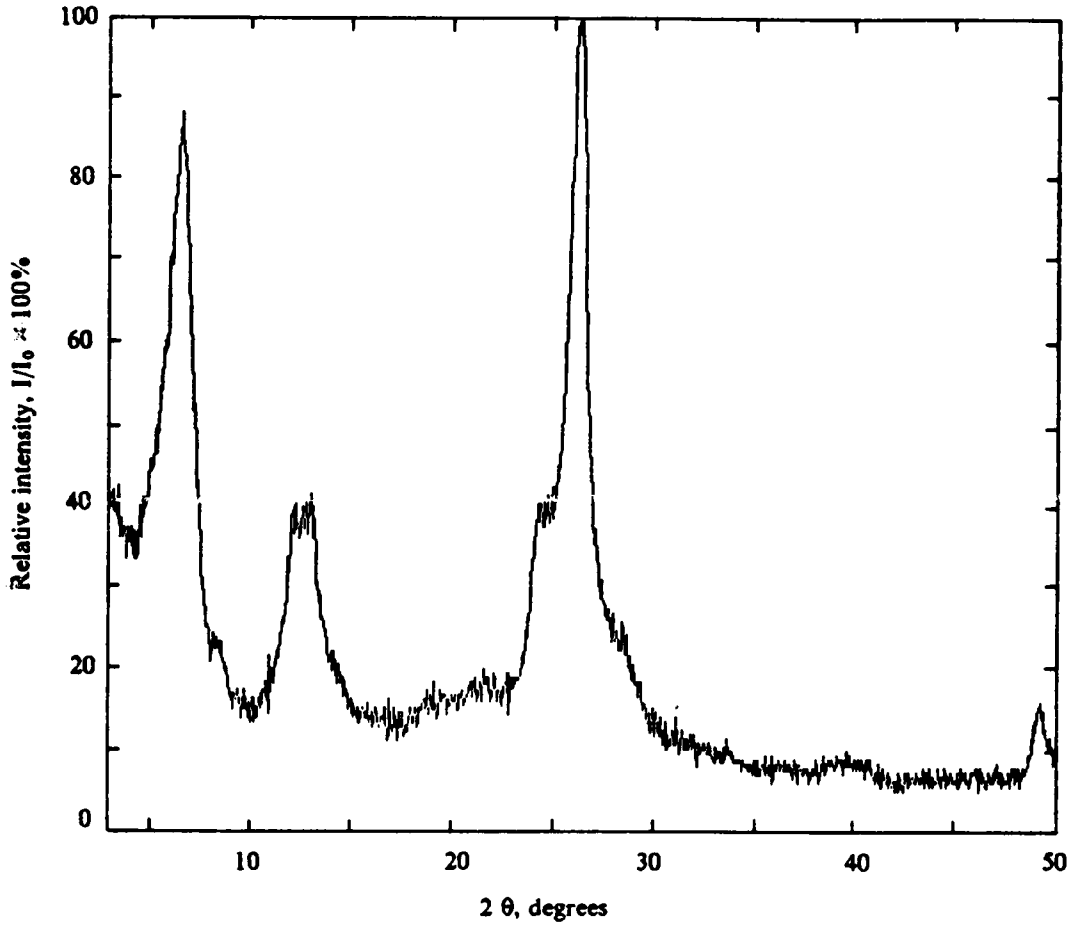

Figure 90. X-ray diffraction pattern of H-Magadiite: Parent Na-Magadiite synthesized at 100 °C.

Figure 90 on page 244 for H-Magadiite. Brindley[82] concluded that the structure of Na-Magadiite lost some of its regularity because of dehydration. Thus, Brindley as well as Lagaly and Beneke[77] correlated distortions in the structure of Magadiite with a decrease in the interlayer spacing.

As shown in Figure 91, the XRD pattern of H-Magadiite obtained from Na-Magadiite synthesized at 175 °C displays only a weak reflection at $2\theta < 10$ degrees. An identical pattern was obtained when the H-Magadiite whose parent had been synthesized at 100 °C was calcined at 400 °C. If the weak reflection at $2\theta < 10$ degrees is assumed to be representative of the interlayer distance, then the distance of H-Magadiite (parent material synthesized at 175 °C) would be 12.1 Å. The calcined H-Magadiite would have an interlayer distance of 11.2 Å.

7.2.2.3 Synthesized compounds

The synthesized compounds will be identified in the following discussion by the number of the experiment as reported in Table 8 on page 237.

Figure 92 on page 247 presents the XRD pattern of SLN1, which was obtained by reaction of phenyltrichlorosilane with H-Magadiite. The broad reflections suggest some irregularities in the structure of the material. By using Bragg's law, the interlayer distance was calculated as being 14.3 Å. XRD patterns of SLN3 and SLN2 air-dried at 150 °C were similar to that of SLN1 and yielded the same interlayer distance of 14.3 Å. Compared to the interlayer distance of 11.2 Å of H-Magadiite calcined at 470 °C., the interlayer spacing would be of the order of 3 Å. According to Endo et al.[71], such an interlayer spacing corresponds to pillars of a single silicon atom.

Figure 93 on page 248 and Figure 94 on page 249 show, respectively, the XRD patterns of compounds SLN4 and SLN5, whose parent Na-Magadiite was synthesized at 175 °C. The pattern of SLN4 resembles that of the original H-Magadiite (Figure 90 on page 244). SLN5, which was synthesized in the absence of ammonium hydroxide, displays several reflections at $2\theta < 10$ degrees. The reflection at $2\theta \cong 5.2$ corresponds to an interlayer distance of 17 Å. These observations suggest

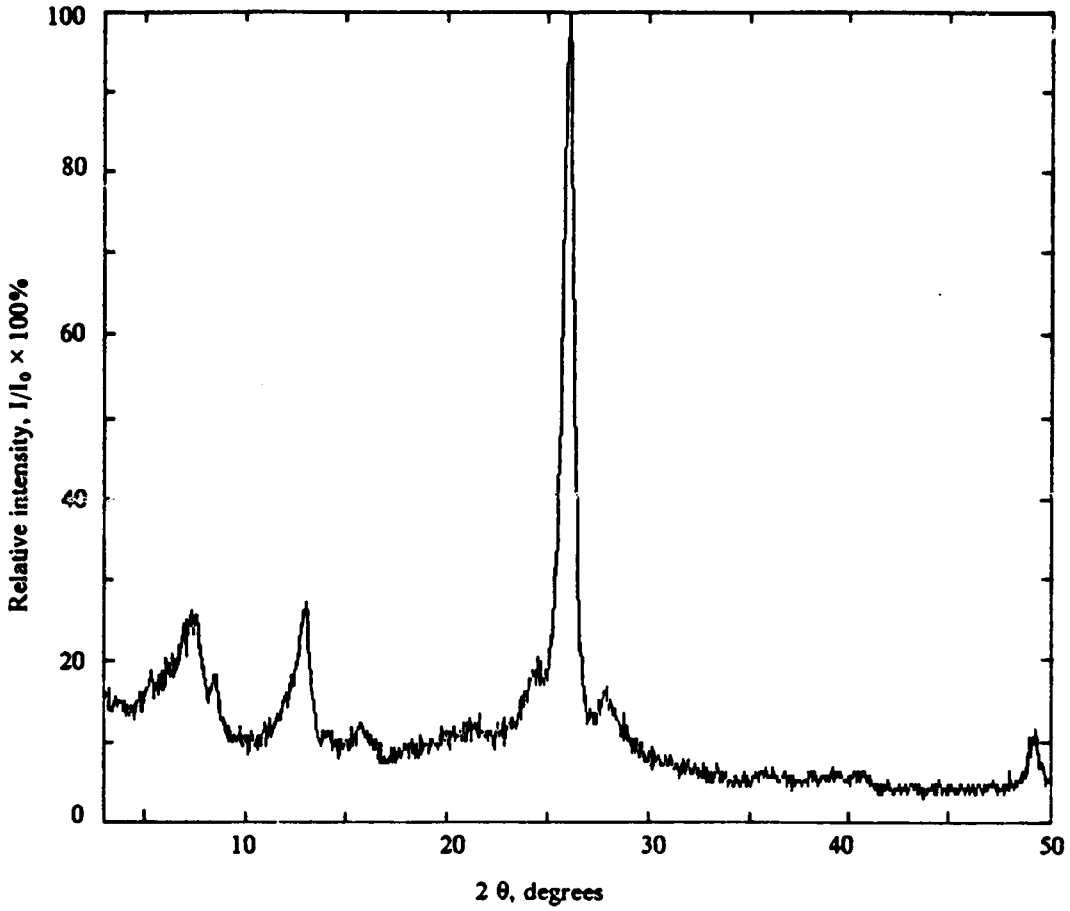

Figure 91. X-ray diffraction pattern of H-Magadiite: Parent Na-Magadiite synthesized at 175 °C.

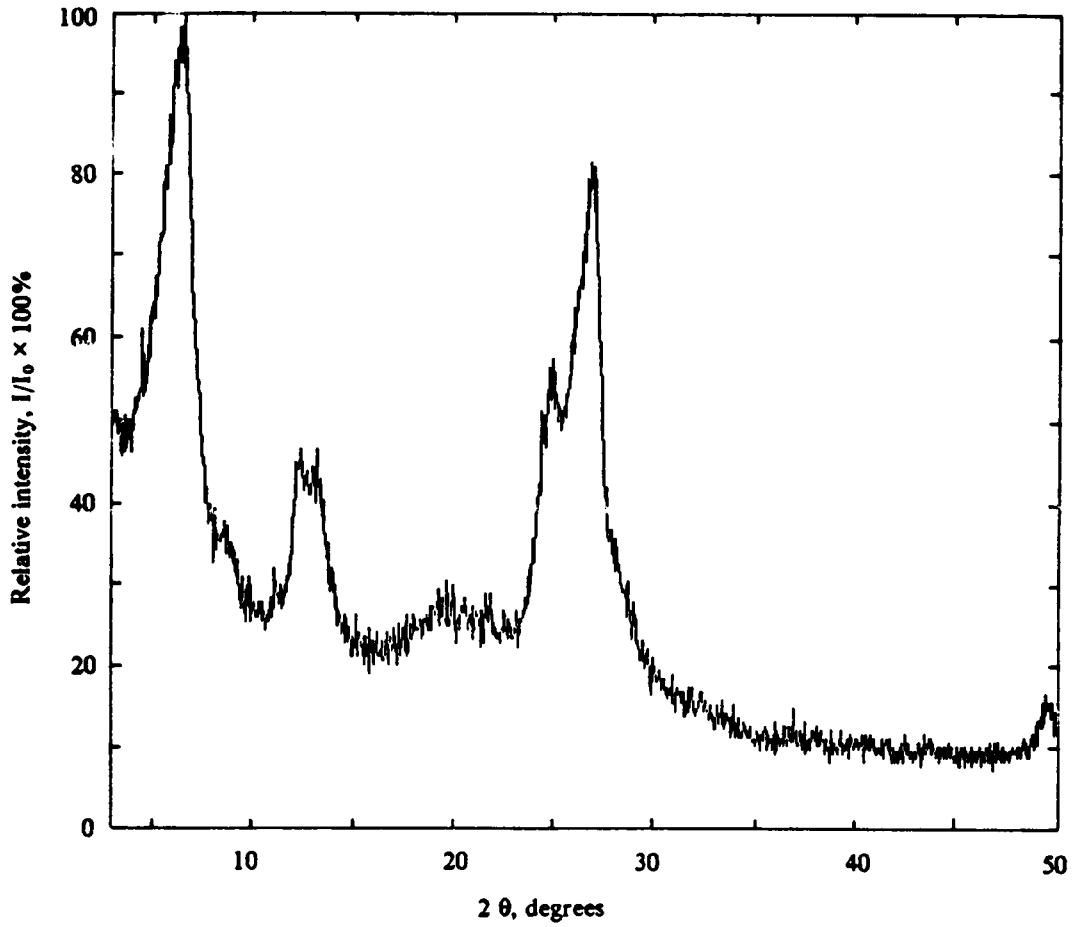

Figure 92. X-ray diffraction pattern of SLN1: H-Magadiite reacted with phenyltrichlorosilane. Parent Na-Magadiite synthesized at 100 °C.

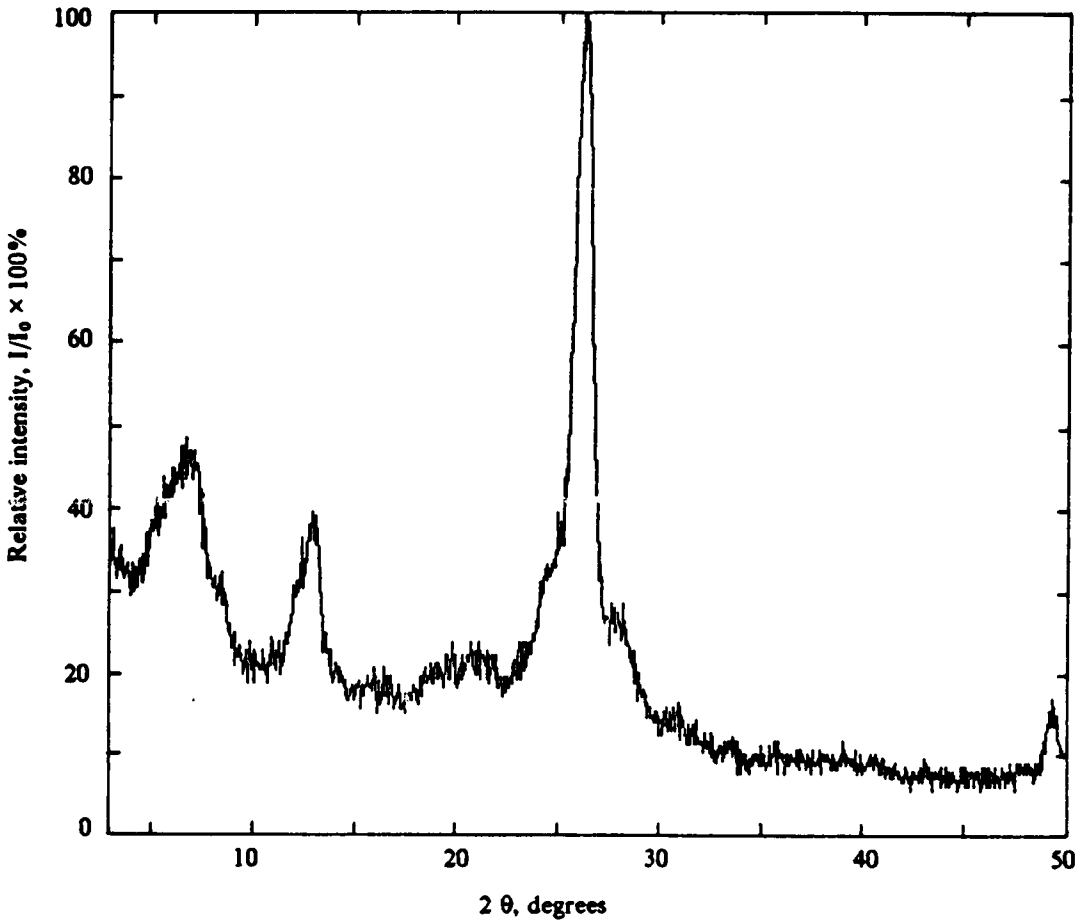

Figure 93. X-ray diffraction pattern of SLN4: H-Magadiite reacted with phenyltrichlorosilane. Parent Na-Magadiite synthesized at 175 °C.

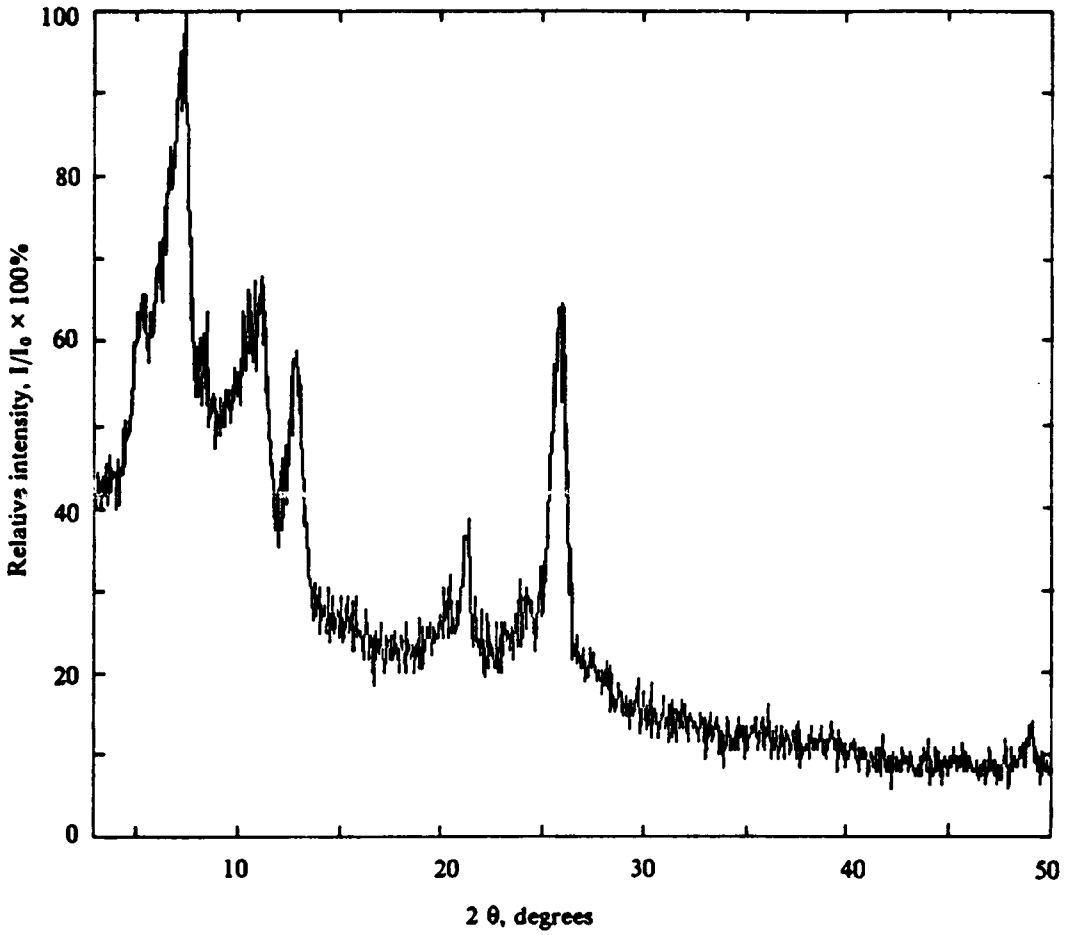

Figure 94. X-ray diffraction pattern of SLN5: H-Magadiite reacted with phenyltrichlorosilane. Parent Na-Magadiite synthesized at 175 °C.

that the characteristics of the synthesized material are strongly dependent on the source of H-Magadiite and the pH of the reaction mixture.

Figure 95 and Figure 96 on page 252 present the XRD patterns of SLN1 calcined, respectively, at 470 and 650 °C. Compared to the pattern of the uncalcined material (Figure 92 on page 247), the reflection at $2\theta \cong 26$ degrees is sharper and the one at 6.2 degrees skewed to lower values of 2θ. The latter observation permitted no interlayer-distance calculation and suggested variations in the interlayer spacing of the calcined materials.

When SLN2 was calcined at 650 °C, the resulting XRD pattern was similar to that of uncalcined SLN4 (Figure 93 on page 248). Calcination of SLN4 and SLN5 has not been investigated.

7.2.3 Thermal analysis

Differential thermal analysis (DTA) and thermogravimetric analysis (TGA) were performed at a heating rate of 30 °C/min in flowing and static air, respectively. The standard for TGA was air. DTA curves were obtained for temperatures ranging from room temperature (22-25 °C) to 650 °C; while for TGA curves, the temperature range was extended up to 850 °C.

7.2.3.1 Na-Magadiite

Figure 97 on page 253 presents DTA and TGA curves for Na-Magadiite synthesized at 100 °C. The DTA curve shows two endothermic peaks below 200 °C., which correspond to water losses. According to Lagaly and Beneke[76], this two-step process is characteristic of Na-Magadiite, and they attributed the second step to dehydration of the interlayer space.

No other processes, either endothermic or exothermic, were apparent. TGA and DTA curves suggest that no phase transformations occur in Na-Magadiite below 850 °C. This behavior differed

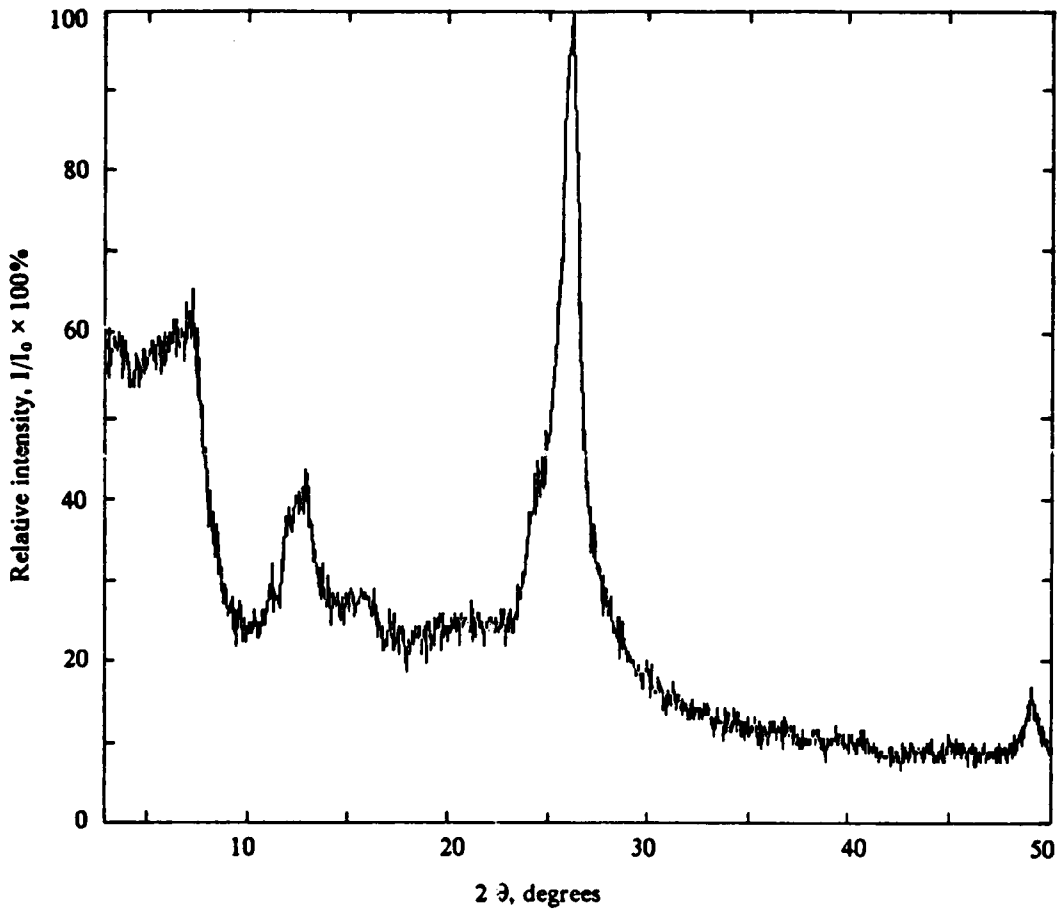

Figure 95. X-ray diffraction pattern of SLN1 calcined at 470 °C: H-Magadiite reacted with phenyltrichlorosilane. Parent Na-Magadiite synthesized at 100 °C.

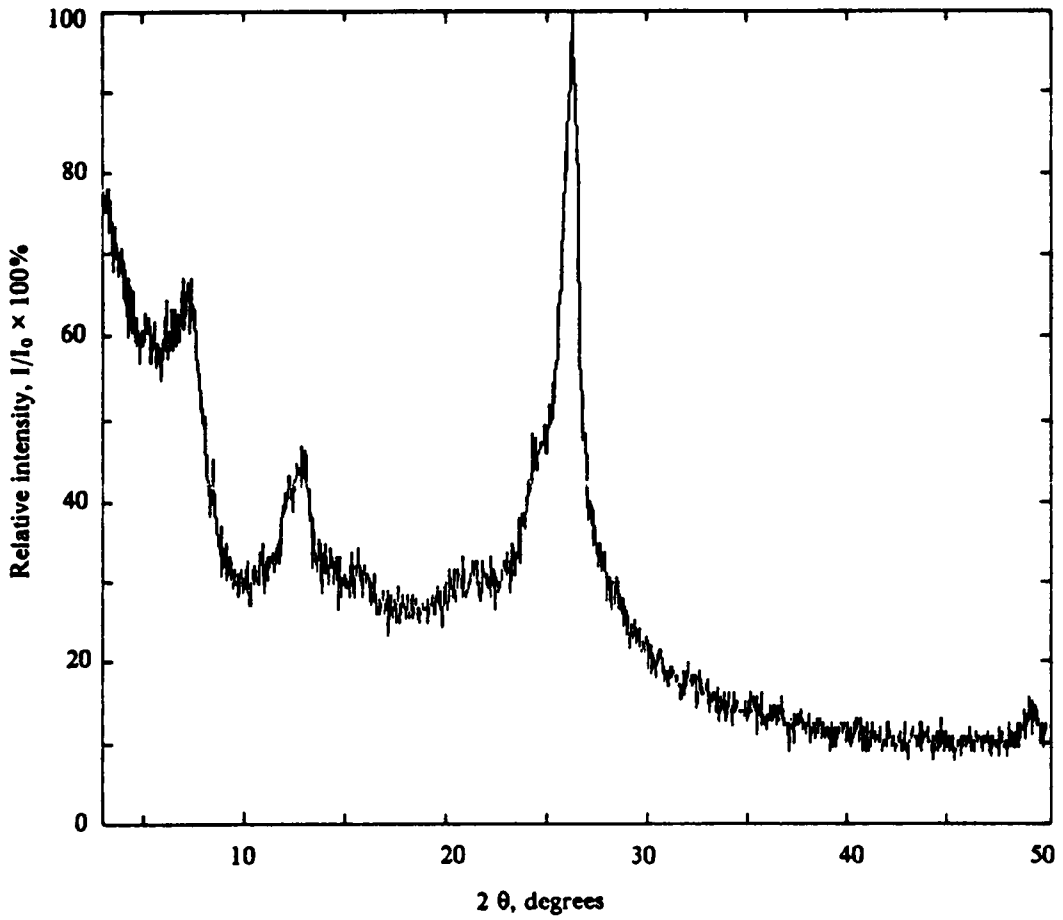

Figure 96. X-ray diffraction pattern of SLN1 calcined at 650 °C: H-Magadiite reacted with phenyltrichlorosilane. Parent Na-Magadiite synthesized at 100 °C.

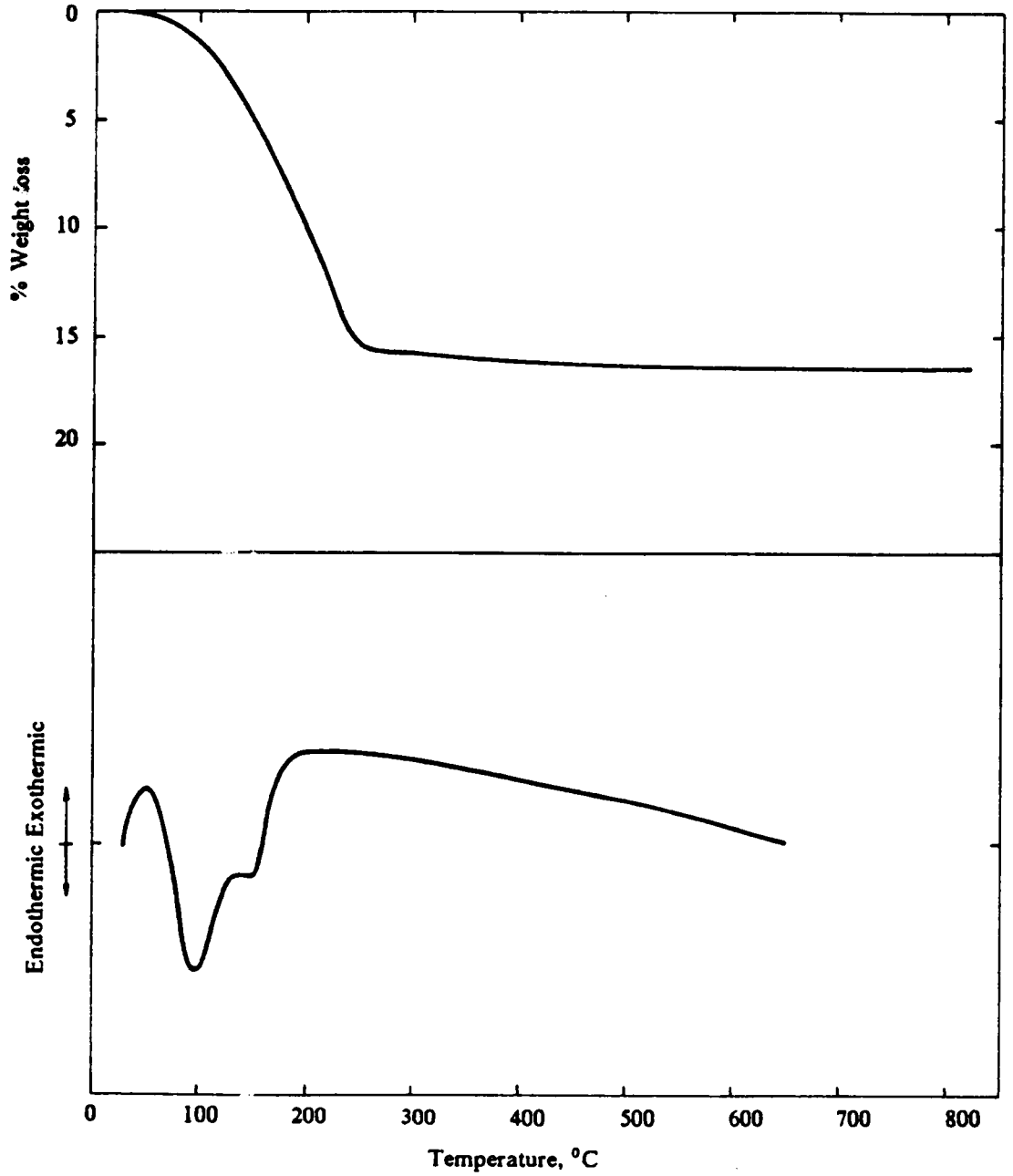

Figure 97. DTA and TGA curves of Na-Magadiite synthesized at 100 °C

from that observed by Lagaly and Beneke, who detected the transformation of Na-Magadiite into quartz at 500 °C and then into tridymite at 700 °C. They found, however, that Na-Magadiite exchanged with organic cations transformed into quartz at a temperature of 600 °C with no formation of tridymite up to 1100 °C. Lagaly and Beneke synthesized Na-Magadiite at the same temperature that was used in the present investigation, 100 °C, but started with different compositions of reagents.

Na-Magadiite synthesized at 175 °C had DTA and TGA curves similar to those for Magadiite synthesized at 100 °C. The former Magadiite water content (10%) was, however, smaller than that of the latter one (15%). No phase transitions were detected in the Magadiite synthesized at 175 °C.

7.2.3.2 H-Magadiite

DTA and TGA curves for H-Magadiite are shown in Figure 98. The parent Na-Magadiite was prepared at 100 °C. The water content below 200 °C was approximately 10%, which was less than that of 15% for Na-Magadiite. The endothermic dehydration peak in the DTA curve was not as strong as that for Na-Magadiite. According to Lagaly and Beneke[77], weight losses above 300 °C are caused by the formation of siloxane bonds between adjacent layers of H-Magadiite.

After calcining this H-Magadiite at 470 °C and exposing it to air at ambient conditions, the TGA curve showed a weight loss below 200 °C of only 2%.

H-Magadiite prepared from Na-Magadiite at 175 °C had a lower water content than that of Magadiite prepared at 100 °C. Thus, Magadiite synthesized at higher temperatures contains less water than that prepared at lower temperatures. Also, these data suggest that the sharpness of reflections in XRD patterns at 2θ-values below 10 degrees might be related to the degree of hydration. As shown in Figure 90 on page 244 and Figure 91 on page 246, the reflections for H-Magadiite are broader and less intense for samples where the degree of hydration was reduced.

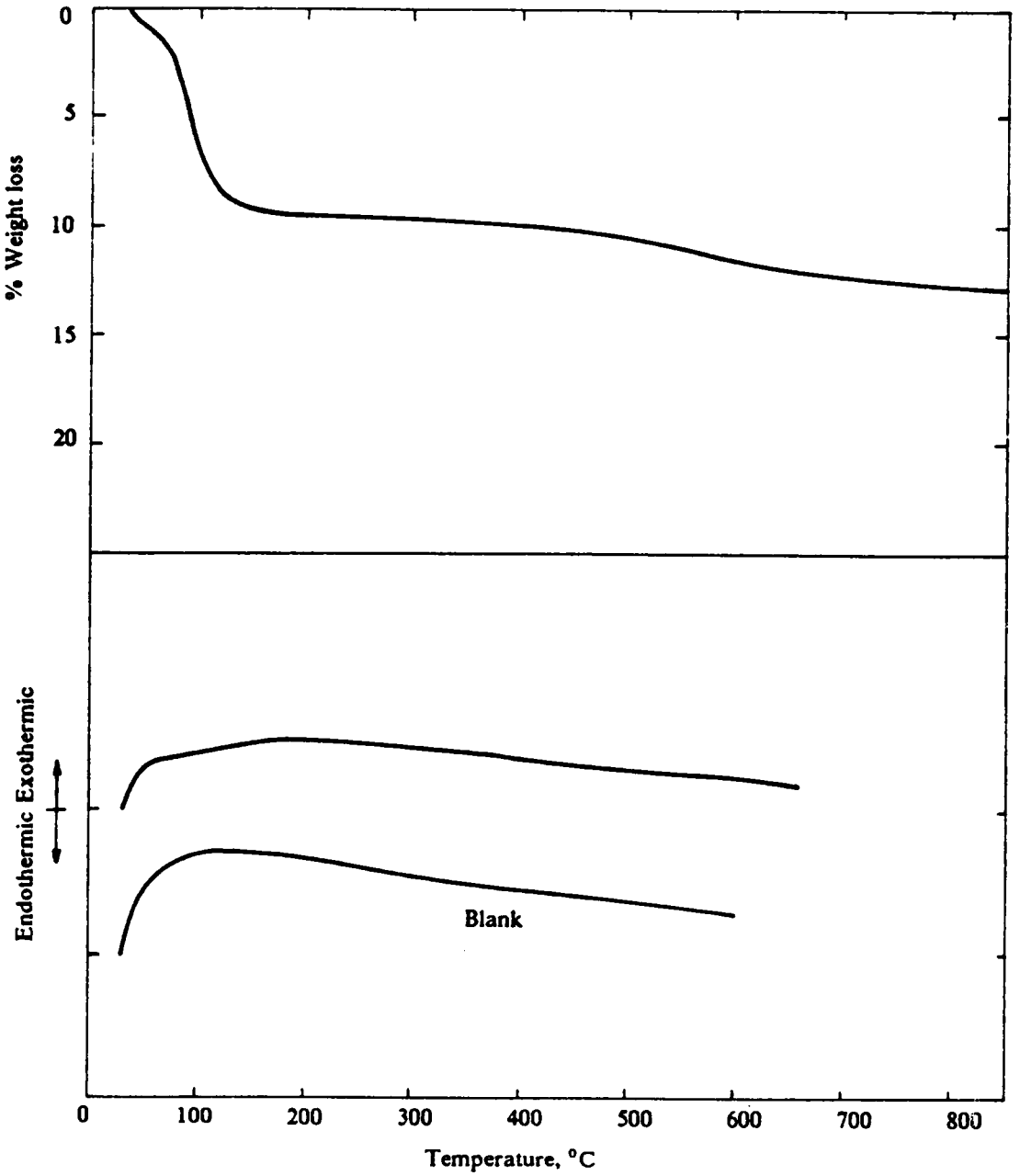

Figure 98. DTA and TGA curves of H-Magadiite: Parent Na-Magadiite synthesized at 100 °C.

7.2.3.3 Synthesized compounds

DTA and TGA curves seemed to indicate the reaction of trichlorosilanes with H-Magadiite. As shown in Figure 99, the total weight loss of SLN1 in the TGA was approximately 20%, which was twice that of H-Magadiite (Figure 98 on page 255). An exothermic weight loss of 13% occurred between 350 and 650 °C, in which range the loss for H-Magadiite was only approximately 3%. The water content of SLN1 was about 5%. SLN1 was synthesized with phenyltrichlorosilane.

The TGA curve of SLN3 showed a weight loss of 5% between 350 and 650 °C and a total loss of only 11.7%. In the synthesis of SLN3, ammonium hydroxide was added to the reaction solution before it was poured into the H-Magadiite suspension. As reported in section 7.3.1, a very sticky and dense phase was observed to form in this experiment. These data suggest that the size of a considerable fraction of the oligomers was sufficiently large to prevent diffusion into H-Magadiite, most probably resulting in the less reaction than for SLN1.

As illustrated in Figure 100 on page 258, TGA and DTA curves for H-Magadiite reacted with cyclohexyltrichlorosilane (SLN2) reveal two strong exothermic processes occurring one at 250 and another at 350 °C. The occurrence of these processes was not observed in any of the materials synthesized with phenyltrichorosilane. One of the peaks is probably associated with the decompositon of the ammonium ions that for exchanged for protons. No satisfactory explanation was found for the second one. The total weight loss was higher than that for SLN1, but the loss between 350 and 650 °C was lower (7%).

SLN5, which was prepared from Na-Magadiite synthesized at 175 °C, exhibited a TGA curve that was similar to those shown in Figure 99 and Figure 100 on page 258. The water content of SLN5, however, was lower. SLN5 showed an exothermic weight loss at 650 °C that was not observed for the compounds derived from Magadiite synthesized at 100 °C.

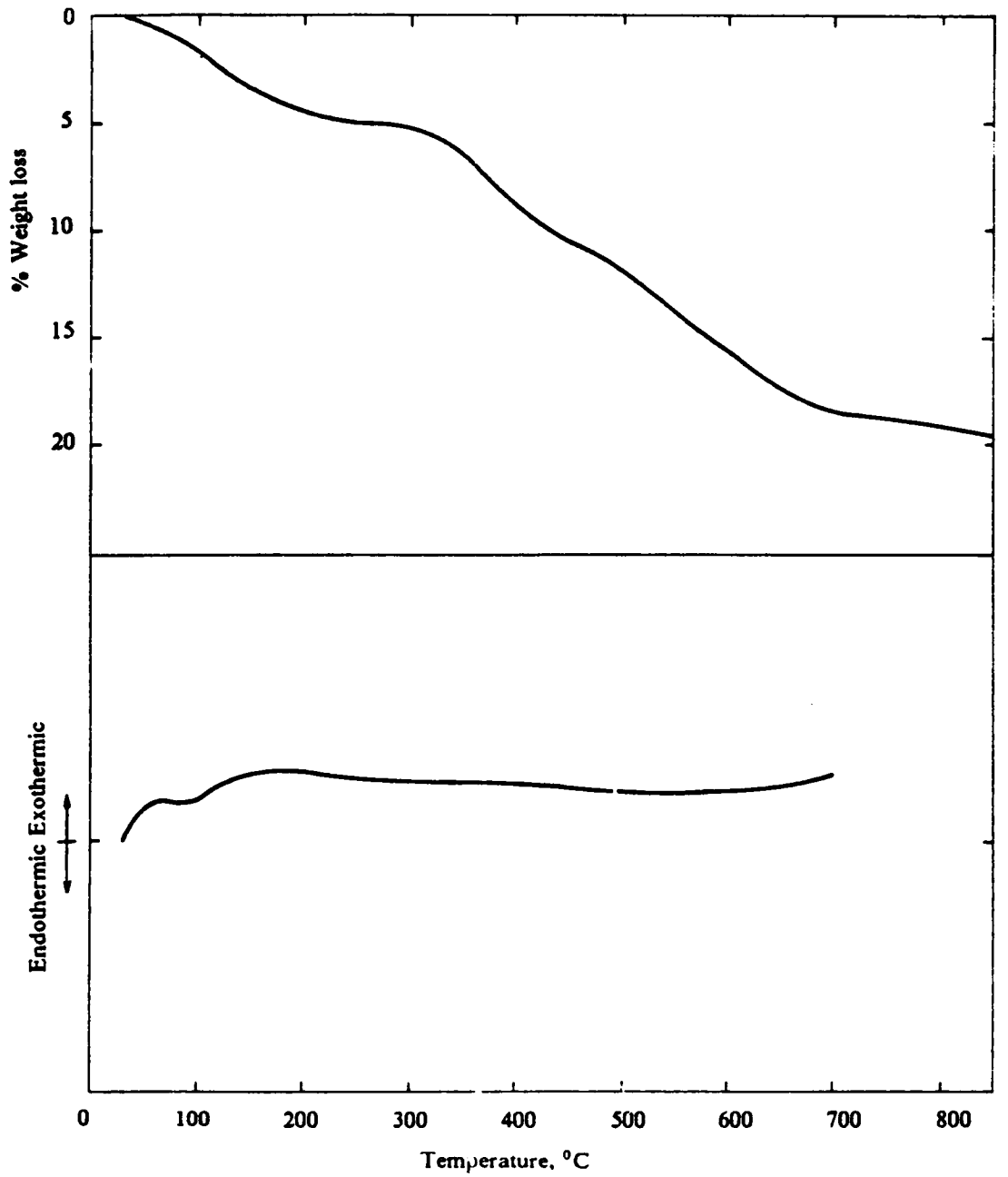

Figure 99. DTA and TGA curves of SLN1: Reaction with phenyltrichlorosilane. Parent Na-Magadiite synthesized at 100 °C.

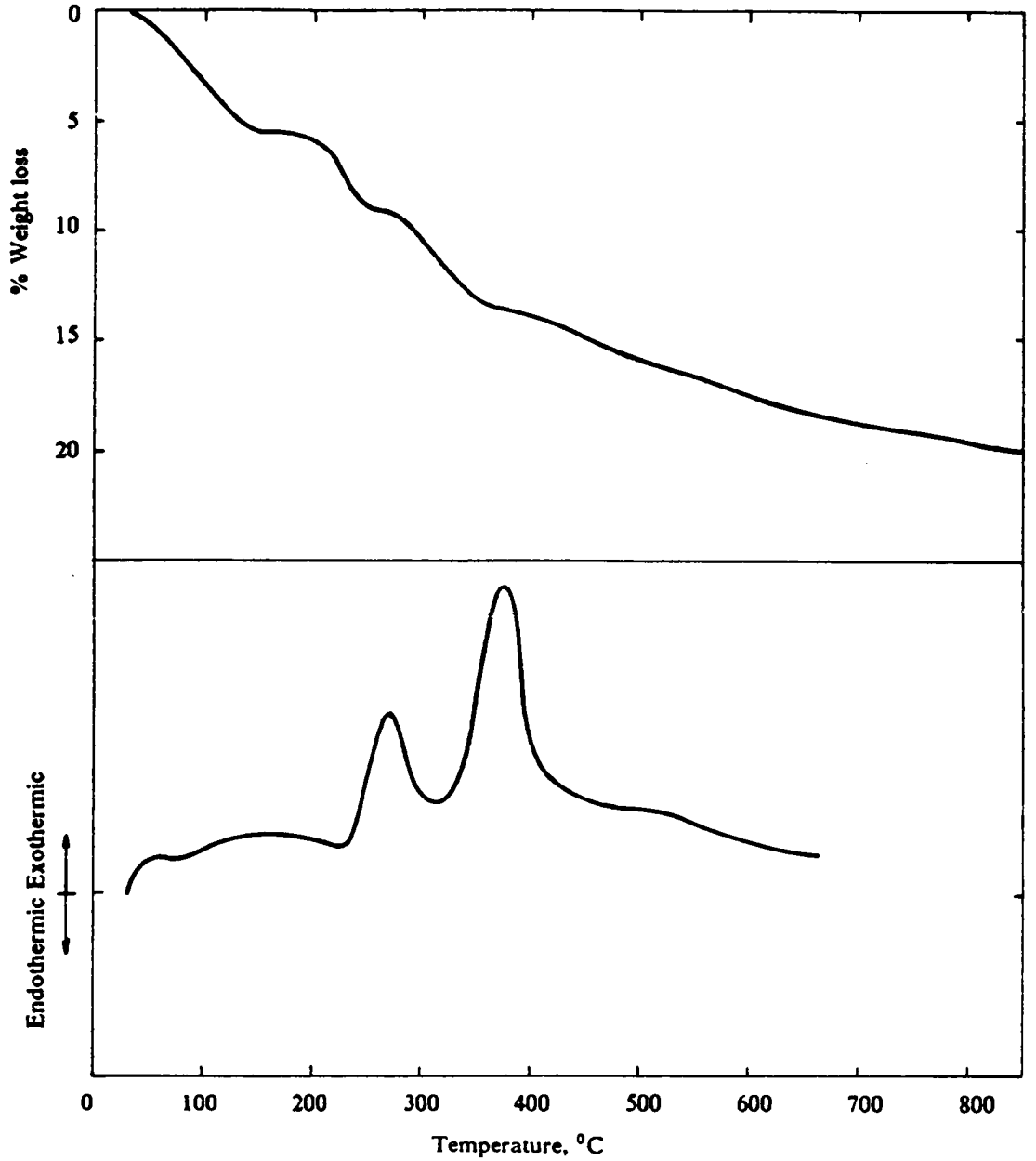

Figure 100. DTA and TGA curves of SLN2: Reaction with cyclohexyltrichlorosilane. Parent Na-Magadiite synthesized at 100 °C.

7.2.4 Infrared spectra

Fourier-Transform-Infrared (FTIR) spectra were obtained by using the KBr-pellet technique. IR analysis provided information on the presence of silanol and organic groups in the samples.

7.2.4.1 H-Magadiite

Figure 101 presents the spectra of H-Magadiite dehydrated "in-situ" by evacuating and heating the cell containing the sample above 200 °C. This H-Magadiite was prepared from Na-Magadiite synthesized at 100 °C. The TGA curve of H-Magadiite (Figure 98 on page 255) showed that at 250 °C this material was already dehydrated. Therefore, the absorption bands at 3650 and 3490 cm^{-1} can be assumed to correspond to silanol groups. The band at 3490 cm^{-1} tended to disappear as the dehydration temperature was increased from 250 to 470 °C. Rojo et al.[79] assigned this latter band to silanol groups with strong hydrogen bonds, which would condense into siloxane bonds at higher temperatures. The formation of siloxane bonds at temperatures above 400 °C was also suggested by Lagaly and Beneke[77]. These researchers observed that above a temperature of 400 °C H-Magadiite could no longer be intercalated with organic compounds.

The spectrum of hydrated H-Magadiite displayed a broad absorption band at 3420 cm^{-1}, which was caused by the water of hydration.

7.2.4.2 Synthesized compounds

The IR-spectra of SLN1 and SLN2 are presented in Figure 102 on page 261. These spectra were obtained at room temperature and atmospheric pressure. SLN1 and SLN2 were synthesized with phenyl and cyclohexyltrichlorosilane, respectively. The parent Na-Magadiite had been prepared at 100 °C.

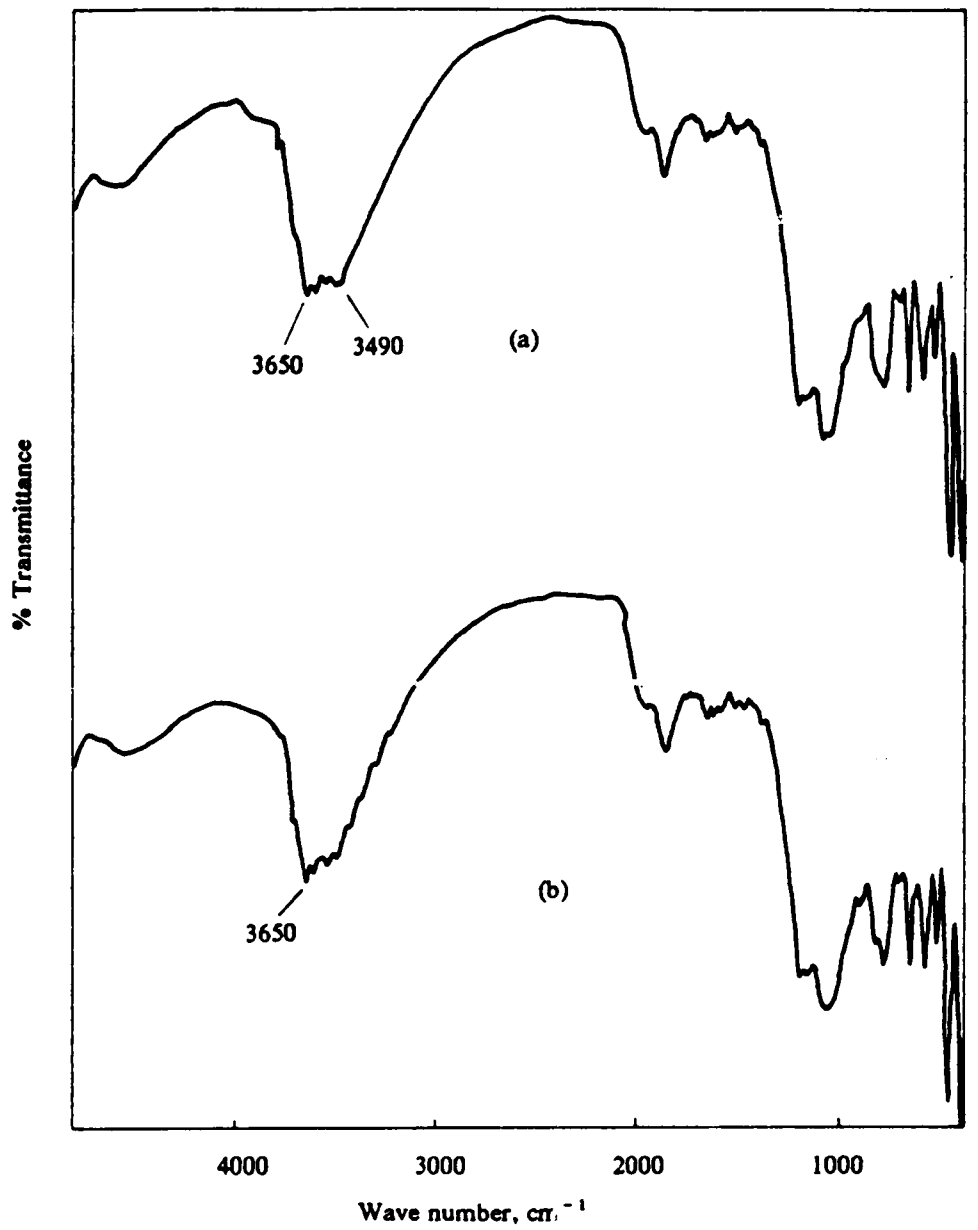

Figure 101. Infrared spectra of H-Magadiite dehydrated in vacuum: (a) at 250 °C; (b) at 470 °C.

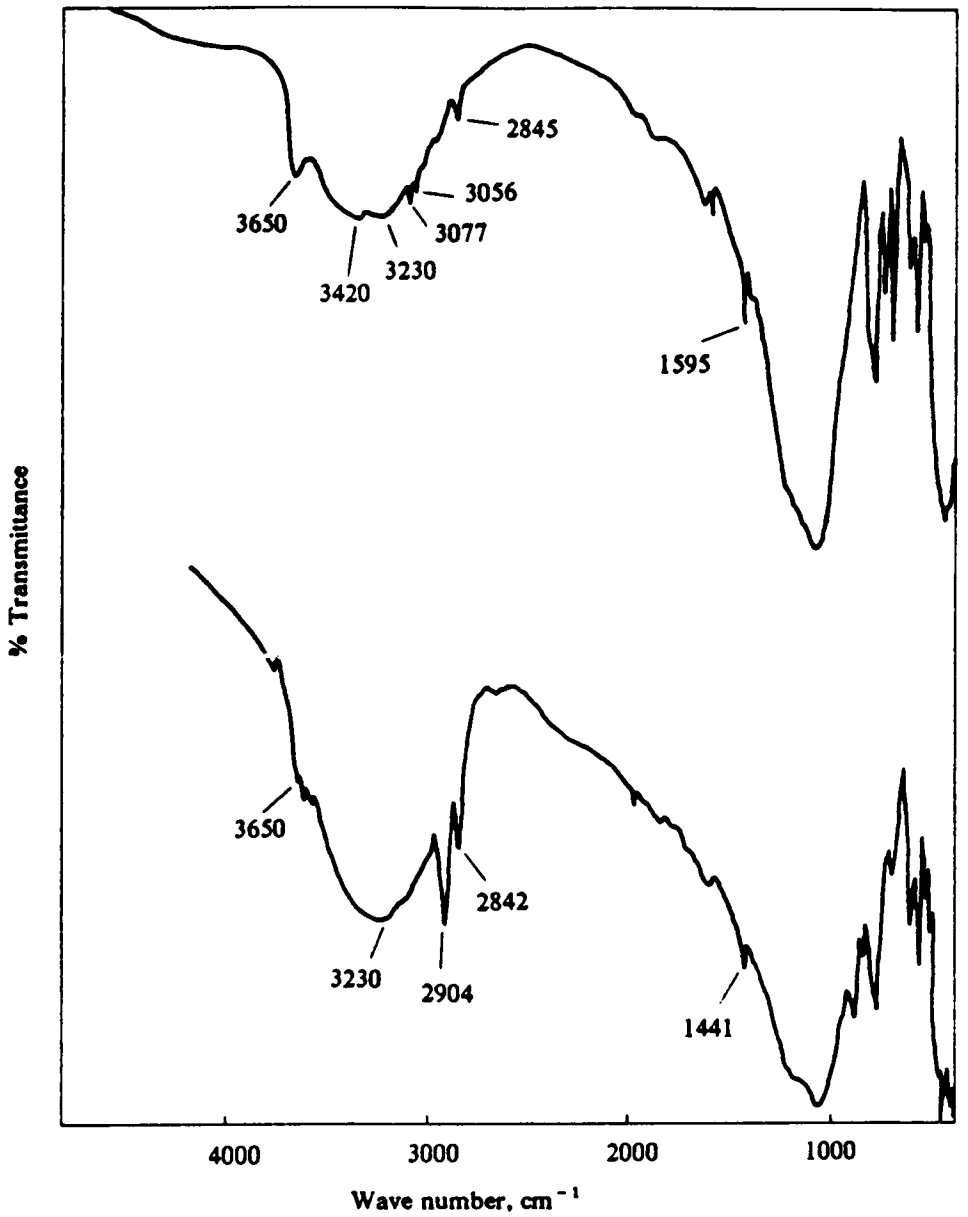

Figure 102. Infrared spectra of synthesized compounds: (a) SLN1; (b) SLN2.

SLN1 showed a strong absorption band at 3650 cm^{-1}, indicating the presence of silanol groups. The broad band at 3420 cm^{-1} corresponds to water; the same band was present in hydrated H-Magadiite. The presence of ammonium ions in SLN1 is demonstrated by the also broad absorption band at 3230 cm^{-1}. Ammonium ions absorb infrared radiation at wave numbers between 3300 and 3030 cm^{-1} (Lange's Handbook of Chemistry[85]). Weaker bands at 3077, 3056, and 1595 as well as the band at 741 cm^{-1} were assigned to phenyl groups.

As seen in Figure 102 on page 261, the spectrum of SLN2 displays much stronger absorption bands than that of SLN1. Bands at 2904, 2842, and 1441 cm^{-1} appeared in the spectrum because of the $-CH_2-$ in the cyclohexyl ligand. Since water in hydrated H-Magadiite caused a broad absorption band to appear at 3420 cm^{-1}, the band at 3230 cm^{-1} could be due to a combination of the absorption bands for water and ammonium ions. The band corresponding to silanol groups (3650 cm^{-1}) is either weak or hidden by the bands of water and ammonium-ions.

The spectra of SLN1 and SLN2 help to explain the differences in the respective DTA and TGA curves (Figure 99 on page 257 and Figure 100 on page 258). It appears that the adsorption of ammonium ions and of the cyclohexyl derivative are larger in SLN2 than the adsorption of ammonium and the phenyl derivative in SLN1.

Figure 103 shows spectra of SLN1 dehydrated at 160 ^0C in vaccum and of calcined SLN1 dehydrated in vacuum at 250 ^0C. The former spectrum displays a broad IR-absorption band at 3250 cm^{-1}, confirming the presence of ammonium ions. The latter shows no bands for ammonium ions and indicates the presence of silanol groups in the calcined material. The silanol groups are of the same nature as those in H-Magadiite calcined at 470 ^0C (Figure 101 on page 260).

7.2.5 Surface area and adsorption

Surface areas were determined from nitrogen adsorption at a temperature of 77 ^0K by using the BET method. Adsorption of organic species of different kinetic diameters were utilized to obtain information on interlayer and interpillar spacings. Adsorption experiments were performed in

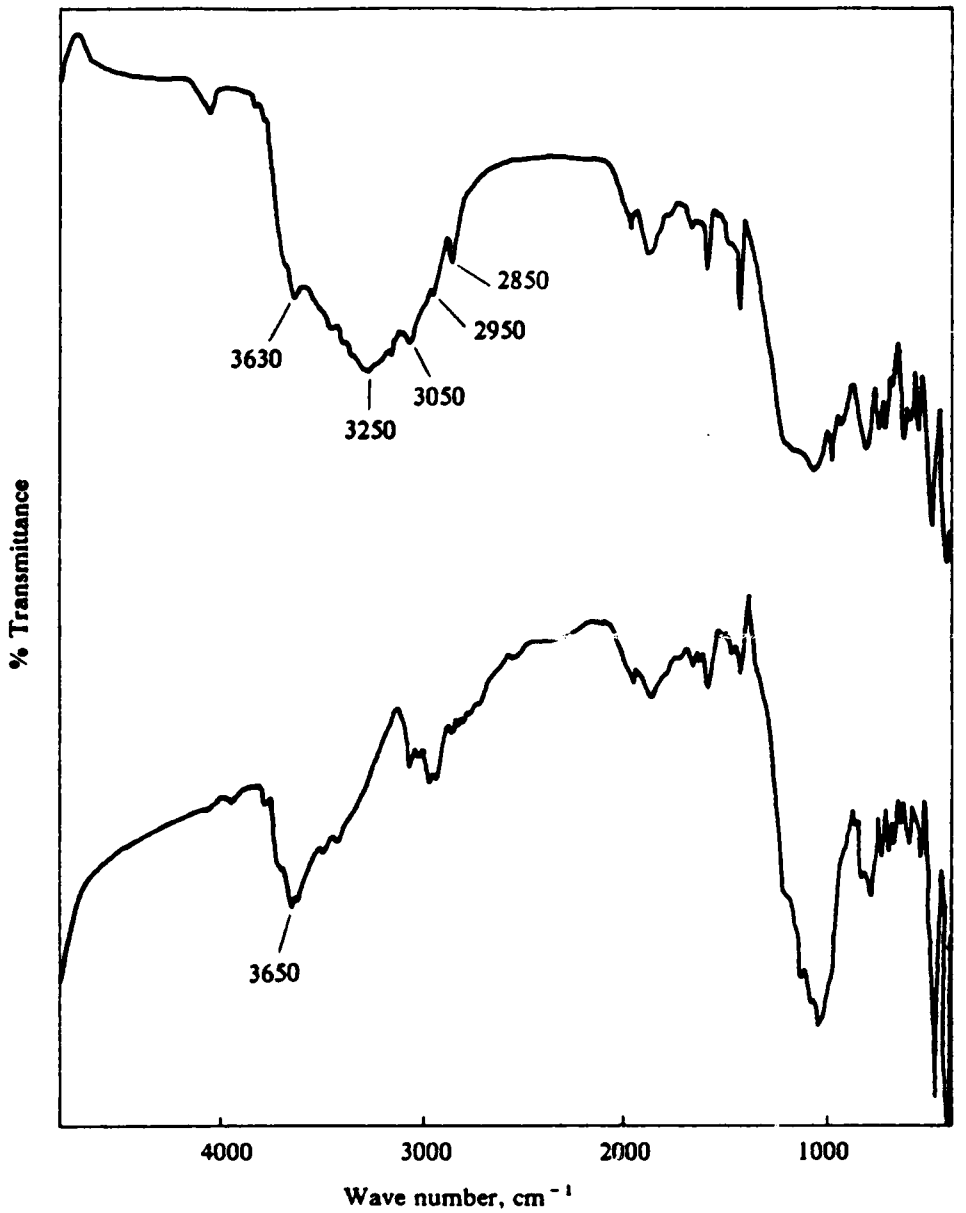

Figure 103. Infrared spectra of SLN1: (a) dehydrated at 160 °C in vacuum; (b) calcined at 470 °C and dehydrated in vacuum at 250 °C.

an adsorption chamber made by the Virginia Tech glass shop. The adsorption chamber was equipped with a quartz spring and sample holder for determining the amount of material adsorbed by the sample. Samples were pre-treated in high vaccuum at a temperature of 350 °C for approximately 8 hours.

7.2.5.1 Nitrogen adsorption and surface area

Figure 104 shows nitrogen adsorption data for the calcined, synthesized solids as well as for H-Magadiite. Calcined and uncalcined H-Magadiite adsorbed approximately the same amount of nitrogen. This amount was very low when compared with that of the synthesized compounds.

Nitrogen adsorption was largest for SLN1, which had been prepared with phenyltrichlorosilane. The material prepared with cyclohexyltrichorosilane (SLN2) adsorbed less nitrogen. Partially neutralizing the oligosilsesquioxane solution with NH_4OH before reaction with H-Magadiite (SLN3) resulted in a material which showed low nitrogen adsorption. Materials calcined at 450 °C adsorbed more nitrogen at low values of P/P_0 (P is the pressure in the adsorption chamber, and P_0 is the vapor pressure of the adsorbate) than those calcined at 650 °C. As P/P_0 was increased, the amounts of nitrogen adsorbed by a material calcined at different temperatures tended to approach the same value. Although the complete adsorption isotherms were not determined, these observations suggest that the pore structure of the synthesized materials change with the calcination temperature.

Surface areas computed by the BET method are listed in Table 9 on page 266. SLN1 calcined at 470 °C displayed the highest surface area, 205 m^2/g of material. This value is about six-fold larger than that for H-Magadiite, which is only 35 m^2/g. Increasing the calcination temperature of SLN1 to 650 °C, decreased its surface area to 176 m^2/g, a reduction of only 15%. Surface areas of SLN2 calcined at 470 and 650 °C were 148 and 131 m^2/g, respectively; while the area of SLN3 calcined at 470 °C was only 86 m^2/g.

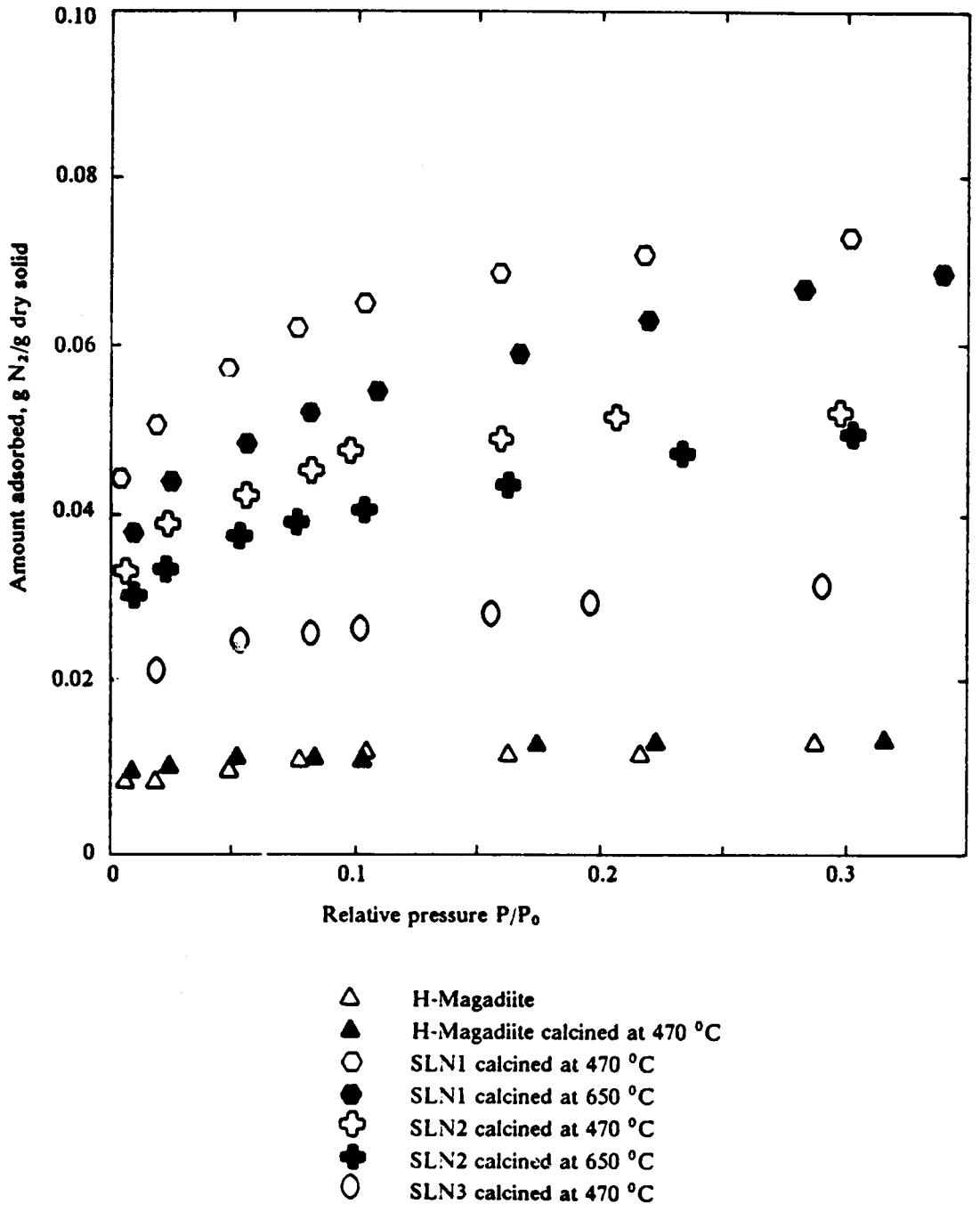

Figure 104. Nitrogen adsorption at 77 °K by layered materials

Table 9 : Surface areas and adsorption data for layered materials

Adsorbate		Amount adsorbed, cm^3 liq/g						
		HMagadiite	HMag-470	SLN1-470	SLN1-650	SLN2-470	SLN2-650	SLN3-470
Nitrogen:	$P/P_0 = 0.3$	0.0152	0.0156	0.0904	0.0827	0.0656	0.0626	0.0403
Hexane:	$P/P_0 = 0.3$			0.0657	0.0634	0.0432		0.0266
	$P/P_0 = 1.0$					0.179		
Cyclohexane:	$P/P_0 = 0.3$			0.0561	0.0557	0.0302		0.0234
	$P/P_0 = 1.0$					0.167		
Neopentane:	$P/P_0 = 0.4$			0.0725				
Triisopropylbenzene	$P/P_0 = 1.0$			0.0697	0.0488	0.0499		0.0280
Surface area, m^2/g		33	35	205	176	148	131	86

The nitrogen-adsorption data suggest that: (i) nitrogen cannot penetrate into the interlayer space of H-Magadiite; (ii) trichloroorganosilanes penetrate into and separate the layers of H-Magadiite, permitting interlayer-adsorption of nitrogen by the resulting synthesized materials; (iii) the resulting synthesized compounds are thermally stable up to temperatures of 650 ^{0}C; (iv) the properties of the synthesized compounds are dependent on the nature of the organic ligand in the trichloroorganosilane; and (v) the HCl formed during the preparation of the oligosilsesquioxane solution should not be neutralized.

7.2.5.2 Adsorption of organic species

The following organic species were utilized in adsorption experiments: hexane, cyclohexane, neopentane, and triisopropylbenzene. Hexane is a linear cylindrical molecule of diameter of 4.3 Å[83]. Cyclohexane is a planar molecule of about the same thickness as hexane and width of 6.0 Å[83]. Neopentane is bulky and spherical; its diameter is 6.2 Å[83]. These molecular dimensions are known as the kinetic diameter of the molecule. The kinetic diameter of triisopropylbenzene and nitrogen are, respectively, 8.5 and 3.64 Å. McCauley[84] reported for triisopropylbenzene a critical molecular diameter of 9.4 Å and a critical molecular thickness of 5.3 Å. The critical diameter is defined as the mininal cross-sectional dimension in the plane of the aromatic ring, and the critical thickness as the mininal dimension perpendicular to the aromatic ring.

During adsorption of hexane and cyclohexane at their vapor pressure, condensation was observed at the walls of the glass chamber. The results for these adsorbates cannot be considered reliable. Wall condensation was, however, not present during adsorption of triisopropylbenzene at its vapor pressure. Since these latter results also showed consistency with the remaining adsorption data, they were utilized in the analysis of the experimental results.

As shown in Table 9 on page 266, the adsorption of hexane, cyclohexane, neopentane, and triisopropylbenzene on SLN1 calcined at 470 ^{0}C occurred at approximately the same amount. Apparently, the same void volume was available for all of these adsorbates. Considering the mo-

lecular dimensions of neopentane. the access to this volume must be at least a slit of 6.2 Å by 6.2 Å. This indicates that interlayer and interpillar spacings cannot be less than 6.2 Å. The dimensions of triisopropylbenzene, however, demonstrate that either the interlayer or the interpillar spacing must be of the order of 9.4 Å. Therefore, the dimensions of the pores formed by pillars and layers in SLN1 calcined at 470 °C cannot be smaller than 6.2 Å by 9.4 Å.

The interlayer porosity decreased in the order: SLN1 > SLN2 > SLN3. Both SLN2 and SLN3 were synthesized at higher temperatures, and were accompanied by the formation of a tacky phase. This latter phenomenon was more pronounced in the preparation of SLN3, whose intercalating solution was partially neutralized with NH_4OH before being added to the suspension of H-Magadiite. This suggests that SLN2 and SLN3 were intercalated with high-molecular oligomers that had access to the interlayer space, thus generating less free volume in the expanded layers than the lower-molecular oligomers in SLN1.

7.2.6 Ion Exchange

Ion-exchange experiments involved cobalt and sodium ions. Exchange with sodium ions was expected to transform the intercalated compound into Na-Magadiite if no cross-linking between layers had occurred during intercalation. Exchange with cobalt ions was expected to provide visual information on the exchange process by color changes in the exchanged material.

7.2.6.1 Sodium Exchange

H-Magadiite calcined at 470 °C as well as SLN2 calcined at 470 and 650 °C were suspended in deionized water, and the pH of the suspension adjusted to 9.2 with a 0.1N solution of NaOH over a period of 6 hours. The suspension was then filtered, and the solid vaccum-dried at room temperature.

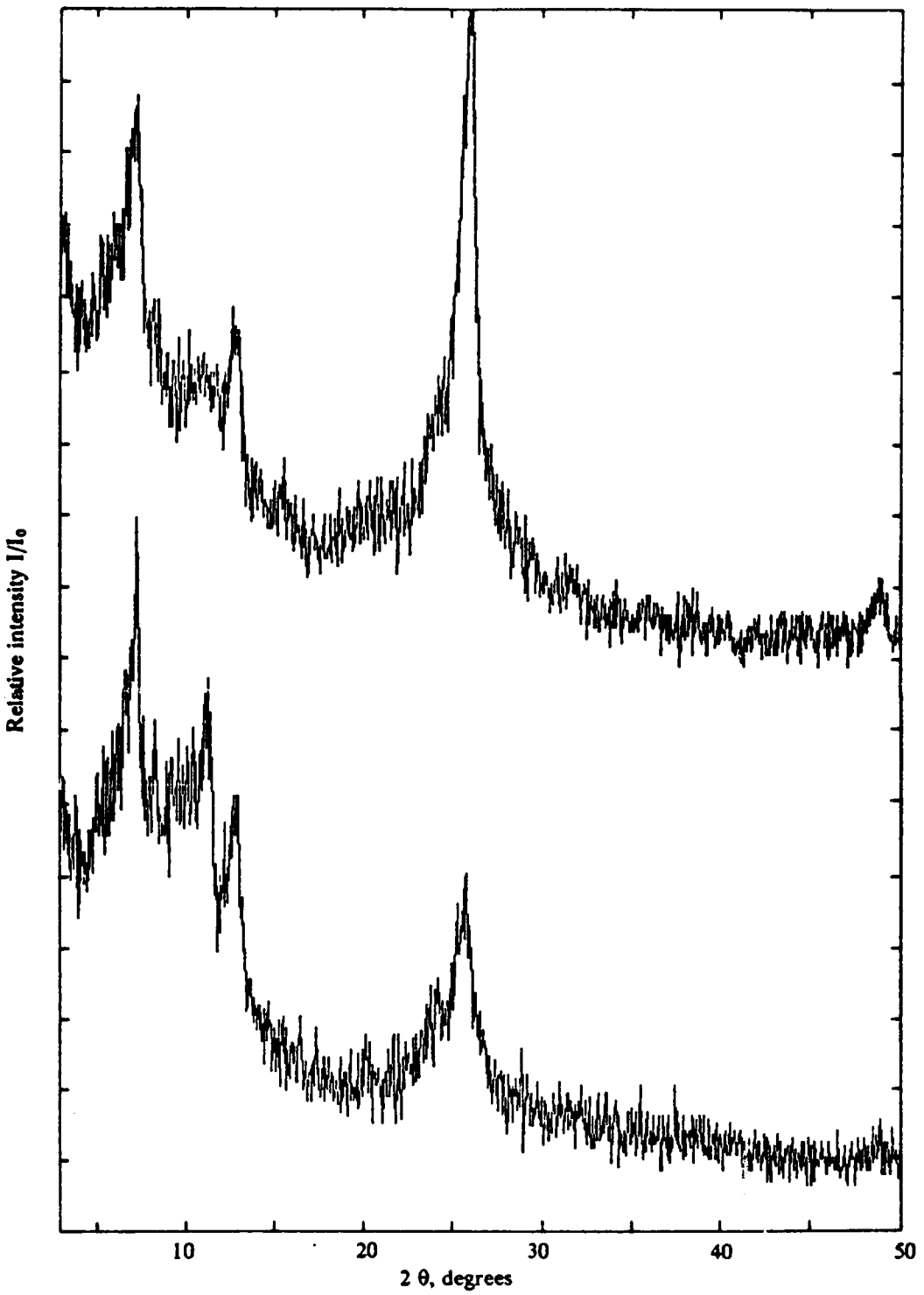

Figure 105. XRD pattern of SLN2 calcined at 470 °C: (a) before sodium-ion exchange; (b) after sodium-ion exchange.

The XRD patterns of H-Magadiite calcined at 470 °C before and after the exchange were found to be identical, revealing no sodium exchange. The XRD patterns for SLN2 calcined at 470 °C are shown in Figure 105. Compared to the pattern of Na-Magadiite (Figure 89 on page 243), no tendency for restoring Na-Magadiite was detected. The interlayer distance of the exchanged SLN2 is the same as that for the unexchanged material. Exchange with sodium seemed to only introduce additional distortions in the atomic structure of the layers of SLN2. Similar results were obtained for the exchange in SLN2 calcined at 650 °C. The results suggested that: (i) the layers of H-Magadiite calcined at 470 °C were cross-linked by siloxane bonds, not allowing the insertion of Na ions; and (ii) the layers of SLN2 were cross-linked by pillars of the intercalating material, which were bonded to the internal silica surfaces by siloxane bonds formed during the thermal treatment of the material at 470 °C.

7.2.6.2 Cobalt exchange

H-Magadiite, Na-Magadiite, and SLN1 calcined at 470 °C as well as at 650 °C were exposed to cobalt solutions. A $0.2.10^{-3}$M solution of $CoCl_2.6H_2O$ was used to prepare a suspension of 50 g of solids per liter of solution. The color of the cobalt remained pink. The results are summarized in Table 10.

When Na-Magadiite was contacted with the cobalt solution, the white color turned to blue after a few minutes. No color changes were observed for the other samples. After 24 hours of exchange, only Na-Magadiite showed a color change; the initial blue turned into a lighter blue. The pH of the Na-Magadiite suspension was 6.9, while the pH's of the other suspensions were approximately 5.2. By adjusting the pH's to approximately 8 with NH_4OH, the light-blue color of Na-Magadiite became grey-dark blue. The white color of H-Magadiite as well as the light-grey color of SLN1 calcined at 650 °C turned to a light-orange/brown color. After 5 hours of exchange, the suspensions were filtered, and the solids air-dried at 100 °C. No other changes in colors were noticed.

Table 10 : Colors of materials exchanged with cobalt ions

Material	Before	During Exchange			After	After heating
	exchange	After 5 min	After 24 hrs	w/NH_4OH	drying	to 850 °C
Na-Magadiite	white	blue	light-blue	grey-blue	grey-blue	dark-grey/blue
Na-Magadiite	white	blue				blue
H-Magadiite	white	white	white	light-orange/ brown	light-orange/ brown	dark-grey/black
SLN1-470	orange-brown	orange-brown	orange-brown	orange-brown	orange-brown	dark-grey/black
SLN1-650	light-grey	light-grey	light-grey	light-orange/ brown	light-orange/ brown	dark-grey/black

After thermal treating the dry materials at temperature up to 850 °C, all the materials were dark-grey/black in color, except for Na-Magadiite which was dark-grey/blue. The dark-grey color indicated the presence of either Co_2O_3 or Co_3O_4. The form of the cobalt prior to thermal treatment was not identified.

In a separate experiment with Na-Magadiite, the suspension was filtered and dried after a one-hour exchange. The product was blue before and dark-blue after the thermal treatment. According to Breck[83], blue is characteristic of dehydrated and pink of hydrated cobalt ions. This suggested that cobalt had been exchanged for sodium in Magadiite, and that cobalt was not sufficiently hydrated to turn into its pink form.

The exchange experiments revealed that (i) no interchange of cobalt for protons had occurred in H-Magadiite and SLN1; (ii) cobalt ions were readily exchanged for sodium ions in Na-Magadiite; and (iii) utilizing NH_4OH to adjust the pH of the exchanging suspension resulted in a material that contained cobalt oxide after thermal treatment at temperatures of approximately 850 °C.

7.2.7 Scanning electron microscopy (SEM)

SEM provided information about the morphology of H-Magadiite and the synthesized compounds. Micrographs were obtained with the scanning electron microscope of the Polymer Group in the Department of Chemical Engineering - VPI.

Figure 106, Figure 107 on page 274, and Figure 108 on page 275 illustrate the effect of reaction conditions in the synthesis of Na-Magadiite on the morphology of H-Magadiite. The H-Magadiites shown in the figures were prepared by the same experimental procedure (section 7.2.2) from Na-Magadiite obtained from three different sources: (i) Dow Chemical (Figure 106); (ii) synthesis at 175 °C (Figure 107 on page 274); and (iii) synthesis at 100 °C (Figure 108 on page 275). The aggregates shown in the figures consist of sheets of H-Magadiite, each sheet containing many layers. Packing of the sheets into aggregates is, however, dependent on the parent Na-Magadiite. Packing changes from a kind of random stack-packing in Figure 107 on page 274 to a

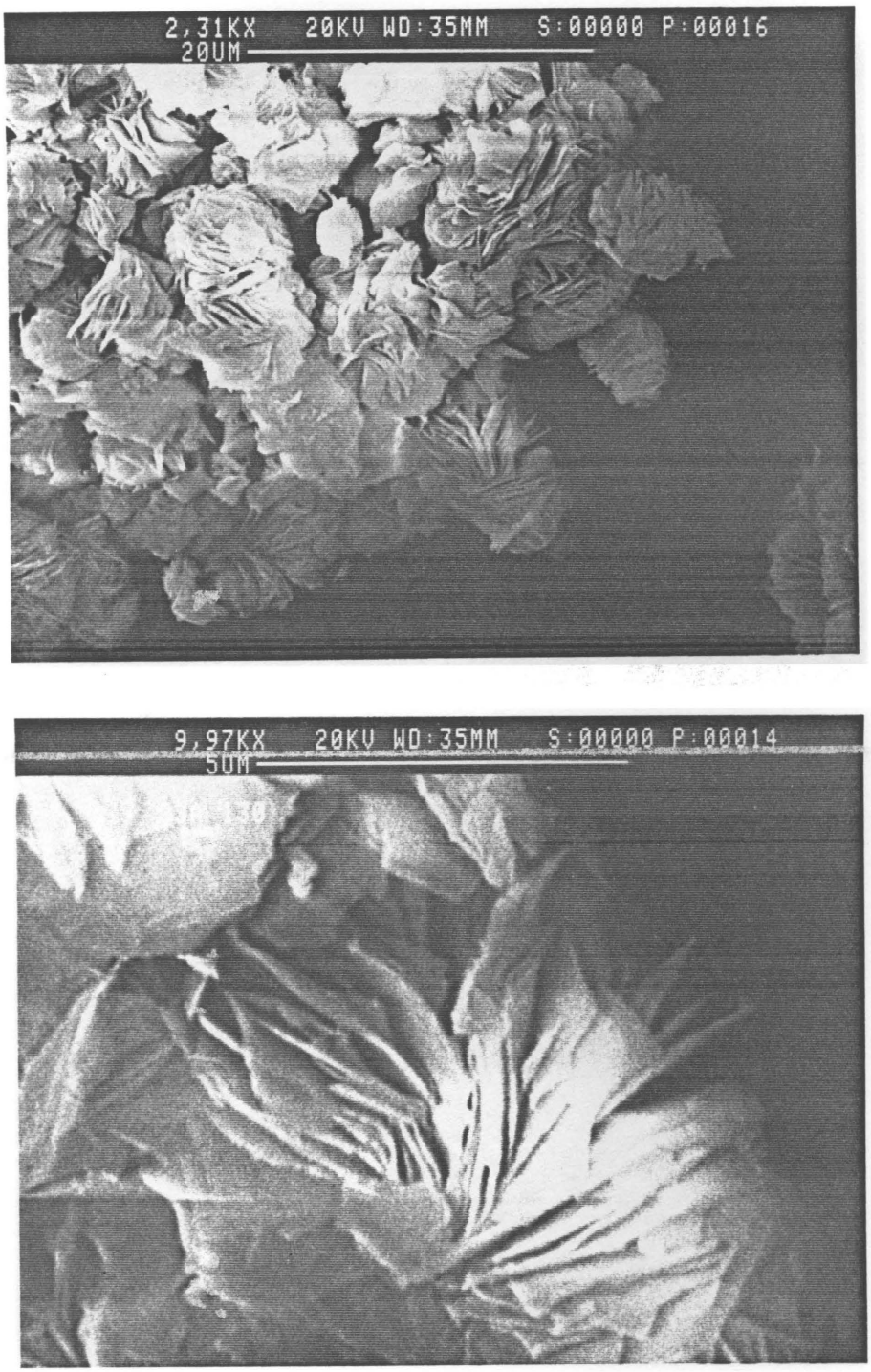

Figure 106. Micrograph of H-Magadiite provided by Dow Chemical Company

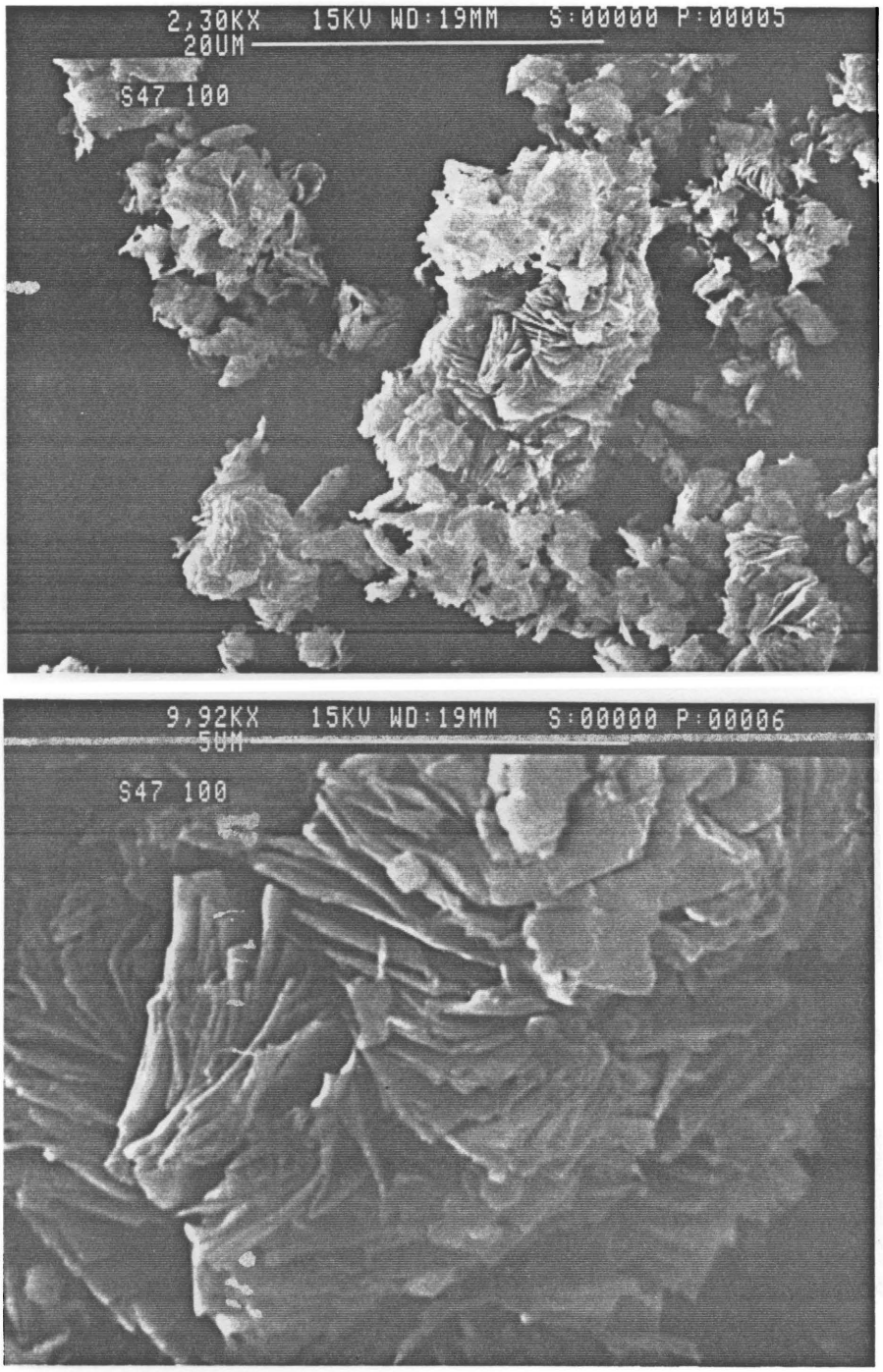

Figure 107. Micrograph of H-Magadiite synthesized at 175 ^{0}C

Figure 108. Micrograph of H-Magadiite synthesized at 100 °C.

packing that tends to form spherical aggregates as in Figure 108 on page 275. H-Magadiite in spherical aggregates had the highest water content and the most intense X-ray reflections at $2\theta <$ 10 degrees. The morphology of the H-Magadiite shown in Figure 108 on page 275 is similar to that reported by Lagaly and Beneke[78]. The effect of morphology on intercalation was not determined.

The micrographs that follow refer to materials whose parent Na-Magadiite was synthesized at 100 °C. Figure 109 shows a micrograph of H-Magadiite after it had been submitted to a TGA at temperatures up to 850 °C. This micrograph indicates the morphology is the same as that of the original H-Magadiite (Figure 108 on page 275).

Figure 110 on page 278, Figure 111 on page 279, and Figure 112 on page 280 exhibit micrographs of SLN1 dried at 150 °C, calcined at 650 °C, and after TGA, respectively. The figures illustrate that: (i) the morphology of SLN1 is similar to that of H-Magadiite; (ii) no new phases were formed during synthesis; (iii) the same morphology was maintained in thermal treatments up to temperatures of 650 °C; and (iv) heating SLN1 to 850 °C (TGA) modified the original morphology.

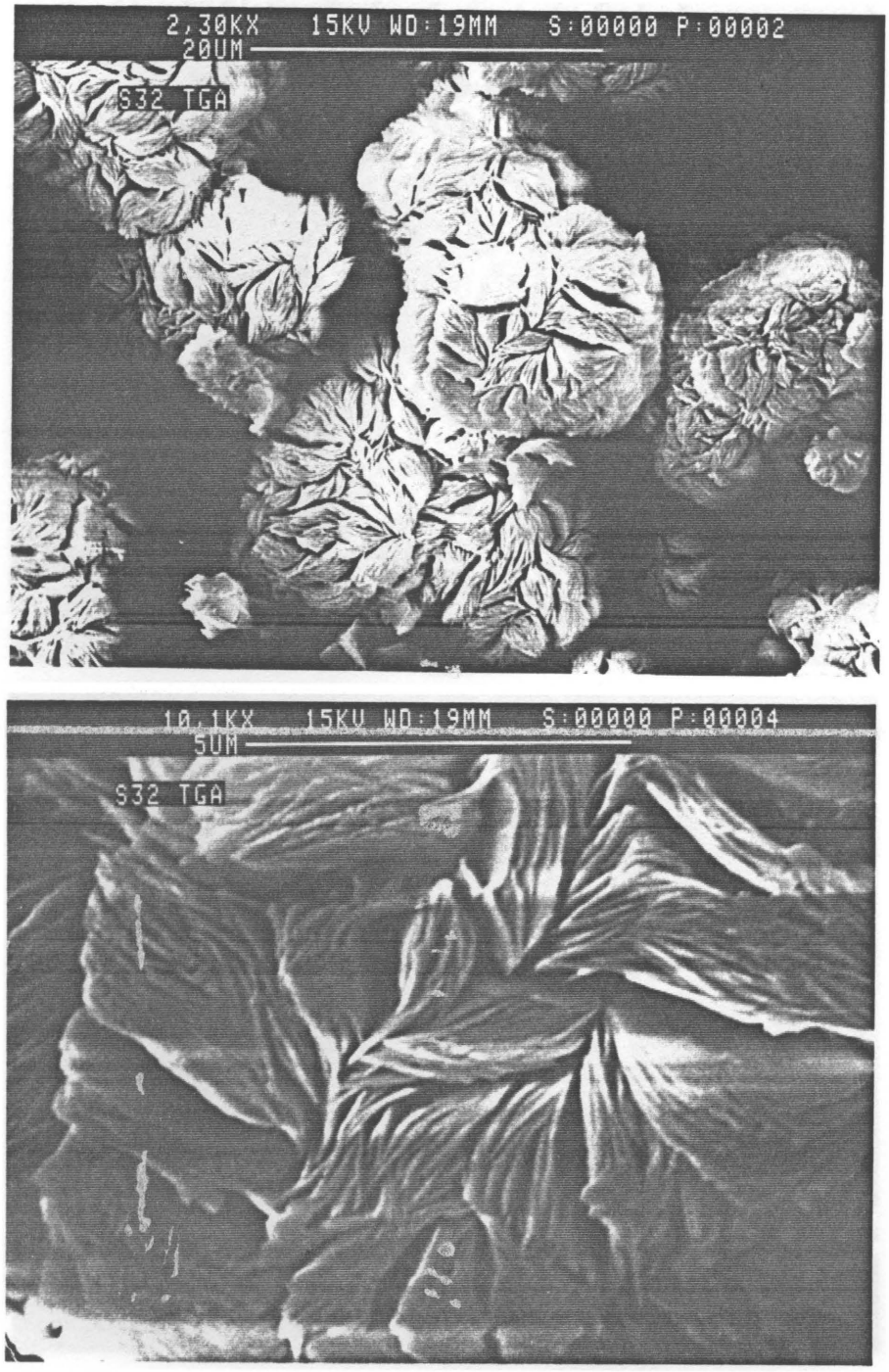

Figure 109. Micrograph of H-Magadiite after TGA (850 °C)

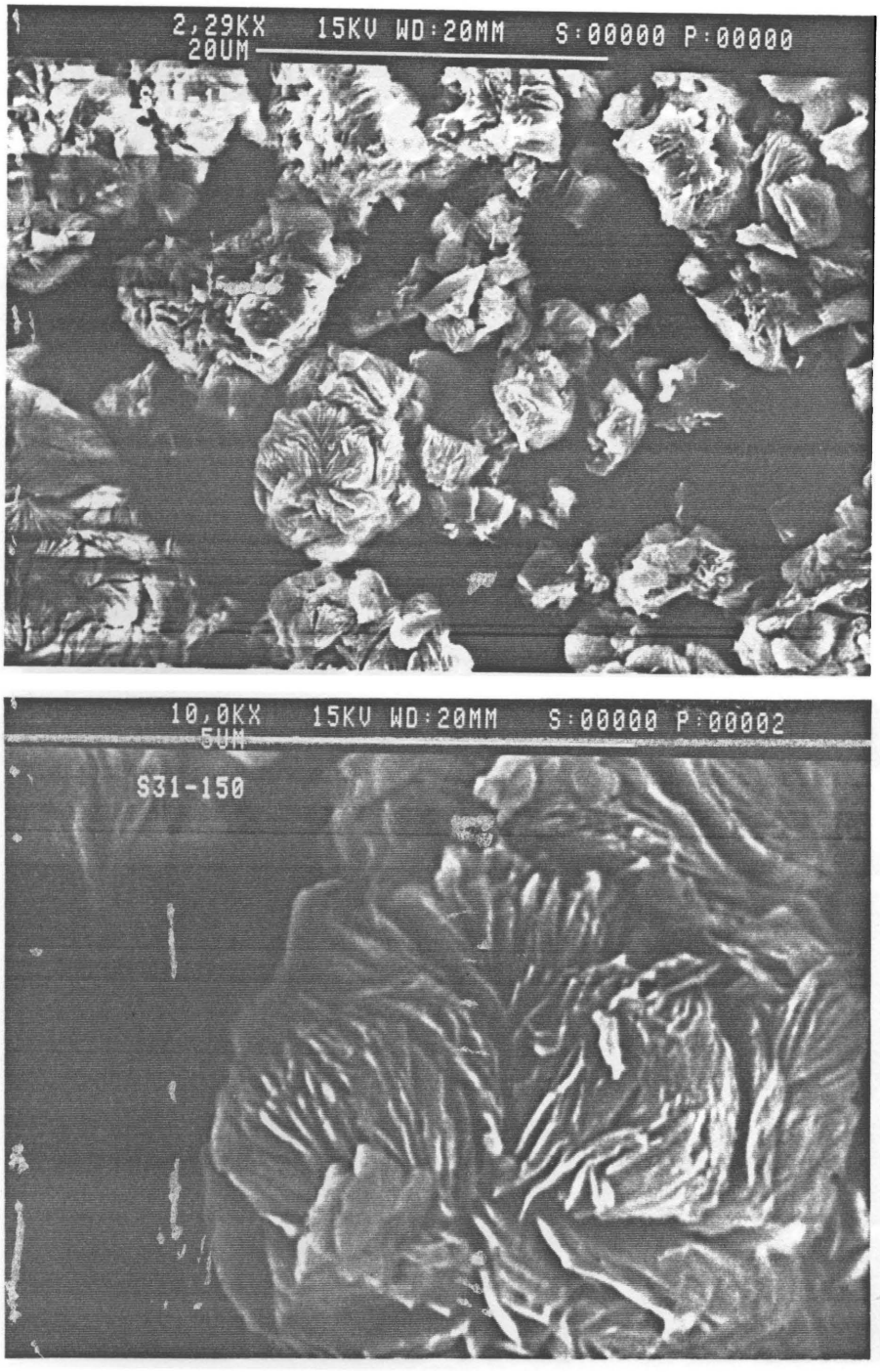

Figure 110. Micrograph of SLN1 dried at 150 °C

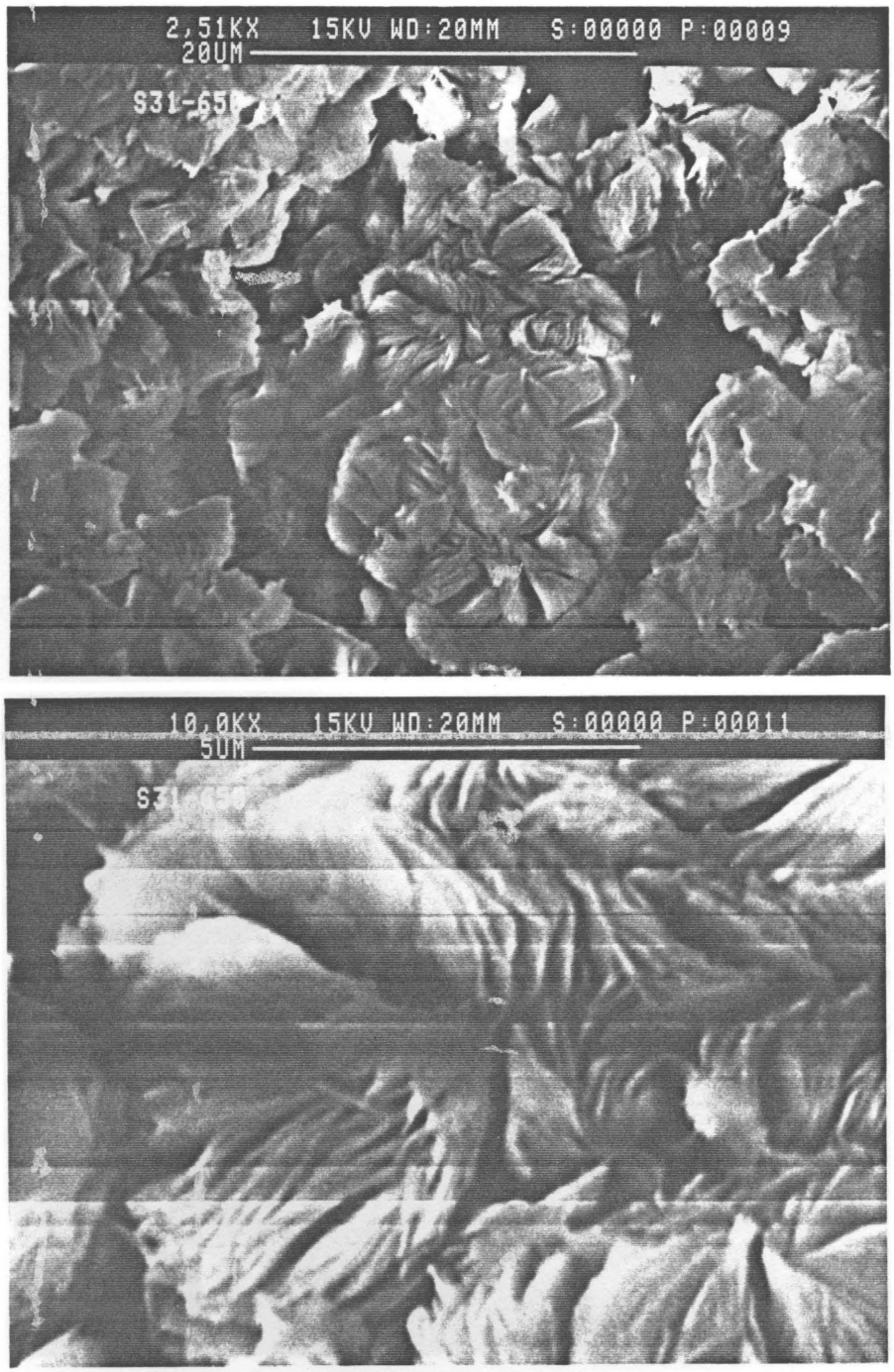

Figure 111. Micrograph of SLN1 calcined at 650 °C

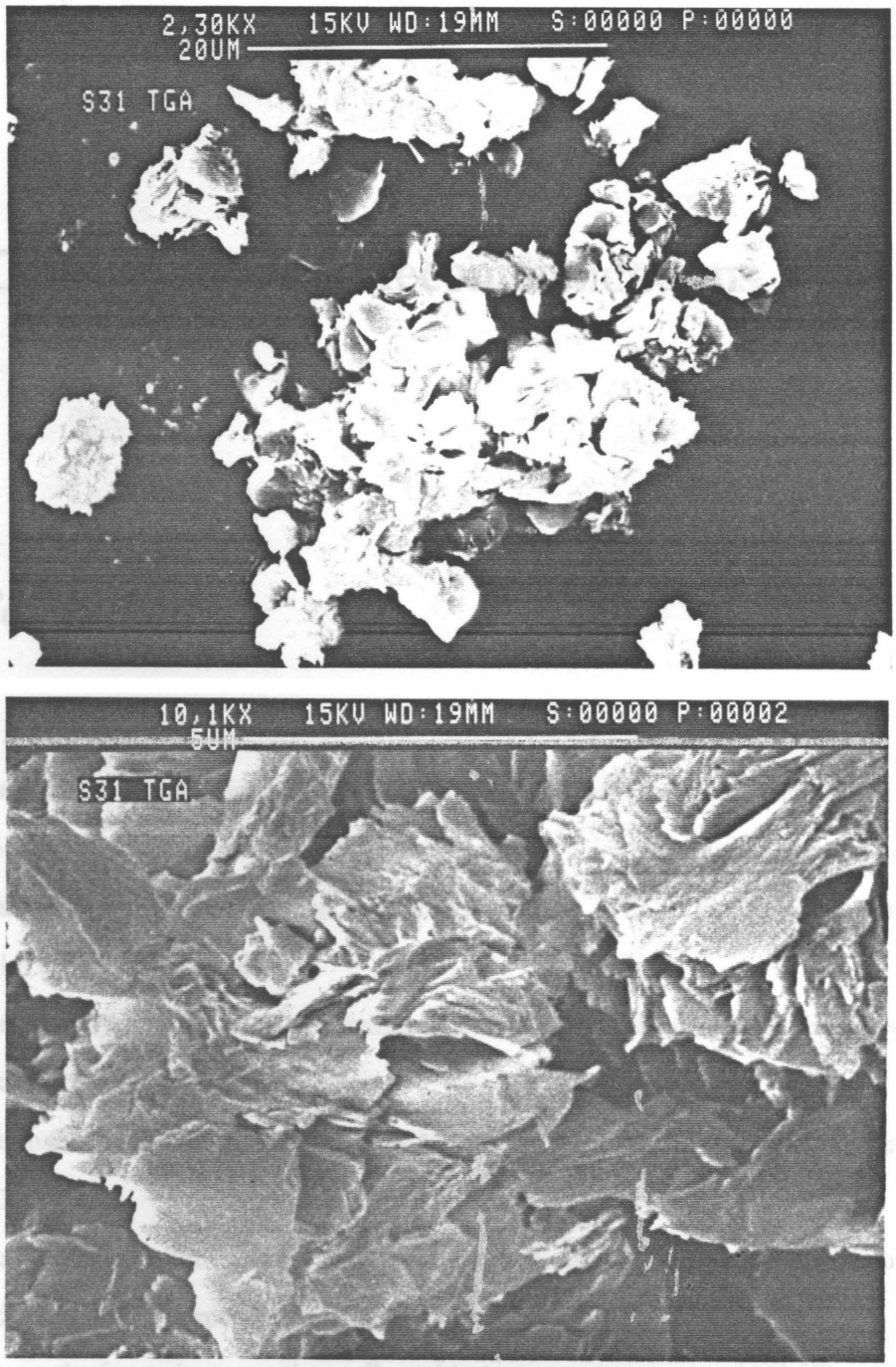

Figure 112. Micrograph of SLN1 after TGA (850 °C)

8.0 Conclusions and Recommendations

8.1 Conclusions

The reactions of organosilicon compounds with H-Magadiite were investigated. H-Magadiite was prepared by exchanging protons for sodium ions in Na-Magadiite. A trisiloxane and two trichlorosilane compounds were used as intercalating agents. The following conclusions were derived from the experimental results:

(1) The interlayer space of H-Magadiite was sucessfully expanded by the intercalation of trichloroorganosilanes.

(2) The insertion of chlorosilanes into H-Magadiite increased its accessible surface area from 35 to 100-200 m^2/g.

(3) The interlayer volume can be accessed through pores with minimum dimensions of 6.? Å and 9.5 Å (dimensions at perpendicular directions).

(4) The synthesis products are thermally stable up to temperatures of 650 ^0C.

(5) The surface areas of the synthesis products are strongly dependent on the pH and the temperature of the intercalating suspension. Low pH and temperatures close to 0 ^0C yield the highest surface areas.

(6) Expansion of the interlayer space of H-Magadiite by reaction with a trisiloxane compound is not possible.

8.2 Recommendations

(1) Analysis of pillared compounds by solid NMR to determine the environment of intercalated silicon atoms.

(2) Preparation of Na-Magadiite at different temperatures between 100 and 175 ^{o}C and determination of the thermal stability as well as surface area and pore size of the resulting pillared compounds.

(3) Further investigation of the effect of utilizing ammonium hydroxide and room temperature in the intercalation process.

(4) Utilization of trichloroorganosilanes with alkyl ligands of varying size in order to control the interpillar spacing.

(5) Investigation of the effect of pH on the exchange of metallic cations for protons in pillared materials.

(6) Extension of the technique of insertion of cobalt oxide into the pillared compound to other metallic oxides, and reduction of the oxide to the corresponding metal by reaction with hydrogen.

(7) Testing of metal-containing pillared compounds as hydrogenation-isomerization catalysts.

Bibliography

1. Pakowski, Z., A. S. Mujumdar, and C. Strumillo, "Theory and Applications of Vibrated Beds and Vibrated Fluid Beds for Drying Processes," *Advances in Drying, Vol. 3*, A. S. Mujumdar, Ed., Hemisphere Publishing Corp., Washington (1984), p. 245.

2. Reed, T. M., and M. R. Fenske, "Effects of Agitation on Gas Fluidization of Solids," *Ind. Eng. Chem.*, **47**, No. 2, 275 (1955).

3. Bretsznajder, S., M. Jaszczak, and W. Pasiuk, "Increasing the Rate of certain Industrial Chemical Processes by the Use of Vibration," *Int. Chem. Eng.*, **3**, No.4, 496 (1963).

4. Bachman, D., *Verfahrenstechnik Z.V.D.I. Beiheft*, No. 2, 43 (1940). (Cited by Gutman[14].)

5. Kroll, W., *Forschung auf der Gebiete des Ingenieurwesen*, **20**, EdA (1), 2 (1954). (Cited by Gutman[14].)

6. Kroll, W., "Fliesserscheinungen an Haufwerken in schwingenden Gefassen," *Chemie Ing. Techn*, **27**, No. 1, 33 (1955).

7. Chlenov, V. A., and N. V. Mikhailov, "A New Principle in the Production of a Fluidized Bed," *Dokl. Akad. Nauk SSSR*, **154**, No. 3, 703 (1964).

8. Chlenov, V. A., and N. V.Mikhailov, "Vibro-Fluidized Bed," *Russian J. Phys. Chem.*, **39**, No. 2, 250 (1965).

9. Lyul'ko, V. G., L. V. Krasnichenko, V. D. Kishko, and V. I. Litvinenko, "Final Reduction Annealing of Iron Powder in a Vibrating Bed," *Poroshk. Metall.*, No. 7, 1 (1979).

10. Kossenko, G. D., E. G. Reshetnikov, N. I. Syromjatnikov, and B. G. Sapozhnikov, "Model Studies of Tube-to-Bed Heat Transfer in a Vibro-fluidized Bed," *Institute of Fuel Symposium Series No.1: Fluidized Combustion*, B4-1 (1975).

11. Mal'chenko, V. M., and V. M. Bograd, "Heat Transfer in a Recuperative Heat Exchange Employing Fluidized Solid Spheres Conveyed by Vibration over a Closed Loop," *Heat Transfer - Soviet Research*, **8**, No. 5, 133 (1976).

12. Bukareva, M. F., V. A. Chlenov, and N. V. Mikhailov, "The Drying of Finely Dispersed Powders in Vibro-fluidized Beds," *Int. Chem. Eng.*, **10**, No. 3, 384 (1970).

13. Strumillo, C., and Z. Pakowski, "Drying of Granular Products in Vibro-fluidized Beds," *Drying'80, Vol. 1: Developments in Drying*, A. S. Mujumdar, Ed., Hemisphere Publishing Corp., Washington, 211 (1980).

14. Gutman, R. G., "Vibrated Beds of Powders," Ph.D. Dissertation, University of Cambridge, England (1974).

15. Xavier, A. M., and J. F. Davidson, "Heat Transfer in Fluidized Beds: Convective Heat Transfer in Fluidized Beds," *Fluidization, 2nd. Edition*, J. F. Davidson, R. Clift, and D. Harrison, Eds., Academic Press Inc., Florida, 437 (1985).

16. Botterill, J. S. M., *Fluid-Bed Heat Transfer*, Academic Press Inc., New York (1975).

17. Grace, J. R., "Fluidized-Bed Heat Transfer," *Handbook of Multiphase Systems*, G. Hetsroni, Ed., Hemisphere Publishing Corp., Washington (1982), p. 8-65.

18. Zabrodsky, S. S., *Hydrodynamics and Heat Transfer in Fluidized Beds*, The M.I.T. Press, Cambridge, Massachusetts (1966).

19. Mikolajczuk, A., *Biul. Inf. IChP.*, **22**, 9 (1974). (Cited by Pakowski et al.[1].)

20. Chlenov, V. A., and N. V. Mikhailov, "Some Properties of a Vibrating Fluidized Bed," *Inzh.-Fiz. Zh.*, **9**, No. 2, 196 (1965).

21. Belyi, V. A., and O. R. Yurkevich, "Estimating the Specific Weight and Initial State of a Bed of Polymer Material," *Inzh.-Fiz. Zh.*, **14**, No. 1, 55 (1968).

22. Ryzhkov, A. F., A. P. Baskakov, and V. A. Munts, "Heat Transfer from a Hot Surface to a Vibrated Fluidized Bed," *Heat Transfer - Soviet Research*, **8**, No. 5, 136 (1976).

23. Ivashchenko, V., and I. Golubev, *Poroshkovaya Metallurgiya*, No. 12, 13 (1965). (Cited by Gutman[14].)

24. Gutman, R. G., "Vibrated Beds of Powders Part I: A Theoretical Model for the Vibrated Bed," *Trans. Instn. Chem. Engrs.*, **54**, 174 (1976).

25. Chlenov, V. A., and N. V. Mikhailov, *Vibrokipyashchii Sloi*, (Vibro-fluidized beds), Izdatel'stvo Nauka, Moscow (1972). (Cited by Pakowski et al.[1].)

26. Bukareva, M. F., D. A. Tatevosyan, V. A. Chlenov, and N. V. Mikhailov, *Teoret. Osn. Khim. Teknol.*, 1 (1974). (Cited by Pakowski et al.[1].)

27. Bukareva, M. F., V. A. Chlenov, and N. V. Mikhailov, "Investigation of Heat Transfer between Heating Surfaces and a Vibro-Fluidized Bed," *Int. Chem. Eng.*, **9**, No. 1, 119 (1969).

28. Buevich, Yu. A., A. F. Ryzhkov, and N. M. Kharisova, "Instability of a Vibrational Fluidized Bed," *Inzh.-Fiz. Zh.*, **37**, No. 4, 626 (1979).

29. Gutman, R. G., and J. F. Davidson, "Darcy's Law for Oscillatory Flow," *Chem. Eng. Sci.*, **30**, 89 (1975).

30. Buevich, Yu. A., and V. L. Galontsev, "Vibrational Fluidization of a Shallow Granular Bed," *Inzh.-Fiz. Zh.*, **34**, No. 3, 394 (1978).

31. Hirt, D., C. W. Cheah, Y. A. Liu, and A. M. Squires, "A Vibrofluidized-Bed Heat Exchanger for Heat Recovery from a Hot Gas. Part I. Feasibility Study of a Pilot-Scale System," *Powder Technology*, in press (1987).

32. Markovskii, V. M., B. G. Sapozhnikov, and N. I. Syromyatnikov, *Teoret. Osn. Khim. Teknol.*, 6 (1969). (Cited by Pakowski et al.[1].)

33. Gray, W. A., and G. T. Rhodes, "Energy Transfer during Vibratory Compaction of Powders," *Powder Tecnol.*, No. 6, 271 (1972).

34. Ryzhkov, A. F., and A. P. Baskakov, "Equations of Motion of the Material in a Shaker," *Inzh.-Fiz. Zh.*, **27**, No. 1, 15 (1974).

35. Ryzhkov, A. F., and A. P. Baskakov, "Motion of a Granular Material in a Tall Vibrating System," *Inzh.-Fiz. Zh.*, **34**, No. 6, 1048 (1977).

36. Sapozhnikov, B. G., Ye. G. Reshetkov, G. D. Kosenko, and N. M. Kharisova, "Investigation of Local Coefficients of Heat Transfer from Bundles of Horizontal Tubes to a Vibrated Fluidized Bed," *Heat Transfer - Soviet Research*, **8**, No. 5, 141 (1976).

37. Malhotra, A., and A. S. Mujumdar, "Flow Patterns for Cylinders Immersed in an Aerated Vibrated Bed," *Can. J. Chem. Eng.*, **63**, 22 (1985).

38. Suzuki, A., H. Takahashi, and T. Tanaka, "Behavior of a Particle Bed in a Field of Vibration II. Flow of Particles through Slits in the bottom of a Vibrating Vessel," *Powder Technol.*, **2**, 72 (1968/69).

39. Geldart, D., "Types of Gas Fluidization," *Powder Technol.*, **7**, 285 (1973)

40. Yoshida, T., and Y. Kousaka, "Mechanism of Vibratory Packing of Granular Solids," *Kagaku Kogaku*, **30**, 1019 (1966).

41. Ringer, D. U., "Calculation of Heat Transfer in Vibrating Conveyors," *Drying'80, Vol. 2: Proceedings of the Second International Symposium*, A. S. Mujumdar, Ed., Hemisphere Publishing Corp., Washington (1980), p. 144.

42. Muchowski, E., "Heat Transfer from the Bottoms of Vibrated Vessels to Packings of Spheres at Atmospheric Pressure and under Vacuum," *Int. Chem. Eng.*, **20**, No. 4, 564 (1980).

43. Zabrodskii, S. S., I. L. Zamnius, S. A. Malyukovich, and A. I. Tamarin, "The Transfer of Heat from a Bed of Finely Dispersed Material Fluidized by a Stream of Gas or through Application of Vibrations," *Inzh.-Fiz. Zh.*, **14**, N0. 3, 448 (1968).

44. Kal'tman, I. I., and A. I. Tamarin, "Investigating the Transfer of Heat between a Vibration-Fluidised Bed of Disperse Material and a Body that is Being Cooled within This Material," *Inzh.-Fiz. Zh.*, **16**, No. 4, 630 (1969).

45. Zamnius, I., A. Tamarin, and S. Zabrodskii, *Teplo i Massoperenos*, Nauka i Tekhnika, Minsk, **5**, 142, (1968) (Cited by Gutman[14]).

46. Sapozhnikov, V. G., and N. I. Syromyatnikov, "Study of Heat Transfer in Pulsating Bed under Vacuum," *Heat Transfer-Soviet Research*, **1**, No. 6, 22 (1969).

47. Sapozhnikov, B. G., and N. I. Syromyatnikov, "Investigating the Effective Thermal Conductivity of a Vibrating Bed in a Vacuum," *Inzh.-Fiz. Zh.*, **16**, No. 6, 1039, (1969).

48. Gutman, R.G., "Vibrated Beds of Powders: Part II - Heat Transfer in and Energy Dissipation of a Vibrated Bed," *Trans. Instn. Chem. Engrs.*, **54**, 251 (1976).

49. Mickley, H., and D. Fairbanks, "Mechanism of Heat Transfer to Fluidized Beds," *AIChE J.*, **1**, No. 3, 374 (1955).

50. Sprung, R., B. Thomas, Y. A. Liu, and A. M. Squires, "Shallow Vibrated Beds of Master Beads," *Fluidization V: Proceedings of the Fifth Engineering Foundation Conference on Fluidization, Denmark*, K. Ostergaard and A. Sorensen, Eds., Engineering Foundation, New York (1986), p. 417.

51. Thomas B., R. Sprung, Y. A. Liu, and A. M. Squires, "Heat Transfer from a Heated Tube in Shallow Vibrated Beds," *AIChE Annual Meeting: Symposium on Fundamentals of Fluidization and Fluid-Particle Systems*, Miami, Florida (1986).

52. Huang, H. H., "Heat Transfer between a Shallow Fluidized Bed and a Single Horizontal Tube Immersed in the Bed," Master Thesis, Virginia Polytechnic Institute and State University, United States (1983).

53. Incropera, F. P. and D. P. De Witt, *Fundamentals of Heat Transfer*, John Wiley and Sons (1981).

54. Dwyer, J., "Zeolite Structure, Composition and Catalysis," *Chem. & Ind.*, **7**, 258 (1984).

55. Greenwood, N. N., and A. Earnshaw, *Chemistry of the Elements*, Pergamon Press, New York (1986), p. 412.

56. Rupert, J. P., W. T. Granquist, and T. J. Pinnavaia, "Catalytic Properties of Clay Materials," *Chemistry of Clays and Clay Materials*, A. C. D. Newman, Ed., Wiley-Interscience, New York (1987), p.275.

57. Thomas, C. L., *Catalytic Processes and Proven Catalysts*, Academic Press, New York (1970), p. 173.

58. Swift, H. E., "Catalytic Properties of Synthetic Layered Silicates and Alumino-Silicates," *Advanced Materials in Catalysis*, J. J. Burton and R. L. Garten, Eds., Academic Press, New York (1977), p. 209.

59. Granquist, W. T., "Synthetic Silicate Materials," *US Pat. 3,252,757* (1966).

60. Capell, R. G., and W. T. Granquist, "Cracking Catalyst and Process of Cracking," *US Pat. 3,252,889* (1966).

61. Granquist, W. T., *US Pat. 3,852,405* (1974).

62. Black, E. R., and H. E. Swift, *Ind. Eng. Chem.*, **13**, 106 (1974).

63. Whittingham, M. S., "Intercalation Chemistry: An Introduction," *Intercalation Chemistry*, M. S. Whittingham and A. J. Jacobson, Eds., Academic Press, New York (1982), p. 1.

64. Barrer, R. M., and D. N. McLeod, "Activation of Montmorillonite by Ion Exchange and Sorption Complexes of Tetraalkylammonium Montmorillonites," *Trans. Faraday Soc.*, **51**, 1290 (1955).

65. Barrer, R. M., *Zeolites and Clay Minerals as Sorbents and Molecular Sieves*, Academic Press, New York (1978), p. 461.

66. Brindley, G. W., and R. E. Sempels, "Preparation and Properties of Some Hydroxy-Aluminum Beidellites," *Clays and Clay Minerals*, **12**, 229 (1977).

67. Lussier, R. J., J. S. Magee, and D. E. W. Vaughan, "Pillared Interlayered Clay Cracking Catalyst - Preparation and Properties," *7th Canadian Symposium on Catalysis*, Edmonton, Alberta (1980), p. 88.

68. Yamanaka, S., and G. M. Brindley, "High Surface Area Solids Obtained by Reaction of Montmorillonite with Zirconyl Chloride," *Clays and Clay Minerals*, **27**, 119 (1979).

69. Brindley, G. W., and S. Yamanaka, "A Study of Hydroxy-Chromium Montmorillonites and the Form of the Hydroxy-Chromium Polymers," *Amer. Mineral.*, **64**, 830 (1979).

70. Sterte, J., "Synthesis and Properties of Titanium Oxide Cross-Linked Montmorillonite," *Clays and Clay Minerals*, **34**, No. 6, 658 (1986).

71. Endo, T., M. M. Mortland, and T. J. Pinnavaia, "Intercalation of Silica in Smectite," *Clays and Clay Minerals*, **28**, 105 (1980).

72. Endo, T., M. M. Mortland, and T. J. Pinnavaia, "Properties of Silica-Intercalated Hectorite," *Clays and Clay Minerals*, **29**, 153 (1981).

73. Lewis, R. M., K. C. Ott, and R. A. Van Santen, "Silica-Clay Complexes," *US Pat. 4,510,257* (1985).

74. Eugster, H. P., "Hydrous Sodium Silicates from Lake Magadi, Kenya: Precursors of Bedded Chert," *Science*, **157**, 1177 (1967).

75. Lagaly, G., K. Beneke, and A. Weiss, "Organic Complexes of Synthetic Magadiite," *Proc. Int. Clay Conf. Madrid 1972*, Madrid (1973), p.663.

76. Lagaly, G., and K. Beneke, "Magadiite and H-Magadiite: I. Sodium Magadiite and Some of Its Derivatives," *Amer. Mineral.*, **60**, 642 (1975).

77. Lagaly, G., and K. Beneke, "Magadiite and H-Magadiite: II. H-Magadiite and Its Intercalation Compounds," *Amer. Mineral.*, **60**, 650 (1975).

78. Lagaly, G., "Crystalline Silicic Acids and Their Interface Reactions," *Adv. in Colloid and Interf. Sci.*, **11**, 105 (1979).

79. Rojo, J. M., E. Ruiz-Hitzky, J. Sanz, and J. M. Serratosa, "Characterization of Surface Si-OH Groups in Layer Silicic Acids by IR and NMR Spectroscopy," *Rev. Chem. Minerale*, **20**, 807 (1983).

80. Arkles, B., "Silane Coupling Agent Chemistry," *Silicon Compounds: Register and Review*, Petrarch Systems, Inc., Pennsilvania (1984), p. 71.

81. Saldarriaga, C., *Personal Communication*, Department of Chemical Engineering, Virginia Polytechnic Institute and State University (1986).

82. Brindley, G. W. "Unit Cell of Magadiite in Air, in Vacuo, and under Other Conditions," *Amer. Mineral.* 54, 1583 (1969).

83. Breck, D. W., *Zeolite Molecular Sieves*, R .E. Krieger Publ. Co., Florida (1984), p.636.

84. McCauley, J. R., *Catalytic Cracking Properties of Cross-Linked Montmorillonite (CLM) Molecular Sieves*, Master Thesis, University of Utah (1983), p. 30.

85. Dean, J. A., Editor, *Lange's Handbook of Chemistry*, 13th Edition, McGraw-Hill Book Co. (1985).

The two page vita has been removed from the scanned document. Page 1 of 2

The two page vita has been removed from the scanned document. Page 2 of 2